technische universität
dortmund

Dissertation

Polarization- and time-resolved nonlinear optical spectroscopy of excitons in Cu_2O

submitted in partial fulfillment of the
requirements for the degree of

Dr. rer. nat.

to the Faculty of Physics of the
TU Dortmund University, Germany

by

Andreas Farenbruch

Dortmund, March 2023

Accepted by the Faculty of Physics of the TU Dortmund University, Germany.

Day of the oral examination: 17th May 2023

Examination board:

Prof. Dr. Dmitri R. Yakovlev
Dr. Doris Reiter
Prof. Dr. Shaukat Khan
Prof. Dr. Zhe Wang

External Reviewer:

Prof. Dr. Bernhard Urbaszek

Polarization- and time-resolved nonlinear optical spectroscopy of excitons in Cu_2O

Contents

Abstract

Excitons are Coulomb-bound states of a negatively charged electron in the conduction band and a positively charged hole in the valence band of a semiconductor or an insulator. Their hydrogen-like absorption spectrum was first detected in 1951 in cuprous oxide (Cu_2O). In 2014, a spectral scan using an ultra-narrow bandwidth laser extended the P exciton series in a natural Cu_2O crystal to a principal quantum number of $n = 25$. This breakthrough opened up the field of Rydberg physics in semiconductors leading to numerous experimental and theoretical studies investigating their behavior in external fields as well as exciton-plasma and exciton-exciton interactions.

The present study reports on second harmonic generation (SHG) spectroscopy of dark- and bright excitons in Cu_2O. SHG is forbidden for laser light propagating along the high-symmetry [110] and [001] crystal axis. By applying a magnetic field up to 10 T perpendicular to the light direction, SHG becomes allowed due to the Zeeman- (ZE) and magneto-Stark effect (MSE). The polarization selection rules for both mechanisms are derived from point group theory considerations. The linear polarization angles of the incoming and outgoing light can be controlled in order to differentiate between both SHG mechanisms.

The spin-forbidden dark paraexcitons are activated by admixture of the $M = 0$ component of the bright orthoexcitons in a magnetic field. The Rydberg series of dark paraexcitons up to a quantum number of $n = 6$ is detected using this method. Due to the electron-hole exchange interaction, the paraexcitons are generally located energetically below the orthoexcitons. This order is found to be reversed for the $n = 2$ state due to mixing of the yellow $2S$ orthoexciton with the green $1S$ orthoexciton.

The blue series of excitons involves the same valence band as the yellow series but the second-lowest conduction band. Accessing these states using linear optical spectroscopy is challenging due to the high absorption in this spectral range. MSE and ZE-induced SHG has been shown to be a suitable investigation method enabling the detection of blue $1S$, $2S$, and $2P$ excitons and magneto-excitons up to $n = 8$. By analyzing their magnetic-field shift and polariton effect, key properties of blue excitons, such as the resonance energies, the exciton radius, the band gap, the reduced exciton mass, and the anisotropic conduction band mass, are obtained.

Difference frequency generation with two-photon excitation (2P-DFG) allows experimental investigations of excitons in the time domain. The pulses of the first laser induce a coherent exciton population by a two-photon excitation process. The pulses of the second laser stimulate the emission of photons with the energy difference between the excitons and the stimulating photons. By delaying the pulses of the second laser, the 2P-DFG signal is measured as a function of time. This technique is used to measure the coherence times of $1S$ and higher n excitons and magnetic-field-induced quantum beats of the three $1S$ orthoexciton states.

Zusammenfassung

Exzitonen sind Coulomb-gebundene Zustände eines negativ geladenen Elektrons im Leitungs- und positiv geladenen Lochs im Valenzband eines Halbleiters oder Isolators. Ihr wasserstoffähnliches Absorptionsspektrum wurde 1951 erstmals in Kupferoxydul (Cu_2O) nachgewiesen. Die P-Exziton-Serie wurde 2014 über einen spektralen Scan mit einem schmalbandigen Laser an einem natürlichen Cu_2O-Kristall auf eine Hauptquantenzahl von $n = 25$ erweitert. Dies eröffnete das Forschungsfeld der Rydberg-Physik in Halbleitern und führte zu zahlreichen experimentellen und theoretischen Untersuchungen in externen Feldern sowie zur Wechselwirkung von Exzitonen mit einem Elektronplasma und anderen Exzitonen.

Hier berichten wir über die Spektroskopie an dunklen und hellen Exzitonen in Cu_2O durch die Erzeugung der optischen zweiten Harmonischen [second harmonic generation (SHG)]. SHG ist für Laserlicht, das entlang der Kristallachsen [110] und [001] eingestrahlt wird, verboten. Durch Anlegen eines Magnetfelds bis zu 10 T senkrecht zur Einstrahlrichtung wird SHG durch den Zeeman- (ZE) und den Magneto-Stark-Effekt (MSE) erlaubt. Für beide Mechanismen werden die Polarisations-Auswahlregeln aus Symmetriebetrachtungen abgeleitet. Die Winkel des linear polarisierten ein- und ausfallenden Lichts können so eingestellt werden, dass zwischen den jeweiligen SHG-Mechanismen unterschieden werden kann.

Die spinverbotenen dunklen Paraexzitonen werden durch Beimischung des $M = 0$-Anteils der hellen Orthoexzitonen in einem Magnetfeld aktiviert. Die Rydberg-Serie der dunklen Paraexzitonen wird mit dieser Methode bis zu einer Hauptquantenzahl von $n = 6$ detektiert. Aufgrund der Elektron-Loch-Austauschwechselwirkung liegen die Paraexzitonen energtisch unterhalb der zugehörigen Orthoexzitonen. Diese Ordnung wird für den $n = 2$ Zustand aufgrund der Mischung des gelben $2S$ und des grünen $1S$ Orthoexzitons invertiert.

An der blauen Exziton-Serie ist das gleiche Valenzband wie bei der gelben Serie beteiligt, aber das nächsthöhrere Leitungsband. Die Detektion dieser Zustände durch lineare optische Spektroskopie stellt aufgrund der hohen Absorption in diesem spektralen Bereich eine Schwierigkeit dar. MSE und ZE-induzierte SHG ist eine geeignete Untersuchungsmethode, um die Detektion von blauen $1S$, $2S$ und $2P$ Exzitonen und Magneto-Exzitonen bis $n = 8$ zu ermöglichen. Durch Analyse ihrer magnetfeldinduzierten Verschiebung und des Polariton-Effekts werden die Resonanzenergien, der Exzitonradius, die Bandlücke, die reduzierte Exzitonmasse und die anisotropen Leitungsbandmassen der blauen Exzitonen ermittelt.

Die Differenzfrequenzerzeugung mit Zweiphotonenanregung (2P-DFG) ermöglicht zeitaufgelöste experimentelle Untersuchungen an Exzitonen. Die Pulse des ersten Lasers erzeugen durch einen Zweiphotonenanregungsprozess eine kohärente Exzitonpopulation. Die Pulse eines zweiten Lasers stimulieren die Emission von Photonen mit der Energie-Differenz zwischen den Exzitonen und den stimulierenden Photonen. Durch Verzögerung der Pulse des zweiten Lasers wird das 2P-DFG-Signal in Abhängigkeit der Zeit gemessen. Diese Methode wird verwendet, um die Kohärenzzeiten des $1S$ und höherer Exzitonen sowie magnetfeldinduzierte Quantenbeats der drei $1S$ Orthoexziton-Zustände zu messen.

Chapter 1

Introduction

Semiconductors have revolutionized a wide range of technologies and have become an integral part of our daily lives. Their electrical conductivity can be modified by introducing dopant atoms into their crystal structure. This property lead to the development of the first transistor by Shockley, Bardeen, and Houser Brattain [Bar+48], which is one of the most influential inventions of the 20th century as it accelerated the rate of technological progress. Nowadays, semiconductor materials serve as the fundamental building blocks of electronic devices in the form of processor chips and data storage elements. Not only their tunable electrical conductivity is exploited for applications, but also their optical properties, which are the basis for the light emitting diodes [Dho+20] and solar cells [Sha+15]. Their optical properties are influenced by the excitonic states, which are formed when an electron is excited from the valence into the conduction band, leaving a hole in the valence band. Due to the attractive Coulomb force between their opposite charges, they are bound into hydrogen-like states, analogously described using the principal, angular momentum, and magnetic quantum numbers n, L, and M. They have been theoretically predicted by Frenkel [Fre31] and Wannier [Wan37] in the 1930s. Gross et al. [Gro+52; Gro56] and Hayashi et al. [Hay+50; Hay+52] conducted the first experiments on the so-called yellow exciton series in cuprous oxide (Cu_2O) up to $n = 8$. Measurements of their white light absorption spectrum indicated an n^{-2} scaling of the binding energy similar to the absorption spectrum of hydrogen atoms. The energy series of these odd-parity $P\,(L = 1)$ exciton states has recently been extended to $n = 25$ [Kaz+14], later even to $n = 28$ [Hec+20] and $n = 30$ [Ver+21]. These high n states have diameters up to 3 µm and are called Rydberg excitons. Their experimental discovery opened up the field of Rydberg physics in semiconductors [Aßm+20], a research area previously limited to atoms [Gal94]. The highest n Rydberg exciton state in any other material is $n = 5$ in WS_2 [Che+14]. Therefore Cu_2O is a well-suited host material for investigations of phenomena involving excitons. Numerous theoretical and experimental studies on Rydberg excitons have been performed in recent years involving the influence of externally applied electric [Hec+17a; Hec+18b] and magnetic fields [Rom+20a; Sch+17a; Rom+18; Hec+17b; Hec+18c; Zie+19; Zie+21] and the exciton-plasma [Hec+18a; Sem+19] and exciton-exciton interaction [Wal+18]. Before the Rydberg series has been extended to such high n, the electric quadrupole allowed $1S$ exciton has received a lot of research interest in the two-photon spectroscopy community [Got+97; Frö+87; Kon+96; Nak+99; Nak+00; Liu+05].

The investigations in recent years would not have been possible without the invention of the laser developed by Maiman et al. [Mai60]. The high-intensity coherent radiation allowed the advancement of experimental research in the field of nonlinear optics, which includes processes such as second harmonic generation (SHG), sum frequency generation (SFG),

difference frequency generation (DFG), and four-wave mixing (FWM). Optical harmonics generation is an excellent method for investigations of exciton states in semiconductors [Yak+18]. In this work, we will mainly focus on SHG, which was first demonstrated experimentally in quartz by Franken et al. in 1961 [Fra+61]. It is a coherent conversion of two incoming photons into one outgoing photon of twice the energy and is very sensitive to the symmetry of the addressed quantum state and the photon transitions, as both the two-photon excitation and the single-photon emission processes need to be symmetry allowed. Initially forbidden SHG processes may become allowed by reducing the symmetry of the system by introducing perturbations or changing the crystal axis, along which the laser light is linearly polarized or directed. An understanding of the underlying symmetries can be accessed by measuring the SHG signal intensity as a function of the linear polarization angles ψ and φ of the incoming laser light and outgoing SHG light. If the experimentally acquired polarization diagrams are in good agreement with a simulation that relies on derived polarization selection rules, it suggests that the assumed mechanism and the underlying symmetries are correct.

Previous results on SHG spectroscopy of excitons in external magnetic fields have been achieved using nanosecond pulses emitted by an Nd:YAG laser and tuned in wavelength by an optical parametric oscillator. Various materials such as ZnO [Laf13; Kam10], ZnSe [War+18], GaAs [Sän06; Bru14; War+18], GaN [Bru14], EuTe and EuSe [Laf13; Kam10], CdTe [Sän06] and Cu_2O [Bru14] have been investigated with this setup.

For this work, a more advanced setup is used, which is equipped with a laser system producing high peak intensity femtosecond and picosecond pulses, which are tunable through a wide spectral range from ultra-violet to infrared light, as will be described in chapter 3. It is optimized for nonlinear optical SHG and two-color experiments on various exciton states, as will be presented in chapters 4-7. First nonlinear optical experiments using this setup have been performed by Johannes Mund et al. [Mun19] on ZnO/(Zn,Mg)O and ZnSe/BeTe quantum wells as well as on bulk Cu_2O and ZnSe. The new fixed-wavelength femtosecond pulse method [Mun+18] for measuring SHG spectra was introduced as an alternative to the nanosecond pulse spectral scanning method of previous studies mentioned above. This enabled Mund et al. to acquire high-resolution SHG spectra of even-parity S and D envelope excitons up to $n = 9$ in Cu_2O. Using the point group theory tables of Koster et al. [Kos+63], the SHG intensity was simulated as a function of the linear polarization angles for SHG processes involving even and odd-parity excitons.

A major focus of this work is the extension of polarization selection rules to magnetic-field-induced SHG mechanisms and to other nonlinear optical processes. In previous studies, the SHG intensity was measured only for tuning the linear polarization angles of laser and SHG light in parallel ($\psi = \varphi$) and crossed ($\psi = \varphi + 90°$) configurations from 0° to 360° degrees. For the first time, we will measure and simulate the SHG intensity as a function of all possible combinations of ψ and φ and plot it as two-dimensional diagrams. This will open up more possibilities for identifying new mechanisms, distinguishing between them, and finding (ψ/φ) combinations, which only allow SHG of a single mechanism and suppress all others. This method will turn out to be a powerful tool for magneto-optical spectroscopy of excitons in Cu_2O.

In chapter 4 the polarization selection rules for magnetic-field-induced SHG of yellow-series excitons will be derived and the polarization dependence will be measured for several SHG mechanisms. We choose a sample oriented in such a way, that SHG is symmetry-

forbidden at zero magnetic fields. The Zeeman effect (ZE) and magneto-Stark effect (MSE) are identified as the SHG-inducing mechanisms in a magnetic field.

In chapter 5 we discuss SHG mechanisms of spin-forbidden dark excitons (the so-called paraexcitons), which do not interact with the light field. By applying a magnetic field perpendicular to the laser light direction, optically active components of bright excitons (the so-called orthoexcitons) are admixed, transferring oscillator strength to the paraexcitons and thus inducing an SHG signal. The derived mechanisms will be tested on the $1S$ paraexciton and applied to detect a Rydberg series of paraexcitons. The simulated polarization diagrams allow finding linear polarization angle combinations to suppress SHG of bright orthoexcitons, as they would otherwise overpower the weak SHG signals of dark paraexcitons.

The yellow exciton series is energetically the lowest of the four known exciton series in Cu_2O and received the most interest in the past decade due to the Rydberg states. Investigations of the blue series, which involves optical transitions to the second lowest conduction band, are experimentally difficult to access via linear spectroscopy due to the high absorption in this spectral range. In chapter 6 we will present magneto-optical SHG spectroscopy results of blue-series excitons at an unprecedented level of detail. Important parameters, such as the Rydberg energy, the exciton radius, and reduced mass as well as the anisotropic electron mass of this conduction band for different crystal directions, will be experimentally extracted.

In chapter 7, we will extend the polarization selection rules to a four-wave mixing process, which we call difference frequency generation with two-photon excitation (2P-DFG). The two-photon excitation channel that addresses exciton states in this process remains unchanged from that of SHG. The pulses of a second laser, which are synchronized with the excitation laser pulses, are directed onto the sample and stimulate the emission of a fourth photon, which is detected at the difference frequency of the two-photon excitation energy and the stimulation photon energy. Delaying the stimulating pulses allows spectroscopic measurements of excitons in the time domain. This method will be demonstrated on excitons of the yellow series.

Chapter 2

Theoretical background

In this chapter, we will establish the foundation for understanding the physical phenomena involved in this work. This includes the theoretical background of nonlinear optics and light-matter interaction, which is developed in Secs. 2.1 and 2.2 and covered by textbooks [She84], [Boy08], [Han+10] and [Kli12]. The basic concepts of semiconductor physics, such as the electronic band structure, excitons, exciton-polaritons and magneto-exciton, will be described in Sec. 2.4. The descriptions are based on the textbooks [Gru16], [Kli12] and [Kno63]. Group theory as a tool for understanding the symmetries of states and interactions is explained in Sec. 2.3 based on the textbooks [Dre+08], [Sno+14] and [Kli12]. The point group tables for multiplication, compatibility and coupling coefficients from Koster et al. in Ref. [Kos+63] are of special importance for this work. They will be used in order to derive polarization selection rules for nonlinear optical processes. In Sec. 2.5, we will present an overview of the relevant optical properties of Cu_2O and show previous results on exciton spectroscopy in this material in order to establish a context for the investigations of this work.

2.1 Electromagnetism and nonlinear optics

For the description of electromagnetic phenomena, we start with the four Maxwell's equations. In differential form, they read:

$$\text{Gauss's law:} \qquad \operatorname{div} \boldsymbol{D} = \rho, \tag{2.1}$$

$$\text{Gauss's law of magnetism:} \qquad \operatorname{div} \boldsymbol{B} = 0, \tag{2.2}$$

$$\text{Faraday's law of induction:} \qquad \operatorname{curl} \boldsymbol{E} = -\frac{\partial}{\partial t}\boldsymbol{B}, \tag{2.3}$$

$$\text{Ampère's law:} \qquad \operatorname{curl} \boldsymbol{H} = \frac{\partial}{\partial t}\boldsymbol{D} + \boldsymbol{j}, \tag{2.4}$$

with the electric displacement $\mathbf{D}$, the charge density ρ, the magnetic flux density $\boldsymbol{B}$, the electric field strength $\boldsymbol{E}$, the magnetic field strength $\boldsymbol{H}$ and the electrical current density $\boldsymbol{j}$. The relation between $\mathbf{D}$ and the polarization density in a medium $\mathbf{P}$, the permettivity of vacuum ε_0 and of a medium ε_r and the electric susceptibility χ is expressed by:

$$\mathbf{D} = \varepsilon_0 \mathbf{E} + \mathbf{P} = \varepsilon_0 \mathbf{E} + \varepsilon_0 \chi \mathbf{E} = \varepsilon_0 \underbrace{(1+\chi)}_{\varepsilon_r} \mathbf{E}. \tag{2.5}$$

The relation between $\mathbf{B}$ and the magnetization density in a medium $\mathbf{M}$, the permeability of vacuum μ_0 and of a medium μ_r and the magnetic susceptibility χ_m is expressed by:

$$\mathbf{B} = \mu_0(\mathbf{H} + \mathbf{M}) = \mu_0\mathbf{H} + \mu_0\chi_m\mathbf{H} = \mu_0 \underbrace{(1 + \chi_m)}_{\mu_r} \mathbf{H}. \tag{2.6}$$

The Lorentz force

$$\mathbf{F}_\mathrm{L} = q(\mathbf{E} + \mathbf{v} \times \mathbf{B}), \tag{2.7}$$

represents the final equation required to establish the foundation of electromagnetism. It acts upon a particle with a charge q propagating through an electromagnetic field with a velocity $\mathbf{v}$.

Electromagnetic radiation, such as light, is described by the electromagnetic wave equation in a vacuum

$$\Delta \boldsymbol{E} - \frac{1}{c^2}\frac{\partial^2}{\partial t}\boldsymbol{E} = 0, \tag{2.8}$$

which is derived (see e.g. Ref. [Nol11]) from Maxwell's Eqs. (2.1), (2.3) and (2.4) assuming $\rho = \mathbf{j} = \mathbf{M} = 0$. Here, $c = 1/\sqrt{\varepsilon_0\mu_0}$ is the vacuum speed of light.

A simple solution of this equation is the transverse plane wave described by

$$\mathbf{E}(\mathbf{r}, t) = \mathbf{E}_0 e^{i(\mathbf{kr}-\omega t)}, \tag{2.9}$$

which propagates along the direction given by the wave vector $\mathbf{k}$ with a field amplitude E_0. For a fixed point $\mathbf{r}$ in space, the electric field oscillates with the angular frequency ω in time t. If the electric field oscillates along one axis, the electromagnetic wave is called linearly polarized. Circular polarization is described by two perpendicular electric field components with a phase shift of $\pi/2$. In this work, we will only consider linear polarization. An equivalent expression to Eq. (2.9) can be derived for the magnetic field component of the radiation. The electric and magnetic fields of the wave are perpendicular to each other and to the propagation direction and oscillate in phase. Therefore the wave is completely described just by the electric component, so we will not further consider the magnetic component. The relation between $\mathbf{k}$, ω and the wavelength λ is given by:

$$|\mathbf{k}| = k = \frac{\omega}{c} = \frac{2\pi}{\lambda}. \tag{2.10}$$

The group and phase velocities v_g and v_ph are defined by:

$$v_\mathrm{g} = \frac{\partial\omega(k)}{\partial k}, \qquad\qquad v_\mathrm{ph} = \frac{\omega(k)}{k}. \tag{2.11}$$

As seen in Eq. (2.10), the group and phase velocities are both equal to c in a vacuum. This is usually not the case for light propagating through a dielectric medium with a nonlinear dispersion relation $\omega(k)$. Electromagnetic waves in a dielectric medium are described by the equation [She84]:

$$\Delta \boldsymbol{E} - \frac{1}{c^2}\frac{\partial^2}{\partial t}\boldsymbol{E} = \frac{1}{\epsilon_0 c^2}\frac{\partial^2}{\partial t}\boldsymbol{P}. \tag{2.12}$$

The electric field entering the medium displaces the charges inducing a polarization, which in turn drives an electromagnetic field.

In general, the charges are not displaced along the electric field. Therefore, $\mathbf{P}$ is not parallel to $\mathbf{E}$. The orientation of $\mathbf{P}$ depends on the symmetry of the crystal described by the $\chi^{(n)}$ tensors. For strong light fields, as those induced by high peak power laser radiation, the displacement of the charges reaches the nonlinear part of the potential within a noncentrosymmetric crystal, so that $\mathbf{P}$ is expressed in a series expansion [Boy08]:

$$P_i = \epsilon_0[\chi_{ij}^{(1)}E_j + \chi_{ijk}^{(2)}E_jE_k + \chi_{ijkl}^{(3)}E_jE_kE_l + ...]. \tag{2.13}$$

The indices i, j, k, and l represent the directional components of the polarization and electric fields with respect to the spatial basis of x, y, and z. $\chi_{ij}^{(1)}$ are the components of a 3×3 second rank tensor for the linear susceptibility. The higher order susceptibilities $\chi_{ijk}^{(2)}, \chi_{ijkl}^{(3)}, ...$ are necessary for the description of nonlinear optical phenomena. In this work, we will investigate the properties of these tensors not directly but by the group theoretical methods later described in Sec. 2.3.

Now we consider two monochromatic light waves with frequencies ω_1 and ω_2, which enter a medium. The oscillating electric fields are then described by

$$\boldsymbol{E}(t) = \boldsymbol{E}_1 e^{-i\omega_1 t} + \boldsymbol{E}_2 e^{-i\omega_2 t} + \text{c.c.} \tag{2.14}$$

in a fixed point $\mathbf{r} = 0$. "c.c." are the complex conjugate terms. By inserting Eq. (2.14) into Eq. (2.13) we get the second order polarization

$$\begin{aligned}\boldsymbol{P}^{(2)}(t) = \epsilon_0\chi^{(2)}[&\overbrace{\boldsymbol{E}_1^2 e^{-i2\omega_1 t} + \boldsymbol{E}_2^2 e^{-i2\omega_2 t}}^{\text{SHG}} + \overbrace{2\boldsymbol{E}_1\boldsymbol{E}_2 e^{-i(\omega_1+\omega_2)t}}^{\text{SFG}} + \overbrace{2\boldsymbol{E}_1\boldsymbol{E}_2^* e^{-i(\omega_1-\omega_2)t}}^{\text{DFG}} \\ &+ \underbrace{2(\boldsymbol{E}_1\boldsymbol{E}_1^* + \boldsymbol{E}_2\boldsymbol{E}_2^*)}_{\text{OR}} + c.c.].\end{aligned} \tag{2.15}$$

The $2\omega_i$ terms describe second harmonic generation (SHG), which is sketched in Fig. 2.1(a). Two light waves of frequency ω_1 are coherently converted into a light wave of double frequency. In a particle picture, the light wave is quantized into the smallest possible energy packet $E_{\text{ph}} = \hbar\omega$ carried by a photon. $\hbar$ is the reduced Planck constant. SHG can then be thought of as an absorption of two photons and a coherent emission of one photon with twice the energy. The lower horizontal line in Fig. 2.1(a) is the ground state of the unexcited crystal. The top line is the excited state, which is usually an exciton state in this work.

The $\omega_1 + \omega_2$ and $\omega_1 - \omega_2$ terms describe sum-frequency generation (SFG) and difference-frequency generation (DFG) and are sketched in Figs. 2.1(b) and 2.1(c), respectively. Two incoming photons of different frequencies are converted into an outgoing photon with the sum or the difference of the incoming frequencies.

The last term in Eq. (2.15) represents optical rectification (OR). This process will not be considered in this work.

The process in Fig. 2.1(d) is called difference-frequency generation with two-photon excitation (2P-DFG), which is similar to DFG, but with two instead of a single photon in the excitation channel. It is a special case of a process called four-wave mixing (FWM) involving four photons. Here, we only consider the special case of the experiments in Sec. 7 involving two photons from the first laser and one from the second laser. Thus the oscillating electric fields of the combined laser light for the 2P-DFG process are described by:

$$\boldsymbol{E}(t) = 2\boldsymbol{E}_1 e^{-i\omega_1 t} + \boldsymbol{E}_2 e^{-i\omega_2 t} + \text{c.c.}\,. \tag{2.16}$$

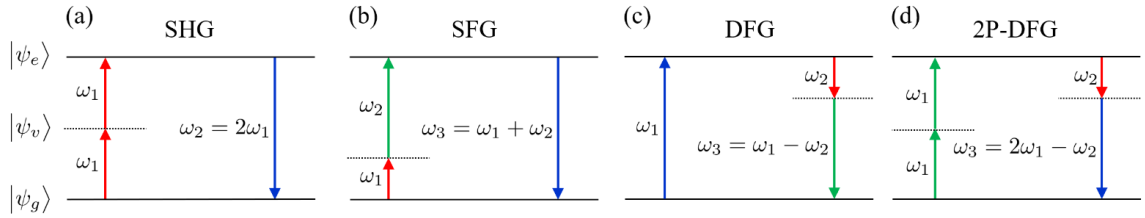

Figure 2.1 Energy schemes of nonlinear optical processes: (a) Second harmonic generation (SHG), (b) sum-frequency generation (SFG), (c) difference frequency generation (DFG) and (d) difference-frequency generation with two-photon excitation (2P-DFG). Later in Sec. 7 the DFG process will be called 1P-DFG analogously to the 2P-DFG terminology. The horizontal lower (upper) line marks the energy level of the ground (excited) state. The dotted lines mark the energy levels of states involved in virtual multi-photon transitions. The arrows represent optical transitions with the photon-frequency ω_i corresponding to the arrow length.

Inserting this equation into the third order term in Eq. (2.13) would lead to 216 terms. Here we only show the relevant terms for 2P-DFG:

$$\boldsymbol{P}^{(3)}_{\text{2P-DFG}}(t) = \epsilon_0 \chi^{(3)} [12 \boldsymbol{E}_1^2 \boldsymbol{E}_2^* e^{-i(2\omega_1 - \omega_2)t} + \text{c.c.}]. \tag{2.17}$$

For the highest conversion efficiency, the phase matching conditions [Boy08]

$$\text{SHG:} \qquad \boldsymbol{k}_{2\omega_1} = 2\boldsymbol{k}_{\omega_1}, \tag{2.18}$$

$$\text{SFG:} \qquad \boldsymbol{k}_{\omega_1+\omega_2} = \boldsymbol{k}_{\omega_1} + \boldsymbol{k}_{\omega_2}, \tag{2.19}$$

$$\text{DFG:} \qquad \boldsymbol{k}_{\omega_1-\omega_2} = \boldsymbol{k}_{\omega_1} - \boldsymbol{k}_{\omega_2}, \tag{2.20}$$

$$\text{2P-DFG:} \qquad \boldsymbol{k}_{2\omega_1-\omega_2} = 2\boldsymbol{k}_{\omega_1} - \boldsymbol{k}_{\omega_2} \tag{2.21}$$

need to be fulfilled.

2.2 Light-matter interaction

In Sec. 2.1, we have delivered a macroscopic description of nonlinear optical processes. Here we will provide a microscopic description of the interaction between light and matter. We start with the Hamiltonian for an electron with mass m_0 and momentum $\mathbf{p}$ in a periodic crystal potential $V(\mathbf{r})$ and apply the minimal coupling $\mathbf{p} \to \mathbf{p} - e\mathbf{A}$, with elementary charge e and vector potential $\mathbf{A}$, in order to treat the light field as a small perturbation [Nol11; Kli12], which only slightly affects the electron eigenenergies:

$$\mathbf{H}_{\text{el}} = \frac{\mathbf{p}^2}{2m_0} + V(\mathbf{r}) \tag{2.22}$$

$$\Rightarrow \mathbf{H} = \frac{(\mathbf{p} - e\mathbf{A})^2}{2m_0} + V(\mathbf{r})$$

$$= \underbrace{\frac{\mathbf{p}^2}{2m_0} + V(r)}_{\mathbf{H}_{\text{el}}} \underbrace{- \frac{e}{m_0}\mathbf{pA}}_{\mathbf{H}_{\text{int}}} + \underbrace{\frac{e^2}{2m_0}\mathbf{A}^2}_{\mathbf{H}_{\text{dia}}}.$$

The Hamiltonian can then be separated into three terms: The first one is again the initial Hamiltonian of a single electron in a crystal potential. The last term is quadratic in $\mathbf{A}$ and describes the effect of electric and magnetic fields on the electron eigenenergies, such as the diamagnetic shift. In the following, we will only consider the second term $\mathbf{H}_{\text{int}}$, which describes the light-matter interaction. For the $\mathbf{A}$ we use the plane wave ansatz [Kli12]

$$\mathbf{A}(t) = \mathbf{e}A_0 e^{i(\mathbf{kr}-\omega t)} \tag{2.23}$$

$$\approx \mathbf{e}A_0\Big[1 + \frac{i\mathbf{kr}}{1!} + O((i\mathbf{kr})^2)\Big], \tag{2.24}$$

for which the exponential function is approximated via a Taylor series up to the second term. A_0 is the amplitude of the plane wave. According to Fermi's golden rule [Kli12], the optical transition rate between the ground state and an excited state is given by

$$w_{g\to e} = \frac{2\pi}{\hbar}\big|H^{\text{int}}_{g\to e}\big|^2 \rho(E_e). \tag{2.25}$$

$\rho(E_e)$ is the density of states at the energy of the excited state and $H^{\text{int}}_{g\to e}$ is the transition probability

$$H^{\text{int}}_{g\to e} = \langle\psi_e|\mathbf{H}_{\text{int}}|\psi_g\rangle \tag{2.26}$$

$$\approx \frac{\mathbf{e}A_0}{m}\langle\psi_e|\mathbf{e}\cdot\mathbf{p}|\psi_g\rangle + \frac{i\mathbf{e}A_0}{m}\langle\psi_e|(\mathbf{e}\cdot\mathbf{p})(\mathbf{k}\cdot\mathbf{r})|\psi_g\rangle.$$

$\langle\psi_e|$ is the excited and $|\psi_g\rangle$ the ground state. The $(\mathbf{e}\cdot\mathbf{p})$ term is known as the electric dipole (ED) approximation of an optical transition and the $(\mathbf{e}\cdot\mathbf{p})(\mathbf{k}\cdot\mathbf{r})$ term contains the electric quadrupole (EQ) and magnetic dipole (MD) transitions [Kli12; Ell61]. The symmetries of these processes and their role in optical selection rules in Cu_2O will be discussed in Sec. 4.1.

Second harmonic generation is described in third-order perturbation theory involving three optical transitions. Its transition rate is expressed by

$$w^{\text{SHG}}_{g\to v\to e\to g} \propto \sum_v \frac{\langle\psi_g|\mathbf{H}_{\text{int}}(2\hbar\omega)|\psi_e\rangle\langle\psi_e|\mathbf{H}_{\text{int}}(\hbar\omega)|\psi_v\rangle\langle\psi_v|\mathbf{H}_{\text{int}}(\hbar\omega)|\psi_g\rangle}{(E_e - E_g - 2\hbar\omega)(E_v - E_g - \hbar\omega)}. \tag{2.27}$$

$|\psi_v\rangle$ are eigenstates, which are virtually excited as intermediate states in the two-photon excitation sub-process. The SHG selection rules will be discussed in Sec. 2.3. The denominator ensures, that the total expression increases for the photon energies matching the resonance energy.

2.3 Group theory for semiconductor optics

Group theory is a powerful mathematical tool for the investigation of symmetry properties of physical objects such as molecules or crystals. A group G is an algebraic structure, which is constructed by a set of elements $\{a, b, c, ...\}$ connected via an operation " $\circ$ " satisfying the following four criteria [Dre+08]: i) Connection of any two elements of the group via the specific operation results in another element of the group: $a \circ b = c$ with $a, b, c \in G$. ii) Associativity must apply: $(a \circ b) \circ c = a \circ (b \circ c)$. iii) An identity element E must exist: $a \circ E = a$ for any group element. iv) Any group element has to have an inverse element:

$a \circ a^{-1} = E$. A subgroup is a subset of the group elements which fulfill all group criteria by themselves. As an example, all real numbers form a group with respect to the operation of multiplication. All integers form a subgroup, as they still satisfy all criteria and are a subset of the real numbers.

In solid-state physics, the symmetry of crystals is described by point groups. A point group is a set of all symmetry operations which map the crystal onto itself. These symmetry operations include space inversion, reflections on mirror planes, rotations and combined rotations followed by a reflection on a mirror plane.

The crystal structure of Cu_2O is composed of a body-centered cubic oxygen sub-lattice and a face-centered cubic copper sub-lattice, which is shifted by a quarter of a space diagonal. The unit cell of both sub-lattices is shown in Fig. 2.3(a). Each oxygen atom is surrounded by four copper atoms in a tetrahedral arrangement. Therefore the crystal symmetry of Cu_2O is characterized by the T_d point group in Schönflies notation ($\bar{4}3m$ in Hermann-Mauguin notation), which contains all geometric operations mapping a tetrahedron into itself. Each copper atom is surrounded by two oxygen atoms on opposite sides. Therefore inversion symmetry is satisfied with a copper atom as the reference point for the symmetry operation. In literature, the Cu_2O crystal structure is generally said to be described by the O_h group [Kli12] in Schönflies notation ($m\bar{3}m$ in Hermann-Mauguin notation, which contains all (in total 48) geometric operations mapping an octahedron or a cube into itself. This is not strictly the case due to the fact that there are no proper 90° rotations, which map the crystal onto itself. However, considering optical properties, which are determined by the two lowest CBs and two highest VBs, all stemming from copper orbitals as later shown in Fig. 2.3(c), the lower-lying electronic states of oxygen orbitals are basically not involved and screen the Coulomb potential of the oxygen sub-lattice. Ignoring the oxygen atoms would therefore lead to O_h symmetry for the copper sub-lattice, so parity is considered a good quantum number.

Next, we explain the important concept of group representations. Dealing with geometric operations as group elements, it is convenient to describe them by $n \times n$ matrices (e.g. rotation and reflection matrices). A set of these matrices (one for each group element), which exhibits the transformation behavior as stated in the multiplication table of the group, is called a representation. In principle, there are infinitely many representations. A representation is called reducible if the matrices can be brought into a block diagonal form. More useful is the finite number of irreducible representations for a point group, of which the matrices cannot be further simplified into a block diagonal form. They are denoted by $\Gamma_i^{\pm}$ with a lower counting index i and $\pm$ for even or odd parity. In our case, they are used to specify the transformation behavior and therefore the symmetry of physical states (such as band electrons, excitons, and the induced polarization by photons in a solid) and external perturbations (such as strain, electric and magnetic fields).

Introducing an additional influence on a physical system usually lowers the symmetry so that the symmetry of the perturbed system is fully described by a subgroup. If a representation Γ_ψ of a physical state $|\psi\rangle$ is irreducible in the group G but reducible in its subgroup G_{sub}, then the state splits into multiple states with different symmetries and lower degeneracies. This behavior is specified in the compatibility tables. Note that group theory only specifies the symmetries and degeneracies of split or coupled states, not their energetic order or the absolute splitting energy, which have to be found out by quantum mechanical methods.

For example, d orbitals of a copper atom in free space transform as D_2^+ in the full rotation group SO(3), as they have even parity and an angular momentum of $l = 2$. If these d orbitals are brought into a crystal field with O_h symmetry, their levels split into Γ_3^+ and Γ_5^+ states according to the compatibility table A.1. This is shown in Fig. 2.3(c) and explains the VB symmetry in a crystal field. The degeneracy of the states is specified in the identity element column (usually the first column) of the character table A.2 of the O_h group.

In order to take the spin-orbit coupling for the VB into consideration, we look up the symmetry of the spin 1/2 of the electron in the same compatibility table. In the full rotation group, it has a $D_{1/2}^+$ representation corresponding to a Γ_6^+ symmetry in the O_h group. To find out the symmetry of the spin-orbit coupled VB states, one has to calculate the tensor product of their irreducible representations. The product leads to reducible matrices, which can be block diagonalized into sub-matrices, which are the irreducible representations of the new eigenstates. The results are specified in the multiplication table of the O_h group shown in Fig. A.3. The Γ_5^+ VB splits into a Γ_7^+ and a Γ_8^+ VB, as sketched in Fig. 2.3(c).

Now we turn to the symmetry considerations for selection rules of optical transitions [Pas+91]. Group theory cannot specify quantitatively how strong an optical transition is, but it can predict which transitions are and which are not allowed by symmetry. For an optical transition between an initial and a final state to be symmetry allowed, the equation

$$\langle \psi_f | \mathbf{H}_{\mathrm{int}} | \psi_i \rangle \rightarrow \langle \Gamma_f | \Gamma_{\mathrm{pol}} | \Gamma_i \rangle = \langle \Gamma_f | \Gamma_{\mathrm{pol}} \otimes \Gamma_i \rangle \neq 0 \tag{2.28}$$

has necessarily to be satisfied. The initial state perturbed by the light field and the final state therefore need to share the same symmetry component. As an example, single-photon excitation from the ground state to a yellow series S exciton is only possible for the orthoexciton state by a Γ_5^+ electric quadrupole transition:

$$\langle \Gamma_S | \Gamma_{\mathrm{pol}} | \Gamma_G \rangle = \langle \underbrace{\boldsymbol{\Gamma_5^+}}_{\text{ortho}} \oplus \underbrace{\Gamma_2^+}_{\text{para}} \,|\, \underbrace{\Gamma_4^-}_{\text{ED}} \oplus \underbrace{\Gamma_4^+}_{\text{MD}} \oplus \underbrace{\Gamma_3^+ \oplus \boldsymbol{\Gamma_5^+}}_{\text{EQ}} \rangle = \langle \Gamma_{\mathrm{ortho}} | \Gamma_{\mathrm{EQ}} \rangle \neq 0. \tag{2.29}$$

The symmetries are calculated in Sec. 4 in Eqs. (4.51),(4.52) and (4.53) for yellow-series excitons and are stated in Eqs. (4.54), (4.55) and (4.56) for the light-induced polarization in the solid.

An external perturbation, such as a magnetic field, can mix exciton states of different symmetry and thus allows previously forbidden transitions. As an example, a single-photon transition

$$\langle \Gamma_{\mathrm{para}} | \Gamma_B | \Gamma_{\mathrm{ortho}} \rangle \langle \Gamma_{\mathrm{ortho}} | \Gamma_{\mathrm{pol}} | \Gamma_G \rangle \neq 0 \tag{2.30}$$

to the Γ_2^+ paraexciton state can be allowed by an applied magnetic field due to mixing with the EQ allowed orthoexciton state:

$$\langle \underbrace{\Gamma_{\mathrm{para}}}_{\Gamma_2^+} \,|\, \underbrace{\Gamma_B}_{\Gamma_4^+} \,|\, \underbrace{\Gamma_{\mathrm{ortho}}}_{\Gamma_5^+} \rangle = \langle \boldsymbol{\Gamma_2^+} | \boldsymbol{\Gamma_2^+} \oplus \Gamma_3^+ \oplus \Gamma_4^+ \oplus \Gamma_5^+ \rangle \neq 0. \tag{2.31}$$

The SHG transition rate has been expressed in Eq. (2.27). Although each individual transition of an SHG process may be, in principle, symmetry allowed, the whole SHG process can still be forbidden for $\mathbf{k}$ along certain crystal axes or for certain combinations of the polarization of incoming and outgoing light. Therefore we need to consider how

the spatial components of eigenstates and perturbations are coupled. This information is given in the **coupling coefficient tables** in Figs. A.4-A.9 from Ref. [Kos+63], which contain the Clebsch-Gordon coefficients for the coupling of states of various symmetries. They specify how the spatial components of two states with certain symmetries need to be linearly combined so that the result exhibits the symmetry of the final state. This is the basis for the derivation of the polarization-dependent SHG intensity, which will be presented in great detail in Sec. 4.1.

2.4 Semiconductor optics: excitons, exciton-polaritons and magneto-excitons

A **semiconductor** consists of atoms in a periodic structure, which are bound by covalent or ionic bonds [Kit04; Gru16]. The valence orbitals of neighboring atoms share a significant overlap so that their binding and antibonding states form electronic bands due to the Pauli exclusion principle. Semiconductors have a bandgap E_g in the order of a few eV, which is a forbidden energy interval for electronic states. At the temperature $T = 0$, the valence band (VB) is fully occupied by electrons and the conduction band (CB) is empty, so the semiconductor acts as an insulator exhibiting zero conductivity. For undoped semiconductors, thermal excitations into the conduction band are vanishingly small at temperatures of about 1.4 K, which are the temperatures of our experiments. For so-called direct semiconductors, the maximum of the VB and the minimum of the CB are located at the same k in a band structure diagram, as shown schematically in Fig. 2.2(a). An electronic band is approximated as a parabola close to its dispersion extremum. The effective mass of an electron is proportional to the inverse of the band curvature:

$$m_\mathrm{e} = \hbar \left[\frac{\partial^2 E_\mathrm{CB}(k)}{\partial^2 k^2} \right]^{-1} \tag{2.32}$$

An electron can be excited from the VB into the CB by absorbing a photon with an energy of at least the bandgap $\hbar\omega_\mathrm{ph} \geq E_\mathrm{g}$. For a direct semiconductor, the optical transition does not require the involvement of a phonon, the quasiparticle of a quantized crystal vibration. As the electron in the CB is no longer bound to its initial atom, a positively charged electron vacancy remains in the VB, which is treated as a quasiparticle called a hole. It has the opposite wavevector to the electron, positive charge and an effective mass according to the curvature of the according VB [Eq. (2.32)].

Now we turn to the concept of **excitons**, which are the quasiparticles investigated in this work. Excitons are electron-hole pairs bound by the Coulomb interaction and are therefore hydrogen-atom-like states in semiconductors and are described by the same quantum numbers n (principal), l (angular) and m (magnetic). The exciton wave function [Kli12]

$$\psi_X(\mathbf{K}) = \frac{e^{i\mathbf{KR}}}{\sqrt{\Omega}} \psi_e(\mathbf{r}_e)\psi_h(\mathbf{r}_h)\psi^\mathrm{env}_{n,l,m}(\mathbf{r}_e - \mathbf{r}_h) \tag{2.33}$$

is composed of the Bloch functions ψ_e and ψ_h of electron and hole, the envelope function $\psi^\mathrm{env}_{n,l,m}$ describing the relative motion of electron and hole, the center of mass ($\mathbf{R} = [m_e\mathbf{r}_e + m_h\mathbf{r}_h]/[m_e + m_h]$) motion $e^{i\mathbf{KR}}$ and a normalization factor $\Omega^{-1/2}$. The excitonic

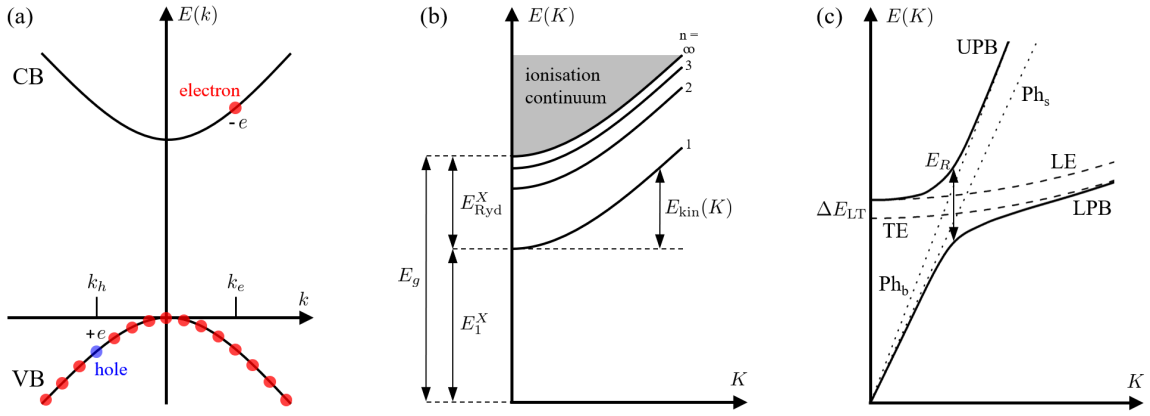

Figure 2.2 (a) Schematic band dispersion of a direct semiconductor with an excited electron in the conduction band (CB) and a hole in the valence band (VB). (b) Exciton dispersion according to Eq. (2.34). (c) Exciton-polariton dispersion displays the upper polariton branch (UPB) and lower polariton branch (LPB) as solid lines. The vertical double arrow marks the Rabi energy. The upper (lower) parabolic dashed line represents the dispersion of the longitudinal (transverse) state. The straight dashed lines represent the photon dispersion considering the background and static dielectric constants: Ph_b according to $E(k) = ck/(\sqrt{\varepsilon_b}\hbar)$ and Ph_s according to $E(k) = ck/(\sqrt{\varepsilon_s}\hbar)$.

eigenenergies and their dispersion relations are sketched in Fig. 2.2(b) and expressed by [Gru16]:

$$\begin{aligned} E_n^X(\mathbf{K}) &= E_\mathrm{g} + E_\mathrm{kin}(\mathbf{K}) - E_\mathrm{bind} \\ &= E_\mathrm{g} + \frac{\hbar^2\mathbf{K}^2}{2M} - \underbrace{\frac{\mu}{m_0}\frac{1}{\varepsilon_r^2}\overbrace{\frac{m_0 e^4}{2(4\pi\varepsilon_0\hbar)^2}}^{E_\mathrm{Ryd}^\mathrm{H}}}_{E_\mathrm{Ryd}^\mathrm{X}}\frac{1}{n^2} \end{aligned} \tag{2.34}$$

They form a hydrogen-like series with binding energies proportional to n^{-2} for increasing n below the bandgap E_g with a parabolic dispersion $E_\mathrm{kin}(\mathbf{K}^2)$, where $\mathbf{K} = \mathbf{k}_e + \mathbf{k}_h$ is the combined wavevector of electron and hole. $M = m_e + m_h$ is the total and $\mu = \frac{m_e m_h}{m_e + m_h}$ the reduced exciton mass. The exciton radius is given by [Kli12]

$$r_n^X = \underbrace{\frac{m_0\varepsilon_r}{\mu}a_\mathrm{B}^\mathrm{H}}_{a_B^X} n^2, \tag{2.35}$$

with the hydrogen Bohr radius $a_\mathrm{B}^\mathrm{H} = 0.053\,\mathrm{nm}$ [Gru16] and the exciton Bohr radius a_B^X. There are two types of excitons classified by the size of their Bohr radius. If the exciton Bohr radius is significantly larger than the lattice constant in the range of several nm and a binding energy of less than about 200 meV, it is considered a Mott-Wannier exciton [Kli12]. Due to the large Bohr radius, the excitonic wave function extends over many crystal unit cells, which keeps the effective mass approximation valid. The so-called Frenkel excitons are confined to one unit cell and have therefore a large binding energy usually above 200 meV and a small Bohr radius in the range of one lattice constant [Kli12].

As already mentioned in Sec. 2.1, an electromagnetic wave entering a dielectric medium induces a polarization, which in turn drives an outgoing light wave. This coupling of the photon to the polarization of an exciton in the medium leads to a new hybrid quasiparticle, which is called the **exciton-polariton**. For the dispersion relation $\omega(k)$ of exciton-polaritons, we start with the polariton equation

$$\varepsilon(\omega) = \frac{c^2\mathbf{k}^2}{\omega^2}, \tag{2.36}$$

which is a solution of the wave equation in a medium, see Eq. (2.12) with the ansatz in Eq. (2.14).

The dielectric constant for a single exciton resonance $\hbar\omega_X$ is given by [And95]:

$$\varepsilon(\omega) = \varepsilon_b + \frac{4\pi\beta(\hbar\omega_X)^2}{(\hbar\omega_X)^2 - (\hbar\omega)^2 - i\hbar\omega\gamma}. \tag{2.37}$$

The background dielectric constant ε_b takes all higher frequency contributions into account and γ is the radiative damping of the state. β is the oscillator strength density per unit cell, which quantifies the coupling strength between the light field and the exciton and leads to an energy splitting

$$\Delta E_{\mathrm{LT}} = \frac{2\pi\hbar\omega_X}{\varepsilon_b}\beta \tag{2.38}$$

of the state into a transverse and a higher energy longitudinal component [Kli12]. Combining both equations leads to an implicit expression for the exciton-polariton dispersion of a single state:

$$\varepsilon(\omega) = \frac{c^2\mathbf{k}^2}{\omega^2} = \varepsilon_b + \frac{4\pi\beta(\hbar\omega_X)^2}{(\hbar\omega_X)^2 - (\hbar\omega)^2 - i\hbar\omega\gamma} \tag{2.39}$$

ω_X is the frequency of the transverse exciton state. The dispersion relation is sketched for the simplified case neglecting damping in Fig. 2.2(c). It shows the quadratic dispersion of the longitudinal and transverse exciton state as well as the photon dispersions considering the background dielectric constant ϵ_b for high and the background dielectric constant ϵ_s for low-frequency contributions. The exciton-photon coupling induces an anticrossing leading to an upper polariton branch (UPB) and a lower polariton branch (LPB). For small k values, the UPB is considered exciton-like as it is close to the longitudinal exciton dispersion with a small group velocity. For increasing k it approaches the light dispersion $\omega(k) = kc/\sqrt{\epsilon_b}$. The LPB starts photon-like for small k with a dispersion of $\omega(k) = kc/\sqrt{\epsilon_s}$ and approaches the quadratic transverse exciton dispersion for increasing k. The smallest energetic difference between the branches for the same k value is called the Rabi energy [Kli12]

$$E_R = \hbar\Omega_R = \sqrt{\frac{\Delta E_{\mathrm{LT}} E_X(0)}{2}}, \tag{2.40}$$

which is also a measure of the coupling strength. The exciton-polariton dispersion will be extended to multiple exciton resonances and calculated for non-vanishing dampings in Sec. 6.1 for blue-series excitons.

In the following, we will explain the concept of **magneto-excitons** by briefly summarizing the effects of external magnetic fields on excitons. The direct impact of a magnetic field on the excitonic magnetic moment, which may be given by the spin or the orbital angular momentum of its envelope function, is called the Zeeman effect (ZE). The linear energy splitting of an exciton resonance in a magnetic field is given by [Kli12]

$$\Delta E_{\mathrm{ZE,spin}} = \pm\frac{1}{2}|g_e \pm g_h|\mu_B B \tag{2.41}$$

for the spin ZE, with the Landé g-factors g_i of electron and hole and the Bohr magneton $\mu_B = e\hbar/2m_0$. The orbital ZE-induced energy splitting is given by

$$\Delta E_{\mathrm{ZE,orb}} = \pm g_{\mathrm{orb}}\mu_B B. \tag{2.42}$$

Due to the positive parity of magnetic fields, only states of the same parity may be mixed. More details are given in Sec. 5.1 for the yellow series $1S$ exciton in a magnetic field.

Another phenomenon called the magneto-Stark effect (MSE) arises due to the center of mass motion of an exciton perpendicular to a magnetic field and is therefore maximal in Voigt and absent in Faraday geometry. The Lorentz force [see Eq. (2.7)] acting in opposite directions on the oppositely charged electron and hole separates their charge distributions leading to an effective electric field [Tho+61]

$$\mathbf{E}_{\mathrm{MSE}} = \frac{\hbar}{M}\mathbf{K}\times\mathbf{B} \tag{2.43}$$

with negative parity. Therefore only opposite parity states may be mixed by the MSE. The mixing mechanism between exciton states induced by the MSE and ZE will be considered for polarization dependence of magnetic-field-induced SHG in Sec. 4.1

The envelope of the exciton wave function is deformed by the Lorentz force, which can also be treated as an admixture of other exciton states with different angular momentum and increases linearly with increasing B. Additionally, the energy of a magnetic dipole also increases proportionally to B, leading in total to a quadratic diamagnetic shift of the exciton energies for increasing magnetic fields according to [Kli12]

$$\mathbf{H}_{\mathrm{dia}}(B) = \frac{e^2}{8\mu}\frac{2}{3}\langle r_{n,l}^2\rangle B^2 \tag{2.44}$$

with the average of the squared exciton radius [Tai72]

$$\langle r_{n,l}^2\rangle = \frac{a_B^{X\,2}}{2}n^2[5n^2+1-3l(l+1)]. \tag{2.45}$$

A more extensive description of the diamagnetic shift will be given in Sec. 6.4.1 in the case of blue-series excitons.

Another magnetic field effect on electrons and holes is characterized by the cyclotron energy [Kli12]

$$E_{\mathrm{c},n_{\mathrm{L}}}(B) = (n_{\mathrm{L}}-\frac{1}{2})\hbar(\omega_{\mathrm{c,e}}+\omega_{\mathrm{c,h}}) \tag{2.46}$$

$$= (n_{\mathrm{L}}-\frac{1}{2})\frac{\hbar e}{\mu}B. \tag{2.47}$$

forming Landau levels similar to a quantum harmonic oscillator with the Landau quantum number n_L resulting in a linear energy shift with increasing magnetic field. The Lorentz force also affects the relative motions of electrons and holes, forcing them, in a classical picture, on quantized circular trajectories in the plane perpendicular to the magnetic field leading to a shrinking of the excitonic radius. As the Lorentz force vanishes for motion along the magnetic field, the free particle description for electron and hole is still valid in this direction.

The quadratic diamagnetic shift dominates for the low-field regime, in which the exciton binding energy is much larger than the cyclotron energy. In the high-field regime, the exciton energies shift linearly as the cyclotron energy becomes larger than the binding energy. More details will be given in Sec. 6.5 dealing with blue series magneto-excitons.

2.5 Exciton spectroscopy in Cu_2O

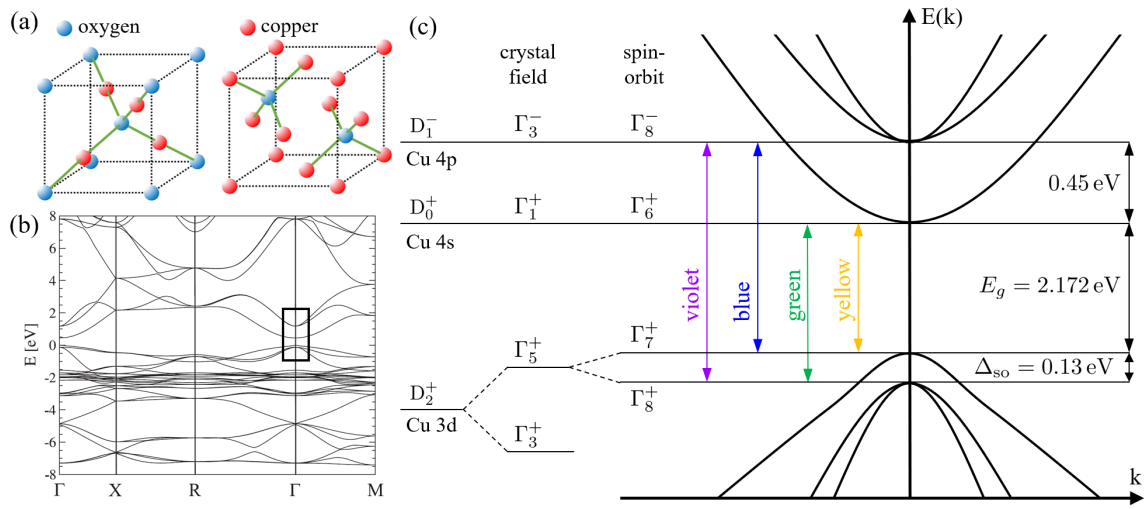

Figure 2.3 (a) Cu_2O crystal structure, of which the bcc oxygen and fcc copper unit cells are depicted. (b) Complete Cu_2O band structure calculated by spin density functional theory in Ref. [Fre+09]. The rectangle marks the important region at the Γ point, including the four optically relevant electronic bands, which are sketched in (c) in more detail: Symmetries of the relevant copper orbitals in the full rotation group $SO(3)$ as well as their O_h group symmetries in a crystal field and for included spin-orbit coupling. The band-to-band transitions for the four exciton series are marked by colored vertical arrows. Note the non-parabolicity of the highest VB.

Cu_2O is a direct semiconductor with a cubic crystal structure and a lattice constant of $a_{lat} = 4.27$ Å [Pei+09]. The copper atoms form a fcc and the oxygen atoms a bcc lattice with a shift of a quarter space diagonal, as can be seen in Fig. 2.3(a). As explained in Sec. 2.3, O_h is the relevant point group for optical properties. A spin density functional theory calculation of the electronic band structure by French et al. [Fre+09] is shown in Fig. 2.3(b). The region at the Γ point marked by the black rectangle involves the four relevant bands, which are shown in a scheme in Fig. 2.3(c). Optical transitions between

them lead to four exciton series denoted by the color of their light emission.

The yellow series has a band gap of $E_{g,\mathrm{y}} = 2.172\,08\,\mathrm{eV}$ [Kaz+14] and involves the highest VB composed by copper $3d$ orbitals, which have a Γ_5^+ symmetry in the crystal field and a Γ_7^+ symmetry if spin-orbit interaction is included. The CB stems from copper $4s$ orbitals with Γ_1^+ symmetry in a crystal field. The spin-orbit coupling leads to a Γ_6^+ symmetry. The effective electron and hole masses of the CB and VB are $m_e = 0.985\,m_0$ and $m_h = 0.575\,m_0$, respectively, resulting in a reduced exciton mass of $\mu_\mathrm{y} = 0.363\,m_0$ and $M_\mathrm{y} = 1.56\,m_0$ [Nak+12].

After Gross et al. [Gro+52] measured the yellow P exciton series up to a quantum number of $n = 8$, the number of measured yellow exciton shells (states with specific n, L configuration) has been extended to about 60, which are shown in the energy level scheme in Fig.2.4. The exciton energy levels n are plotted for the angular momentum quantum number L up to 5, which corresponds to an H envelope. The P series has been extended in 2014 up to $n = 25$ [Kaz+14] and later to 30 [Ver+21].

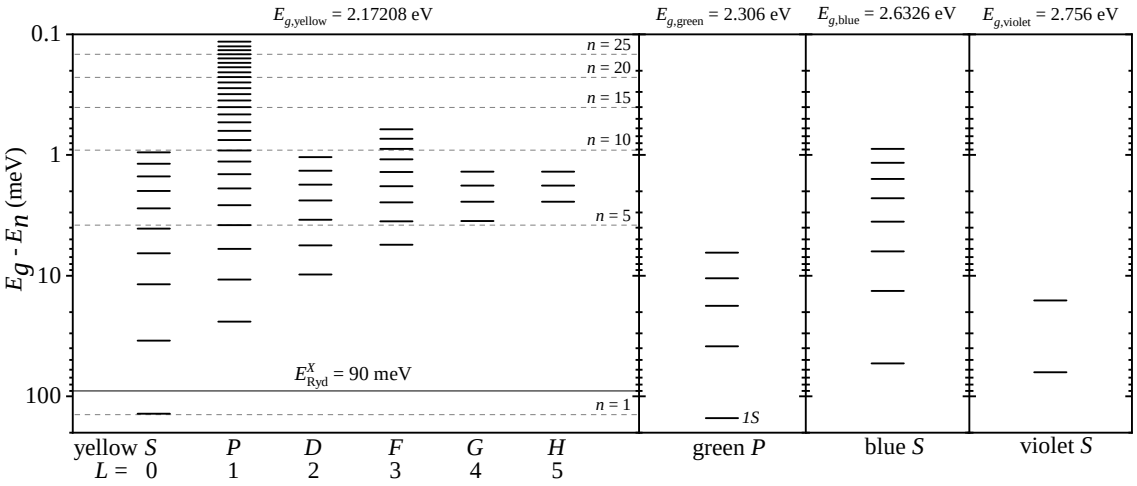

Figure 2.4 Binding energy levels of all excitons shells of the (a) yellow [Kaz+14; Hec+17a; Hec+20; The+15], (b) green (Fig. 2.6), (c) blue [Far+21] and (d) violet series [Dau+66], which have been experimentally observed. The angular momentum quantum number L is stated below and the band gap above each series.

Excitons in Cu_2O are generally considered to be of Mott-Wannier type. An exception is the $1S$ yellow exciton partly having Frenkel-like characteristics with a rather large binding energy of 130 meV and a small radius of 7 Å [Kav+97]. As a consequence of the small radius with a similar size as the lattice constant, the exciton is spread in K space covering a significant portion of the Brillouin zone so that the non-parabolic distortions, which are indicated in the band structure scheme in Fig. 2.3(c), need to be considered. Thus the so-called central-cell correction is taken into consideration as described in Ref. [Sch+17b].

As the lowest CB and upmost VB have the same parity, direct transitions are ED forbidden, leading to a small oscillator strength. S and other even parity excitons are optically allowed for EQ transitions. P and other odd parity excitons are ED-allowed due to their envelope function.

A spectrum of the yellow series measured in one photon absorption experiments by scanning a narrow bandwidth laser through the relevant spectral range is shown in Figs. 2.5(a) and 2.5(b). The spectrum is taken from Ref. [Hec20]. At 2.0328 eV in Fig. 2.5 the EQ allowed $1S$ ground state is seen. It is a four-fold state consisting of three singlet-triplet mixed bright orthostates and one pure spin-triplet dark paraexciton, the latter of which is the narrowest spectral exciton line [Bra+07] in semiconductor optics and will be investigated in SHG experiments in Sec. 5. Above 2.145 eV, the yellow P series starts including the $2P$ up to the $22P$ in this measurement. The P excitons form a hydrogen-like series according to Eq. (2.34) with a Rydberg energy of 92 meV [Kaz+14] and a Bohr radius of 11.1 Å [Kav+97]. A small deviation from the $1/n^2$ binding energy scaling is explained by a positive quantum defect of $\delta \approx 0.3$ for Rydberg P states modifying the scaling according to $1/(n-\delta)^2$, which results from the spin-orbit interaction affecting the two highest VBs, as derived in Ref. [Sch+16a]. The resonances are getting spectrally narrower and weaker in intensity for increasing n. Energetically above the bandgap, the absorption starts to increase steadily. The P states interfere with a phonon continuum starting at about 2.0464 eV, the sum of the $1S$ exciton and Γ_3^- phonon of 13.6 meV [Tak+18].

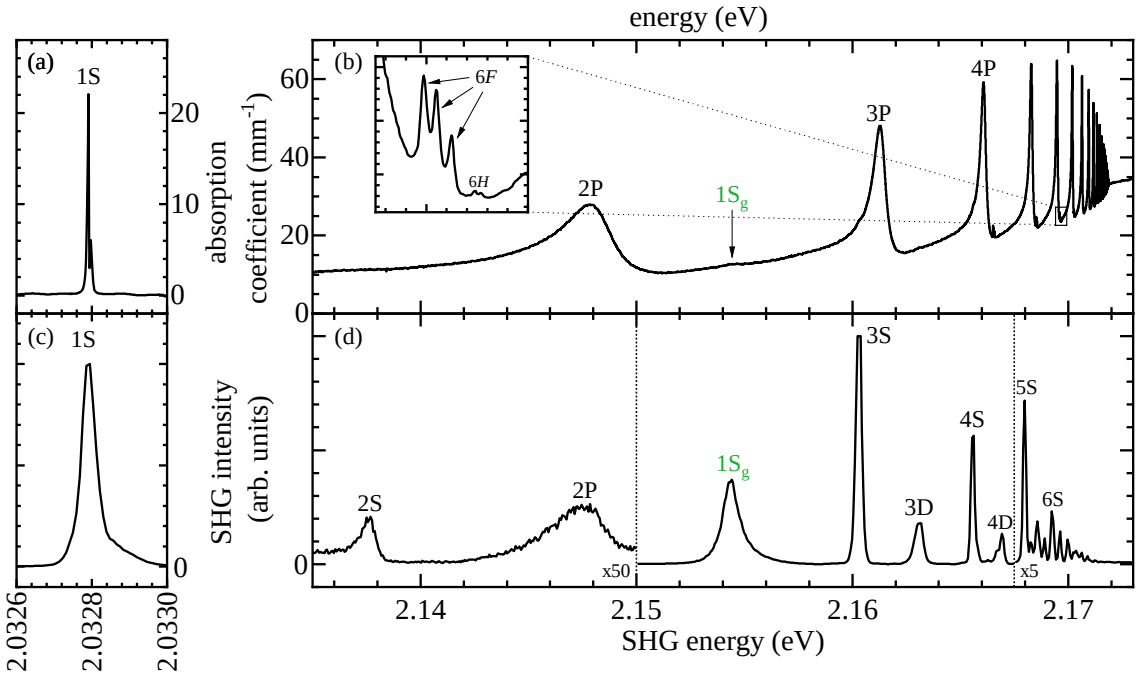

Figure 2.5 Experimentally obtained spectra of the yellow exciton series: One-photon absorption spectrum of (a) the EQ allowed $1S$ exciton and (b) the ED allowed P exciton series with weak features of F and H states zoomed in the inset. The data are taken from Ref. [Hec20]. The SHG spectrum in the same spectral range is taken from Ref. [Mun+18]. The excitons are excited by fs pulses as described in Sec. 3.3: ED-ED excited (c) $1S$ and (d) higher n S and D exciton states. A weak feature of the ED-EQ excited $2P$ exciton is observed. The $1S$ exciton of the green series, which is only weakly visible in panel (b), gives a stronger signal in SHG and is spectrally located between the $2P$ and the $3S$ exciton.

Figures 2.5(c) and 2.5(d) show the SHG spectrum of S and D excitons up to $n = 9$ in the same energy range. The data is taken from Ref. [Mun+18]. The $1S$ exciton is by far the most intense line in the series and its line width is limited by the resolution of the spectrometer. There are only weak features of the $2P$ and $3P$ excitons in the SHG spectrum. The $1S$ exciton of the green series, which is only weakly visible in the one-photon absorption spectrum, exhibits a rather strong intensity compared to the yellow series Rydberg states. It is energetically located between the yellow $2S$ and $3S$ states leading to a strong yellow-green mixing. The green part in yellow excitons is quantified in Ref. [Sch+17b]. Each S exciton has a lower energy dark paraexciton state, which is not visible in this spectrum but can be activated by magnetic fields, as will be described in Sec. 5.5. In Sec. 4, we will identify the magnetic-field inducing SHG mechanisms that mix the S, P and D states and induce an SHG signal. This will be demonstrated by simulating and measuring the linear polarization dependence of the SHG signal.

The green series with a bandgap of $E_{g,\mathrm{g}} = 2.306\,\mathrm{eV}$ (see Fig. 2.6) involves the same CB as the yellow series but the second highest VB with Γ_8^+ symmetry, which also stems from copper $3d$ orbitals. A one-photon transmission spectrum of green series P excitons up to $n = 5$ is shown in Fig. 2.6. The acquired resonance energies from the second derivative of the spectrum are plotted as dots in Fig. 2.6(b). Fitting them with Eq. (2.34) modified with the quantum defect leads to $\delta_{\mathrm{green}} = -0.16 \pm 0.14$, which has the expected opposite sign to δ_{yellow} [Kaz+14]. Rommel et al. recently performed extensive numerical investigations on the green-series excitons in Ref. [Rom+20b].

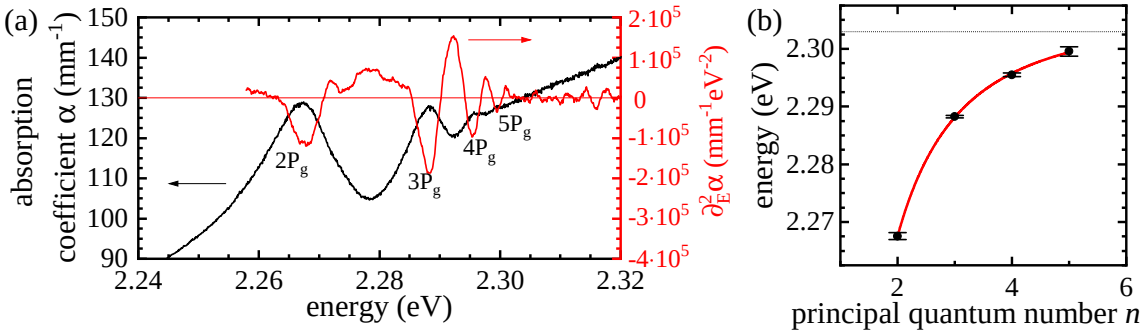

Figure 2.6 (a) White-light absorption spectrum of the green exciton series up to $n = 5$. The light is focused onto a 6 µm thick part of a wedge-shaped natural sample. The resonance energies are obtained in the second derivative of the spectrum shown as the red line and plotted in panel (b): A fit according to Eq. (2.34) modified with a quantum defect parameter $n \to n - \delta$ indicates a quantum defect of $\delta = -0.16 \pm 0.14$ with the opposite sign compared to the yellow series. The resulting band gap of $E_{g,\mathrm{g}} = 2.306\,\mathrm{eV}$ is shown as the dotted line.

The blue series has a bandgap of $E_{g,\mathrm{b}} = 2.6326\,\mathrm{eV}$ [Far+21] and involves the same VB as the yellow series and the second lowest CB, which stems from the copper $4P$ orbitals. In a crystal field, these copper states form electronic bands with a Γ_3^- symmetry, which turns into a Γ_8^- symmetry, including spin-orbit coupling. Transitions are ED allowed resulting in a large oscillator strength density of $\beta_{\mathrm{b}} = 2.93 \times 10^{-3}$ [Dau+66] and thus a strong polariton effect, which will be investigated in Sec. 6. In comparison, the oscillator strength density

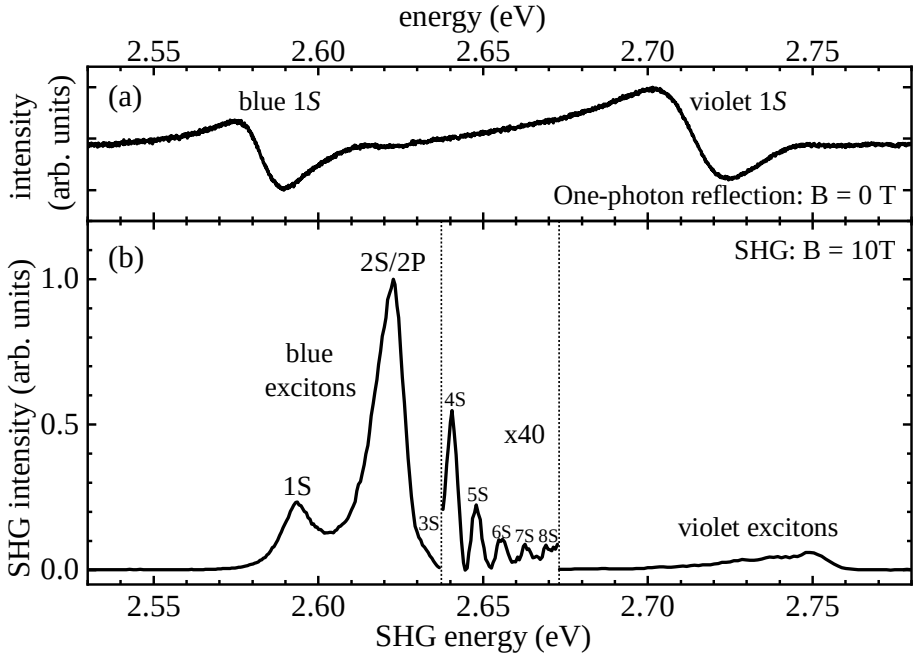

Figure 2.7 (a) One-photon reflection spectrum in the spectral range of the blue and violet excitons. (b) SHG spectrum in the same spectral range at a magnetic field of 10 T in Voigt configuration displaying blue series S type magneto-excitons up to $n = 8$ and no distinct violet series resonances.

of blue-series excitons is about seven orders of magnitude larger than $\beta_{\mathrm{y}} = 3.1 \times 10^{-10}$ [Frö+06] of yellow-series excitons. The effective mass of electrons in this conduction band is anisotropic and will be analyzed in Sec. 6.5.

The violet series has a bandgap of $E_{g,\mathrm{v}} = 2.756\,\mathrm{eV}$ [Dau+66] and involves the same VB as the green series and the same CB as the blue series and is therefore also allowed for ED transitions with an even larger oscillator strength density of $\beta_{\mathrm{b}} = 4.62 \times 10^{-3}$ [Ito+98].

One photon absorption measurements of blue and violet-series excitons in bulk crystals are not possible due to the high absorption. A one-photon reflection spectrum of the blue-violet spectral range is shown in Fig. 2.7(a). The visible spectral features are induced by the $1S$ excitons of each series and are not very insightful. Fig. 2.7(b) shows the SHG spectrum at a magnetic field of 10 T, in which blue series magneto-excitons up to $n = 8$ are detected. Extensive experimental results will be presented in Sec. 6. The violet series consists of broad lines with hardly any features resolved.

An energy level scheme for all measured states beyond the yellow exciton series, including the results of this work, is shown in Fig. 2.4.

Chapter 3

Experimental details

Our experimental setup is depicted in Fig. 3.1 and allows a wide range of nonlinear optical spectroscopy experiments, applying processes such as second harmonic generation (SHG) and difference frequency generation with two-photon excitation (2P-DFG) for polarization and time-dependent measurements. The setup features a sophisticated laser system with two separately tunable pulsed laser light sources with a wide spectral range, high peak intensities and a repetition rate of 30 kHz. Two spectrometer setups allow for measuring high-resolution spectra. The cryostat provides temperatures as low as 1.4 K and constant magnetic fields up to 10 T. A collection of about 100 high-quality natural Cu_2O crystals in various orientations and thicknesses allows choosing the most suitable sample for the different nonlinear optical experiments.

A detailed description of the beam path and the most important instruments will be given in Sec. 3.1. The experimental methods are described in Secs. 3.2 to 3.5 and all samples used are characterized in Sec. 3.6.

3.1 Setup

The setup for SHG experiments is shown in Fig. 3.1(a). The laser system provides the setup with two separately tunable sources of laser pulses with a pulse duration of 200 fs and 3.3 ps corresponding to the spectral full width at half maximum (FWHM) of 10 meV and 0.7 meV, respectively, with a repetition rate of 30 kHz and an energy per pulse of up to 10 µJ. The fs pulses are tunable in a wavelength range of 620 to 2900 nm and the ps pulses from 315 to 2700 nm. A more detailed description of the laser system is given in Sec. 3.1.1.

The laser light paths are directed along the setup by silver mirrors with a 1 inch diameter. Two iris diaphragms (I) in front of the polarization optics ensure a reproducible adjustment. With a neutral density filter wheel (FW) between the irises the average power of the laser light can be continuously adjusted. The Glan-Thompson prism (GT) is set horizontally or vertically to let through the linearly polarized signal or idler beam. The spectral ranges, in which they are used, are marked in Fig. 3.3. If the half-wave plate (HWP) is rotated by an angle $\psi/2$, the linear polarization of the laser light is turned by the angle ψ. A long pass filter (F1) behind the polarization optics blocks SHG light induced in the HWP. The average laser power, which is adjusted via the filter wheel, can be measured in front of the cryostat window with a power meter. A lens in front of the cryostat with a focal length of 20 cm focuses the laser beam with a width of about 2 mm onto the sample with a spot size of about 70 µm. The sample is mounted strain-free and cooled in super-fluid helium within the VTI of the cryostat to a temperature as low as 1.4 K. A magnetic field of up to 10 T can be applied in Faraday ($\mathbf{B} \parallel \mathbf{k}$) or Voigt geometry ($\mathbf{B} \perp \mathbf{k}$) by rotation of the cryostat, which

has one coil pair and windows on all four sides. The cryostat is depicted in Fig. 3.4. A lens behind the cryostat with a focal length of 25 cm collimates the light emerging from the sample. A short pass filter (F3) blocks the laser light and allows the generated SHG light to pass through. An HWP followed by a GT in the collimated beam path selects a specific linear polarization with the angle φ for further detection. The GT is set to the preferred polarization angle of the spectrometer, which is horizontal for the Acton and vertical for the Spex spectrometer in the visible range. A lens with a focal length of 6.5 cm focuses the light that emerged from the sample onto the slit of the spectrometer. With an adjustable slit width down to 20 µm the spectral resolution of the Acton spectrometer is 80 µeV and that of the Spex spectrometer 20 µeV in first and 10 µeV in second diffraction order. More details on both spectrometers will be given in Sec. 3.1.3. The spectrally resolved signal light is focused on the chip of a nitrogen-cooled charge-coupled device (CCD) camera for detection and is read out via the WinSpec or LightField software. The CCD camera attached to the Acton spectrometer has a pixel size of 20 µm with a chip size of 1340 × 400 pixels. The CCD camera attached to the Spex spectrometer has a pixel size of 13.5 µm with a chip size of 2048 × 512 pixels. An additional telescope with a ×4 magnification is placed in front of the CCD camera in order to exploit the high resolution of the Spex spectrometer. Both chips are silicon-based with a sensitive wavelength range from 200 to 1080 nm.

For 2P-DFG experiments, as will be presented in Sec. 7, the setup is modified and shown in Fig. 3.1(b). Both laser beams are simultaneously used for the experiment. An additional delay line equipped with a retro reflector, which can be moved remotely over a rail of 1 m in steps of 100 nm, is placed into the ps laser light path. The ps pulses can therefore be delayed by a total distance of 2 m corresponding to about 6.67 ns. Due to the longer path of the light through the SHBC and the ps OPA of the ps pulses, the fs pulses have to be delayed behind the fs OPA by about 4 m in order to establish a time overlap of both ps and fs pulses in the sample. Therefore four additional mirrors are used to extend the fs light path. Analogously to the exciting fs laser, additional polarization optics are placed for the stimulating ps laser light, which turns its linear polarization by the angle θ. Two more irises ensure the reproducibility of the laser light adjustment. A prism with a rectangular triangle base is placed about 1 cm below the fs light path in front of the focusing lens in order to reflect the ps light from the side towards the sample and adjust the spatial overlap of both laser beams. As the spectral resolution of 2P-DFG experiments is determined by the spectral width of the stimulating ps laser, only the Acton spectrometer is used as it provides a better signal-to-noise ratio and a larger spectral range, which is mapped onto the CCD chip. As the laser light paths are about 4 m longer than in SHG experiments, the laser light diverges to a larger beam diameter. Therefore the 6.5 cm focal length lens in front of the Acton spectrometer is replaced by a lens with a focal length of 10 cm.

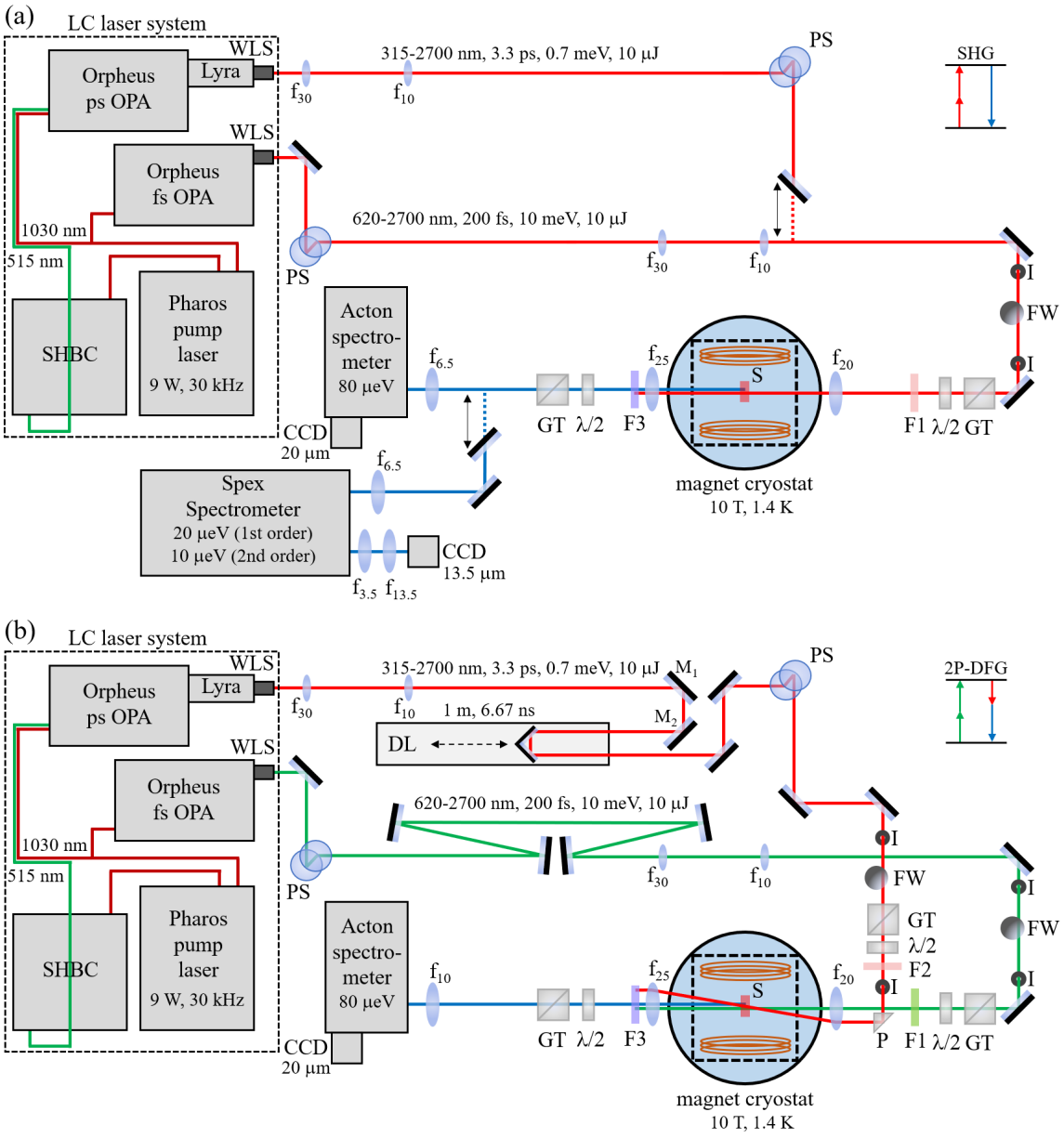

Figure 3.1 Setup configurations for (a) SHG and (b) 2P-DFG experiments: CCD - charge-coupled device camera, DL - delay line, F1/F2 - long pass filter, F3 - short pass filter, f_x - lens with x-cm focal length, FW - neutral density filter wheel, GT - Glan Thompson linear polarizer, I - iris diaphragm, $\lambda/2$ - half-wave plate, LC - Light Conversion, M_i - mirrors relevant for DL adjustment (see Sec. 3.4), OPA - optical parametric amplifier, P - prism, PS - periscope, S - sample, SHBC - second harmonic bandwidth compressor, WLS - wavelength separator.

3.1.1 Laser system

The laser system manufactured by Light Conversion consists of five devices, which are shown in Fig. 3.1. The main device is the "**Pharos**" pump laser, which generates femtosecond pulses and feeds all other devices. For the spectral tuning of the femtosecond pulses, the optical parametric amplifier (OPA) "**Orpheus**" is additionally needed. For the conversion to picosecond pulses and their spectral tuning, the second harmonic bandwidth compressor "**SHBC**", the ps-OPA "**Orpheus-ps**" and the wavelength extender "**Lyra**" are required. More in-depth descriptions of these devices are found in their respective manuals.

Pharos contains a short pulse oscillator generating narrow bandwidth pulses ($10-25$ nm corresponding to $70-90$ fs) at a repetition rate of 76 MHz and an average power of up to 2 W using Kerr lens mode locking. By the principle of chirped pulse amplification, the pulses are spatially stretched to lower their peak intensity. Then they pass through the regenerative amplifier, which contains the gain medium Yb:KGW (ytterbium-doped potassium gadolinium tungstate), which is pumped by CW laser diodes. An internal Pockels cell controls the injection and extraction of the pulses. A second Pockels cell acts as an electro-optical pulse-picker setting the repetition rate of the emitted pulses. The amplified pulses up to an average power of 9 W are compressed back to about 200 fs using the same transmission diffraction grating as during the stretching. Heated components of Pharos are cooled by the water-to-water chiller "Termotek P307" with a cooling power of 570 W.

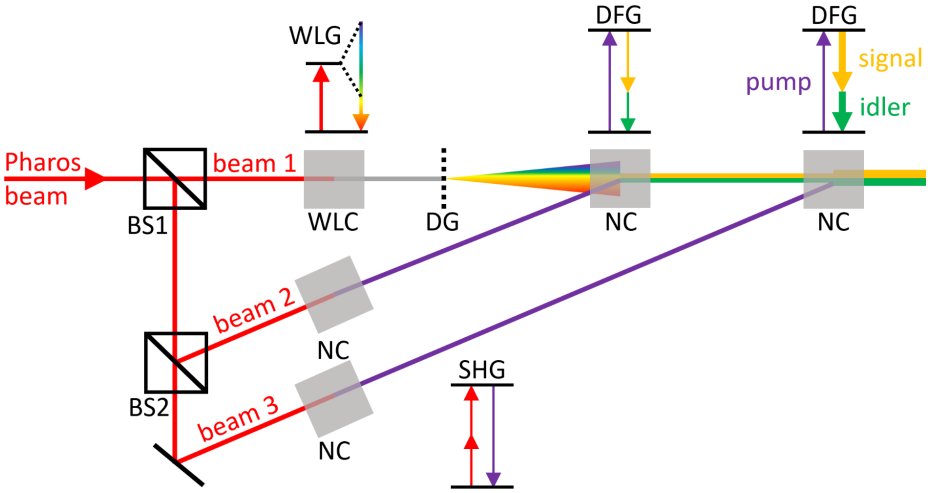

Figure 3.2 Scheme outlines the processes in an OPA. BS - beam splitter, DG - diffraction grating, NC - nonlinear crystal, WLC - white light generation crystal, WLG - white light generation.

The Pharos pulses pump the fs-OPA **Orpheus**. The basic principle of the OPA is sketched in Fig. 3.2. The entering Pharos beam is divided by beam splitter BS1. "Beam 1" passes through a white light generation crystal and generates a supercontinuum ($450-1200$ nm). A small spectral region of the white light is selected by a diffraction grating and acts as the seed beam for a DFG process in a nonlinear crystal. The wavelength can be tuned by changing the grating angle and therefore selecting a different wavelength for the amplification process.

The other part of the split Pharos beam is divided by beam splitter BS2 into "beam 2" and "beam 3" for two amplification stages achieved by difference frequency generation processes. "Beam 2" passes through a nonlinear crystal, in which the second harmonic with a wavelength of 515 nm is generated, which acts as the pump beam for the DFG process. The DFG process occurs in a nonlinear crystal, in which the seed beam from the white light generation process and the SHG of "beam 2" emerging from the nonlinear crystal are superimposed. For optimal phase matching of the DFG process, the rotation angle of the crystal is adjusted. Light with the difference frequency is generated and is called the idler. The seed beam is amplified, gaining power from "beam 2" in the DFG process and is called the signal beam while being linearly polarized orthogonal to the idler. The pump "beam 2" therefore loses power after this process.

"Beam 3" is also frequency doubled in the same nonlinear crystal as in the first stage and is used as the pump beam for the second amplification stage. Depending on the required wavelength, either the signal or the idler is chosen to pass through a wavelength separator (WLS) mounted at the exit of Orpheus.

Now we turn to the conversion and spectral tuning of the picosecond pulses. First, the $\approx$ 200 fs pulses of 1030 nm from Pharos need to be stretched to $\approx$ 3 ps pulses of 515 nm within the second harmonic bandwidth compressor **SHBC**. A beam splitter divides the beam path. The two beams are inversely chirped by a transmission grating and prisms and then superimposed in a nonlinear crystal, barium beta borate (BBO), so that the sum frequency of both beams is generated and the pulses are stretched in time and therefore spectrally compressed.

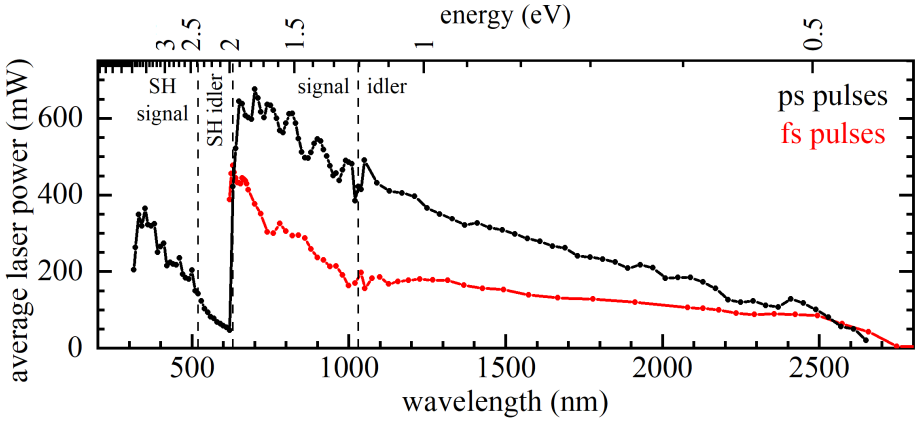

Figure 3.3 Average laser power output for the ps and fs OPAs.

Next the 1030 nm fs Pharos and 515 nm ps SHBC pulses feed the **Orpheus-ps**, in which the ps pulses are spectrally tuned and amplified. Its tuning principle is similarly implemented as in the Orpheus. The difference is, that the SHG stages for the Pharos beam are not required, as the SHBC provides 515 nm wavelength. The Orpheus-ps additionally has a third amplification stage, which keeps up to 95 % of the initial SHBC beam intensity.

For wavelengths above 630 nm the ps pulses just pass the following **Lyra** without further modification. By inserting a nonlinear crystal into the light path, wavelengths from 630 to 520 nm are reached by SHG of the Orpheus-ps idler beam in a nonlinear crystal. For

wavelengths from 520 to 315 nm the second harmonic of the Orpheus-ps signal beam is generated. The wavelength separators for the specific spectral regions are mounted at the exit of Lyra in order to select the signal or idler.

The average output power for the ps and fs OPAs for the whole operational spectral range is shown in Fig. 3.3.

3.1.2 Cryostat

The superconducting split coil cryostat of the model "Spectromag SM4000-11" is manufactured by Oxford Instruments. A technical drawing of its layout is shown in Fig. 3.4

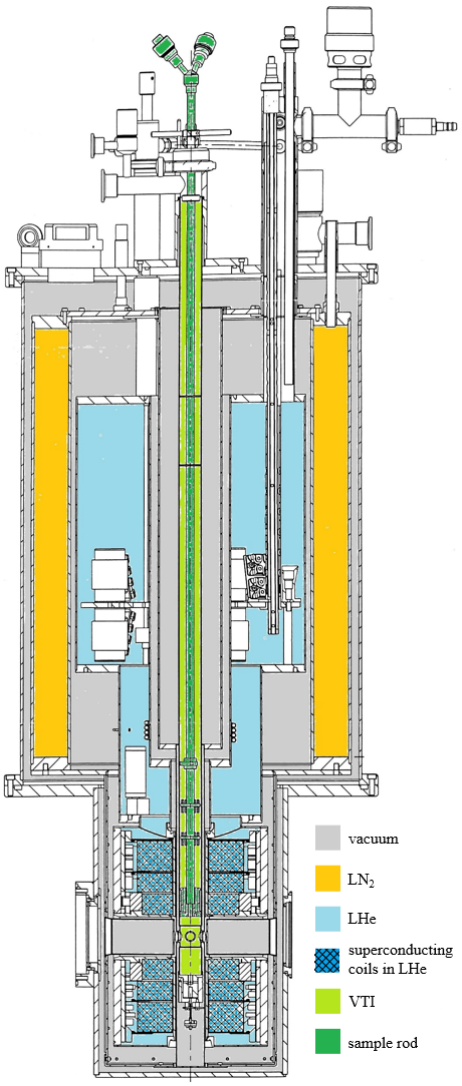

Figure 3.4 Scheme of the superconducting split coil cryostat. Adopted from its manual.

Its upper part has a coaxial structure with multiple layers including the variable temperature insert (VTI) in the center surrounded by a 20 L liquid helium (LHe) reservoir with an exhaust into the helium recovery system. In order to reduce the helium evaporation rate, a surrounding 24 L liquid nitrogen (LN2) reservoir with attached copper shields thermally screens the liquid helium from the surrounding room temperature and therefore reduces the losses due to thermal radiation, which scales with the fourth power of the temperature difference according to the Stefan-Boltzmann law [Nol17]. Once the cryostat is in an operational condition, the LHe evaporates into the recovery system at a rate of about 168 mL/h in standby and about 400 mL/h at the maximum magnetic field. The LN2 evaporates at a rate of about 492 mL/h and is released into the surrounding air. A vacuum chamber with a pressure of about 10^{-6} mbar thermally isolates the VTI, the liquid gas tanks from each other and the surrounding room temperature air.

The lower part of the cryostat has a rectangular cross-section containing the Helmholtz coil consisting of wound NbTi fibers in a copper matrix [Bal96]. The coils are located at the bottom of the helium reservoir and are therefore in a superconducting state at a temperature of 4.2 K enabling magnetic fields of up to 10 T requiring an electric current of 9.6 A/T. The current can be injected into the coils with an external power supply after the coil heater warms up the coil material and partially breaks the superconductivity. Then the current is increased until the targeted magnetic field is reached. The heater is then turned off and the power supply is ramped down to zero while the current still persists in the superconducting coils. In this mode, the magnetic field has a very low decay

rate of about 0.01 % per hour. Before the magnetic field can be changed again, the external power supply has to be ramped up in current to match the value in the coils and connected via the heater. The magnetic field is swept at a rate of 1 T/min below and 0.5 T/min above 7 T.

The sample is located within the VTI in the center of the coil pair. The cryostat has one window on each side at the height of the sample chamber allowing for magneto-optical transmission and reflection experiments in Faraday and Voigt geometry. The sample is mounted strain free and screwed onto the lower part of a sample rod, which is inserted into the VTI through an opening on the top side. For the cooling of the sample within the VTI, a needle valve is opened letting LHe from the reservoir into the VTI. This allows setting temperatures between 4.2 and 300 K, which can be stabilized with a PID controller, balancing the setting of the needle valve and the VTI heater. For all experiments in this work, the temperature has been set to 1.4 K by filling the VTI completely with liquid helium, closing the needle valve and lowering the pressure in the VTI with an external helium pump below 50 mbar, reaching sub lambda point temperatures (2.17 K), at which the helium becomes superfluid. The temperature can be precisely measured with a calibrated resistance cryogenic temperature sensor.

3.1.3 Spectrometers

The main spectrometer used for this work is the Acton series SpectraPro-2500i by Princeton Instruments. It has a Czerny-Turner layout, as depicted in Fig. 3.5(a) and is corrected for astigmatism. The signal beam emerging from the sample is focused onto its side slit, of which the width can be manually adjusted from 10 to 3000 µm with a micrometer screw. Then the light is reflected by a plane silver mirror behind the slit onto a concave mirror with a focal length of $f_{spec} = 500\,mm$, which reflects the parallel light onto a reflective grating with vertical grooves, which is blazed for 500 nm. Its rotation around the vertical axis is set, so that its first optical diffraction maximum is directed onto the second identical concave mirror, which focuses the spectrally resolved light onto the CCD camera chip. The spectral resolution mainly depends on the number of grooves on the grating. For most experiments in this work the $G_{Acton} \times G_{Acton} = 68\,mm \times 68\,mm$ sized grating with 1800 grooves per mm was used, which has a theoretical resolution of $1800/mm \cdot 68\,mm = 122400$ grooves. Consequently, a resolution of $2.0325\,eV/122400 = 16.6\,\mu eV$ is expected for the $1S$ yellow exciton. Experimentally, a line width of 80 µeV is measured with the Acton spectrometer as shown in Fig. 3.5(b). The reason for the large discrepancy is the insufficiently small size of the CCD pixels. A widening telescope behind the focusing plane of the spectrometer, which would magnify the spectral image on the CCD chip, could improve this issue. This technique will be used for the Spex spectrometer. In order to achieve the best resolution, the grating has to be illuminated as much as possible by the signal light beam, but not over-illuminated, so that intensity is lost. Therefore, the focal length of the focusing lens in front of the spectrometer slit has to be chosen correctly. For this, the aperture $A_{spec} = f_{spec}/G \approx 7.35$ of the spectrometer has to be considered. Given a typical signal beam diameter in SHG experiments of $d = 1\,mm$, a lens with a focal length of $f_{lens} = A_{spec} \cdot d = 7.35\,cm$ has to be chosen. Thus the best available lens with a focal length of 6.5 cm is used. An important remark to mention is, that the laser spot size on the sample is about 60 µm in diameter. The focus diameter of the signal beam on the slit is then reduced by a factor determined

by the ratio 20 cm/6.5 cm ≈ 3 of the collimating lens behind the cryostat and the focusing lens in front of the spectrometer and is therefore comparable to the minimum slit width of 20 µm set for the best resolution. Therefore no intensity is blocked by the slit, which would be the case for a larger laser spot size in the sample.

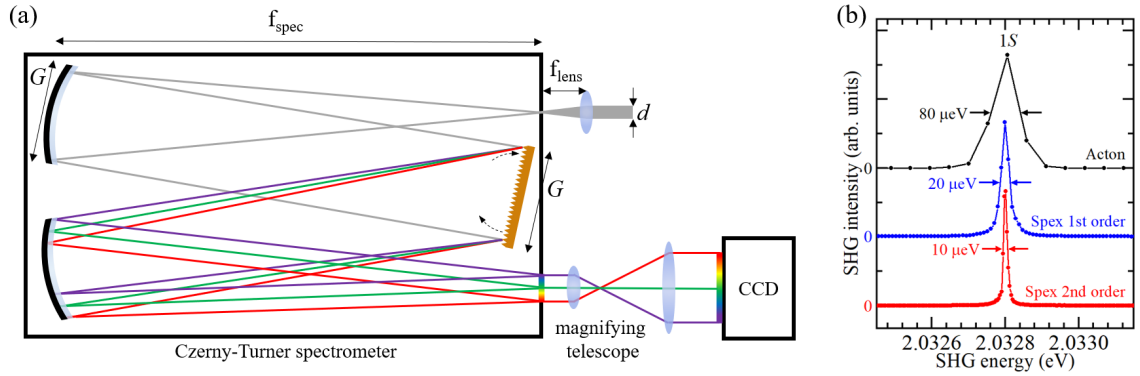

Figure 3.5 (a) Scheme of a Czerny-Turner spectrometer with two spherical mirrors with a focal length f_{spec} and a square shaped diffraction grating with $G \times G$ dimensions. The spectrum is focused on the CCD chip, which is placed at the position of the exit slit, as done for the Acton spectrometer. Alternatively, the focal plane containing the spectrum is magnified by two lenses and the CCD chip is placed at the focal plane behind the telescope. For optimal resolution and intensity of the detected spectrum, the focal length of the focusing lens has to be properly adjusted to the ratio f_{spec}/G of the spectrometer and the width d of the laser beam. (b) Resolution demonstration of both spectrometers using the zero-field SHG spectrum of the 1S orthoexciton (sample: H24, $\psi/\varphi = 0°/90°$).

The second option for spectral analysis of the signal is the Spex 1704 spectrometer, which also has a Czerny-Turner layout with a focal length of 1 m. The $G_{Spex} \times G_{Spex}$ = 100 mm × 100 mm sized grating has 1200 grooves per mm and thus a theoretical resolution of 1200/mm · 100 mm = 120000, which would enable to measure the yellow 1S exciton with an experimental line width of 2.0325 eV/120000 = 16.9 µeV. As shown in Fig. 3.5(b), the experimental line width is 20 µeV, which is very close to the expected value. The reason for this is the smaller pixel size of the CCD camera of 13.5 µm and the ×4 magnified spectral image onto the CCD chip using an objective with a 35 mm followed by a 135 mm lens. An additional advantage is, that with this grating the yellow exciton series in Cu_2O can be measured in second optical diffraction order by setting the grating angle to twice of the analyzed wavelength. The resolution is then expected to be improved by a factor of two, as confirmed in Fig. 3.5(b). Due to the larger focal length and the magnification in front of the CCD chip, the intensity per pixel with the Spex spectrometer is reduced by a factor of about 13 in the first and about 56 in the second order compared to the Acton spectrometer, see Ref. [Far18]. Therefore, the Spex spectrometer is only used, whenever the best resolution is necessary. In this work, this was only the case for precise measurements of the yellow 1S exciton energy.

The calibration of both spectrometers is done with spectral lamps suitable for the investigated spectral region (Neon for the yellow series). The spectral lines are identified using the NIST database [NIS23] and the vacuum wavelength in nm of each line is converted into

an energy in eV according to

$$E[\mathrm{eV}] = \frac{1239.842 \frac{[\mathrm{eV}]}{\mathrm{nm}}}{\lambda[\mathrm{nm}]}. \tag{3.48}$$

3.2 Spectral scanning method with picosecond pulses

SHG is a second-order nonlinear optical process and therefore requires a coherent light source with high peak intensity, preferably in the range of GW/cm^2. This can be provided by high-power pulsed lasers and focusing the laser beam down to a diameter of a few tens of micrometers. Historically, SHG spectra have usually been measured by spectrally scanning a high-power Nd:YAG nanosecond laser with a pulse duration of about 7 ns and a spectral width of about 1 meV, as demonstrated in Ref. [Sän+06b; Sän+06a; Laf+13a; Laf+13b; Bru+15].

As described in Sec. 3.1, our setup provides a picosecond pulsed laser with a pulse duration of 3.3 ps and a spectral width of about 0.7 meV. Although its spectral width is similar to that of the Nd:YAG lasers used in the past, the big advantage is, that it provides a significantly higher repetition rate of 30 kHz compared to the 10 Hz of Nd:YAG lasers. This high repetition rate reduces the scanning times for the same signal-to-noise ratio.

The measurement protocol is done as described in the following: The first step is to select a spectral range for the scan so that all investigated resonances are included within this range. If the resonance energies are already known from previous measurements or publications, the range can be set directly. Otherwise, scanning of the laser energy by hand and identifying all the relevant lines are required to choose an appropriate range, so that all relevant lines are included in the scanning interval. Next one has to choose a reasonable step size. It should be smaller than the line width of the resonances, although not much smaller than the spectral resolution of the spectrometer. If the spectrum has larger gaps without any resonances, e.g. the range between the $1S$ and the $2S$ excitons in the yellow series [see Fig. 2.5], one can decide to exclude this range from the measurement, as nothing interesting is expected. After that, one has to choose an appropriate integration time for each energy step. On the one hand, the integration time should be long enough to ensure a sufficient signal-to-noise ratio for the weakest resonances. On the other hand, the SHG intensity of the strongest exciton line should not exceed 2^{16} counts = 65536 counts for each readout CCD pixel column, as it gets saturated and no additional counts are registered. If the strongest and weakest exciton lines differ too much in their SHG intensity, one could split the scanned spectral range into multiple parts with different and more suitable integration times.

As soon as the spectral range and step size as well as the integration time are chosen, the measurement procedure can be started. The spectrometer grating angle is set, so that the central pixel column is set to the lower boundary of the chosen energy scanning range. The laser is set to half of this energy and the SHG spectrum for this specific position is integrated for the chosen integration time. Then the spectrometer energy setting is increased by the chosen energy step size and the laser energy is increased by half of it and the spectrum is integrated for the chosen time. This process is repeated until the whole chosen spectral range is scanned.

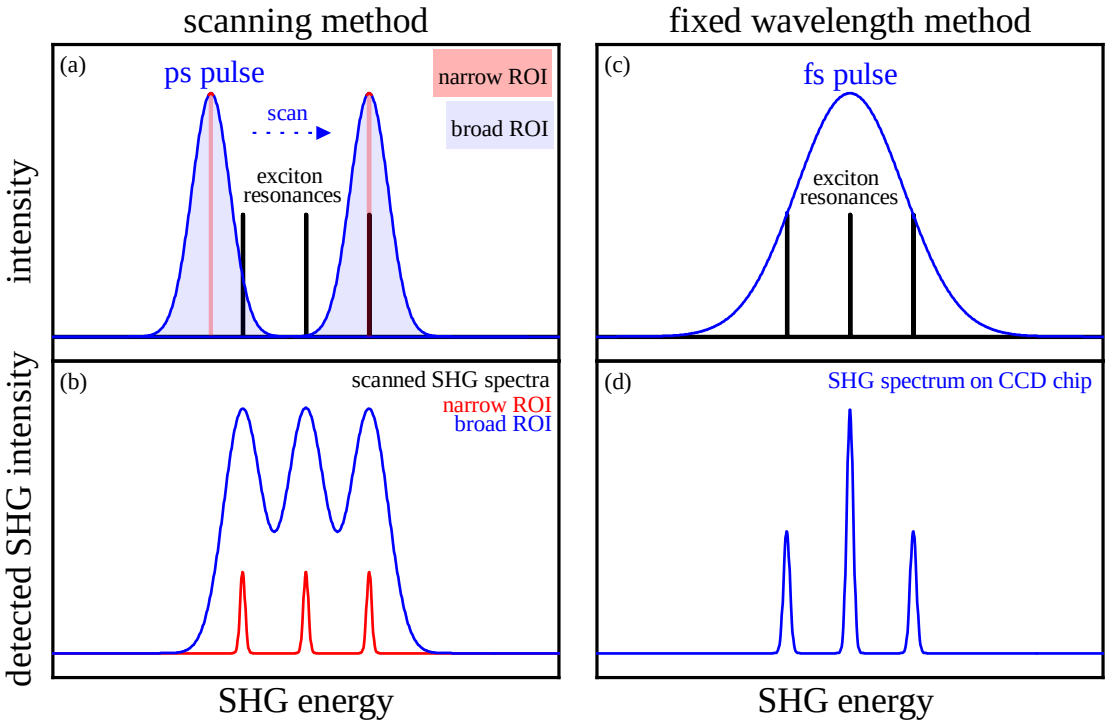

Figure 3.6 Methods for acquisition of SHG spectra. (a) The ps pulses are scanned through the range of three narrow exciton resonances with small steps. For each step, the SHG signal is collected within the region of interest (ROI) on the CCD chip, which may be chosen to be broad (blue-shaded area) or as narrow as only the central pixel of the power spectrum (red-shaded area). (b) The obtained spectrum with the broad ROI yields more signal intensity, but the resolution is given by the width of the ROI. The narrow ROI results in less intense lines with a resolution limited by the spectrometer and the scanning step size. (c) The fs pulses are fixed to half of the exciton resonance energy. The power spectrum covers all three resonances, of which the SHG signal is spectrally detected on the CCD chip, as shown in panel (d). The resolution is limited by the spectrometer.

Once the whole spectral range is scanned, the measured data have to be evaluated. There are different possibilities for how to process the data to obtain the SHG spectrum with different advantages and disadvantages.

In the past, the SHG spectra, that have been measured with 10 Hz nanosecond pulses, have been obtained by integration of the signal over the whole line width of the nanosecond laser, as shown by the blue area in Fig. 3.6(a). Due to the low repetition rate, the signals were comparably small and the signal-to-noise ratio could therefore be increased. The disadvantage is, that the resolution of the obtained SHG spectrum will be given by the spectral line width of the laser of about 1 meV, as shown by the blue line in Fig. 3.6(b). For resonances with significantly larger line widths, e.g. blue and violet excitons with line widths of at least 7 meV, such limitations in spectral resolution are not relevant. As the ps pulses with a high repetition rate provide sufficient signals in most cases, one can apply a different analysis method to obtain the SHG spectrum. Instead of integrating the signal over the whole spectral width of the laser, one can only take the intensity of the central

pixel column of the laser pulse, emphasized by the red area in Fig. 3.6(a). Although this leads to a worse signal-to-noise ratio, the resulting resolution of the SHG spectrum will only be limited by either the scanning step size or the resolution of the spectrometer, as depicted by the red line in Fig. 3.6(b). This method would be more suitable for the yellow exciton series, as it has sufficient SHG signals and requires a better resolution due to the narrow line widths.

Note, that the second evaluation method is not suitable for 2P-PLE experiments, as one can not select only the central energy of the laser to contribute to the PL intensity value for a certain laser energy setting. As the PL intensity is immediately generated, if the exciton line and the laser pulse overlap spectrally.

The final part is to ensure a correct calibration of the SHG spectrum. As the energy, which is entered into the laser software Topas4, does not correspond exactly to the actual laser energy and can vary slightly depending on the adjustment of the OPA and the ambient temperature, an exact calibration is needed each measurement day. If the laser energy is below the CCD sensitivity wavelength of 1050 nm, the laser power spectrum can be measured directly by setting the spectrometer to the laser energy. Of course, one has to reduce the laser power by several orders of magnitude first by placing many gray filters into the beam path, and removing them one by one until the laser intensity is detectable. For this measurement, the spectrometer has to be calibrated with a spectral pen lamp, as described in Sec. 3.1.3. If the laser energy is above the CCD sensitivity wavelength, one has to measure it indirectly by measuring its SHG signal generated in a BBO crystal, which is placed into the beam path and calibrating the spectrometer for this setting.

This measurement should be done for the lower and upper energy of the scanned spectral interval. The actual energies of the steps in between can then be interpolated linearly.

3.3 Fixed wavelength method with femtosecond pulses

A disadvantage of the scanning method is the long acquisition time for a single spectrum. If a measurement plan requires varying one or even more parameters for the spectrum, the total measurement time can quickly become unreasonably long. An elegant alternative SHG measurement method was introduced by Johannes Mund et. al [Mun+18] in 2018, which provides major benefits in some circumstances. Spectrally broad fs pulses have been used not for scanning the spectrum as described in the previous chapter, but by fixing the laser energy at half of the exciton energy and integrating for a reasonable amount of time and thus obtaining the SHG spectrum of several exciton lines, as sketched in Fig. 3.6(c). The broad power spectrum of the fs laser covers multiple exciton lines spread across a few meV with line widths in the range of 80 µeV. Although the fs pulses are spectrally broad, the SHG signal is only generated at the resonance energies. Therefore the spectral resolution is only limited by the spectrometer, as shown in Fig. 3.6(d). As described in Sec. 3.1.3, we have access to the Acton spectrometer with a spectral resolution of about 100 µeV and the Spex spectrometer with a resolution of about 20 µeV or 10 µeV in second optical order.

As an example, the described advantage is especially important for the measurement of the 2D polarization diagrams of several lines. The typical measurement time for one diagram at a fixed excitation energy is about one hour. The total measurement time with the scanning method would therefore scale with the number of investigated lines,

whereas the femtosecond integration method would require only one polarization scan, as all resonance lines are excited with one energy setting.

Finally one can draw the conclusion, that the picosecond pulse scan method is more suitable if one has to spectrally scan a large range with spectrally broad lines. It is especially beneficial, as the relative intensities of all lines are correctly measured, while providing larger total signals compared to the femtosecond pulses, due to the larger power density. The disadvantage of this method is the long acquisition time for a single SHG spectrum, due to many scanning steps. Here lies the big advantage of the femtosecond pulse integration method, as a whole SHG spectrum is measured with one laser energy setting. Although the relative intensities of the exciton lines are distorted due to the Gaussian shape of the power spectrum, this method is beneficial, if the focus of the investigations is put on the energies of the resonances. If multiple parameters are varied, e.g. the magnetic field strength or linear polarization angle settings, this method is significantly faster than the scanning method. It is most suitable for multiple spectrally narrow lines, which are energetically located in a small spectral interval of a few meV. An example of such a case is given in Fig. 4.12.

3.4 Difference-frequency generation with two-photon excitation

Difference-frequency generation with two-photon excitation (2P-DFG) is a nonlinear optical process involving a resonant two-photon excitation of exciton states. An additional pulsed laser is directed into the sample creating an overlap with the excitation laser, resulting in a two-photon process in the emission channel. It is a special case of four-wave mixing [Boy08], a third order nonlinear process characterized by $\chi^{(3)}$, with a degenerate two-photon excitation frequency ω_{exc} and a different stimulation frequency ω_{stim} driving a new light wave with a frequency of $\omega_{\mathrm{DFG}} = 2\omega_{\mathrm{exc}} - \omega_{\mathrm{stim}}$, as depicted in Fig. 2.1(d). The excitation laser creates an exciton population propagation coherently through the crystal in the form of exciton-polaritons with quite a small group velocity of $\approx 10^4$ m/s. The pulses of the second laser can be delayed using a delay line, and their linear polarization angle can be rotated using equivalent polarization optics as used for the excitation laser. It is directed towards the sample by a total reflection within a prism, the basis area of which is shaped like an isosceles right triangle. The light should enter and exit the prism at a normal angle to reduce refraction at the surfaces. The total reflection occurs at an angle of 45°. It is crucial to mention that both laser beams should not be collinear before entering the sample, as this third-order nonlinear process occurs in all transparent dielectric materials, such as the lenses, the cryostat windows and filters, leading to an additional detected 2P-DFG signal origination outside the sample and distorting the measurement. Therefore it is important, that both beams are directed parallel with an offset onto the focusing lens in front of the cryostat so that the lens focuses them into the sample leading to an overlap exclusively in the sample and nowhere else. The exact spatial overlap is adjusted with a rotation and tilt of the prism.

In the following, it is explained how to set up a 2P-DFG experiment considering the aspects mentioned above. The first point to ensure is a correct and careful adjustment of the delay line for the stimulating laser. It is achieved in two steps. A less accurate pre-adjustment by hand and a more exact instrument-assisted adjustment.

The first adjustment step requires two adjustable mirrors in front of the delay line and a

card, which is glued onto a metallic sheet folded at a right angle so that the angle can be pressed against the edge of the delay line rail. When the card is positioned onto the delay line and the metallic sheet is pressed against the rail edge, one can mark the position on the card with a cross, in which the beam should enter the retro reflector, and pierce a pinhole through the cross. Viewed from the front onto the round retro-reflector, the cross position should be half a radius to the right of the center, so that the beam exits half a radius to the left of the center. Next, the retro-reflector is moved as far back from mirror M_2 as possible and the card is positioned in the front of the delay line [see Fig. 3.1(b)]. Mirror M_1 is adjusted so that the beam passes with maximum intensity through the pinhole on the card. Then the card is positioned in the back of the delay line and mirror M_2 is adjusted so that the beam passes through the pinhole with maximum intensity. This is repeated for several iterations until the beam passes through the hole in the front and back positions of the card.

The second adjustment step requires an adjustment of the last mirror M_2 in front of the delay line and a power meter sensor head with a spatial resolution, which is able to display at which position the beam hits the sensor. The sensor head is positioned behind the delay line by hand so that the exiting beam hits the sensor in the center as well as possible. The sensor head must not move during the adjustment process. The button "relative" is pressed, which defines the beam spot on the sensor as the new central position. Then the retro-reflector is moved to the back position. The beam spot will move on the sensor display and has to be put back into the center by adjustment of the mirror M_2. Next, the retro-reflector is moved to the front position and the button relative is pressed again. This is one iteration, which should be repeated several times with increasing zoom of the power display up to $\times 16$, until the beam spot on the sensor stays in the center while moving the delay line through the whole range. The delay line is now adjusted.

Once the delay line is adjusted, the ps- and fs-laser beams have to be adjusted for an overlap within the sample. Therefore the ps-beam is reflected within a prism, which is positioned about 1 cm to the side of the fs-laser beam. The cryostat is removed from the beam path and an infrared indication card is positioned at the initial position of the sample. Then the tilt and rotation screws of the prism are adjusted so that both beams overlap on the infrared indication card.

Some experiments presented in Sec. 7 are performed with the excitation and stimulation beam coming from the same direction, as shown in Fig.7.1(a), a better way is to shoot them from opposite directions due to momentum conservation reasons, as shown in Fig. 7.1(b). For this, the prism has to be placed behind the collimating cryostat lens about 1 cm to the side of the fs-beam. As the infrared indication card can not be used for the adjustment of the overlap of both beams, as they hit the card from opposite sides, a suitable way for this adjustment is to use a thin paper card with a small pinhole. It should be placed at the initial sample position on an adjustable XY-stage so that the excitation laser goes through the pinhole with maximum intensity. The stimulation laser beam coming from the backside should then be adjusted with the prism to go through the pinhole with maximum intensity, resulting in an overlap of both beams within the pinhole.

The next step after the adjustment of the overlap in either geometry is to find the temporal overlap of the ps- and fs- laser pulses. When adjusting it for the first time, the exact delay distance between the ps- and fs-pulses is not known. Comparing at the beam exit points of both OPAs, the ps-pulses are delayed by approximately 4 m compared to the fs-pulses, as

they have a significantly longer beam path passing through the SHBC as seen in Fig. 3.1. One suitable way to find out the delay distance is to place a fast diode into the overlap at the initial position of the sample and read out the signal with an oscilloscope. One has to insert enough gray filters for the protection of the diode. Once both pulses are seen, the delay line is scanned to establish a temporal overlap of both pulses. If the delay is exceeding the delay line range, additional mirrors have to be installed for a further delay of the fs-laser, so that the temporal overlap is achievable within the range of the delay line. The temporal overlap should occur at the beginning of the delay line so that the ps-pulses responsible for the stimulation can be delayed over the leftover range of the delay line.

To find the exact delay line position, for which the temporal overlap between both pulses is achieved, a BBO crystal is placed at the spatial overlap of both beams and the spectrometer is set to the wavelength of the sum frequency generation (SFG). Then the delay line is scanned and one has to look for the SFG signal. As the pulse duration of 3.3 ps corresponds to a spatial width of about 1 mm, the SFG signal is only found within a range of 0.5 mm on the delay line. Once it is detected, it has to be improved by further adjustments of the prism, the transversal translation of the spectrometer lens and the beam spot on the sample. At this point, the 2P-DFG signal should be visible, when the spectrometer is set to the 2P-DFG wavelength. After minor adjustments to maximize this signal the cryostat is moved back into the beam path and the 2P-DFG signal from the sample is detectable.

For time-resolved measurements, the narrow exciton signal should be adjusted as follows. The delay line has to be set to a short delay time of about 10 ps after the temporal overlap. Then the signal intensity of the exciton is maximized by adjusting the prism and the rotation of the sample around the vertical axis for several iterations. If the exciton signal is adjusted for the time overlap setting instead of a short delay setting as suggested, the time-dependent signal might show an initial increase of the intensity within the first few hundreds of ps before the following expected exponential decay.

As the experiment is adjusted, one can measure the time dependence of the 2P-DFG signal following this protocol: As already described for other measurement types, one has first to select the interesting delay line range, the step size and the integration time. Then the delay line is scanned across the chosen range and for each step, the signal is measured for the chosen integration time and saved for later analysis. For the analysis, the pixel of maximum intensity of the resonance line is read out of each spectrum and plotted against the delay time. The retro-reflector position in units of millimeters is converted into the delay time

$$t_{\mathrm{delay}} = 2xn_{\mathrm{air}}/c \tag{3.49}$$

in units of picoseconds, with the retro reflector position x, the refractive index n_{air} of air and the vacuum speed of light c.

3.5 Polarization dependence

The measurement of the polarization dependence is of crucial importance. Coherent nonlinear optical processes are influenced by the symmetry of the excited states, the light interaction and possible perturbations as strain or external electric or magnetic fields. They

therefore underlay polarization selection rules, as introduced in Sec. 2.3 and further described in Sec. 4.1. For the observation of the signal, it is required, that the excitation and emission channel of the process are allowed by symmetry. By systematically measuring the signal intensity of an exciton resonance while varying the incoming and outgoing polarization angles one can investigate and identify the underlying optical mechanism. In previous works, only two cases of the polarizations have been shown in polar diagrams. Specifically, the case in which the incoming and outgoing polarization are parallel and turned simultaneously also referred to as the parallel configuration, and the case, in which the incoming and outgoing polarizations are orthogonal to each other and are turned simultaneously, is also referred to as the crossed configuration. In principle, those two configurations are sufficient for the identification of the process. In reality, small distortions or deviations from the simulated diagrams are often difficult to detect and therefore leading to some uncertainty in the identification of the underlying optical process. A more extensive picture is given by measuring all possible polarization angle combinations, of course with a finite angular step size of about 10°, and showing the results in a contour plot, in which the signal intensity is represented by a color scale in dependence of the linear polarization angles of the incoming and outgoing light as the horizontal and vertical axis, respectively. By comparisons to the simulated diagrams, small deviations are more easily revealed, and the optical process for the simulation can be adjusted for a better match to the measurements.

The Glan-Thompson prism (GT) reflects the s-polarized light to the side and only lets through the p-polarized light. The transmission axis is marked by a white line. It is positioned into the laser beam and oriented horizontally or vertically depending on if the signal- or idler-beam is in use for the set wavelength. The GT of the analyzer should be oriented along the preferred direction of the spectrometer grating, which is horizontal for the Acton spectrometer in the visible range. The half-wave plate is a birefringent crystal, which has different refractive indices for the fast axis, marked by a line, and the axis perpendicular to it. Consequently, the polarization component of the fast axis propagates faster through the plate, leading to a phase difference of half a wavelength compared to the orthogonal component, which results in an effective rotation of the linear polarization of the incoming light. In particular, the linear polarization of the light is rotated by the angle ψ, if the half-wave plate is rotated by the angle $\psi/2$. As $\psi = 0°$ in this work is defined along the horizontal direction, the fast axis of the half-wave plate has to be exactly between the horizontal orientation and the orientation of the Glan-Thompson prism for the zero-position. As an example, if the GT is set to 90°, the half-wave plate has to be set to 45°, so that the linear polarization angle corresponds to 0°. The Glan Thompson prisms are oriented by hand but the rotation of the half-wave plates is controlled by motorized rotation stages from OWIS. The motorized stages are accessed by the OWIS software, which is also integrated in a Labview program for automated polarization dependence measurements.

The measurement protocol is described in the following. First, the exciton signal is adjusted for maximum intensity. In many cases, in which the resolution is not important, one can open the spectrometer slit and also switch to a grating with less line density for an increase of the signal intensity. With an integration time of 1 s the measurement of the full polarization dependence takes about one hour. Therefore the integration time should not exceed about one second. The linear polarization angle ψ of the incoming light and ϕ of the outgoing light are set to 0° and the spectrum is measured and saved. ϕ stays fixed and ψ is set to 10° and the spectrum is saved again. The measurements are repeated

until $\psi = 360°$. The ψ-scan is repeated for ϕ settings up to 360° in 10° increments. Note, that in many cases ϕ is only varied up to 180°, as the signals are 180°-periodic, and the 10° to 180° measurements can just be copied for the 190° to 360° range. The parallel and crossed configurations can in principle be extracted from the full polarization dependence diagram as the diagonals starting from $\psi/\phi = 0°/0°$ and $\psi/\phi = 0°/90°$. Nevertheless, it is recommended to measure them separately, because one can choose longer integration times for a better signal-to-noise ratio and smaller angular increments, as their measurement takes much less time. Another reason is the fluctuating signal over the long measurement time of the full polarization dependence. This can occur due to a change in temperature, a drift in laser power or in the case of 2P-DFG experiments a worsening of the spatial overlap of both lasers.

3.6 Samples

All used samples in this work (see Tab. 3.1) are cut out of a high-quality Cu_2O crystal from the Tsumeb mine in Namibia. This particular crystal has served in numerous investigations of Rydberg excitons in the past two decades. To this day, about 120 samples with various orientations and thicknesses have been cut out from this crystal and mounted strain-free in brass sample holders as shown in Fig. 3.7(a). The experimental orientation of the sample is shown in Fig. 3.7(b). In this chapter, the specific samples used for the experiments of this work are characterized and the criteria for choosing the most suitable sample for different optical experiments are described.

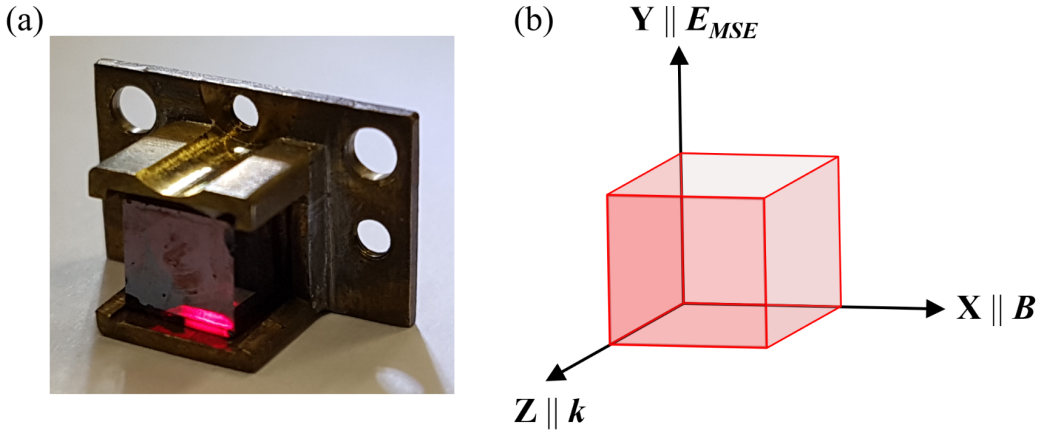

Figure 3.7 (a) Photo of sample H106 (see Tab. 3.1) in a brass holder with the cover plate removed. Holes on all four sides allow for light transmission along different crystal axes. (b) Experimental orientation of the sample with the orthogonal crystal axes **X**, **Y** and **Z**, along which the light **k**, the magnetic field in Voigt geometry **B** and the effective electric field $\mathbf{E}_{\mathrm{MSE}}$ of the MSE are directed.

For the magnitude of the SHG signal the crystal thickness is not significantly relevant, as the fundamental beam passes through the sample without noticeable absorption but the SHG photon is reabsorbed strongly with an absorption coefficient of about $25\,\mathrm{mm}^{-1}$ for the $1S$ exciton [Hec20]. Therefore the detectable SHG signal originates from the last few tens

of micrometers in the sample and an additional thickness does not contribute significantly. However, in very thin samples Fabry-Perot interferences can occur in the SHG spectra. Although this is not noticeable, while the exciton lines are narrow as in the case of the yellow series, it can distort the SHG spectra of spectrally broad exciton lines as in the case of the blue excitons. On the other hand, the crystal orientation is crucial for SHG experiments. For the case of Cu_2O, SHG is allowed for excitation along the [111] and [112] and forbidden along the [110] and [001] crystal axis. If the intent is to investigate the crystallographic SHG effect the former two orientations should be chosen. The latter two orientations are suitable if the intent is to measure magnetic-field-induced SHG contributions to avoid the more complex interference with the crystallographic contribution. For a separation of different magnetic-field induced SHG contribution, e.g. magneto-Stark effect and Zeeman effect, one has to check the simulated polarization diagrams (see Figs. 4.7 and 4.10) and choose the appropriate horizontal crystal axis. In contrast to SHG, the 2P-PLE signal scales with the crystal thickness and therefore thick samples are recommended for excitation spectroscopy. A special case occurs for the SHG experiments of paraexcitons. As the paraexciton is spectrally close to the Γ_3^- phonon side band of the orthoexciton, which emits a strong PL signal, the weak SHG contribution can be overpowered by the Γ_3^- phonon side band emission in thick samples. In this case, very thin samples are recommended.

Table 3.1 List of used Cu_2O samples with their internal designation, orientation and thickness. Cuboid-shaped samples can be used for both horizontal directions by rotating the sample holder by 90° and are therefore indicated by *a* and *b*.

sample designation	**Z** || **k** ||	**Y** ||	**X** || **B** ||	thickness (µm)
H2a	[111]	$[1\bar{1}0]$	$[11\bar{2}]$	3663
H2b	$[11\bar{2}]$	$[1\bar{1}0]$	[111]	4998
H13	$[1\bar{1}0]$	[110]	[001]	252
H24	[111]	$[11\bar{2}]$	$[1\bar{1}0]$	30
H45b	$[1\bar{1}0]$	[001]	[110]	4880
H45a	[001]	$[1\bar{1}0]$	[110]	3424
H98	[001]	$[\bar{1}10]$	[110]	46
H100	$[1\bar{1}0]$	[001]	[110]	50
H106a	[001]	$[1\bar{1}0]$	[110]	5325
H106b	$[1\bar{1}0]$	$[1\bar{1}0]$	[001]	5245

For 2P-DFG experiments, it is also recommended to use thick samples, as the crystal is transparent for all photons involved in the process. Therefore the detectable signal can be collected from the whole sample volume. Thick crystals have the additional benefit, that the portion of polaritons, which are reflected at the back surface of the crystal at a certain time, is negligible compared to the total number of polaritons. The DFG contribution of reflected polaritons in the direction of the spectrometer vanishes due to the conservation of momentum, which has to be considered for this process. Samples, which are a few millimeters thick have the additional benefit of being able to be used along the other horizontal axis, as long, as the mounting has additional openings. All the samples, which have been chosen for the experiments of this work are depicted in Table 3.1 with their orientation and thickness. Up to four sample mountings can be screwed onto the sample rod and can be

interchanged during the experiment by moving the sample rod vertically. An additional Cernox resistance can be mounted onto the sample rod for a more accurate measurement of the temperature in the vicinity of the samples.

Chapter 4

Magnetic-field-induced SHG of yellow-series excitons

In this chapter, we investigate the yellow-series excitons in Cu_2O under the influence of an externally applied magnetic field **B** perpendicular to the light direction **k** using SHG spectroscopy. The yellow series has been extensively investigated in the past. Excitons have been discovered in 1952 by Gross et al. by measuring the absorption spectrum of the yellow P exciton series up to a principal quantum number of $n = 8$ [Gro+52]. The series has been extended by Kaziemierczuk et al. in 2014 up to $n = 25$ by scanning a spectrally narrow laser through this spectral range [Kaz+14]. The odd parity series of S and D excitons has first been measured by Fröhlich et al. in 1979 by two-photon absorption without applying external perturbations [Frö+79] and further investigated by Uihlein et al. [Uih+81]. In 1996, the $1S$ exciton was observed via SHG by Shen et al. [She+96]. The SHG spectrum of the spectrally narrow S and D Rydberg states up to $n = 9$ was measured by Mund et al. in 2018 by using spectrally broad femtosecond laser pulses [Mun+18].

SHG as a nonlinear optical process has the advantage, that it is highly dependent on the symmetry of the investigated material and its exciton states. It exhibits a characteristic dependence of the SHG intensity on the linear polarization angles of the three involved photons obeying the polarization selection rules, which can be derived by a symmetry analysis using group theoretical multiplication and coupling coefficient tables from Ref. [Kos+63], the important ones of which are shown in Sec. A. As explained in Sec. 3.5, this polarization dependence can also be measured experimentally. A comparison of the experimentally measured polarization dependencies and the theoretically derived ones contributes to the understanding of the underlying SHG mechanism. A good agreement suggests the correctness of the proposed mechanism.

The crystal structure of Cu_2O exhibits a cubic symmetry including space inversion and is characterized by the O_h point group. For Cu_2O as a centrosymmetric material, no SHG is expected. Therefore SHG requires higher order optical transitions involving the light vector **k** such as the electric quadrupole and magnetic dipole, as introduced in Sec. 2.2.

As demonstrated in Refs. [Mun+18] and [Mun+19], SHG on excitons in Cu_2O is allowed for **k** pointing along the low symmetry directions [111] and [11$\bar{2}$] but is forbidden for **k** along the high symmetry directions [110] and [001]. However, in the case of perturbation effects such as internal strain, SHG might get allowed in forbidden **k** geometries as demonstrated for the $1S$ exciton by Mund et al. [Mun+19].

Another type of perturbations are externally applied electric or magnetic fields, as demonstrated for Cu_2O in Refs. [Zhi+69; Sch+17a; Rom+18; Aßm+16; Hec+17a].

In this work, we will investigate various mechanisms of the magnetic field-induced SHG.

Of special interest is the Voigt geometry, in which the magnetic field is applied perpendicular to the light direction, as one would expect an influence of the magneto-Stark effect (MSE) resulting in an effective electric field due to the excitonic center of mass motion [Tho+60; Gro62] perpendicular to the magnetic field, as explained in Sec. 2.4. The MSE was demonstrated in 1961 by Thomas et al. [Tho+61] in CdS and was recently identified as the SHG-inducing mechanism in experiments on ZnO [Laf+13a].

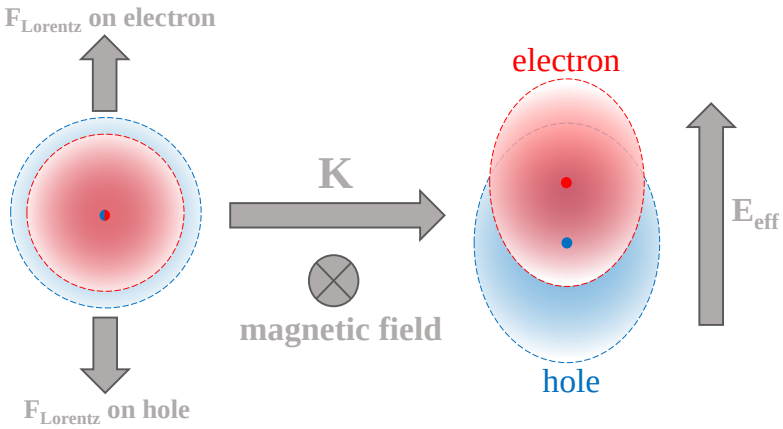

Figure 4.1 Sketch of the magneto-Stark effect. It shows a bound electron-hole pair subject to Lorentz forces acting in opposite directions due to a motion perpendicular to an external magnetic field. It results in an effective electric field, which separates the charge distributions of electron and hole.

A visualization of the MSE in our geometry is sketched in Fig. 4.1. On the left, an S exciton is shown by overlapping spherical charge distributions of the electron and hole sharing the same center of charge. By moving along the excitation direction $\mathbf{k}$ perpendicular to the magnetic field, the Lorentz force acts in opposite directions onto the electron and hole, due to their opposite charges, leading to a separation of both charge distributions along the Lorentz force axis. Evidently, this appears as if an electric field $\mathbf{E}_{\mathrm{MSE}} \propto \mathbf{k} \times \mathbf{B}$ is acting upon them. The influence of the magnetic field on the excitons wave function is associated with the Zeeman effect (ZE) and the influence of the effective electric field is associated with the MSE. Therefore the MSE is absent in Faraday geometry, in which the light vector and the magnetic field are aligned.

This chapter is structured in the following way: In Sec. 4.1 the method for the derivation of polarization selection rules is explained and demonstrated for crystallographic, ZE-induced, MSE-induced and interfering SHG mechanisms. In Sec. 4.2 we will present experimentally obtained magnetic field series of ZE- and MSE-induced SHG spectra and the polarization dependence diagrams for isolated and interfering magnetic-field induced SHG mechanisms. The average excitation power of the fs-pulsed laser is set to about 10 mW. The results of this chapter are published in Ref. [Far+20b].

4.1 Simulation of polarization dependencies

In this section, we will derive the crystallographic and magnetic-field-induced SHG intensity as a function of the two linear polarization angles of the incoming laser light and the outgoing SHG light for various mechanisms. SHG schemes, as shown in Figs. 4.3, 4.6 and 4.9, turned out to be a very helpful visualization tool for finding and calculating the polarization selection rules. They include the symmetries of the photon transitions, the exciton states and the external fields.

Although SHG is a coherent process, in which two photons are converted into a single photon, for our symmetry analysis it can be considered as a two-photon excitation, represented by the two up-pointing arrows on the left from the ground state (lower line) to the exciton state (upper line), followed by a single-photon emission corresponding to the down-pointing arrow on the right. The horizontal arrow between the exciton states represents the coupling of these states by an external field.

For the derivation of the polarization-dependent SHG intensity, it is crucial to take into account the exciton symmetry and the symmetries of the one- and two-photon processes.

We start with the derivation of the symmetries of the yellow series S, P and D excitons. As an exciton is a bound state of an electron and a hole, its symmetry is given by the product of symmetries of the conduction band, the valence band and the envelope function:

$$\Gamma_{\mathrm{X}} = \Gamma_{\mathrm{VB}} \otimes \Gamma_{\mathrm{CB}} \otimes \Gamma_{\mathrm{env}}. \tag{4.50}$$

Γ_i are the irreducible representations, which indicate the transformation behavior of a state and therefore characterize its symmetry, as explained in Sec. 2.3. As shown in Fig. 2.3(c), the yellow series involves the highest valence band with Γ_7^+ symmetry and the lowest conduction band with Γ_6^+ symmetry. The symmetry of the envelope function depends on the orbital quantum number L. S orbitals ($L = 0$) are spherical and have positive parity resulting in a Γ_1^+ symmetry. The symmetry of S excitons is thus given by:

$$\begin{aligned} \Gamma_S &= \Gamma_7^+(2) \otimes \Gamma_6^+(2) \otimes \Gamma_1^+(1) \\ &= \Gamma_2^+(1) \oplus \Gamma_5^+(3). \end{aligned} \tag{4.51}$$

The single Γ_2^+ exciton is a pure spin-triplet state and therefore optically inactive for single-photon transitions. In Cu_2O, it is called the paraexciton and we will discuss the SHG mechanisms and the Rydberg series of these states in Sec. 5.

P orbitals are isotropic around one axis and have negative parity resulting in a Γ_4^- symmetry. For P excitons we therefore get:

$$\begin{aligned} \Gamma_P &= \Gamma_7^+(2) \otimes \Gamma_6^+(2) \otimes \Gamma_4^-(3) \\ &= \Gamma_2^-(1) \oplus \Gamma_3^-(2) \oplus \Gamma_4^-(3) \oplus 2\Gamma_5^-(3). \end{aligned} \tag{4.52}$$

D orbitals are similar to quadrupole fields resulting in a Γ_5^+ and Γ_3^+ symmetry. The symmetry of D excitons is thus calculated by:

$$\begin{aligned} \Gamma_D &= \Gamma_7^+(2) \otimes \Gamma_6^+(2) \otimes [\Gamma_5^+(3) \oplus \Gamma_3^+(2)] \\ &= [\Gamma_2^+(1) \oplus \Gamma_5^+(3)] \otimes [\Gamma_5^+(3) \oplus \Gamma_3^+(2)] \\ &= \Gamma_1^+(1) + 2\Gamma_3^+(2) + 3\Gamma_4^+(3) + 2\Gamma_5^+(3) \end{aligned} \tag{4.53}$$

For a strong coupling between an exciton state and a photon, both are required to exhibit the same symmetry, as explained in Sec. 2.3 by Eq. (2.29).

The symmetry of the electric dipole (ED) in the first term of the expansion of Eq. (2.26) and the symmetries of the electric quadrupole (EQ and EQ_3) and magnetic dipole (MD) in the second term are given by

$$\Gamma_{\mathrm{D}} = \Gamma_4^-, \tag{4.54}$$

$$\Gamma_{\mathrm{Q}} = \Gamma_5^+ \oplus \Gamma_3^+, \tag{4.55}$$

$$\Gamma_{\mathrm{MD}} = \Gamma_4^+. \tag{4.56}$$

Consequently, it follows from Eqs. (4.54), (4.55) and (4.56), that S excitons interact with the light field in electric quadrupole approximation (Γ_5^+), P excitons in electric dipole approximation (Γ_4^-) and D excitons in electric quadrupole ($\Gamma_5^+ \oplus \Gamma_3^+$) and magnetic dipole approximations (Γ_4^+).

The experimental geometry is shown in Fig. 4.2. The laboratory coordinate system

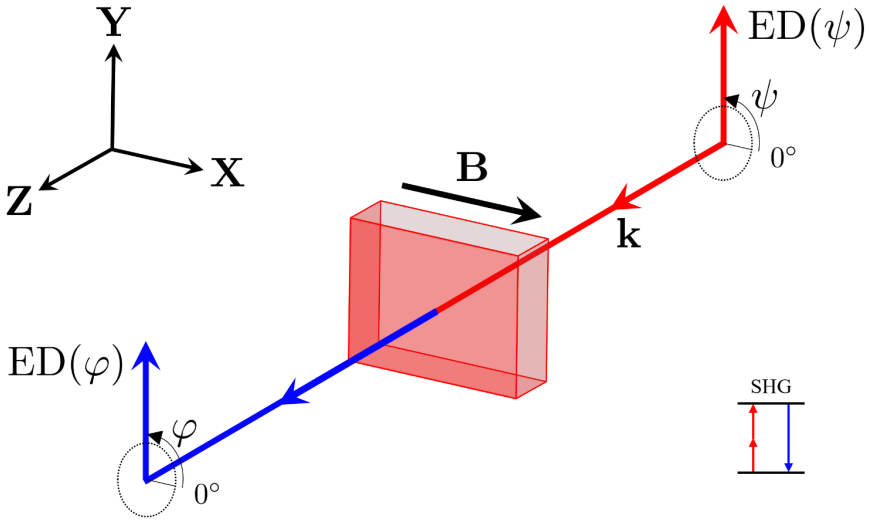

Figure 4.2 Experimental geometry displaying the sample with the crystal axis **X**, **Y** and **Z** and the relevant directions of the laser and SHG light (**k**), the magnetic field (**B**) in Voigt configuration, the effective electric field ($\mathbf{E}_{\mathrm{MSE}}$) and the linear polarization angles ψ and φ. The chosen sample for the experiments of this chapter is H100 (see Tab. 3.1) resulting in $\mathbf{Z} \parallel \mathbf{k} \parallel [1\bar{1}0]$, $\mathbf{X} \parallel \mathbf{B} \parallel [110] \parallel \mathbf{E}(\psi = \varphi = 0°)$ and $\mathbf{Y} \parallel \mathbf{E}_{\mathrm{MSE}} \parallel [001] \parallel \mathbf{E}(\psi = \varphi = 90°)$.

consists of the crystal axis vectors **X**, **Y** and **Z** and is specified for each investigated sample. The wavevector of the light

$$\mathbf{k} = \begin{pmatrix} k_1 \\ k_2 \\ k_3 \end{pmatrix} \tag{4.57}$$

is directed along the **Z** direction of the sample. The magnetic field **B** is oriented along the **X** direction of the sample, which also corresponds to a linear polarization angle of ψ or $\varphi = 0°$.

As the electric dipole vector is always perpendicular to the $\mathbf{k}$ vector, it can be parameterized by rotating the horizontal crystal axis $\mathbf{X}$ by the angle ψ around $\mathbf{k}$. For this, we need the general rotation matrix

$$\mathbf{M}_{\mathrm{rot}}(\mathbf{k},\psi) = \tag{4.58}$$

$$\begin{pmatrix} k_1^2(1-\cos\psi)+\cos\psi & k_1k_2(1-\cos\psi)-k_3\sin\psi & k_1k_3(1-\cos\psi)+k_2\sin\psi \\ k_2k_1(1-\cos\psi)+k_3\sin\psi & k_2^2(1-\cos\psi)+\cos\psi & k_2k_3(1-\cos\psi)-k_1\sin\psi \\ k_3k_1(1-\cos\psi)-k_2\sin\psi & k_3k_2(1-\cos\psi)+k_1\sin\psi & k_3^2(1-\cos\psi)+\cos\psi \end{pmatrix}.$$

The electric dipole vector O_{D} can be expressed as the multiplication of the rotation matrix $\mathbf{M}_{\mathrm{rot}}$ and the $\mathbf{X}$ vector:

$$O_{\mathrm{D}}(\psi) = \begin{pmatrix} d_1(\psi) \\ d_2(\psi) \\ d_3(\psi) \end{pmatrix} = \mathbf{M}_{\mathrm{rot}}(\mathbf{k},\psi)\cdot\mathbf{X} \tag{4.59}$$

The components of the electric dipole vector are denoted as d_i, as they will be relevant for many other optical couplings in this section.

The electric quadrupole with $\Gamma_5^+ \oplus \Gamma_3^+$ symmetry and the magnetic dipole with Γ_4^+ symmetry originate from the second term in the expansion in Eq. (2.26). For their vector expression, one has to couple the electric dipole vector (Γ_4^- symmetry) with the $\mathbf{k}$ vector (Γ_4^- symmetry) according to the coupling coefficient table A.7 for $\Gamma_4^- \otimes \Gamma_4^- \to \Gamma_5^+$ from Ref. [Kos+63]. The Γ_5^+ electric quadrupole vector is therefore expressed by

$$O_{\mathrm{Q}}(\mathbf{k},\varphi) = \frac{1}{\sqrt{2}}\begin{pmatrix} k_2d_3(\varphi)+k_3d_2(\varphi) \\ k_3d_1(\varphi)+k_1d_3(\varphi) \\ k_1d_2(\varphi)+k_2d_1(\varphi) \end{pmatrix} = \begin{pmatrix} q_1(\mathbf{k},\varphi) \\ q_2(\mathbf{k},\varphi) \\ q_3(\mathbf{k},\varphi) \end{pmatrix} \tag{4.60}$$

and its components are denoted as q_i for further couplings. The Γ_4^+ magnetic dipole vector is constructed as

$$O_{\mathrm{MD}}(\mathbf{k},\varphi) = \frac{1}{\sqrt{2}}\begin{pmatrix} k_2d_3(\varphi)-k_3d_2(\varphi) \\ -k_1d_3(\varphi)+k_3d_1(\varphi) \\ k_1d_2(\varphi)-k_2d_1(\varphi) \end{pmatrix} = \begin{pmatrix} m_1(\mathbf{k},\varphi) \\ m_2(\mathbf{k},\varphi) \\ m_3(\mathbf{k},\varphi) \end{pmatrix} \tag{4.61}$$

and its components are denoted as m_i for further couplings. The Γ_3^+ electric quadrupole vector is consequently given by

$$O_{\mathrm{Q3}}(\mathbf{k},\varphi) = \frac{1}{\sqrt{6}}\begin{pmatrix} -k_1d_1(\varphi)-k_2d_2(\varphi)+2k_3d_3(\varphi) \\ -\sqrt{3}k_1d_1(\varphi)-\sqrt{3}k_2d_2(\varphi) \end{pmatrix} = \begin{pmatrix} q_{3,1}(\mathbf{k},\varphi) \\ q_{3,2}(\mathbf{k},\varphi) \end{pmatrix}, \tag{4.62}$$

with its components $q_{3,i}$.

Now we have all the necessary single-photon interaction vectors, which will be coupled to higher order process vectors in the following paragraphs.

4.1.1 Crystallographic SHG

Let us now turn to the derivation of the polarization-dependent SHG intensity for crystallographic processes. First one has to find and identify all possible crystallographic SHG processes by a symmetry consideration using the SHG schemes and the multiplication table A.3 from Ref. [Kos+63]. As mentioned above we have already found all possible one-photon processes for the SHG emission channel. Next, one has to find all two-photon processes for the excitation of excitons with Γ_3^+, Γ_4^+, Γ_5^+ and Γ_4^- symmetry, so that Eq. (2.28) is fulfilled.

Let us start with even parity excitons as they already involve a higher-order process in the single-photon emission channel. So we only have to check, if they are excitable by an ED-ED two-photon process. For this we use the multiplication table A.3 for the O_h group from Ref. [Kos+63] and get

$$\Gamma_\mathrm{D} \otimes \Gamma_\mathrm{D} = \Gamma_4^- \otimes \Gamma_4^- \rightarrow \Gamma_1^+ \oplus \Gamma_3^+ \oplus \Gamma_4^+ \oplus \Gamma_5^+. \tag{4.63}$$

Therefore the even parity Γ_3^+, Γ_4^+ and Γ_5^+ excitons are in principle symmetry allowed via ED-ED two-photon excitation combined with EQ, MD and EQ3 single-photon emission. The SHG schemes are shown in Fig. 4.3.

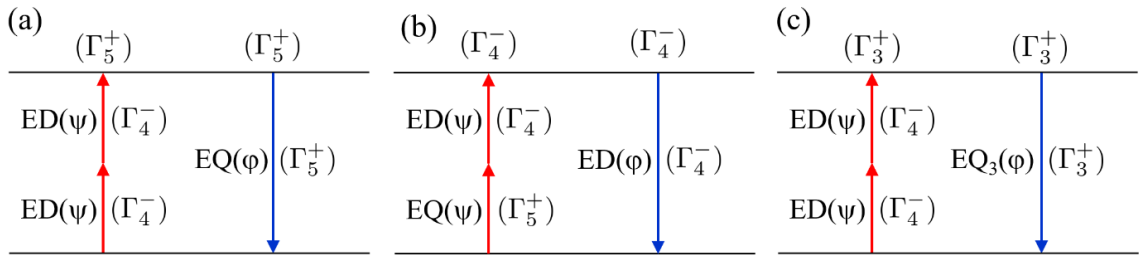

Figure 4.3 Schematics of the crystallographic SHG processes for (a) even-parity Γ_5^+ (b) odd-parity Γ_4^- and (c) even-parity Γ_3^+ exciton states at zero magnetic field.

For the construction of the ED-ED excitation vector O_DD^{5+} for Γ_5^+ excitons one has to couple two O_D^{4-} vectors using the coupling coefficient table A.7 for $\Gamma_4^- \otimes \Gamma_4^- \rightarrow \Gamma_5^+$ from Ref. [Kos+63]:

$$O_\mathrm{DD}^{5+}(\psi) = \frac{1}{\sqrt{2}} \begin{pmatrix} d_2(\psi)d_3(\psi) + d_3(\psi)d_2(\psi) \\ d_1(\psi)d_3(\psi) + d_3(\psi)d_1(\psi) \\ d_1(\psi)d_2(\psi) + d_2(\psi)d_1(\psi) \end{pmatrix} = \sqrt{2} \begin{pmatrix} d_2(\psi)d_3(\psi) \\ d_1(\psi)d_3(\psi) \\ d_1(\psi)d_2(\psi) \end{pmatrix}. \tag{4.64}$$

In this nomenclature, the lower index denotes optical ED-ED (DD) transition in order to address an exciton with Γ_5^+ (5+) symmetry. For the SHG intensity, we have to take the absolute value squared of the scalar product of the excitation channel O_DD^{5+} and emission channel O_Q^{5+}:

$$I_\mathrm{even}^\mathrm{SHG}(\mathbf{k}, \psi, \varphi) = I_\mathrm{DD/Q}^{5+}(\mathbf{k}, \psi, \varphi) \propto \left| O_\mathrm{DD}^{5+}(\psi) O_\mathrm{Q}(\mathbf{k}, \varphi) \right|^2. \tag{4.65}$$

The polarization diagram of this expression is plotted for $\mathbf{k} \parallel [111]$ and $\mathbf{X} \parallel [1\bar{1}0]$ in three different diagram types in Fig. 4.4. Historically, the polarization dependence of an

SHG mechanism has been displayed in polar plots for the parallel ($\psi = \varphi$) and crossed ($\psi = \varphi + 90°$) polarization configurations as in Fig. 4.4(a). However, by plotting all possible ψ/φ combinations in a 2D contour plot as in Fig. 4.4(b), more information is displayed. Additionally, different SHG mechanisms can be distinguished more clearly. The parallel and crossed configurations are contained in the 2D plots and marked as the black and red diagonal tuning lines. A cartesian plot of both configurations is shown in Fig. 4.4(c).

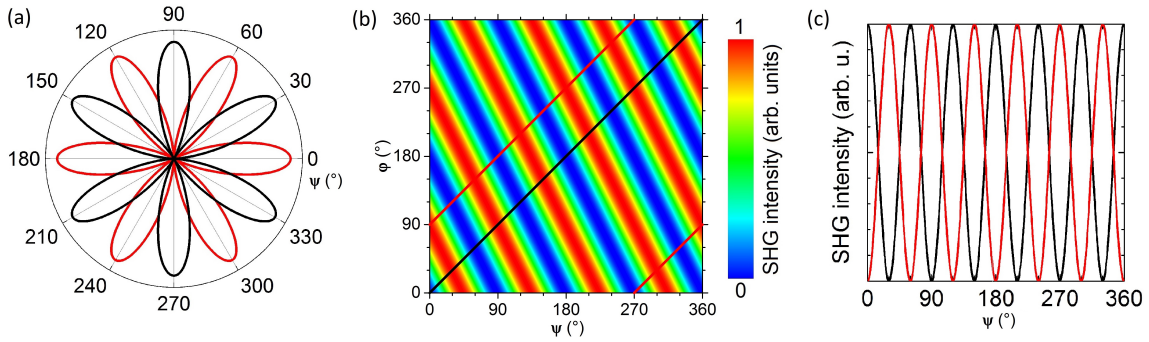

Figure 4.4 Polarization dependent SHG intensity as a function of the linear polarization angles ψ of the laser and φ of the SHG light in three different diagram types for the crystallographic SHG process of Γ_5^+ excitons (Fig. 4.3(a) and Eq. (4.65)): (a) Historically used polar plot for the parallel ($\psi = \varphi$) and crossed ($\psi = \varphi + 90°$) polarization tuning. (b) 2D contour plot for all linear polarization angle combinations. The SHG intensity is represented by a rainbow color scale. Blue corresponds to zero and red to maximum SHG intensity. The parallel and crossed configurations are contained as the black and red diagonal lines. (c) Cartesian plot analogous to panel (a).

The 2D polarization diagrams for **k** along various crystal axis for the process in Fig. 4.3(a) [Eq. (4.65)] are plotted in the first row of Fig. 4.5. As can be seen in Fig. 2.5 the Γ_5^+ S and D excitons show much stronger SHG intensity compared to odd parity Γ_4^- P excitons, as only the $2P$ exciton is comparable to the $2S$ exciton. For higher principal quantum numbers the P excitons are barely detectable, if at all. Therefore we call this mechanism the **dominant crystallographic mechanism**.

Now we derive the **weak crystallographic SHG mechanisms**. Let us start with an ED-ED excitation of Γ_4^+ D excitons, for which we use the coupling coefficient table A.7 for $\Gamma_4^- \otimes \Gamma_4^- \to \Gamma_4^+$ from Ref. [Kos+63] and get

$$O_{\mathrm{DD}}^{4+}(\psi) = \frac{1}{\sqrt{2}} \begin{pmatrix} d_2(\psi)d_3(\psi) - d_3(\psi)d_2(\psi) \\ -d_1(\psi)d_3(\psi) + d_3(\psi)d_1(\psi) \\ d_1(\psi)d_2(\psi) - d_2(\psi)d_1(\psi) \end{pmatrix} = \begin{pmatrix} 0 \\ 0 \\ 0 \end{pmatrix}. \tag{4.66}$$

Here it becomes evident, that the ED-ED excitation of Γ_4^+ states is impossible for two photons having the same linear polarization angle as in our experiment with only one laser. Therefore this process is not relevant for our considerations here. However, using two separate lasers with different linear polarization angles, this process will give an SHG contribution.

Let us continue with ED-ED excitation of Γ_3^+ D excitons, for which we use the coupling

coefficient table A.7 for $\Gamma_4^- \otimes \Gamma_4^- \rightarrow \Gamma_3^+$ from Ref. [Kos+63] and get

$$O_{\mathrm{DD}}^{3+}(\psi) = \frac{1}{\sqrt{6}} \begin{pmatrix} -d_1(\psi)d_1(\psi) - d_2(\psi)d_2(\psi) + 2d_3(\psi)d_3(\psi) \\ -\sqrt{3}d_1(\psi)d_1(\psi) - \sqrt{3}d_2(\psi)d_2(\psi) \end{pmatrix} \tag{4.67}$$

Thus, for the SHG intensity of Γ_3^+ D excitons with ED-ED excitaion and EQ3 emission we get

$$I_{\mathrm{even\ Q3}}^{\mathrm{SHG}}(\mathbf{k}, \psi, \varphi) = I_{\mathrm{DD/Q3}}^{3+}(\mathbf{k}, \psi, \varphi) \propto \left| O_{\mathrm{DD}}^{3+}(\psi) \cdot O_{\mathrm{Q3}}(\mathbf{k}, \varphi) \right|^2 . \tag{4.68}$$

Next, we derive the SHG intensity of odd-parity Γ_4^- P excitons, which emit light by ED transition. For their excitation, we combine the odd-parity ED photon vector with the even-parity EQ photon vector in order to address odd-parity P excitons. We use the coupling coefficient table A.8 for $\Gamma_4^- \otimes \Gamma_5^+ \rightarrow \Gamma_4^-$ from Ref. [Kos+63]. The vector for this two-photon transition consequently reads

$$O_{\mathrm{DQ}}^{4-}(\mathbf{k}, \psi) = \frac{1}{\sqrt{2}} \begin{pmatrix} q_3(\mathbf{k}, \psi)d_2(\psi) + q_2(\mathbf{k}, \psi)d_3(\psi) \\ q_1(\mathbf{k}, \psi)d_3(\psi) + q_3(\mathbf{k}, \psi)d_1(\psi) \\ q_2(\mathbf{k}, \psi)d_1(\psi) + q_1(\mathbf{k}, \psi)d_2(\psi) \end{pmatrix} . \tag{4.69}$$

The polarization-dependent SHG intensity is then calculated by

$$I_{\mathrm{odd}}^{\mathrm{SHG}}(\mathbf{k}, \psi, \varphi) = I_{\mathrm{DQ/D}}^{4-}(\mathbf{k}, \psi, \varphi) \propto \left| O_{\mathrm{DQ}}^{4-}(\mathbf{k}, \psi) O_{\mathrm{D}}(\varphi) \right|^2 , \tag{4.70}$$

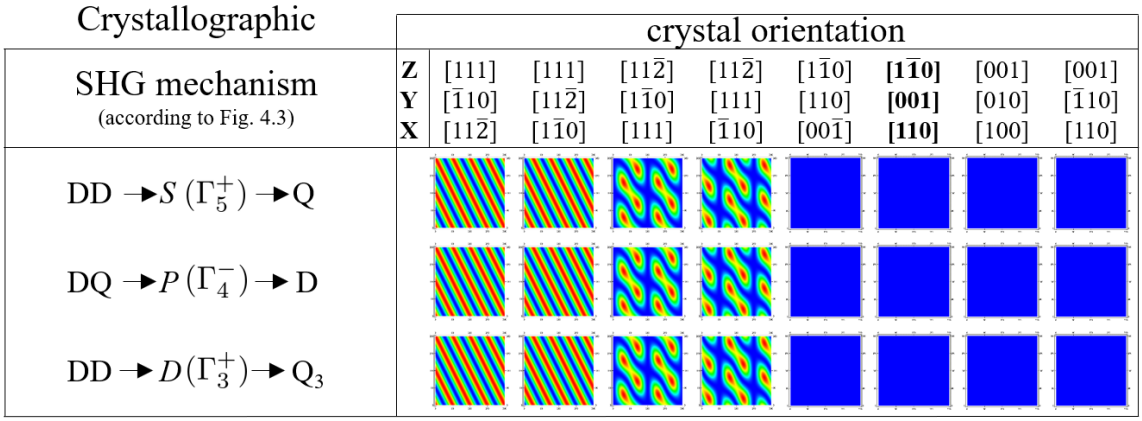

Figure 4.5 Simulated 2D SHG polarization diagrams for the crystallographic SHG processes for all relevant crystal orientations as expressed by Eqs. (4.65), (4.70) and (4.68) and sketched in Fig. 4.3.

Now we have derived all possible crystallographic processes with only one higher-order transition. Their polarization diagrams for various typical crystal orientations are plotted in Fig. 4.5. It is striking, that for each crystal orientation, the mechanisms show the same polarization dependence. It is therefore not possible to distinguish between them by selecting a specific polarization angle setting. It also becomes evident, that the SHG signal is absent for all polarization angles, if $\mathbf{k}$ is directed along the high-symmetry crystal [001] and [110] axis.

4.1.2 Zeeman-effect induced SHG

In this section, we derive the polarization dependence for different mechanisms of Zeeman effect-induced SHG, which involves an even-parity magnetic-field coupling between exciton states of the same parity. Therefore we need a general magnetic field vector

$$\mathbf{B} = \begin{pmatrix} B_1 \\ B_2 \\ B_3 \end{pmatrix}. \tag{4.71}$$

The distinction between Voigt and Faraday geometry is made later by inserting the crystal axis, along which the magnetic field is applied. In order to find all possible mechanisms one can take the crystallographic mechanisms as shown in Fig. 4.3 and extend each of them by a magnetic-field coupling between same-parity excitons. All the mechanisms obtained by this method are shown in Fig. 4.6. Similar to the dominant crystallographic SHG mechanism, the **dominant mechanism for ZE induced SHG** is expected to involve Γ_5^+ excitons both for the excitation and emission channel, which are additionally coupled by a magnetic field, as shown in Fig. 4.6(a). Thus we take the ED-ED excitation operator from Eq. (4.64)

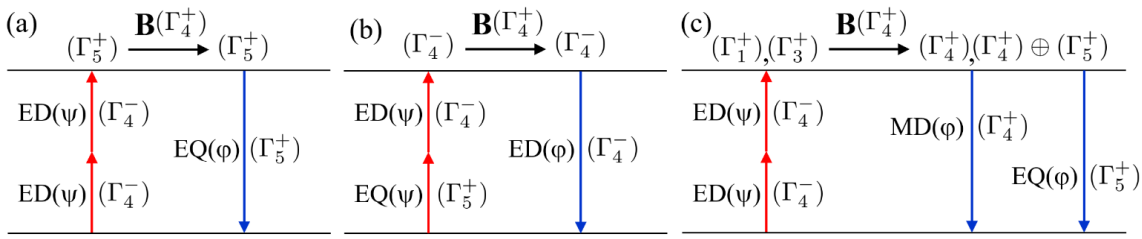

Figure 4.6 Schematics of the ZE-induced SHG processes for (a) even-parity Γ_5^+ (b) odd-parity Γ_4^- and (c) even-parity Γ_1^+ and Γ_3^+ coupled to Γ_4^+ and Γ_5^+ exciton states.

for Γ_5^+ excitons and couple it with the Γ_4^+ magnetic field from Eq. (4.71) to a Γ_5^+ operator using the coupling coefficient table A.8 for $\Gamma_5^+ \otimes \Gamma_4^- \to \Gamma_5^+$ from Ref.[Kos+63] and get

$$O_{\mathrm{DD}}^{5+\mathrm{B}5+}(\psi) = \frac{1}{\sqrt{2}} \begin{pmatrix} B_2 O_{\mathrm{DD},3}^{5+}(\psi) - B_3 O_{\mathrm{DD},2}^{5+}(\psi) \\ -B_1 O_{\mathrm{DD},3}^{5+}(\psi) + B_3 O_{\mathrm{DD},1}^{5+}(\psi) \\ B_1 O_{\mathrm{DD},2}^{5+}(\psi) - B_2 O_{\mathrm{DD},1}^{5+}(\psi) \end{pmatrix} \tag{4.72}$$

$$= \begin{pmatrix} B_2 d_1(\psi) d_2(\psi) - B_3 d_3(\psi) d_1(\psi) \\ -B_1 d_2(\psi) d_1(\psi) + B_3 d_2(\psi) d_3(\psi) \\ B_1 d_1(\psi) d_3(\psi) - B_2 d_2(\psi) d_3(\psi) \end{pmatrix}. \tag{4.73}$$

The nomenclature for the operators is now extended in the upper index by adding **B** for the coupling mechanism and additionally a "5+" referring to the Γ_5^+ symmetry of the excitons in the emission channel, to which the two-photon excited states are coupled to. With the Zeeman operator of the dominant process [Eq.(4.73)] and a quadrupole emission we get

$$I_{\mathrm{ZE}}^{\mathrm{SHG}}(\mathbf{k}, \psi, \varphi) = I_{\mathrm{DD/Q}}^{5+\mathrm{B}5+}(\mathbf{k}, \psi, \varphi) \propto \left| O_{\mathrm{DD}}^{5+\mathrm{B}5+}(\psi) O_{\mathrm{Q}}(\mathbf{k}, \varphi) \right|^2. \tag{4.74}$$

The lower index denotes the two-photon excitation with two electric dipoles (DD) and the electric quadrupole emission (Q). The upper index again implies, that Γ_5^+ excitons are

excited (first "5+") and coupled by a magnetic field (B) to other Γ_5^+ states (last "5+"), from which the light is emitted. The polarization diagrams are shown for different crystal orientations in the first line of Fig. 4.7 for the Voigt configuration and in the first line of Fig. 4.8 for the Faraday configuration.

We continue with the derivation of **weak processes for ZE induced SHG** involving odd-parity P excitons with Γ_4^- symmetry and even parity D excitons with Γ_4^+, Γ_3^+ and Γ_1^+ symmetries [see Eq. (4.53)]. We start with the weak mechanism of odd-parity Γ_4^- P excitons, as sketched in Fig. 4.6(b), which can be excited by a combined ED-EQ transition, as already shown in Eq. (4.69). We take this vector and couple it with a magnetic field to a Γ_4^- P exciton state, as it is the only odd parity single-photon operator. The excitation vector of ED-EQ excited and magnetic field coupled states then reads

$$O_{\mathrm{DQ}}^{4-\mathrm{B}4-}(\psi) = \frac{1}{\sqrt{2}} \begin{pmatrix} B_2 O_{\mathrm{DQ},3}^{4-}(\mathbf{k},\psi) - B_3 O_{\mathrm{DQ},2}^{4-}(\mathbf{k},\psi) \\ -B_1 O_{\mathrm{DQ},3}^{4-}(\mathbf{k},\psi) + B_3 O_{\mathrm{DQ},1}^{4-}(\mathbf{k},\psi) \\ B_1 O_{\mathrm{DQ},2}^{4-}(\mathbf{k},\psi) - B_2 O_{\mathrm{DQ},1}^{4-}(\mathbf{k},\psi) \end{pmatrix}. \tag{4.75}$$

The SHG intensity is calculated by the scalar product with an ED transition, of which the absolute value is then squared:

$$I_{\mathrm{DQ/D}}^{4-\mathrm{B}4-}(\mathbf{k},\psi,\varphi) \propto \left| O_{\mathrm{DQ}}^{4-\mathrm{B}4-}(\mathbf{k},\psi) \cdot O_{\mathrm{D}}(\varphi) \right|^2 \tag{4.76}$$

Note, that for blue excitons the process described in Eq. (4.76) is the dominant one, as it addresses magnetic-field coupled blue S excitons. This will be discussed later in Section 6.

We continue with the weak ZE processes, for which the even parity Γ_3^+ D excitons are excited by two photons in ED approximation, as sketched in Fig. 4.6(c) and expressed in Eq. (4.67). According to the multiplication table A.3 of Ref. [Kos+63], the Γ_3^+ excitons can be coupled by a magnetic field to Γ_4^+ and Γ_5^+ excitons, which then can emit light by MD and EQ transitions, respectively. Thus we get

$$O_{\mathrm{DD}}^{3+\mathrm{B}5+}(\psi) = \frac{1}{2\sqrt{6}} \begin{pmatrix} -\sqrt{3} B_1 O_{\mathrm{DD},1}^{3+} - B_1 O_{\mathrm{DD},2}^{3+} \\ \sqrt{3} B_2 O_{\mathrm{DD},1}^{3+} - B_2 O_{\mathrm{DD},2}^{3+} \\ 2 B_3 O_{\mathrm{DD},2}^{3+} \end{pmatrix}, \tag{4.77}$$

$$O_{\mathrm{DD}}^{3+\mathrm{B}4+}(\psi) = \frac{1}{2\sqrt{6}} \begin{pmatrix} -B_1 O_{\mathrm{DD},1}^{3+} + \sqrt{3} B_1 O_{\mathrm{DD},2}^{3+} \\ -B_2 O_{\mathrm{DD},1}^{3+} - \sqrt{3} B_2 O_{\mathrm{DD},2}^{3+} \\ 2 B_3 O_{\mathrm{DD},1}^{3+} \end{pmatrix} \tag{4.78}$$

for these magnetic field coupled Γ_3^+ exciton vectors and

$$I_{\mathrm{DD/Q}}^{3+\mathrm{B}5+}(\mathbf{k},\psi,\varphi) \propto \left| O_{\mathrm{DD}}^{3+\mathrm{B}5+}(\psi) O_{\mathrm{Q}}(\mathbf{k},\varphi) \right|^2, \tag{4.79}$$

$$I_{\mathrm{DD/MD}}^{3+\mathrm{B}4+}(\mathbf{k},\psi,\varphi) \propto \left| O_{\mathrm{DD}}^{3+\mathrm{B}4+}(\psi) O_{\mathrm{MD}}(\mathbf{k},\varphi) \right|^2. \tag{4.80}$$

for their SHG intensities.

Finally, we derive the polarization dependence of ZE-induced SHG mechanisms involving the excitation of Γ_1^+ excitons. Although Γ_1^+ states cannot emit light directly, they can be two-photon excited by a combined ED-ED transition

$$O_{\mathrm{DD}}^{1+}(\psi) = \frac{1}{\sqrt{3}}, \tag{4.81}$$

and coupled by a magnetic field to Γ_4^+ excitons

$$O_{\mathrm{DD}}^{1+\mathrm{B4+}}(\psi) = \frac{1}{\sqrt{3}} \begin{pmatrix} B_1 \\ B_2 \\ B_3 \end{pmatrix}, \tag{4.82}$$

which can emit light by an MD interaction. Consequently, we get

$$I_{\mathrm{DD/MD}}^{1+\mathrm{B4+}}(\mathbf{k}, \psi, \varphi) \propto \left| O_{\mathrm{DD}}^{1+\mathrm{B4+}}(\psi) O_{\mathrm{MD}}(\mathbf{k}, \varphi) \right|^2, \tag{4.83}$$

for the polarization-dependent SHG intensity.

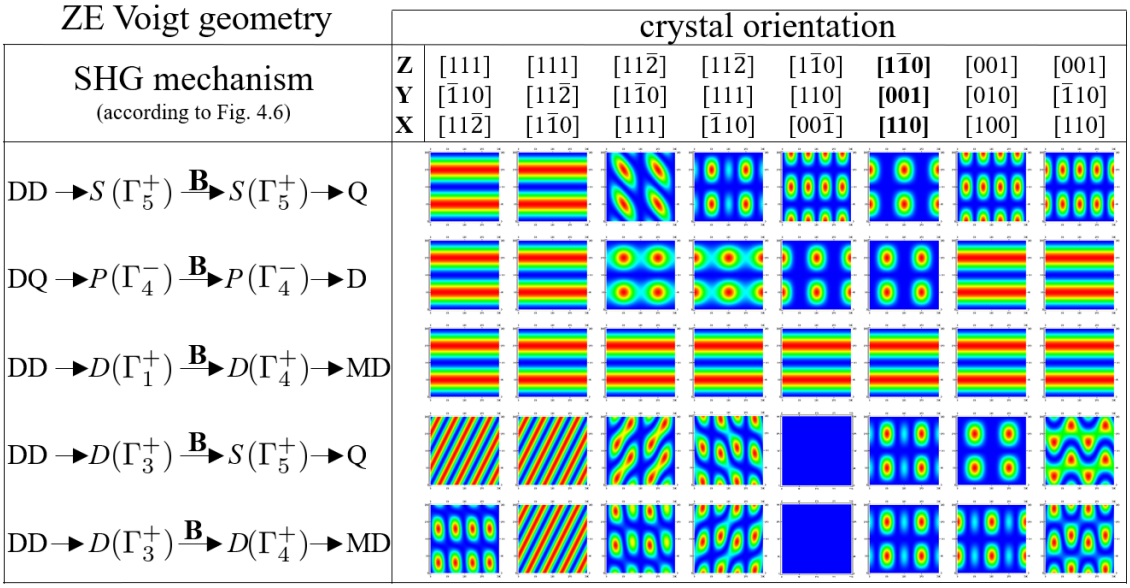

Figure 4.7 Simulated 2D SHG polarization diagrams for the ZE-induced SHG processes in Voigt configuration ($\mathbf{k} \parallel \mathbf{Z}$, $\mathbf{E}_{\mathrm{MSE}} \parallel \mathbf{Y}$ and $\mathbf{B} \parallel \mathbf{X}$) for all relevant crystal orientations as expressed by Eqs. (4.74), (4.76), (4.79), (4.80) and (4.83) and sketched in Fig. 4.6.

At this point, we have derived the polarization dependence of all possible ZE-induced SHG mechanisms, which involve at most one higher-order optical transition. The polarization diagrams for the derived weak ZE mechanisms are plotted in Fig. 4.7 for Voigt and in Fig. 4.8 for Faraday geometry for various typical crystal orientations. In contrast to the crystallographic mechanisms, the polarization plots of different ZE mechanisms all differ significantly in their patterns giving the possibility to separate chosen mechanisms from each other by a specific setting of linear polarization angles, as will be discussed in Sec. 4.2.

It is striking, that the orientations, which are symmetry forbidden in the case of crystallographic mechanisms are still forbidden in Faraday geometry. However, in Voigt geometry, almost all mechanisms with a few exceptions have an SHG contribution for all crystal orientations and differ in their polarization dependence.

Note, that in Faraday geometry the linear polarization angles are rotated due to the Faraday effect. Experimental measurements of the polarization dependence will show shifted

patterns compared to the simulated diagrams. In Voigt geometry, however, this effect is absent. Therefore the polarization diagrams can be measured directly as described in Sec. 3.5.

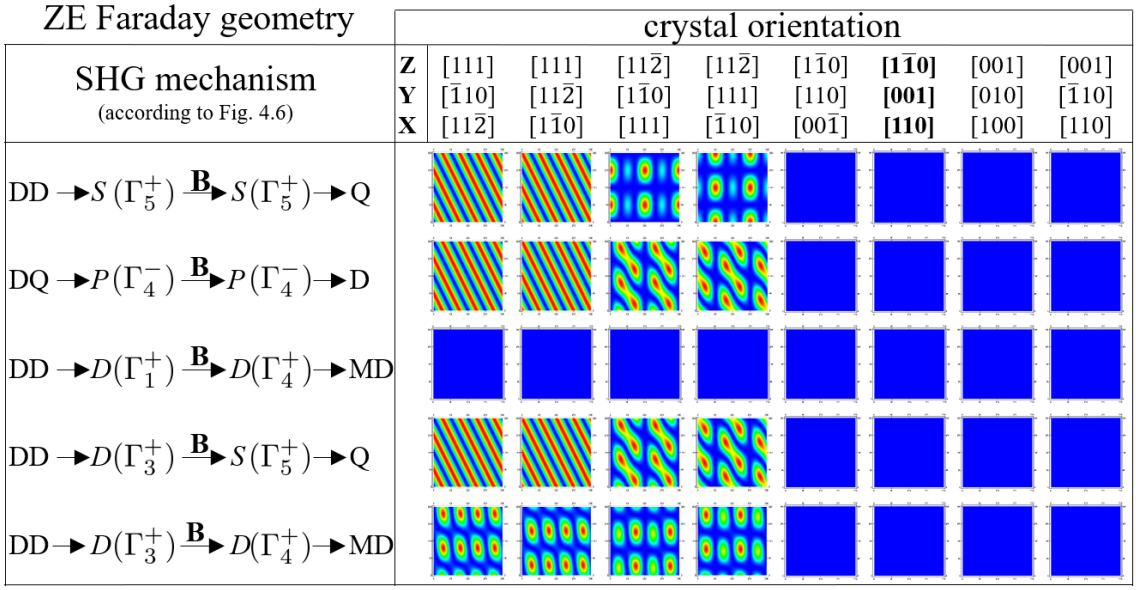

Figure 4.8 Simulated 2D SHG polarization diagrams for the ZE-induced SHG processes in Faraday configuration ($\mathbf{k} \parallel \mathbf{B} \parallel \mathbf{Z}$) for all relevant crystal orientations as expressed by Eqs. (4.74), (4.76), (4.79), (4.80) and (4.83) and sketched in Fig. 4.6.

4.1.3 Magneto-Stark effect induced SHG

In this section, we derive the polarization dependence of MSE-induced SHG mechanisms, which include a coupling of opposite parity exciton states by an effective electric field

$$E_{\mathrm{MSE}} = \begin{pmatrix} E_1 \\ E_2 \\ E_3 \end{pmatrix}, \tag{4.84}$$

which has a negative parity with a Γ_4^- symmetry. We will only consider MSE processes with an excitation of even parity excitons with two ED transitions, which are then coupled by the electric field to odd parity Γ_4^- P excitons resulting in an ED emission. The excitation of odd parity excitons would require a total of two optical transitions of higher order, one in the excitation and one in the emission channel, as the electric field would couple the odd parity excitons with even parity excitons, which could only emit light by EQ, MD or EQ3 transition.

Taking these considerations into account, the **dominant mechanism of MSE-induced SHG** involves an ED-ED two-photon excitation of Γ_5^+ S or D excitons already expressed

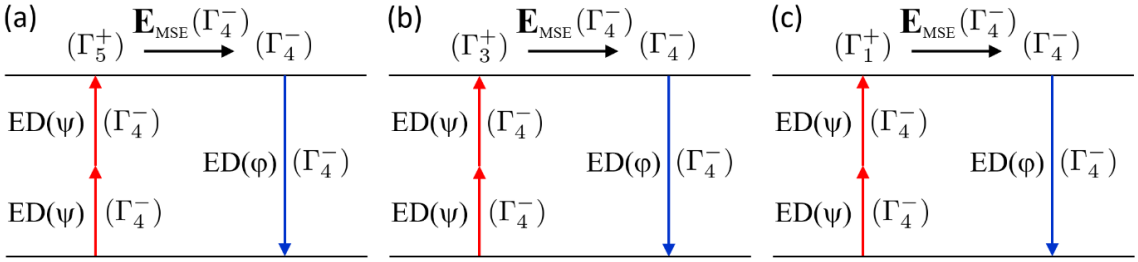

Figure 4.9 Schematics of the MSE-induced SHG processes for (a) Γ_5^+-Γ_4^- (b) Γ_3^+-Γ_4^- and (c) Γ_1^+-Γ_4^- coupled exciton states.

in Eq. (4.64), which are coupled to Γ_4^- P excitons leading to

$$O_{\mathrm{DD}}^{5+\mathrm{E4}-}(\psi) = \frac{1}{\sqrt{2}} \begin{pmatrix} E_2 O_{\mathrm{DD},3}^{5+} + E_3 O_{\mathrm{DD},2}^{5+} \\ E_1 O_{\mathrm{DD},3}^{5+} + E_3 O_{\mathrm{DD},1}^{5+} \\ E_1 O_{\mathrm{DD},2}^{5+} + E_2 O_{\mathrm{DD},1}^{5+} \end{pmatrix} \tag{4.85}$$

$$= \begin{pmatrix} E_2 d_1(\psi) d_2(\psi) + E_3 d_3(\psi) d_1(\psi) \\ E_1 d_2(\psi) d_1(\psi) + E_3 d_2(\psi) d_3(\psi) \\ E_1 d_1(\psi) d_3(\psi) + E_2 d_2(\psi) d_3(\psi) \end{pmatrix}. \tag{4.86}$$

The P excitons can then emit light in ED approximation resulting in the polarization-dependent SHG intensity

$$I_{\mathrm{MSE}}^{\mathrm{SHG}}(\psi, \varphi) = I_{\mathrm{DD}}^{5+\mathrm{E4}-}(\psi, \varphi) \propto \left| O_{\mathrm{DD}}^{5+\mathrm{E4}-}(\psi) O_{\mathrm{D}}(\varphi) \right|^2 \tag{4.87}$$

for this process.

Although the **weak processes for MSE-induced SHG** also include only ED transitions, they involve the excitation of Γ_3^+ and Γ_1^+ D excitons. The vectors for these states are given by

$$O_{\mathrm{DD}}^{3+\mathrm{E4}-}(\psi) = \frac{1}{2\sqrt{6}} \begin{pmatrix} -E_1 O_{\mathrm{DD},1}^{3+} + \sqrt{3} E_1 O_{\mathrm{DD},2}^{3+} \\ -E_2 O_{\mathrm{DD},1}^{3+} - \sqrt{3} E_2 O_{\mathrm{DD},2}^{3+} \\ 2 E_3 O_{\mathrm{DD},1}^{3+} \end{pmatrix}, \tag{4.88}$$

$$O_{\mathrm{DD}}^{1+\mathrm{E4}-}(\psi) = \frac{1}{\sqrt{3}} \begin{pmatrix} E_1 \\ E_2 \\ E_3 \end{pmatrix}. \tag{4.89}$$

With an additional ED transition in the emission channel, the SHG intensities result in

$$I_{\mathrm{DD/D}}^{3+\mathrm{E4}-}(\psi, \varphi) \propto \left| O_{\mathrm{DD}}^{3+\mathrm{E4}-}(\psi) O_{\mathrm{D}}(\varphi) \right|^2, \tag{4.90}$$

$$I_{\mathrm{DD/D}}^{1+\mathrm{E4}-}(\psi, \varphi) \propto \left| O_{\mathrm{DD}}^{1+\mathrm{E4}-}(\psi) O_{\mathrm{D}}(\varphi) \right|^2. \tag{4.91}$$

The polarization diagrams of the derived MSE-induced SHG mechanisms in Voigt geometry are shown in Fig. 4.10 for various crystal orientations. In Faraday geometry the Lorentz force and therefore also the MSE are absent.

Finally, we have derived expressions for the polarization-dependent crystallographic, ZE-induced and MSE-induced SHG processes for yellow excitons in Cu_2O with at most one higher-order optical transition. For each category, a dominant process is identified, which will be backed up by experimental results in Sec. 4.2. The polarization diagram tables will turn out to be useful tools to select experimental geometries in order to isolate certain mechanisms.

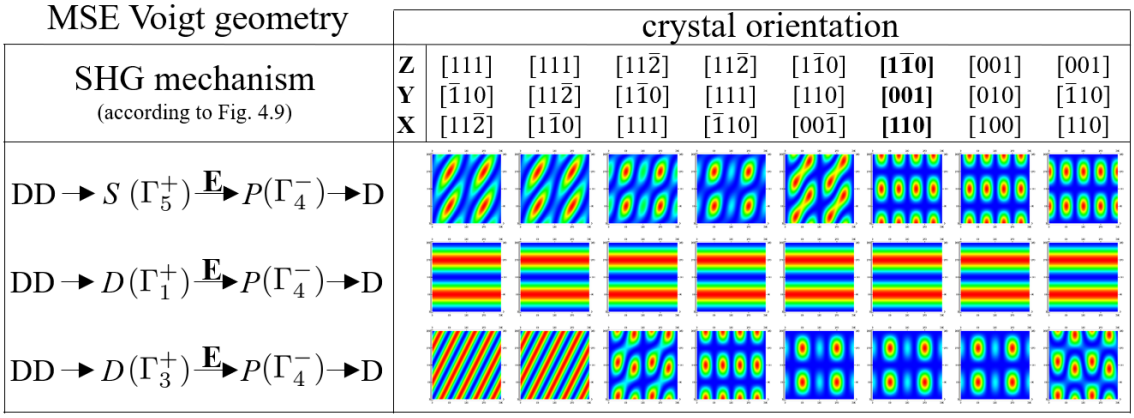

Figure 4.10 Simulated 2D SHG polarization diagrams for the MSE-induced SHG processes in Voigt configuration ($\mathbf{k} \parallel \mathbf{Z}$, $\mathbf{E}_{\mathrm{MSE}} \parallel \mathbf{Y}$ and $\mathbf{B} \parallel \mathbf{X}$) for all relevant crystal orientations as expressed by Eqs. (4.87), (4.90) and (4.91) and sketched in Fig. 4.9.

4.1.4 Interference

The last case we have to discuss is the interference of multiple mechanisms. If SHG of an exciton resonance is induced by multiple mechanisms, an interference of the acting mechanisms will occur. For the resulting SHG intensity, one has to add the operators of the involved mechanisms with coefficients, before taking the absolute value squared. For the experiments in Sec. 4.2 the interference of the dominant ZE [Eq. (4.74)] and MSE [Eq. (4.87)] effects are of special importance and are expressed by

$$I^{\mathrm{SHG}}_{\mathrm{ZE+MSE}}(\mathbf{k},\psi,\varphi) \propto \Big|\Big(\alpha \cdot O^{5+\mathrm{B}5+}_{\mathrm{DD}}(\psi) O_{\mathrm{Q}}(\mathbf{k},\varphi) + \beta \cdot O^{5+\mathrm{E}4-}_{\mathrm{DD}}(\psi) O_{\mathrm{D}}(\varphi)\Big)/\sqrt{\alpha^2+\beta^2}\Big|^2, \tag{4.92}$$

with the coefficients α and β.

4.2 Magnetic-field induced spectra and polarization dependencies of different SHG mechanisms

In Sec. 4.1 we have derived the SHG intensity as a function of the linear polarization angles of the incoming laser- and outgoing SHG light for various crystallographic and magnetic-field-induced mechanisms and presented polarization diagrams for several crystal orientations.

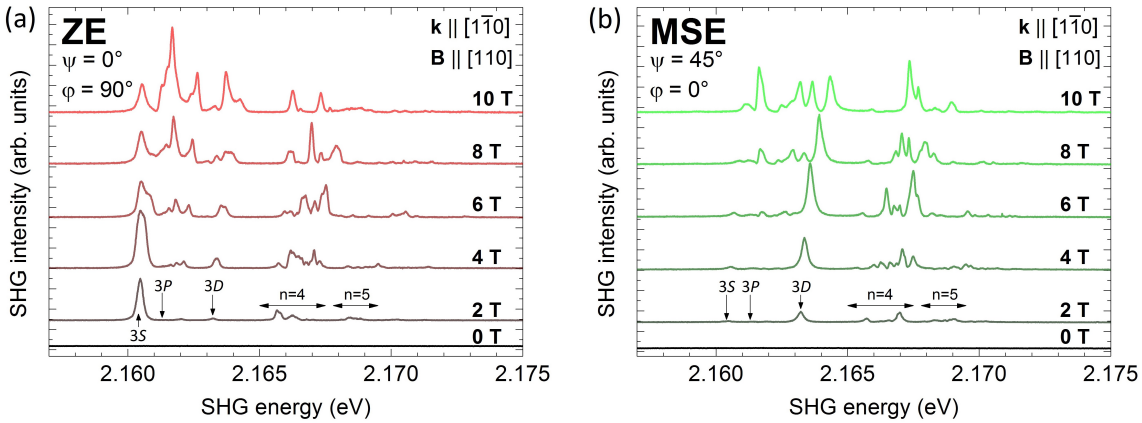

Figure 4.11 Magnetic field series from 10 to 0 T of SHG spectra of yellow $n \geq 3$ excitons induced purely by (a) ZE ($\psi/\varphi = 0°/90°$) and (b) MSE ($\psi/\varphi = 45°/0°$) in the H100 sample (see Tab. 3.1) with $\mathbf{k} \parallel [1\bar{1}0]$ and $\mathbf{B} \parallel [110]$. The central photon energy of the fs-pulses is set to 1.082 eV.

In this section, we will choose a suitable crystal orientation to suppress the crystallographic mechanisms and demonstrate the ZE and MSE, by experimentally acquiring the polarization diagrams and comparing them to the simulations from Sec. 4.1. Then we will isolate all the weak mechanisms from the dominant ones by choosing polarization settings, for which only the weak mechanisms will give an SHG contribution. Moreover, we will identify polarization settings, for which only one of the two dominant magnetic-field-induced mechanisms will contribute to the SHG signal. As each mechanism will have its characteristic spectral features, we will measure the magnetic field series for each mechanism and look for differences between them.

For the decision of which experimental geometry to choose we have to take a few factors into consideration. Our primary focus is the magnetic-field-induced SHG mechanisms, for which the suppression of crystallographic contributions is required. Examining the last four columns in Figs. 4.5, 4.7, 4.8 and 4.10, it becomes evident, that this requirement is fulfilled in Voigt geometry for $\mathbf{k}$ along [001] and [1$\bar{1}$0].

Next, we look at the polarization diagrams for the dominant ZE and MSE mechanisms, which are shown in the first line of Figs. 4.7 and 4.10. One can draw the conclusion, that $\mathbf{k}$ along [001] is therefore not suitable, as the ZE and MSE diagrams are indistinguishable. Consequently, the only suitable crystal orientation is $\mathbf{k}$ along [1$\bar{1}$0]. Between the two orientations, $\mathbf{Y} \parallel [001]$ and $\mathbf{B} \parallel [110]$ is more suitable, as it allows to suppress the SHG intensity of one mechanism for specific polarization angles, for which the other mechanism still contributes. For instance, for a fixed $\psi = 180°$ only the ZE mechanism contributes to the SHG signal with a twofold symmetry. On the other hand, for a fixed $\varphi = 180°$ only the MSE mechanism gives a contribution with a fourfold symmetry. Therefore we choose this experimental orientation for our experiments in this chapter. The "H100" sample exhibits the described orientation (see Tab. 3.1) and is therefore chosen for the experiments presented in this chapter.

If we assume at this point, that the derived polarization diagrams of the mechanisms

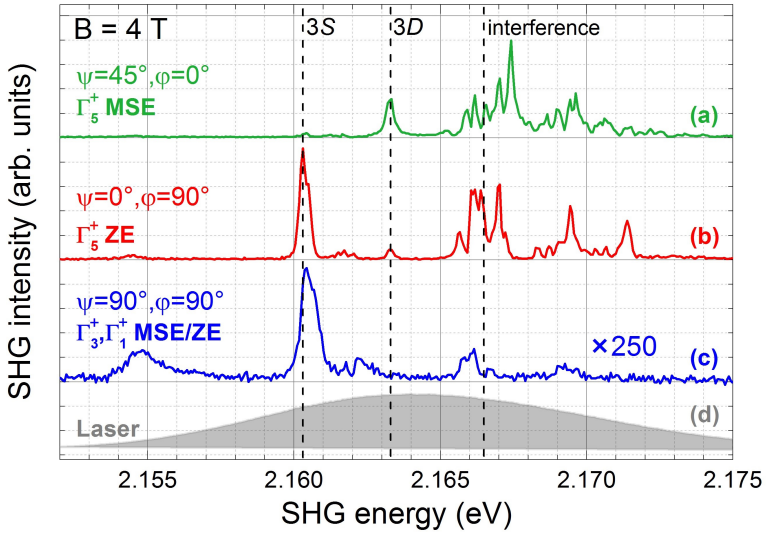

Figure 4.12 Magnetic-field-induced SHG spectra at 4 T of yellow $n \geq 3$ excitons for the (a) dominant MSE ($\psi/\varphi = 45°/0°$), (b) dominant ZE ($\psi/\varphi = 0°/90°$) and the combined weak mechanisms ($\psi/\varphi = 90°/90°$) in the H100 sample (see Tab. 3.1) with $\mathbf{k} \parallel [1\bar{1}0]$ and $\mathbf{B} \parallel [110]$. The central photon energy of the fs-pulses is set to 1.082 eV, as shown by (d) the SH of the fs laser power spectrum as the gray area.

are correct, we have to choose the polarization setting $\psi/\varphi = 0°/90°$ in order to measure the SHG spectra, which are purely induced by the ZE and $\psi/\varphi = 45°/0°$ for purely MSE-induced SHG spectra. By setting the central photon energy of the fs laser at half of the $n = 3$ exciton multiplet and measuring the SHG spectra as described in Sec. 3.3 for magnetic fields from 0 to 10 T in steps of 2 T, we acquire the results which are shown in Fig.4.11.

Figs. 4.11(a) and 4.11(b) show the magnetic field series of SHG spectra purely induced by the ZE and MSE mechanism, respectively. In both cases no SHG signal is detected for $B = 0$ T, as it is the symmetry-forbidden orientation, which confirms the polarization plots of the fifth and sixth row in Fig. 4.5. In general, the SHG spectra induced by the two mechanisms show differences in their spectral features. As an example, Fig. 4.11(a) shows stronger signals in the S- compared to the D excitons. For Fig. 4.11(b) the opposite is true. At low magnetic fields the spectra are similar to the zero-field crystallographic spectra as shown in Fig. 2.5(b). With increasing magnetic field the resonances split, shift to higher energies and new resonances emerge. For both mechanisms, the integrated SHG signal increases with increasing magnetic field, however, for higher n the MSE-induced SHG contribution increase overpowers that of the ZE.

Next, we want to experimentally confirm the polarization dependence, which we have already derived theoretically and shown in Fig. 4.7 and 4.10. For this one has to choose an exciton resonance in Fig.4.11, of which the SHG signal is only induced by one mechanism to avoid an interference between both effects. A suitable exciton state for the ZE is the $3S$ exciton at 4 T, as it is strongly induced by the ZE but has a very weak MSE-induced contribution. For a demonstration of the MSE polarization dependence, we choose by the same logic the $3D$ exciton state, as it is predominantly induced by the MSE. The chosen

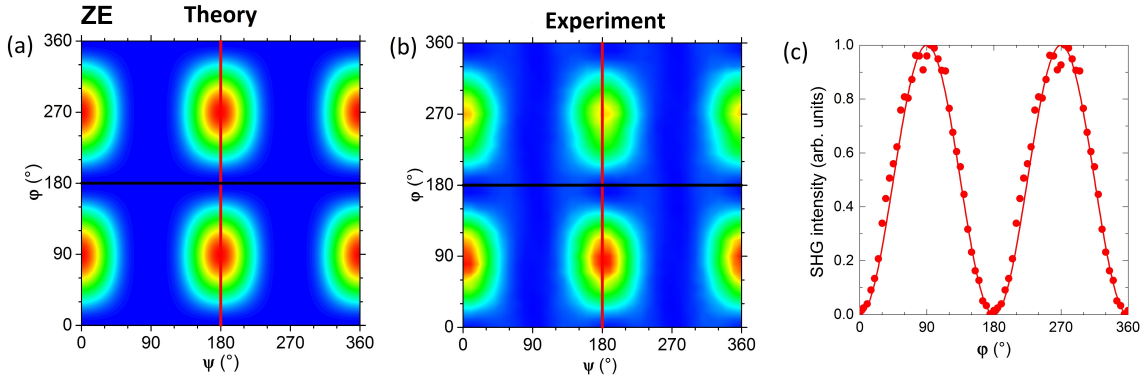

Figure 4.13 (a) Simulated [according to Eq. (4.74) and Fig. 4.6(a)] and (b) experimentally obtained 2D polarization diagrams of the ZE-induced SHG of the $3S$ exciton at $B = 4\,\mathrm{T}$ in the H100 sample (see Tab. 3.1) with $\mathbf{k} \parallel [1\bar{1}0]$ and $\mathbf{B} \parallel [110]$, as shown in Fig. 4.12(a). (c) Polarization-dependent intensity along the $\psi = 180°$ tuning line marked in panels (a) and (b) by the red lines. Symbols represent the experimental data and lines represent the simulation.

spectra are shown in Fig. 4.12 marked as (a) and (b), respectively. The gray spectrum (d) shows the energy-doubled power spectrum of the fs pulse excitation and visualizes the fixed wavelength spectroscopy method described in Sec. 3.3.

For the measurement of the full polarization dependence of the $3S$ exciton, the laser is kept at the same energy setting as shown in Fig. 4.12, the magnetic field is fixed at 4 T and both linear polarization angles ψ and φ are tuned as described in Sec. 3.5. For the evaluation, we take the intensity of the pixel at the dashed line marking the $3S$ exciton energy and plot it according to the rainbow color scale against ψ and φ in the contour plot shown in Fig. 4.13(a). The experimental diagram is in good agreement with the simulation, which is calculated according to Eq. (4.74) and shown in Fig. 4.13(b). This is an indication, that no other mechanism contributes significantly at this energy. The polarization dependence pattern has a twofold symmetry proportional to a $\cos^4$ shape along ψ with broad minima and narrow maxima and a twofold symmetry proportional to a $\sin^2$ shape along φ with equally broad minima and maxima. The maximum intensity is detected at $\psi/\varphi = 0°/90°$ and other equivalent settings shifted by 180° either in ψ or φ.

For the $3D$ exciton we can use the same polarization tuning data set, as it has covered the whole spectral range and includes all exciton lines. For the analogous evaluation we take the intensity of the pixel at the dashed line in Fig. 4.12 marking the $3D$ exciton energy and plot it against ψ and φ in the contour plot shown in Fig. 4.14(a). The experimental diagram is in good agreement with the simulation, which is calculated according to Eq. (4.87) and shown in Fig. 4.14(b). This again indicates, that no other mechanism contributes significantly at this energy. The polarization dependence pattern has a twofold symmetry proportional to a $\sin^2(2\psi)$ shape along ψ and a twofold symmetry proportional to a $\sin^2$ shape along φ with equally broad minima and maxima. The maximum intensity is detected at $\psi/\varphi = 45°/0°$ and other equivalent settings shifted by 90° in ψ or 180° φ.

Comparing the polarization diagrams of the ZE and MSE it becomes evident, that the tuning line for fixed $\psi = 180°$ (and equivalent angles) and varying φ only gives ZE contribu-

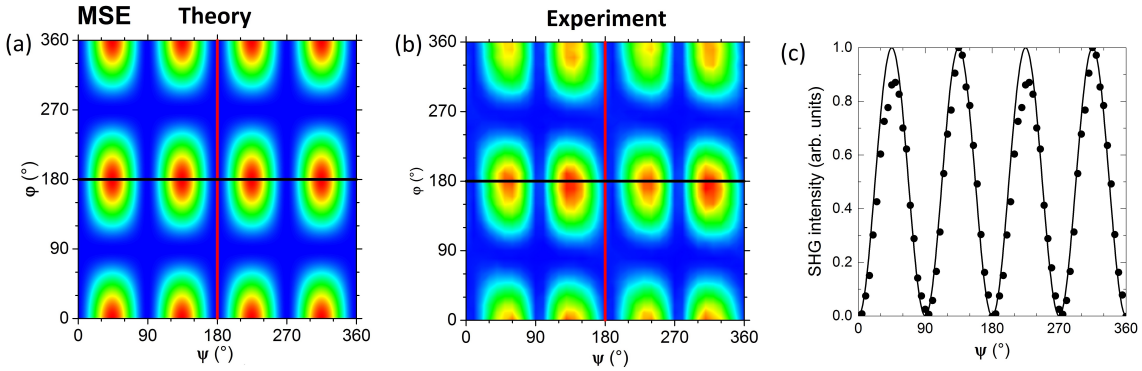

Figure 4.14 (a) Simulated [according to Eq. (4.87) and Fig. 4.9(a)] and (b) experimentally obtained 2D polarization diagrams of the MSE-induced SHG of the $3D$ exciton at $B = 4\,\mathrm{T}$ in the H100 sample (see Tab. 3.1) with $\mathbf{k} \parallel [1\bar{1}0]$ and $\mathbf{B} \parallel [110]$, as shown in Fig. 4.12(b). (c) Polarization-dependent intensity along the $\varphi = 180°$ tuning line marked in panels (a) and (b) by the black lines. Symbols represent the experimental data and lines represent the simulation.

tion for any energy of the SHG spectrum and therefore never leads to an interference with the MSE. The polarization dependence for this tuning line is shown in Fig. 4.13(c) with the symbols representing the experimental data and the line representing the simulation. Analogously, the same is true for the tuning line along ψ for a fixed $\varphi = 180°$ for the opposite case, which is plotted in Fig. 4.14(c). This explains, why we have chosen $\psi/\varphi = 0°/90°$ for the pure ZE spectrum and $\psi/\varphi = 45°/0°$ for the pure MSE spectrum in Fig. 4.12. The tuning line diagrams show a good agreement between theory and experiment and also visualize the shape of the polarization-dependent intensity as a vertical diagram axis instead of the more abstract color scale in the contour plots.

As we have demonstrated the polarization dependence of the pure ZE and MSE we now turn to the more general case of an interference between the two mechanisms. We can again use the same measured data set but choose the spectral position marked by the rightmost dashed line in Fig. 4.12 for the evaluation, as both effects contribute to the SHG intensity. At this energy, the polarization-dependent SHG intensity is plotted in Fig. 4.15(a). The diagram shows a more distorted shape representing interference of the pure diagrams. For the simulation, we use Eq. (4.92) with the coefficient ratio of $\alpha/\beta = 4/3$ and show the resulting simulated polarization dependence in Fig. 4.15(b), which is in good agreement with the experimentally obtained diagram. For better visualization, we arbitrarily choose the tuning line along ψ for a fixed $\varphi = 200°$. The results are shown in Fig. 4.15(c) and confirm the good agreement between theory and experiment.

Next, we turn to the experimental results of the weak ZE and MSE mechanisms. At $\psi/\varphi = 90°/90°$ the contribution of both dominant effects is suppressed but all the weak mechanisms are maximized. As very small signals are expected from the weak effects one has to set ψ very precisely to the minimum contribution of the dominant ZE and MSE at around 90° for optimum suppression. The spectrum is then measured for the same laser energy as before, a magnetic field of 4 T and a significantly longer integration time by a factor of 250. The acquired spectrum is shown in Fig. 4.12(c) and differs in its spectral

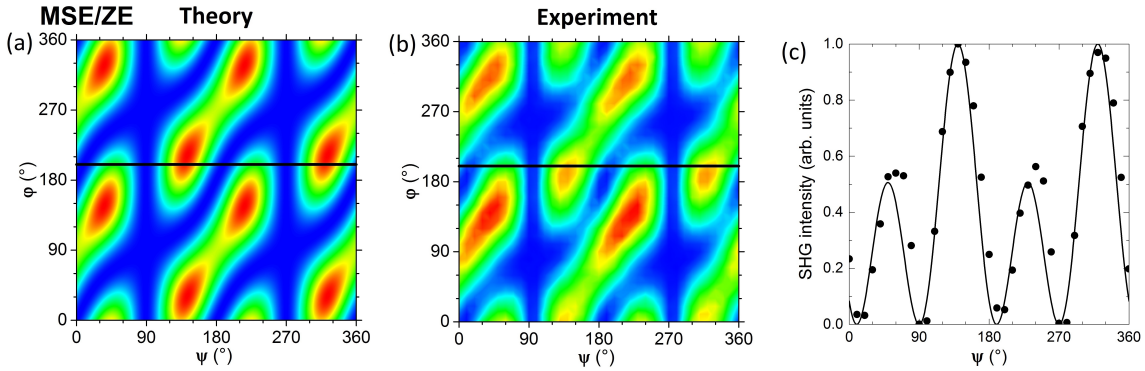

Figure 4.15 (a) Simulated [according to Eq. (4.92) with $\alpha/\beta = 4/3$ and Figs. 4.6 and 4.9] and (b) experimentally obtained 2D polarization diagrams of the interference of ZE- and MSE induced SHG in the $n = 4$ multiplet at $B = 4\,\mathrm{T}$ in the H100 sample (see Tab. 3.1) with $\mathbf{k} \parallel [1\bar{1}0]$ and $\mathbf{B} \parallel [110]$, as shown in Fig. 4.12(a) and 4.12(b). (c) Polarization-dependent intensity along the $\varphi = 200°$ tuning line marked in panel (a) and (b) by the black lines. Symbols represent the experimental data and lines represent the simulation.

features from the spectra of the dominant effects.

The simulated polarization dependencies of the weak mechanisms are shown in Figs. 4.16(a) - 4.16(c). They could be reduced to three different patterns, as many of the mechanisms show an identical polarization dependence pattern. The only possible way to measure the polarization dependence of the weak mechanisms is to fix ψ to 90° and tune φ, as it is the only tuning line at which the dominant mechanisms are suppressed. Luckily all the weak mechanisms show the same twofold symmetry with a $\sin^2(\varphi)$ shape, so no distortive interference between the weak effects is expected. The measured data are shown as symbols in Fig. 4.16(c) and are in good agreement with the simulation represented by the line.

Now we have demonstrated the polarization dependence of the dominant and weak ZE and MSE-induced SHG mechanisms experimentally and confirmed the validity of our method to derive and simulate the polarization dependence using our group theory considerations, which gives us a powerful tool for further SHG and other multi-photon spectroscopy investigations.

As briefly mentioned before we now analyze the ratio of the ZE- and MSE-induced SHG contributions for each multiplet in dependence of n, to find out which effect will dominate the SHG contribution for increasing n. To avoid spectral overlap between adjacent multiplets, especially the higher n ones, but still have enough induced SHG signal, we choose a low but sufficient magnetic field of 1 T. The measured spectra for ZE- and MSE-induced SHG are shown in Figs. 4.17(a) and 4.17(b), respectively. The gray areas mark the spectral range, for which the intensity is integrated for each multiplet. The ratios of MSE- and ZE-induced SHG intensities are shown in Fig. 4.17(c) in dependence of n. For $n = 3$ and 4 they both have a very similar contribution. For $n = 5$ and 6, however, the ratios grow drastically to about 1.7 and 3.2, which results in an exponent of 6.4 ± 1 in a power function fit. The purpose of this analysis is to show qualitatively, that the MSE dominates the ZE for multiplets of increasing n, as only four multiplets are taken into consideration and the $n = 5$ and 6 multiplets share an overlap increasing the errors.

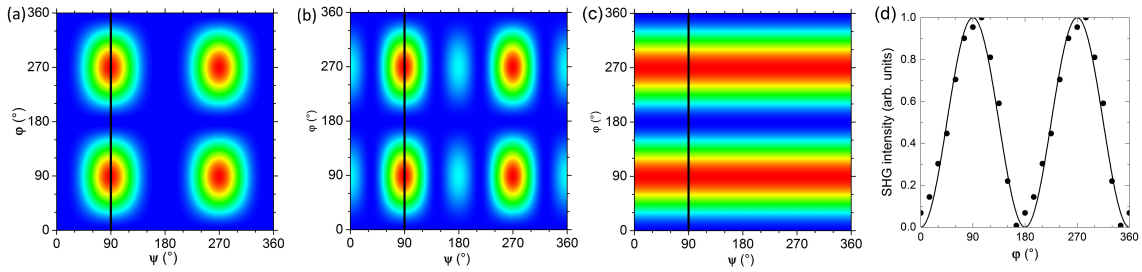

Figure 4.16 Simulated 2D polarization diagrams of the weak magnetic-field induced SHG mechanisms of the $3S$ exciton at $B = 4\,\mathrm{T}$ in the H100 sample (see Tab. 3.1) with $\mathbf{k} \parallel [1\bar{1}0]$ and $\mathbf{B} \parallel [110]$, as shown in Fig. 4.12(c): (a) ZE of excited Γ_4^- states, (b) ZE and MSE of excited Γ_3^+ states and (c) ZE and MSE of excited Γ_1^+ states. (d) Polarization-dependent intensity along the $\psi = 90°$ tuning line marked in panels (a), (b) and (c) by the black lines. Symbols represent the experimental data and lines represent the simulation.

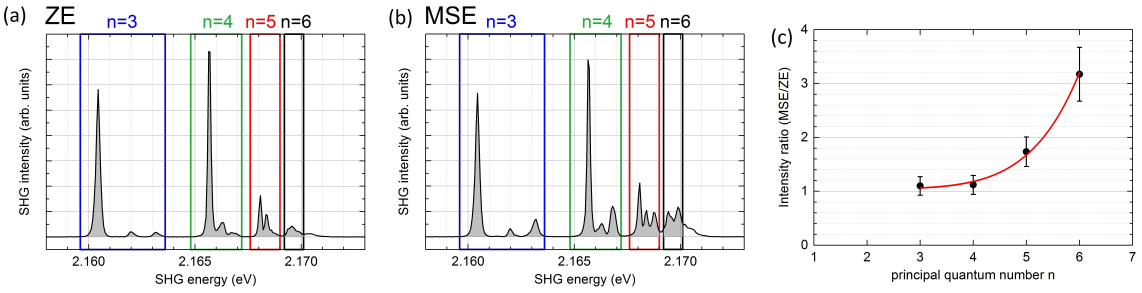

Figure 4.17 Magnetic-field-induced SHG spectra at 4 T of yellow $n \geq 3$ excitons for the (a) dominant ZE ($\psi/\varphi = 45°/0°$) and (b) dominant ZE ($\psi/\varphi = 0°/90°$) in the H100 sample (see Tab. 3.1) with $\mathbf{k} \parallel [1\bar{1}0]$ and $\mathbf{B} \parallel [110]$. The central photon energy of the fs pulses is set to 1.082 eV. The colored boxes show the spectral range for each multiplet, of which the intensity is integrated and plotted in panel (c) as the ratio of MSE to ZE-induced intensity. The power function fit $R(n) = R_0 + n^c$ yields the fit parameters $R_0 = 1.0 \pm 0.1$ and $c = 6.4 \pm 1$.

4.3 Conclusion

In this chapter, we have investigated the SHG mechanisms of yellow-series excitons in a magnetic field in Voigt geometry. The focus was set on excitation along symmetry-forbidden crystal orientations suppressing crystallographic SHG and allowing only magnetic-field-induced contributions such as the Zeeman effect mixing excitons of the same parity and the Magneto-Stark effect, which results from the exciton motion perpendicular to the magnetic field and mixes excitons of opposite parity. One dominant and several weak optical processes involving combinations of different types of transitions (ED, EQ, and MD) and exciton states (S, P, D) of various symmetries are constructed for each effect using the group-theoretical multiplication tables from Ref. [Kos+63]. The polarization-dependent SHG intensity is then derived for each mechanism using coupling coefficient tables from Ref. [Kos+63] and plotted in 2D diagrams, which are a novel extension to the usual polar plots of the parallel and

crossed configurations traditionally used in the SHG community. The information of the parallel and crossed configurations are still included in the 2D diagrams as diagonal tuning lines starting from $\psi/\varphi = 0^\circ/0^\circ$ and $\psi/\varphi = 0^\circ/90^\circ$. This makes the 2D diagrams superior if one tries to choose experimental parameters, such as sample and magnetic field orientations and polarization angles, in order to suppress certain mechanisms and investigate spectral features of isolated SHG-inducing effects.

Using this method we have chosen $\mathbf{k}$ along the $[1\bar{1}0]$ and $\mathbf{B}$ along the [110] crystal axis to suppress crystallographic SHG and set $\psi/\varphi = 0^\circ/90^\circ$ to isolate the dominant ZE, $\psi/\varphi = 45^\circ/0^\circ$ to isolate the dominant MSE and $\psi/\varphi = 90^\circ/90^\circ$ to suppress both dominant mechanisms and allowing all other weak mechanisms simultaneously. With these settings, the magnetic-field series of SHG spectra for both dominant mechanisms is measured. With increasing magnetic fields the emergence of multiple exciton lines is observed, which shift in energy and split into multiple states.

At $B = 4\,\mathrm{T}$ the polarization dependence is measured and plotted for the $3S$ exciton in a contour plot, which agrees with the simulation. In the same way, the polarization plot of the $3D$ exciton is in good agreement with the MSE simulation. For an arbitrarily chosen spectral position in the $n = 4$ multiplet an interference of both dominant mechanisms is observed in the polarization plot, which is modeled with a good agreement using Eq. (4.92). At $B = 1\,\mathrm{T}$ it is shown, that the MSE dominates the ZE in induced SHG intensity for increasing n, as the ratio $I_{\mathrm{MSE}}/I_{\mathrm{ZE}}(n)$ grows with a power of about 6.4 ± 1.

The presented method turns out to be a powerful tool for SHG spectroscopy of excitons, as it can easily be applied to other exciton series in Cu_2O, as will be demonstrated in Sec. 6. For the detection of optically inactive paraexcitons, it is crucial to suppress the SHG of optically active orthoexcitons, in which case this method will turn out to be very useful as well (see Sec. 5). The derivation of polarization dependencies can also be extended to other mechanisms involving external electric fields or strain, to other multi-photon processes such as third harmonic generation (THG) or difference-frequency generation with two-photon excitation (2P-DFG), as will be discussed in Sec. 7, and also to materials with other crystal structures (e.g. ZnSe with T_d symmetry).

Chapter 5

SHG of paraexcitons activated by a magnetic field

Exciton can be classified into bright and dark excitons. The bright excitons, also called orthoexcitons in Cu_2O, are spin-singlet-triplet mixed states which are optically active. The dark excitons, also called paraexcitons in Cu_2O, are pure spin-triplet states and do not couple to the light field in single-photon transitions to all orders of perturbation in the minimal coupling [Eq. (2.26)] as their excitation would require a spin-flip.

Nevertheless, dark excitons can be optically activated by symmetry-reducing perturbations such as stress [San+11; Mys+83; Liu+05; Nak+02] or external magnetic fields [Bra+07; Bay+00], leading to an admixture from optically active orthoexcitons transferring oscillator strength. The electron-hole short-range exchange interaction only affects the orthoexcitons and lifts them energetically above the paraexciton. Due to the small $1S$ exciton radius of 0.7 nm the exchange energy splitting is large. Dark excitons have a large influence on the optical properties of semiconductors. Injected carriers, which relax into the lowest paraexciton, do not lead to a strong light emission, as the large ortho-para splitting suppresses the thermal population of the bright state. This suppression of the radiative decay leads to large lifetimes in the range of several µs [Mys+79] and accordingly to a very narrow spectral line width of 84 neV [Bra+07]. The long lifetimes make dark excitons more suitable for quantum information processing [Poe+10] and also a good candidate for Bose-Einstein condensation [Frö+18; Sno+14; Bei+17], which has recently been experimentally demonstrated in bulk Cu_2O in Ref. [Mor+22]. Furthermore, Brandt et al. have experimentally demonstrated paraexciton polariton propagation beats with dephasing times of a few tens of ns [Bra+09].

The fundamental question arises, whether it is experimentally possible to demonstrate the observability of the Rydberg series of paraexcitons. In a bulk semiconductor, they should also form a hydrogen-like series just as the orthoexcitons. So far only the ground state of dark excitons has been observed in Cu_2O [Bra+07; Far+20a; Kuw+77; San+11] and other semiconductors such as KI [Bee+87]. The n dependent exchange splitting has therefore also never been experimentally investigated. Cu_2O is the most suitable material to look for these excited dark excitons, as it has by far the richest experimentally observed exciton level structure with about 60 observed $\{n,L\}$-shells, including the P exciton series up to $n = 28$ and the highest angular momentum quantum number of $L = 6$ corresponding to the H exciton. Observation of the Rydberg series of paraexcitons would complete this picture of the exciton level structure in Cu_2O. Other popular semiconductors such as GaAs have only two excited bright states [Feh+82] and 2D materials only five [Che+14].

In this chapter, we investigate the $1S$ paraexciton and the corresponding excited states up

to a principal quantum number of $n = 6$ by means of SHG in a magnetic field. Their energies have been theoretically derived in Ref. [Sch+17b]. In Sec. 5.1 we clarify the singlet-triplet terminology by deriving the spin structure of the $1S$ exciton and describing its spectral splitting and shifting behavior in a magnetic field. There are two SHG processes, which we will elaborate on. One involves the ED-ED excitation of the admixed Γ_5^+ part and the other achieves a direct excitation of the Γ_2^+ part by an EQ-MD two-photon process. In Sec. 5.3 we derive the polarization selections rules for both mechanisms and plot the polarization diagrams for the three orthoexciton eigenstates and the paraexciton for various crystal orientations, which will be helpful for choosing the most suitable experimental geometry. Section 5.4 deals with the magnetic field-dependent intensity increase of both processes as a way to recognize the weaker EQ-MD excitation SHG process.

The understanding of the properties and the experimental knowledge achieved in the investigations of the ground paraexciton state will then be applied in the search for the excited Rydberg paraexciton states in Sec. 5.5. The experimental results on the observations of the Rydberg states of $n = 3$ to 6 are shown in Sec. 5.5.1 and the results on the $n = 2$ paraexciton and the green $1S$ paraexciton will be presented and discussed in Sec. 5.5.2. Finally, in Sec. 5.5.3 we discuss the experimentally observed ortho-para splitting energies. The average excitation powers of the fs and ps-pulsed lasers are set to about 10 mW. The results of this chapter are published in Refs. [Far+20a; Far+20c].

5.1 Spin-singlet-triplet terminology and exchange interaction

The optical properties, exchange interaction and mixing behavior in a magnetic field of excitons are highly dependent on the spin composition. In this section, we derive the spin composition of the yellow $1S$ para- and orthoexciton states for a clarification of the singlet-triplet terminology [Das03; Far+20c].

The symmetry of 1/2 spins in the O_h point group is Γ_6^+, as shown in the compatibility table A.1 from Ref. [Kos+63]. As the electrons are excited into the CB with the Wannier function ϕ_s stemming from Cu $4s$ orbitals with Γ_1^+ symmetry the electron spin states are denoted by $|\uparrow_e\rangle$ and $|\downarrow_e\rangle$ and keep the Γ_6^+ symmetry, as sketched in Fig. 2.3(c).

The hole spins $|\uparrow_h\rangle$ and $|\downarrow_h\rangle$ in the VB are subject to the spin-orbit coupling, as the VB with the Wannier functions ϕ_{yz}, ϕ_{zx} and ϕ_{xy} stems from Cu $3d$ orbitals with Γ_5^+ symmetry. For the spin-orbit coupled hole states $|\uparrow_H\rangle$ and $|\downarrow_H\rangle$ we get

$$\begin{aligned} |\uparrow_H\rangle &= -\frac{i}{\sqrt{3}}\phi_{yz}\,|\downarrow_h\rangle - \frac{1}{\sqrt{3}}\phi_{zx}\,|\downarrow_h\rangle + \frac{i}{\sqrt{3}}\phi_{xy}\,|\uparrow_h\rangle\,, \\ |\downarrow_H\rangle &= -\frac{i}{\sqrt{3}}\phi_{yz}\,|\uparrow_h\rangle + \frac{1}{\sqrt{3}}\phi_{zx}\,|\uparrow_h\rangle - \frac{i}{\sqrt{3}}\phi_{xy}\,|\downarrow_h\rangle \end{aligned} \tag{5.93}$$

in a quasi-spin notation according to the coupling coefficient table A.9 for $\Gamma_5^+ \otimes \Gamma_6^+ \to \Gamma_7^+$.

As seen in Eq. (4.50) the Γ_7^+ VB hole states and the Γ_6^+ CB electron states are coupled to the S exciton states consisting of the paraexciton $|P\rangle$ with Γ_2^+ symmetry and the three orthoexciton states $|O_{yz}\rangle$, $|O_{zx}\rangle$ and $|O_{xy}\rangle$ with Γ_5^+ symmetry using the coupling coefficient

table A.6 from Ref. [Kos+63] for $\Gamma_6^+(2) \otimes \Gamma_7^+(2) \to \Gamma_2^+(1) \oplus \Gamma_5^+(3)$. Thus we get

$$\begin{aligned}
|P\rangle &= +\frac{1}{\sqrt{2}} |\uparrow_e \downarrow_H\rangle - \frac{1}{\sqrt{2}} |\downarrow_e \uparrow_H\rangle \,, \\
|O_{yz}\rangle &= +\frac{i}{\sqrt{2}} |\uparrow_e \uparrow_H\rangle - \frac{i}{\sqrt{2}} |\downarrow_e \downarrow_H\rangle \,, \\
|O_{zx}\rangle &= +\frac{i}{\sqrt{2}} |\uparrow_e \uparrow_H\rangle + \frac{1}{\sqrt{2}} |\downarrow_e \downarrow_H\rangle \,, \\
|O_{xy}\rangle &= -\frac{i}{\sqrt{2}} |\uparrow_e \downarrow_H\rangle - \frac{i}{\sqrt{2}} |\downarrow_e \uparrow_H\rangle \,.
\end{aligned} \tag{5.94}$$

for the quasi-spin composition of the para- and the three orthoexciton components. In order to obtain the pure spin composition of these states, Eqs. (5.93) needs to be inserted into Eqs. (5.94). This results in

$$|P\rangle = \frac{1}{\sqrt{6}}\phi_s[i\phi_{xy}(\underbrace{|\uparrow_e\downarrow_h\rangle + |\downarrow_e\uparrow_h\rangle}_{\sqrt{2}|T_0\rangle}) - (\phi_{zx} + i\phi_{yz}) \underbrace{|\uparrow_e\uparrow_h\rangle}_{|T_{+1}\rangle} - (\phi_{zx} - i\phi_{yz}) \underbrace{|\downarrow_e\downarrow_h\rangle}_{|T_{-1}\rangle}], \tag{5.95}$$

$$|O_{xy}\rangle = \frac{1}{\sqrt{6}}\phi_s[-\phi_{xy}(\underbrace{|\uparrow_e\downarrow_h\rangle - |\downarrow_e\uparrow_h\rangle}_{\sqrt{2}|S\rangle}) - (\phi_{yz} - i\phi_{zx}) \underbrace{|\uparrow_e\uparrow_h\rangle}_{|T_{+1}\rangle} - (\phi_{yz} + i\phi_{zx}) \underbrace{|\downarrow_e\downarrow_h\rangle}_{|T_{-1}\rangle}],$$

$$|O_{yz}\rangle = \frac{1}{\sqrt{6}}\phi_s[-\phi_{yz}(\underbrace{|\uparrow_e\downarrow_h\rangle - |\downarrow_e\uparrow_h\rangle}_{\sqrt{2}|S\rangle}) + i\phi_{zx}(\underbrace{|\uparrow_e\downarrow_h\rangle + |\downarrow_e\uparrow_h\rangle}_{\sqrt{2}|T_0\rangle}) + \phi_{xy}(\underbrace{|\uparrow_e\uparrow_h\rangle}_{|T_{+1}\rangle} + \underbrace{|\downarrow_e\downarrow_h\rangle}_{|T_{-1}\rangle})],$$

$$|O_{zx}\rangle = \frac{1}{\sqrt{6}}\phi_s[-\phi_{zx}(\underbrace{|\uparrow_e\downarrow_h\rangle - |\downarrow_e\uparrow_h\rangle}_{\sqrt{2}|S\rangle}) - i\phi_{yz}(\underbrace{|\uparrow_e\downarrow_h\rangle + |\downarrow_e\uparrow_h\rangle}_{\sqrt{2}|T_0\rangle}) - i\phi_{xy}(\underbrace{|\uparrow_e\uparrow_h\rangle}_{|T_{+1}\rangle} - \underbrace{|\downarrow_e\downarrow_h\rangle}_{|T_{-1}\rangle})].$$

$|S\rangle$ denotes the spin-singlet state and $|T_0\rangle$, $|T_{+1}\rangle$ and $|T_{-1}\rangle$ denote the three spin-triplet states. From these equations, it becomes evident, that the paraexciton is composed purely of spin-triplet states and that all three orthoexciton components are mixtures of spin-singlet and spin-triplet states, as indicated by the under brackets.

The light field cannot affect the spin part of the exciton function and is therefore not able to change the spin. As a spin-triplet state has a total spin of $S = s_e + s_h = 1$, it would require a spin flip, which is not possible due to the selection rule for an optical transition of $\Delta S = 0$ [Kli12].

The consequences on the energy of spin-singlet and -triplet states are described by the exchange-interaction Hamiltonian

$$H_{\text{exch}} = \frac{\bar{J}_0}{2}\Big(1 - S^2\Big) V_{\text{uc}} \delta(r) \tag{5.96}$$

with the exchange interaction strength $\bar{J}_0$ related to the exchange integral, the probability density $\delta(r)$ of the electron and hole at $r = 0$ and the volume of the unit cell V_{uc}. Spin-singlet states ($S = 0$) are therefore energetically lifted by the exchange energy ε in contrast to spin-triplet states ($S = 1$), which are not affected by the exchange interaction.

A visual way to picture it would be, that the fermionic function as the product of the spin part and the spatial part needs to be antisymmetric. As the spin part of spin-triplet states is symmetric with even parity, the spatial part needs therefore to be antisymmetric

with a vanishing overlap of the electron and hole and therefore a vanishing exchange energy. A spin-singlet state has an antisymmetric spin part and a symmetric spatial part, which implies, that the overlap of the electron and hole charge distributions gives a non-zero contribution leading to the lifting of this state by the exchange energy ε.

We want to address here the occasional misunderstanding of why the paraexciton is called a triplet exciton, although it is a single state and does not split in a magnetic field. On the other hand, the orthoexciton with its optically active singlet part splits into three states in a magnetic field. The singlet-triplet terminology referring to the optical activity and the exchange interaction is based on the spin composition of the exciton.

But under the influence of an external magnetic field, the $1S$ exciton components form the four eigenstates [Far+20c]

$$\begin{aligned}
|P\rangle &= \frac{1}{\sqrt{2}}(|\uparrow_e\downarrow_H\rangle - |\downarrow_e\uparrow_H\rangle),\\
|O_{M=0}\rangle &= |O_{xy}\rangle = -\frac{1}{\sqrt{2}}(|\uparrow_e\downarrow_H\rangle + |\downarrow_e\uparrow_H\rangle),\\
|O_{M=+1}\rangle &= \frac{1}{\sqrt{2}}(|O_{zx}\rangle - i\,|O_{yz}\rangle) = |\uparrow_e\uparrow_H\rangle\,,\\
|O_{M=-1}\rangle &= \frac{1}{\sqrt{2}}(|O_{zx}\rangle + i\,|O_{yz}\rangle) = |\downarrow_e\downarrow_H\rangle\,,
\end{aligned} \tag{5.97}$$

which are characterized by the magnetic quantum number M. The multiplicity of the state in a magnetic field is therefore determined not in the spin basis but in the total angular momentum basis including the orbital momentum of the band states.

The mixing behavior of the four eigenstates in a magnetic field is described by the matrix [Far+20a]

$$H_{\mathrm{B}}(a,b,B) = \begin{pmatrix} E_{1S_p} & -iaB & 0 & 0\\ iaB & E_{1S_p}+\varepsilon & 0 & 0\\ 0 & 0 & E_{1S_p}+\varepsilon-bB & 0\\ 0 & 0 & 0 & E_{1S_p}+\varepsilon+bB \end{pmatrix}. \tag{5.98}$$

in the basis of the eigenstates $\{|P\rangle\,, |O_{M=0}\rangle\,, |O_{M=-1}\rangle\,, |O_{M=+1}\rangle\}$ from Eq. (5.97). E_{1S_p} is the zero-field energy of the paraexciton, ε the exchange energy, $a = \mu_B(g_c - g_v)/2$ the mixing parameter between the $M = 0$ ortho- and paraexciton with the Bohr magneton μ_B and the g value g_c of the CB and g_v of the VB and $b = \mu_B(g_c+g_v)/2$ the Zeeman parameter of the $M = \pm 1$ eigenstates.

Diagonalization of the matrix yields the eigenenergies

$$E_p(B) = E_{1S_p} + \frac{1}{2}\Big(\varepsilon - \sqrt{\varepsilon^2 + 4a^2B^2}\Big) \approx E_{1S_p} - \frac{a^2B^2}{\varepsilon}, \tag{5.99}$$

$$E_{o,0}(B) = E_{1S_p} + \frac{1}{2}\Big(\varepsilon + \sqrt{\varepsilon^2 + 4a^2B^2}\Big) \approx E_{1S_p} + \varepsilon + \frac{a^2B^2}{\varepsilon}, \tag{5.100}$$

$$E_{o,\pm1}(B) = E_{1S_p} \pm bB. \tag{5.101}$$

of the four states, which are plotted in Fig. 5.1 using the experimentally derived parameters from Sec. 5.2. The $M = \pm 1$ states split linearly apart and the $M = 0$ ortho- and paraexciton

are quadratically repelled. In principle, the k^2 interaction and strain effects need to be taken into consideration, as demonstrated by Mund et al. in Ref. [Mun+19]. As these influences are only in the magnitude of a few µeV, our spectrometer can hardly resolve them. Additionally, their influence is dominated by the magnetic-field-induced shifts far below 0.5 T and can therefore be neglected for our experiments.

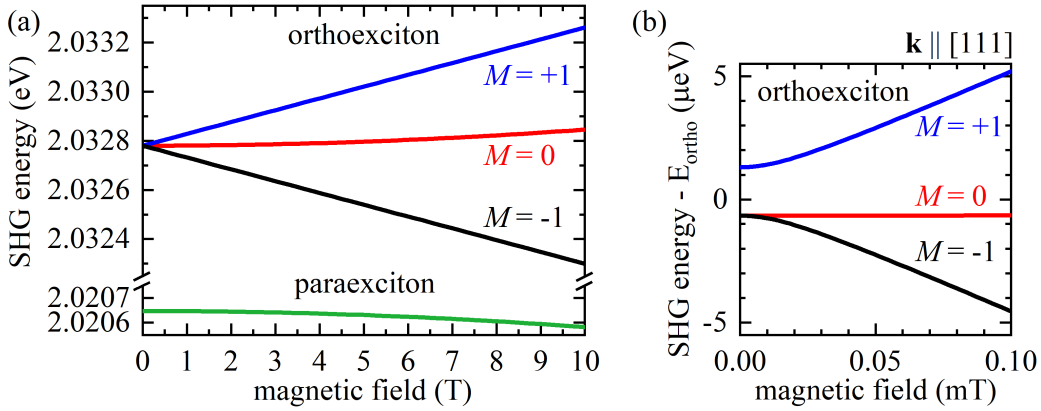

Figure 5.1 (a) Calculated eigenenergies of the four $1S$ exciton eigenstates in a magnetic field in Voigt configuration according to Eqs. (5.99), (5.100) and (5.101). (b) Calculated eigenenergies of the $1S$ orthoexciton eigenstates at magnetic fields below 10 mT including k^2 splitting at zero field [Das+04; Mun+19; Sch+16b] for **k** along the [111] crystal axis.

5.2 Magneto-optical spectroscopy

For the experiments, we have used the Spex spectrometer with a resolution of 10 µeV for spectral measurements and the Acton spectrometer for polarization and magnetic field-dependent intensity measurements. Deviating information will be specified in the figure captions. For the experiments on the $1S$ paraexciton, the ps laser was used without scanning, as it has a higher spectral density and is broad enough to spectrally cover the orthoexciton components at 10 T but is narrow enough to suppress the orthoexciton excitation while exciting the paraexciton, leading to less Γ_3^- phonon emission of the orthoexciton which is in the same spectral region as the paraexciton. For the measurements of the Rydberg series of paraexcitons, the fs laser was used, as it is spectrally broad enough to cover all the Rydberg states. All experiments are performed at $T = 1.4$ K and in magnetic fields of up to $B = 10$ T in Voigt configuration. More detailed specifications on the laser system, the spectrometer and other components of the setup are discussed in Sec. 3.1. A variety of samples have been chosen specifically for different mechanisms and dependencies and are specified for each measurement in the figure caption.

The spectrum at $B = 10$ T of the four $1S$ exciton states is measured with a high resolution of 10 µeV and shown in Fig. 5.2(a). As all lines appear to have the same line width, it suggests that they are physically even narrower. The line width of the paraexciton was experimentally demonstrated to be about 80 µeV [Bra+07] while the orthoexciton states have an FWHM of a few µeV [Das+04]. The orthoexciton is split into three states labeled

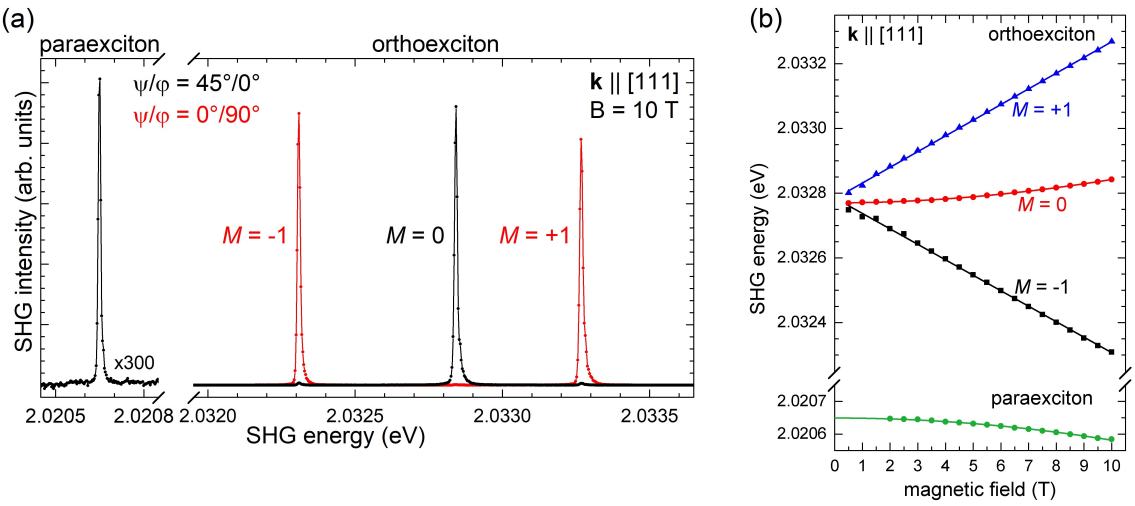

Figure 5.2 (a) SHG spectrum of the para- and three orthoexcitons at a magnetic field of 10 T in Voigt configuration in the H24 sample (see Tab. 3.1). The spectrum is measured with the Spec spectrometer in second order with a resolution of 10 µeV. SHG of the $M = \pm 1$ states appears at a linear polarization angle setting of $\psi/\varphi = 0°/90°$ and that of the paraexciton and $M = 0$ orthoexciton appears at $\psi/\varphi = 45°/0°$. The weak signals of the paraexciton are multiplied by a factor of 300. Note the axis break. (b) Resonance energies of all four $1S$ exciton states for magnetic fields up to 10 T in steps of 0.5 T. Symbols represent experimentally obtained data and the solid lines are fits according to Eqs. (5.99), (5.100) and (5.101). The inset shows a calculation including k^2 splitting [Das+04] at low magnetic fields.

by their magnetic quantum number M. The $|M| = 1$ orthoexciton states are split by about 1 meV. The $M = 0$ state is shifted to slightly higher energies closer to the $M = 1$ state, due to the repulsion with the paraexciton. The paraexciton is about 12 meV lower in energy and its SHG signals are weaker by a factor of about 300. The polarization settings are chosen, so that at $\psi/\varphi = 45°/0°$ only the $M = 0$ components have a contribution by the ED-ED excitation SHG mechanism and at $\psi/\varphi = 0°/90°$ only the $|M| = 1$ components are detectable. The complete polarization dependencies will be derived in Sec. 5.3.

For the investigation of how the exciton states split and shift with an increasing magnetic field, the SHG spectrum is measured for magnetic fields up to 10 T in steps of 0.5 T. Each exciton state in each spectrum is fitted with a Gaussian and the center wavelength is taken as the energy for each state and magnetic field and the results are shown as color symbols in Fig. 5.2(b). The data for the orthoexciton at 0 T are missing, as the three states can not be resolved. The data for the paraexciton below 1.5 T are missing, because the signals are too weak. The $|M| = 1$ states split linearly apart. The $M = 0$ states repel each other quadratically due to mixing by the magnetic field. The experimental data are fitted with the eigenvalues [Eqs. (5.99), (5.100) and (5.101)] of matrix [Eq. (5.98)]. The fit parameters

Table 5.1 Experimental results of the exchange splitting energy ε and the g factors of the VB and CB obtained in this work and previous studies.

source	ε (meV)	g_c	g_v	$\lvert g_c + g_v \rvert$	$\lvert g_c - g_v \rvert$
this work	12.120	2.38	−0.72	1.66	3.1
[Kuw+77]	12	2.68	−1.02	1.66	3.70
[Frö+82]	-	3.17	−1.53	1.64	4.70
[Hög+05]	12.117	-	-	-	3.26
[Cer+64]	-	-	-	1.7	-

are summarized in the following:

$$a = 91 \pm 3 \ \frac{\mu\text{eV}}{\text{T}}, \tag{5.102}$$

$$|g_c - g_v| = 3.1 \pm 0.1, \tag{5.103}$$

$$b = 48.1 \pm 0.3 \ \frac{\mu\text{eV}}{\text{T}}, \tag{5.104}$$

$$|g_c + g_v| = 1.66 \pm 0.01, \tag{5.105}$$

$$\varepsilon = 12.120 \text{ meV}, \tag{5.106}$$

$$f_p(B) = (5.6 \pm 0.4) \times 10^{-5} B^2 \cdot f_o. \tag{5.107}$$

From these one can derive the g factors

$$g_c = 2.38 \pm 0.08, \tag{5.108}$$

$$g_v = -0.72 \pm 0.03. \tag{5.109}$$

of the valence- and conduction band. The fit parameter for the energy splitting and the g factors are compared to the results of previous publications in Table 5.1

5.3 Simulation and measurements of polarization dependencies

The $1S$ paraexciton is a pure spin-triplet state with Γ_2^+ symmetry, as seen in Eq. (5.95), which is optically inactive in single-photon processes and ED-ED forbidden in two-photon processes. However, the paraexciton can be excited by an admixture from the optically active Γ_5^+ orthoexciton by strain [San+11] or a magnetic field [Bra+07]. The Γ_5^+ admixture is then optically addressed by an ED-ED two-photon excitation and an EQ emission. An alternative but a much weaker way for SHG of the paraexciton is to excite the Γ_2^+ paraexciton directly, by replacing both ED photons with even parity EQ and MD photons. Excitation of excitons including MD transitions have been demonstrated for GaAs [Mic+96] and alkali halides [Frö+94]. However, an orthoexciton admixture is again needed for a Γ_5^+ EQ emission for the SHG process.

For the derivation of the polarization dependencies we use the matrix

$$\mathbf{M}_B(a,b,\mathbf{B}) = \begin{pmatrix} -\varepsilon & iaB_x & iaB_y & iaB_z \\ -iaB_x & 0 & -ibB_z & ibB_y \\ -iaB_y & ibB_z & 0 & -ibB_x \\ -iaB_z & -ibB_y & ibB_x & 0 \end{pmatrix}, \tag{5.110}$$

which describes the four states of the $1S$ exciton system in a $\{\Gamma_2^+, \Gamma_{5,yz}^+, \Gamma_{5,xz}^+, \Gamma_{5,xy}^+\}$ basis. Its eigenvectors $|\Lambda_i(B)\rangle$ with $i = 0,1,2,3$ represent the paraexciton and the $M = -1$, $M = 0$ and $M = +1$ eigenstates of the orthoexciton, respectively.

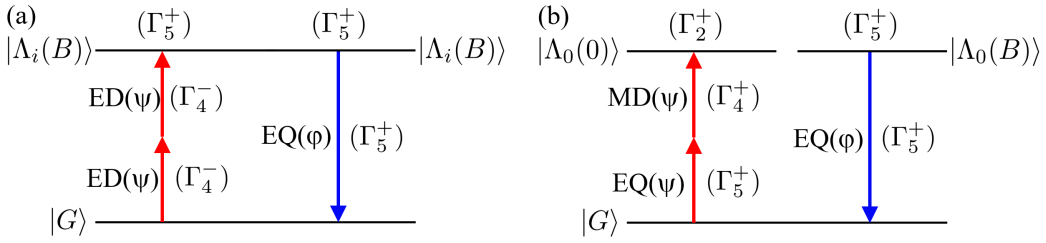

Figure 5.3 Schematics of SHG mechanisms for the $1S$ exciton states in a magnetic field. (a) ED-ED excitation of the Γ_5^+ component of the $1S$ eigenstate $|\Lambda_i(B)\rangle$ followed by an EQ emission of the same state. (b) Direct excitation of the Γ_2^+ component of the $1S$ paraexciton $|\Lambda_0(0)\rangle$ by an EQ-MD transition followed by an EQ emission of its magnetic-field admixed Γ_5^+ component.

The described SHG process for all four states is schematically shown in Fig. 5.3(a). The eigenvector of the state of interest is multiplied by the ED-ED excitation vector, which has already been derived in Eq. (4.64), and also to the EQ emission vector derived in Eq. (4.60). Note, that the vectors are extended to the same basis as the matrix in Eq. (5.110) by an additional Γ_2^+ component in the top line and filling it with a 0. The polarization-dependent TPA intensity is calculated by squaring the absolute value of the expression for the excitation channel, which results in

$$I_{\mathrm{DD},i}^{\mathrm{TPA}}(\mathbf{k},\psi,B) = I_{\mathrm{DD},i}^{5+}(\mathbf{k},\psi,B) \propto |\Lambda_i(B)\cdot O_{\mathrm{DD}}^{5+}(\mathbf{k},\psi)|^2. \tag{5.111}$$

For the SHG intensity, the emission channel has to be multiplied by the excitation channel before squaring the absolute value. Thus we get:

$$\begin{aligned} I_{\mathrm{DD},i}^{\mathrm{SHG}}(\mathbf{k},\psi,\varphi,B) &= I_{\mathrm{DD/Q},i}^{5+}(\mathbf{k},\psi,\varphi,B) \\ \propto |[\Lambda_i(B)\cdot O_{\mathrm{DD}}^{5+}(\mathbf{k},\psi)][\Lambda_i(B)\cdot O_{\mathrm{Q}}^{5+}(\mathbf{k},\varphi)]|^2. \end{aligned} \tag{5.112}$$

The scheme for the SHG process with direct EQ-MD excitation of the paraexciton is shown in Fig. 5.3(b). Using the coupling coefficient table A.8 of Ref. [Kos+63] for $\Gamma_4^+ \otimes \Gamma_5^+ \rightarrow \Gamma_2^+$ the EQ-MD two-photon excitation vector of the paraexciton reads

$$O_{\mathrm{QMD}}^{2+}(\mathbf{k},\psi) = O_{\mathrm{Q}}^{5+}(\mathbf{k},\psi)\cdot O_{\mathrm{MD}}^{4+}(\mathbf{k},\psi)/\sqrt{3}. \tag{5.113}$$

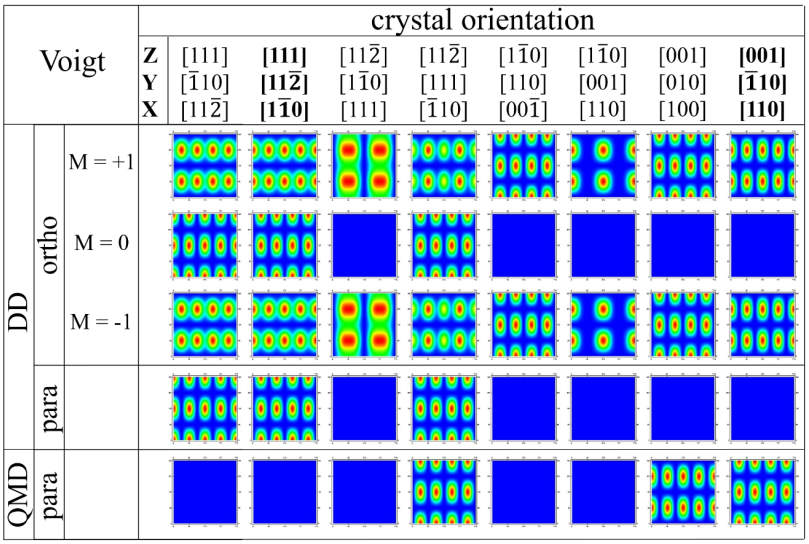

Figure 5.4 Simulated 2D polarization diagrams of the $M = 1$, $M = 0$ and $M = -1$ ortho- and the paraexciton in a magnetic field in Voigt geometry for various crystal orientations for the ED-ED excitation SHG mechanism according to Eq. (5.112). In the last line the polarization diagrams are shown for the EQ-MD excitation SHG mechanism according to Eq. (5.114).

The excitation vector is multiplied with the paraexciton eigenvector $|\Lambda_0(0)\rangle = \{1, 0, 0, 0\}$ at $B = 0$, as it is excited directly with no need of the magnetic field admixture of the orthoexciton. The emission process has the same form, as in the ED-ED process. Consequently, the polarization-dependent SHG intensity for the weak process reads

$$\begin{aligned} I^{\mathrm{SHG}}_{\mathrm{QMD},0}(\mathbf{k}, \psi, \varphi, B) &= I^{2+}_{\mathrm{QMD/Q},0}(\mathbf{k}, \psi, \varphi, B) \\ &\propto |[O^{4+}_{\mathrm{QMD}}(\mathbf{k}, \psi)][\Lambda_0(B) \cdot O^{5+}_{\mathrm{Q}}(\mathbf{k}, \varphi)]|^2. \end{aligned} \tag{5.114}$$

The 2D polarization diagrams of the discussed processes are shown in Fig. 5.4 for the Voigt and in Fig. 5.5 for the Faraday geometry for various crystal orientations. SHG of the $M = \pm 1$ components have the same polarization dependence for each individual crystal orientation and are allowed in all crystal orientations in Voigt geometry but only for $\mathbf{k}$ along [111] and [11$\bar{2}$] in Faraday geometry. The $M = 0$ ortho- and paraexcitons also show the same polarization dependence for each individual crystal orientation but are only allowed for $\mathbf{k}$ along [111] and $\mathbf{k} \parallel$ [11$\bar{2}$] with $\mathbf{B} \parallel$ [$\bar{1}$10] in Voigt geometry, but only for $\mathbf{k}$ along [11$\bar{2}$] in Faraday geometry. The weak EQ-MD SHG process of the paraexciton is only allowed for $\mathbf{k}$ along [001] and $\mathbf{k} \parallel$ [11$\bar{2}$] with $\mathbf{B} \parallel$ [$\bar{1}$10] in Voigt geometry, but only for $\mathbf{k}$ along [11$\bar{2}$] in Faraday geometry.

For our experimental investigations of the ED-ED process we have chosen the H24 sample (see Tab. 3.1) with $\mathbf{k} \parallel$ [111] and $\mathbf{B} \parallel$ [1$\bar{1}$0] in Voigt geometry, as all four eigenstates are allowed in a magnetic field and show characteristic polarization dependencies. The TPA of the ED-ED excitation process is measured in the H2b sample (see Tab. 3.1) oriented such, that $\mathbf{k} \parallel$ [11$\bar{2}$] with $\mathbf{B} \parallel$ [111] in Voigt geometry. For the weak signals of the EQ-MD process, it is crucial to suppress the strong ED-ED process and to be able to distinguish the weak

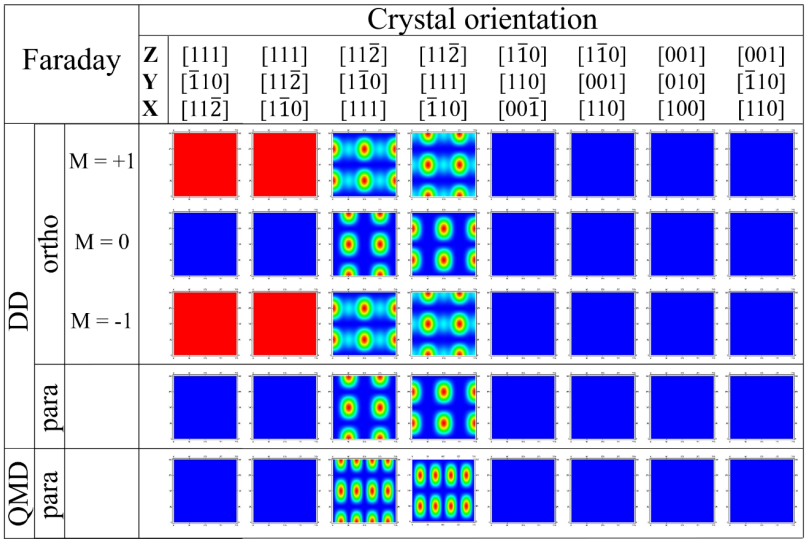

Figure 5.5 Simulated 2D polarization diagrams of the $M = 1$, $M = 0$ and $M = -1$ ortho- and the paraexciton in a magnetic field in Faraday geometry for various crystal orientations for the ED-ED excitation SHG mechanism according to Eq. (5.112). In the last line the polarization diagrams are shown for the EQ-MD excitation SHG mechanism according to Eq. (5.114).

and the strong process by a specific choice of the polarization angle setting. Therefore we have chosen the H98 sample (see Tab. 3.1) with $\mathbf{k} \parallel [001]$ with $\mathbf{B} \parallel [110]$ in Voigt geometry for the experiments.

The polarization dependence of the two-photon excitation process has been measured at $B = 10\,\mathrm{T}$, by monitoring the emission of the Γ_3^- phonon for each $1S$ state. The polarization dependencies are shown in Fig. 5.6(a) of the $M = 0$ components, exhibiting a fourfold shape with two intense and two less intense maxima. Note, that the paraexciton signals are about two orders of magnitude smaller than the orthoexciton signals. Figure 5.6(b) shows the TPA polarization dependencies of the $|M| = 1$ components, having a twofold shape with broader maxima than minima.

The ED-ED SHG polarization dependencies of all four states are measured according to Sec. 3.5 at $B = 10\,\mathrm{T}$. The experimental polarization diagrams are shown in Fig. 5.7(b). A comparison with the simulations according to Eq. (5.112) in Fig. 5.7(a) indicates a good agreement with theory and experiment. In Fig. 5.7(c) the 1D polarization diagrams are shown for the black and red tuning lines of the contour plots. All four states have a twofold symmetry along φ, which is shifted by 90° comparing the $M = 0$ and $|M| = 1$ components. Along ψ all states have a fourfold symmetry, however, the intensity of the $|M| = 1$ components has an additional constant background.

The polarization dependence of the three orthoexciton states is measured for four additional crystal orientations for $\mathbf{k}$ along different crystal axis. The results are shown in Fig. 5.8 and confirm the agreement between the experiment and simulation even more.

As mentioned before, for the measurement of the EQ-MD process the orientation of the sample within the sample mounted and the cryostat, the polarization angles and a strain-

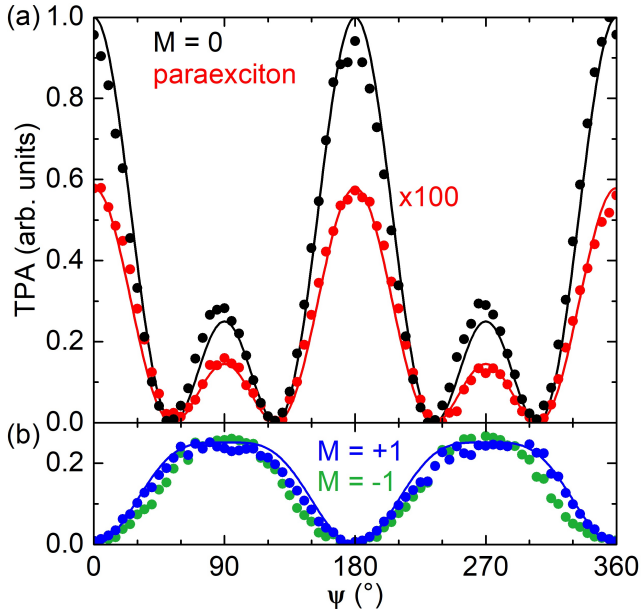

Figure 5.6 ED-ED TPA polarization dependence of the $M = 0$ orthoexciton and the paraexciton in panel (a) and the $M = +1$ and $M = -1$ orthoexciton states in panel (b) in a magnetic field in Voigt geometry for $\mathbf{k}$ along $[11\bar{2}]$ and $\mathbf{B}$ along [111] in the H2b sample, see Tab. 3.1. Symbols represent the experimental data for the Γ_3^- phonon intensity of the corresponding state and the lines represent the simulation according to Eq. (5.111).

reduced position of the laser spot on the sample have to be set precisely so that contributions from the strong ED-ED mechanism are suppressed. The measured polarization dependence at $B = 10\,\mathrm{T}$ is shown in Fig. 5.9. As the signals are very weak, it was not realistic to measure the full 2D diagram with the large integration times. Therefore only the tuning lines for a fixed $\psi = 45°$ and $\varphi = 180°$ are measured. The experimental data (symbols) are in good agreement with the simulation (line) according to Eq. (5.114). The polarization dependence has a fourfold $\cos(\psi)^2$ shape along ψ and a twofold $\sin(2\varphi)^2$ shape along φ. The TPA of the EQ-MD process of the paraexciton without an applied magnetic field could not be detected via the monitoring of the Γ_3^- phonon emission, as it is spectrally positioned within the range of the strong impurity emission, which is induced by relaxation processes of the strong three-photon ED processes above the violet bandgap.

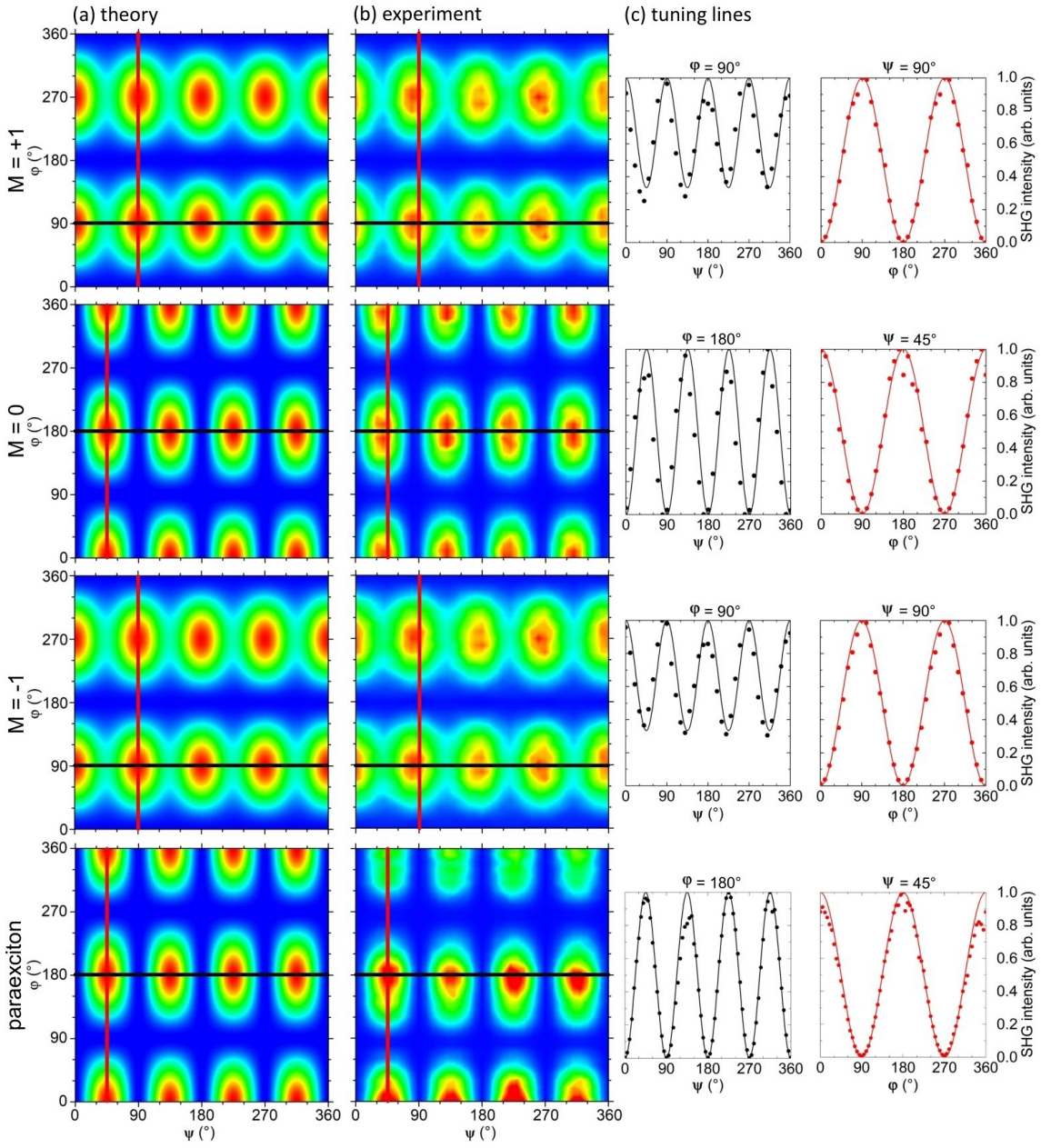

Figure 5.7 (a) 2D polarization diagrams of the simulation of the ED-ED excitation SHG process according to Eq. (5.112) and (b) experimental data of the 2D polarization diagrams of the $M = 1$, $M = 0$ and $M = -1$ ortho- and the paraexcitons in a magnetic field of $B = 10\,\mathrm{T}$ in Voigt geometry for $\mathbf{k}$ along [111] and $\mathbf{B}$ along $[1\bar{1}0]$ in the H24 sample. (c) Polarization-dependent SHG intensity along tuning lines marked in panels (a) and (b) by the red and black lines. Symbols represent the experimental data and lines represent the simulation.

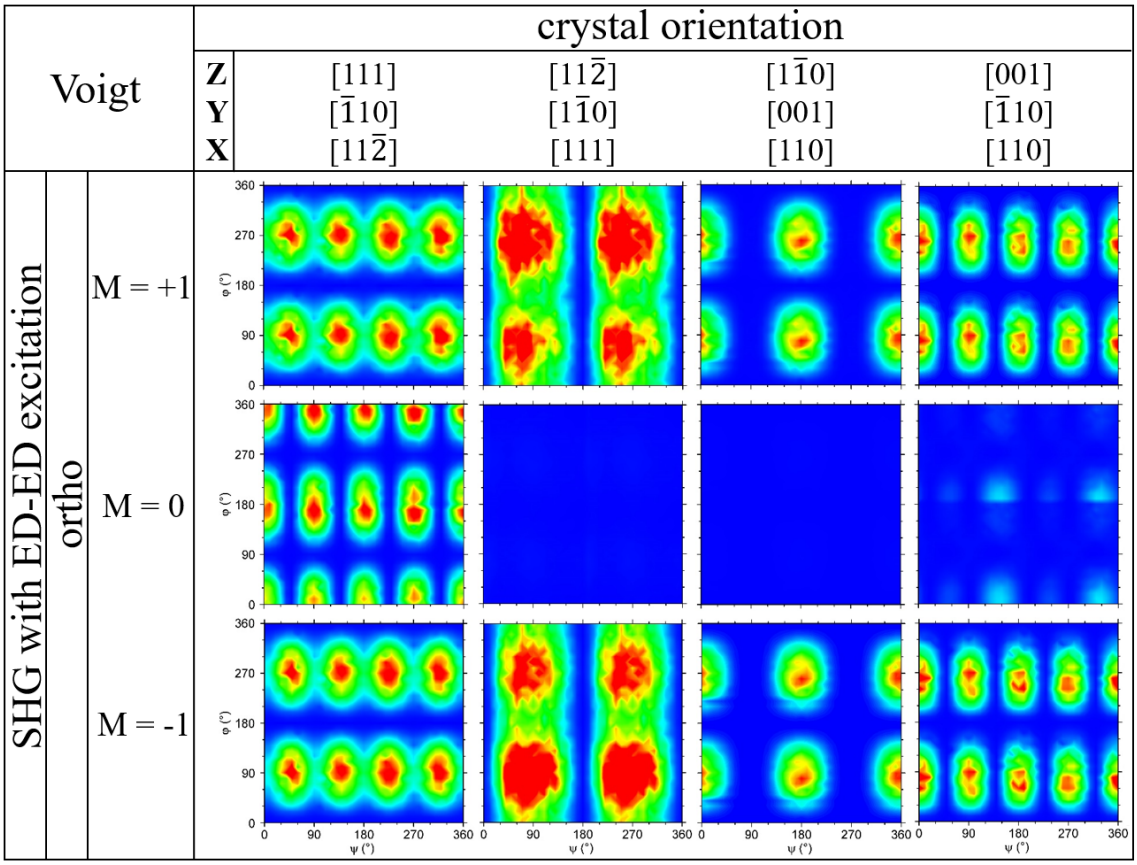

Figure 5.8 Experimental data of the 2D polarization diagrams of the $M = 1$, $M = 0$ and $M = -1$ orthoexciton states in a magnetic field of $B = 10\,\mathrm{T}$ in Voigt geometry for $\mathbf{k}$ the four different crystal axes [111], [11$\bar{2}$], [1$\bar{1}$0] and [001] in the H2a, H2b, H45b and H45a samples, respectively.

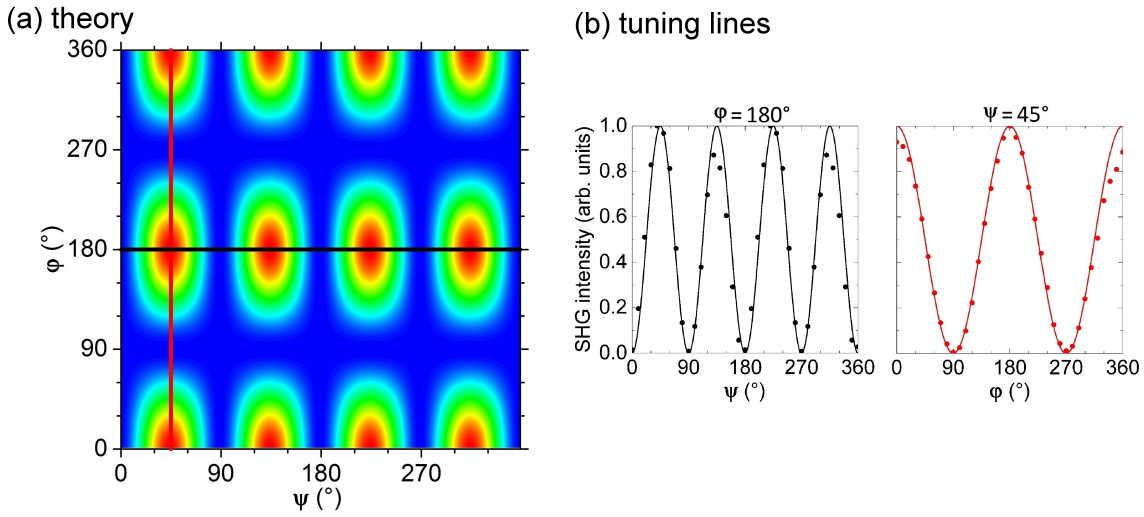

Figure 5.9 (a) 2D polarization diagrams of the simulation of the EQ-MD excitation SHG process according to Eq. (5.114) for the paraexciton in a magnetic field Voigt geometry for **k** along [001] and **B** along [110]. (b) Polarization-dependent intensity along the tuning lines marked in panel (a) by the red and black lines. Symbols represent the experimental data obtained in the H98 sample (see Tab. 3.1) and lines represent the simulation.

5.4 Magnetic-field dependent intensities

In Sec. 5.3, the polarization dependencies of three different optical processes addressing the paraexciton in a magnetic field in Voigt geometry are group-theoretically derived and experimentally demonstrated. In this section, we concentrate on the magnetic field-dependent increase of the intensity for the same processes as an additional method to distinguish between them.

As the magnetic field admixture of the ortho to the paraexciton represented by the parameter "a" grows linearly with increasing magnetic field, the oscillator strength grows quadratically. For the ED-ED TPA process the admixture is only needed once in the excitation channel and therefore the intensity is expected to grow with a power of two. For the ED-ED SHG process, the admixture is needed in the excitation and emission channel leading to a magnetic field-dependent increase of the SHG intensity with the fourth power. However, during the EQ-MD SHG process, the Γ_2^+ paraexciton is excited directly without the need for an admixture, which is only required in the emission channel. Therefore the SHG intensity will grow with the second power. Consequently, the two SHG mechanisms can be experimentally distinguished by the magnetic field-dependent intensity increase.

The experimental data are plotted in Fig. 5.10. The colored symbols represent the experimentally obtained data of the ED-ED SHG in red, the ED-ED TPA in blue and the EQ-MD SHG in green. The lines of the same color are the fits according to the power function $I(B, c, d) = c \cdot B^d$ with the scaling factor c and the power d. The black line visualizes a B^4 and the gray line a B^2 function for comparison as the experimental results deviate from the expected power growth. The magnetic-field-dependent ED-ED SHG intensity grows with a power of 3.71 ± 0.08 deviating only slightly from the expected power of 4 due to

inhomogeneity of the strain on the sample, as the laser spot moves during the time of the measurement over different sample spots due to temperature-dependent contraction of the sample rod. This effect can be reduced by adjusting the laser on a more homogeneous sample spot. The ED-ED TPA with a fitted growth power of 1.91 ± 0.04 does not deviate by much from the expected quadratic growth, as the TPA process is not strongly influenced by strain. The slight deviation might occur due to varying thickness or purity of the sample region. For the power parameter of the EQ-MD SHG process, the fit result is 2.5 ± 0.2, which might be due to a misalignment and therefore a contributing signal from the stronger ED-ED SHG mechanism. Nevertheless, the comparison of the growth parameters of both SHG processes shows a drastic difference and is therefore a good indication that the EQ-MD mechanism is experimentally demonstrated.

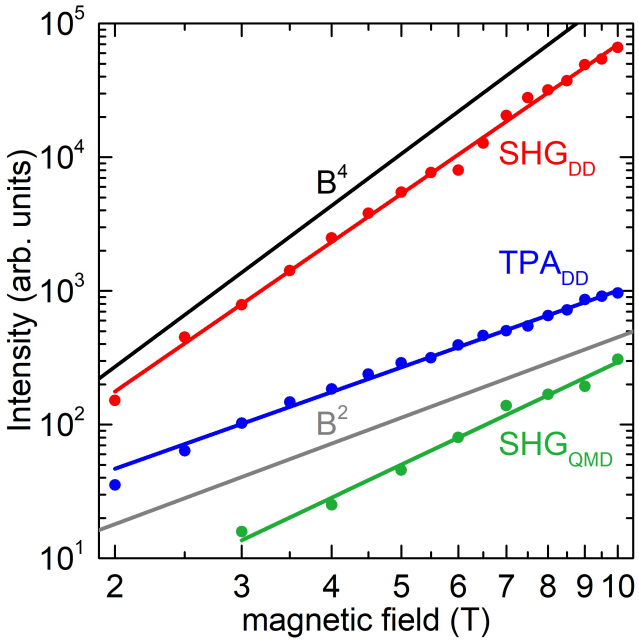

Figure 5.10 Magnetic field dependent intensity of the three discussed optical processes of the paraexciton in a double logarithmic diagram. Color symbols represent the experimental data for the ED-ED excitation SHG process (red), the ED-ED excitation TPA (blue) and the EQ-MD excitation SHG process (green) in the H24, H2b and H98 samples, respectively. The lines represent the fit with a power function according to $I(B, c, d) = c \cdot B^d$. The fit results for the power parameter d of the power function are 3.71 ± 0.08 for the ED-ED SHG, 1.91 ± 0.04 for the ED-ED TPA and 2.5 ± 0.2 for the EQ-MD SHG. The black line visualizes a B^4 and the gray line a B^2 function for comparison.

5.5 Rydberg series of paraexcitons

In the case of the $1S$ exciton, it is very clear to identify the paraexciton, as the ground state multiplet has only four states and is not interfering with any other spectral lines in this region. However, as already seen in Fig. 4.11, the spectral region of yellow Rydberg

excitons exhibits a significantly higher density of different exciton states. It is more difficult to find the weak features of Rydberg paraexcitons, as other more intense orthoexcitons dominate the SHG spectrum and might shift into higher adjacent multiplets. Therefore we need to establish the following criteria, by which we recognize and identify the Rydberg paraexcitons. i) S paraexcitons are single states of Γ_2^+ symmetry, which do not split into multiple states with increasing magnetic field. ii) Due to Hund's rules [Dem10] and the exchange interaction, which only applies to the orthoexcitons with spin-singlet components, the paraexciton is expected to be energetically located below the orthoexciton. iii) The magnetic-field-induced admixture from the optically active orthoexciton to the paraexciton leads to a nonlinear increase in SHG intensity and iv) to a quadratic repulsion with the orthoexciton to lower energies with increasing magnetic field.

For better recognition, we will plot the second derivatives of the SHG spectra in dependence on the magnetic field in a contour plot. As an example, we show the magnetic-field-dependent SHG spectra in the contour plot in Fig. 5.11. The four mentioned criteria above are easily recognized in this contour plot. The paraexciton emerges energetically below the orthoexciton and exhibits a nonlinear SHG intensity increase, a quadratic repulsion to lower energies and does not split into multiple states.

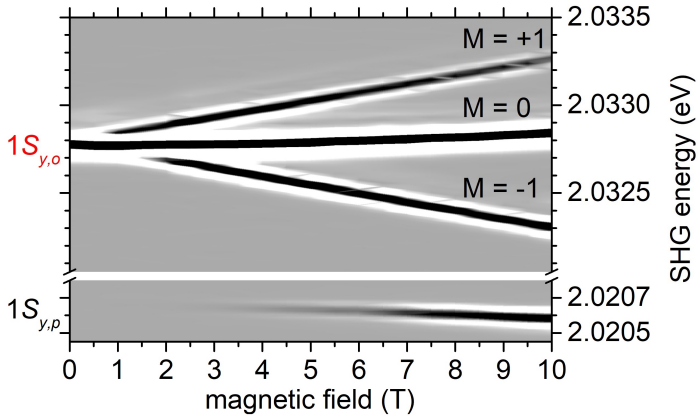

Figure 5.11 Second derivatives of SHG spectra in dependence of a magnetic field of 0 to 10 T in Voigt configuration in the spectral region of the $1S$ para- and orthoexciton states in the H24 sample (see Tab. 3.1) with $\mathbf{k}$ along the [111] and the magnetic field $\mathbf{B}$ along the $[1\bar{1}0]$ crystal axis. For the measurement of the paraexciton, the linear polarization angles are set to $\psi/\varphi = 45°/0°$. In order to detect all three orthoexciton states at once, the polarization angles are set to $\psi/\varphi = 45°/60°$.

5.5.1 $3S$ to $6S$ paraexcitons

Now we turn to the experimental results of the Rydberg S paraexcitons in the multiplets from $n = 3$ to 6. The double photon energy of the femtosecond laser is set to 2.164 eV, as shown in Fig. 4.12, and the SHG spectra are measured for magnetic fields between 0 and 7 T in steps of 0.25 T as described in Sec. 3.3. The second derivatives of the magnetic-field-dependent SHG spectra are shown in the contour plot of Fig. 5.12(a). At $B = 3$ T a single line emerges about 1.5 meV below the $3S$ orthoexciton, which exhibits a nonlinear increase in

intensity and a repulsion with the orthoexciton with increasing magnetic field. Fulfilling the four mentioned criteria, it is therefore identified as the $3S$ paraexciton. The same properties apply to the line emerging at $B = 2\,\mathrm{T}$ about 0.5 meV below the $4S$ orthoexciton and it is consequently labeled the $4S$ paraexciton. Checking the same criteria for the $n = 5$ multiplet, the $5S$ paraexciton is barely visible as a weak shoulder in this experimental configuration. Therefore we have chosen a different configuration, of which the experimental results from 0 to 10 T in steps of 0.2 T are shown in Fig. 5.12(b). The $3S$ and $4S$ paraexcitons are also recognizable in this contour plot and assigned accordingly. Additionally, at about $B = 1\,\mathrm{T}$ a single line appears below the $5S$ orthoexciton fulfilling the criteria and is therefore labeled as the $5S$ paraexciton. At about $B = 5\,\mathrm{T}$ it is already covered by the $4D$ exciton shifting into its spectral range. By zooming into the blue box covering the $n = 6$ multiplet, which is magnified in Fig. 5.12(c), the fourth derivative of the SHG spectra is shown to highlight the very weak feature of the $6S$ paraexciton emerging at about $B = 1\,\mathrm{T}$ but already being covered by the $5D$ exciton at 2 T. No clear experimental demonstrations could be achieved up to now of even higher n paraexcitons.

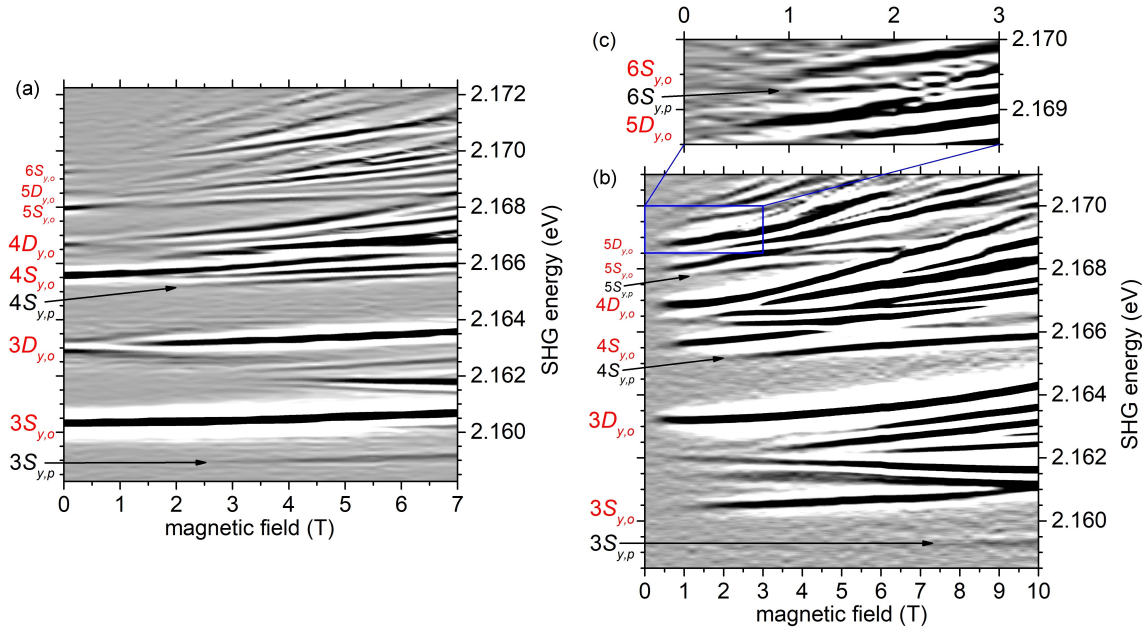

Figure 5.12 Second derivatives of SHG spectra in dependence of a magnetic field in Voigt configuration in the spectral region of the yellow Rydberg exciton states from the $n = 3$ multiplet to the band gap. The orthoexcitons are labeled with an index "o" and the paraexcitons with "p". (a) Experimental data between 0 and 7 T in steps of 0.25 T for $\mathbf{k} \parallel [111]$ and $\mathbf{B} \parallel [11\bar{2}]$ in the H2a sample (see Tab. 3.1). The linear polarization angles are set to $\psi/\varphi = 0°/0°$. (b) Experimental data between 0 and 10 T in steps of 0.2 T for $\mathbf{k} \parallel [1\bar{1}0]$ and $\mathbf{B} \parallel [110]$ in the H100 sample (see Tab. 3.1). The linear polarization angles are set to $\psi/\varphi = 0°/90°$. (c) Fourth derivative of the SHG spectra in the magnified region of the $n = 6$ multiplet marked by the blue box in panel (b).

5.5.2 Inversion of $2S$ para-ortho energetic order and green $1S$ paraexciton

In order to find the $2S$ paraexciton we choose the same experimental configuration as in Fig. 5.12(a), but set the doubled central photon energy of the femtosecond laser to the energy of the $2S$ orthoexciton and measure the SHG spectra for magnetic fields between 0 and 10 T in steps of 0.25 T. The experimental results are shown in Fig. 5.13(a). At about $B = 3$ T a single line emerges with a nonlinear SHG intensity increase exhibiting a repulsion with the $2S$ orthoexciton, which has to be identified as the $2S$ paraexciton. The striking difference to other multiplets is, that it violates criterion ii), as it is energetically located above its corresponding orthoexciton. Remarkably, this reversed energetic order has been predicted by the calculations of Schweiner et al. in Ref. [Sch+17b], in which they diagonalized the Hamiltonian of the yellow exciton series with all angular quantum numbers up to the $n = 5$ multiplet, although they did not discuss the ortho-para inversion for $n = 2$. The yellow exciton series is highly influenced by the green series due to the spin-orbit interaction between the two highest VBs. Therefore the green and yellow excitons are mixed, especially in the case of the adjacent $1S$ green and $2S$ yellow excitons. In Ref. [Sch+17b] the green part for each exciton state is even quantified as a percentage, which is also shown in Tab. 5.2. With this information, we can interpret the reason for the ortho-para inversion qualitatively with the sketched energy scheme in Fig. 5.13(b). Shown are the $2S$ and $3S$ excitons of the yellow and the $1S$ exciton of the green series. In the second column, the orthoexcitons are lifted up in energy due to the exchange interaction. The paraexcitons are basically not affected by the exchange interaction and remain therefore at the initial energy level. The crucial point is, that the exchange energy of the green $1S$ state is so large, that its orthoexciton is lifted up even above the yellow $2S$ orthoexciton. The last row represents the on-switch of the spin-orbit interaction leading to a mixing of yellow and green excitons and therefore to a repulsion between the green $1S$ exciton and the yellow excitons, which is stronger, the larger the mixing percentage of the other series.

The green part of the yellow $3S$ exciton is not negligible with 4.49% [Ref. [Sch+17b]] so it gets pushed slightly to higher energies. This effect becomes smaller for increasing n excitons, as the green part of the $4S$ is 1.53% and that of the $5S$ exciton is 0.81%. The green $1S$ exciton exhibits a strong mixing with yellow Rydberg excitons with its yellow part of 63.12%. The yellow $2S$ exciton has a large green part of 10.88%. It repels from the higher-lying $1S$ green exciton and gets strongly pushed even below its paraexciton, which is not largely influenced by the green-yellow mixing having a small green part of 1.43%. The ortho-para inversion is a rare case in semiconductor physics and has so far only been reported in ceasium lead halide perovskites due to the Rashba effect in Ref. [Bec+18].

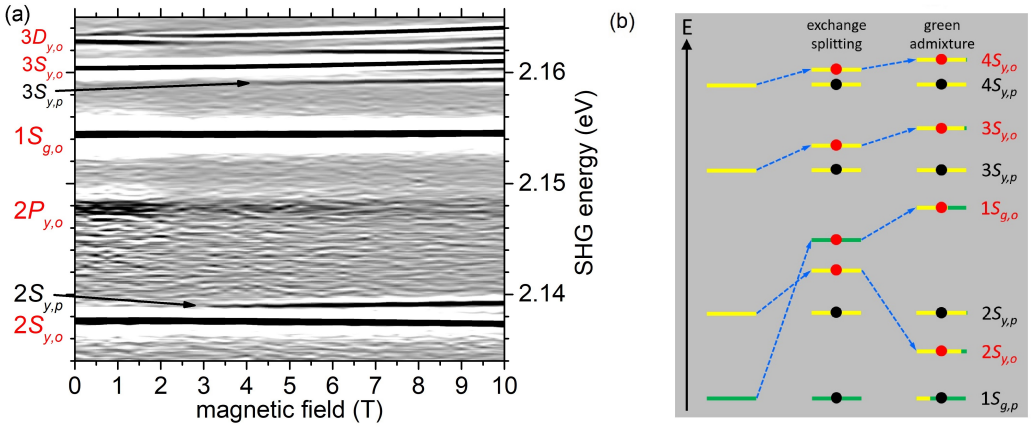

Figure 5.13 (a) Second derivatives of SHG spectra in dependence of a magnetic field between 0 and 10 T in steps of 0.25 T in Voigt configuration in the spectral region of the yellow $2S$ and $3S$ excitons for $\mathbf{k} \parallel [111]$ and $\mathbf{B} \parallel [11\bar{2}]$ in the H2a sample (see Tab. 3.1). The linear polarization angles are set to $\psi/\varphi = 0°/0°$. The orthoexcitons are labeled with an index "o" and the paraexcitons with "p". (b) Energy level scheme including the $2S$ and $3S$ excitons of the yellow and the $1S$ exciton of the green series (first column). In the second column, the exchange interaction is switched on leading to the orthoexcitons being elevated to higher energies. Note, that the $1S$ green orthoexciton is elevated above the $2S$ orthoexciton, due to the large exchange energy. In the third column, the green-yellow mixing is activated leading to a repulsion of the $1S$ green exciton with both the $2S$ and $3S$ excitons. Note, that the $2S$ ortho exciton is pushed below its paraexciton leading to an unexpected inversion of the ortho-para energetic order. Red circles indicate optically active orthoexcitons and black circles mark the optically inactive paraexcitons. The yellow and green coloring of the energy level bars indicates the strength of green-yellow mixing, which is listed in Tab. 5.2 and taken from Ref. [Sch+17b].

As Ref. [Sch+17b] predicted the ortho-para inversion correctly and also provides information about the energy of the green $1S$ paraexciton, we perform the experiment for its detection. According to Ref. [Sch+17b], the green $1S$ paraexciton lies 30.8 meV below its orthoexciton, which is significantly larger than the exchange splitting energy of about 12 meV of the yellow $1S$ exciton. We applied a magnetic field of 10 T in Voigt configuration and directed the laser along the $[1\bar{1}0]$ crystal axis with a doubled central photon energy of the expected paraexciton and measured the SHG spectrum shown in Fig. 5.14. A weak double-peak feature is detected for integration times of 30 minutes about 29 meV below the $1S$ green orthoexciton, which we assign to the $1S$ green paraexciton. Unlike the yellow S paraexcitons with a single Γ_2^+ state, the green S paraexcitons have multiple states with $\Gamma_3^+(2) \oplus \Gamma_4^+(3)$ symmetry, indicated by the double peak structure.

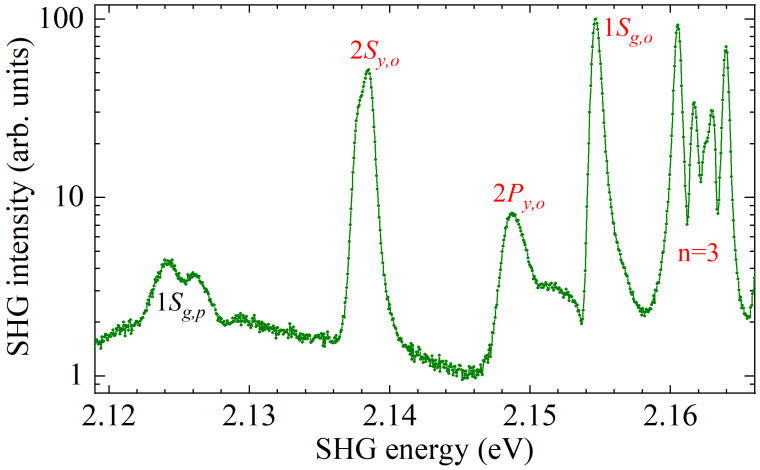

Figure 5.14 SHG spectrum in the energy range between the green $1S$ paraexciton and the yellow $n = 3$ multiplet at $B = 10\,\mathrm{T}$ in Voigt configuration for $\mathbf{k} \parallel [1\bar{1}0]$ and $\mathbf{B} \parallel [001]$ in the H13 sample (see Tab. 3.1). The linear polarization angles are set to $\psi/\varphi = 45°/0°$. The $1S$ green paraexciton appears as a weak doublet peak about 29 meV below its orthoexciton. Note the logarithmic SHG intensity scale.

In conclusion, we have detected the Rydberg series of yellow S paraexcitons up to a quantum number of $n = 6$ and the green $1S$ paraexciton using SHG spectroscopy in a magnetic field in Voigt configuration of up to 10 T.

5.5.3 n-dependent energy splitting

Now we take a look at the splitting energy Δ_n of the yellow S excitons as a function of the principle quantum number n. The ortho- and paraexciton lines in the second derivatives of the SHG spectra are fitted by Gaussians for each magnetic field and the central energy of each Gaussian is taken as the magnetic-field-dependent energy for each line. The magnetic field shift of each line is fitted by a quadratic function to extrapolate to the zero-field energy. The experimental results of the zero-field energy splittings of ortho- and paraexcitons are plotted as open squares in Fig. 5.15 in dependence of n. Note the axis break in the energy axis. The uncertainty of the parabolic fit of the magnetic-field-dependent energy is represented by the error bars. The n dependent exchange splitting in the hydrogen model is proportional to the square of the wave function for zero distance between both charged particles $|\Psi_X(0)|^2$ and scales with n^{-3}. We apply this fit to our experimental results but exclude the $1S$ exciton splitting, as it is additionally affected by the central cell correction, see Ref. [Sch+17b]. We also exclude the $2S$ exciton splitting, as it is majorly affected by the yellow-green mixing resulting in its reversed energetic ortho-para order assigned with a negative splitting energy. We get a reasonable fit for $n \geq 3$ as shown by the red line, although the energy splitting is also highly influenced by the green-yellow mixing due to the spin-orbit interaction between the involved VBs, resulting in a repulsion of the yellow states with the green $1S$ exciton. A detailed theoretical follow-up investigation is done by Rommel et al. in Ref. [Rom+21], in which they could isolate the effects of different types of inter-

actions and calculate the n scaling of the energy splitting for different cases, e.g. without the green-yellow mixing. The full circles in Fig. 5.15 represent the theoretically calculated ortho-para energy splittings taken from Ref. [Sch+17b], which predate our experimental investigations and show a remarkable agreement with our results. The experimentally obtained results for the resonance energies and the ortho-para splitting energies are listed in Tab. 5.2 and compared to the corresponding calculated values from Ref. 5.2.

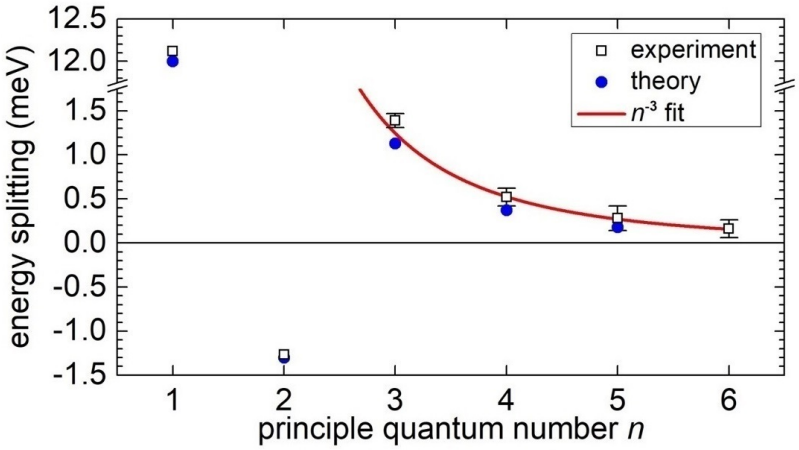

Figure 5.15 Energy splitting between ortho- and paraexcitons as a function of the principal quantum number n for yellow S excitons up to $n = 6$. The squares represent the experimental data evaluated from Figs. 5.11, 5.12 and 5.13. The full blue circles are the theoretically calculated splitting energies taken from Ref. [Sch+17b]. The red line is a $E_{\text{exch.}} = a \cdot n^{-3}$ fit to the experimental data starting from $n = 3$. Note the break of the exchange energy axis.

5.6 Conclusion

In this chapter, we have presented a study on SHG of paraexcitons in Cu_2O under the influence of a magnetic field in Voigt configuration. From magnetic field dependent SHG spectra of the $1S$ paraexciton and $M = 0$ and $M = \pm 1$ orthoexciton states, which are measured with resolutions as low as 10 µeV, the g factors of the highest VB and lowest CB are derived and the exchange energy is determined. The results are compared to previous publications.

The SHG mechanisms of the magnetic-field coupled $1S$ para- and orthoexciton states, including SHG by ED-ED and EQ-MD excitation, are experimentally demonstrated by deriving the SHG polarization rules, simulating the polarization dependence diagrams for various crystal orientations and comparing the simulated results to experimentally obtained data for chosen experimental geometries.

The SHG mechanism by EQ-MD excitation is demonstrated by its quadratic dependence of the SHG intensity on the magnetic field, which differs from the ED-ED excitation SHG, which increases with the fourth power.

The mentioned properties are tested on the ground state exciton and applied for the

Table 5.2 Experimental results for the resonance energies of yellow series ortho- and paraexcitons and their energy splitting Δ_n as a function of the principle quantum number up to $n = 6$. The analogous theoretical results from Ref. [Sch+17b] are shown for comparison up to $n = 5$. Additionally, the green content (GC) is given in the third column.

state	symmetry	GC (%)	E_{theo} (eV)	$\Delta_{n,\text{theo}}$ (meV)	E_{exp} (eV)	$\Delta_{n,\text{exp}}$ (meV)
$1S_{y,p}$	Γ_2^+	5.49	2.0200	12	2.02065	12.12
$1S_{y,o}$	Γ_5^+	7.22	2.0320		2.03277	
$1S_{g,p}$	$\Gamma_{3,4}^+$	71.62	2.1245	30.8	2.1241	30.3
					2.1262	28.2
$1S_{g,o}$	Γ_5^+	36.88	2.1553		2.1544	
$2S_{y,p}$	Γ_2^+	1.43	2.1412	-1.3	2.13898	-1.27
$2S_{y,o}$	Γ_5^+	10.88	2.1399		2.13771	
$3S_{y,p}$	Γ_2^+	0.48	2.15967	1.13	2.15906	1.39
$3S_{y,o}$	Γ_5^+	4.49	2.16080		2.16045	
$4S_{y,p}$	Γ_2^+	0.21	2.16547	0.37	2.16503	0.52
$4S_{y,o}$	Γ_5^+	1.53	2.16584		2.16555	
$5S_{y,p}$	Γ_2^+	0.10	2.16798	0.18	2.16766	0.28
$5S_{y,o}$	Γ_5^+	0.81	2.16816		2.16794	
$6S_{y,p}$	Γ_2^+	-	-	-	2.16919	0.16
$6S_{y,o}$	Γ_5^+	-	-		2.16935	

demonstration of the Rydberg series of paraexcitons. We have found the yellow S paraexciton states up to a quantum number of $n = 6$ and the green $1S$ paraexciton. The para-ortho order for the $2S$ exciton is observed to be reversed, which is explained by the spin-orbit interaction of the involved VBs leading to mixing and therefore to a repulsion between the yellow Rydberg states and the $1S$ green exciton. The zero-field splitting energies between ortho- and paraexcitons are obtained from the magnetic field series of SHG spectra and compared to the calculations of Schweiner et al. [Sch+17b]. It is found that for $n \geq 3$, the splitting energies are in agreement with a n^{-3} scaling as expected from the hydrogen model, although other interactions lead to deviations, which are discussed in great detail in Ref. [Rom+21].

The demonstrated method can be applied to other semiconductors. Kapuściński et al. have recently demonstrated the Rydberg series of dark excitons in monolayer WSe_2 in a magnetic field of up to 30 T [Kap+21].

With a higher spectral resolution, smaller magnetic field increments and lower excitation powers, it is in principle possible to extend the Rydberg series of paraexciton to higher n. Paraexcitons with higher angular momentum quantum numbers do also exist. But their exchange splitting is close to zero, which complicates their detection. An exception are D excitons, of which the orthoexcitons are energetically elevated by the yellow-green mixing with the $1S$ green exciton leading to an energy splitting between the ortho- and para states. The fine structure of D excitons has recently been studied by Heckötter et al. [Hec+21].

Chapter 6

SHG spectroscopy of blue-series excitons

Blue-series excitons involve a hole in the same Γ_7^+ VB as yellow-series excitons. However, the electron is excited to the second lowest CB with Γ_3^- symmetry, which originates from Cu $4p$ orbitals, as shown in Fig. 2.3. Taking the electron spin into account leads to a Γ_8^- symmetry for the conduction band, which is divided into two anisotropic subbands exhibiting different curvatures. Violet-series excitons involve the same CB as blue-series excitons but the second highest Γ_8^+ VB like the green excitons. In contrast to yellow and green excitons, optical transitions to blue and violet-series excitons are ED-allowed, leading to high oscillator strengths. The oscillator strength density of blue excitons is with a value of $\beta_b = 2.93 \times 10^{-3}$ [Dau+66] about seven orders of magnitude larger than the value $\beta_y = 3.1 \times 10^{-10}$ [Frö+06] for yellow excitons, which leads to strong light-matter coupling and therefore requires to take polaritonic effects into consideration. In contrast to yellow-series excitons, which lie energetically below the bandgap, the blue-series excitons are subject to high optical absorption as they are energetically above the yellow and green band gaps.

The high absorption is the reason why single-photon transmission experiments lead to many difficulties for blue-series excitons. The first experiments were done by the method of one-photon reflection in Ref. [Pas61] and only very broad spectral features of blue excitons could be observed. The first single-photon transmission experiments have been made possible by very thin samples in the order of 100 nm of oxidized copper by Daunois et al. in Ref. [Dau+66]. Due to the high strain in these samples, the excitonic spectral features were split and shifted to higher energies. The group of N. Naka recently performed photoluminescence experiments, as described in Ref. [Tak+18], by exciting above the violet bandgap. The $1S$ and $2S$ of the blue series could be detected. Nonlinear optical experiments have been performed before by Schmutzler et al. [Sch+13] using sum-frequency generation involving a resonant EQ transition to the yellow $1S$ exciton and a further ED transition to the blue $1S$ exciton-polariton.

Considering the described difficulties, it becomes evident that SHG is an exceptionally suitable method for experimental investigations of blue-series excitons. High-quality natural bulk crystals of various thicknesses can be used as the fundamental beam passes through the whole sample without significant losses. Although the SHG signal, which is generated along the whole thickness, gets strongly absorbed, the signal of the last few nm can escape the sample and be detected. Picosecond pulses, which can be scanned spectrally through the energy range of blue-series excitons as described in Sec. 3.2, offer a sufficient resolution for the rather broad resonance lines. As SHG is sensitive to changes of the involved symmetries, variation of the crystal orientations and application of magnetic fields will offer several degrees of freedom to study different crystallographic and magnetic-field-induced

SHG mechanisms and uncover key properties of blue-series excitons.

In Sec. 6.1, we calculate the quasi-particle solutions for excitons up to $n = 4$ taking the polariton effect into consideration. Then we derive the polarization dependencies for crystallographic and magnetic-field-induced SHG in Sec. 6.2. In Sec. 6.3, experimental data on all derived SHG mechanisms will be shown for excitation along the symmetry-allowed crystal axis [111]. All SHG spectra are measured with an average ps laser excitation power of about 100 mW. Section 6.4 deals with experimental results, which involve excitation along the symmetry forbidden $[1\bar{1}0]$ crystal axis enabling the suppression of crystallographic SHG. In the chosen crystal orientation, the three relevant magnetic-field-induced SHG mechanisms, including the ZE effects of Γ_4^- and Γ_5^+ states and the MSE can be individually switched on by certain polarization settings of incoming and outgoing light, which will enable measuring the SHG spectra of the $1S$ and $2S$ exciton-polaritons and the $2P$ exciton. By analyzing the magnetic field shifts of $n \leq 2$ exciton resonances in Sec. 6.4.1 and $n \geq 3$ magneto-excitons in high-field regime in Sec. 6.5, several key parameters of blue-series excitons such as the anisotropic effective electron mass, the reduced exciton mass, the exciton Bohr radius and the transverse resonance energies as well as the resonance energies on the upper polariton branch will be obtained. The results of this chapter are published in Ref. [Far+21].

6.1 Polaritonic effect

In this section, we will briefly derive the quasi-particle solution for the blue series exciton-polariton dispersion relation up to $n = 4$, which will expand our understanding of the experimentally obtained results. The calculations have been done by H. Stolz and are described in more detail in Refs. [Far+21; Sto+18]. In order to obtain the exciton-polariton dispersion, one has to solve the classical polariton equation [And95]

$$\frac{c_0^2 K^2}{\omega^2} = \varepsilon(\mathbf{K}, \omega) = \varepsilon_b + \sum_{n=1}^{N} \frac{4\pi\beta_n E_{Xn}^2(\mathbf{K})}{E_{Xn}^2(\mathbf{K}) - (\hbar\omega)^2 - i\hbar\omega\gamma_n}. \tag{6.115}$$

for a fixed $\mathbf{K}$ and not a fixed photon energy. c_0 is the vacuum speed of light, $\mathbf{K}$ the exciton wavevector, ω the frequency, ε the dielectric function, ε_b the background dielectric constant, n the principal quantum number, β_n the oscillator strength density, $E_{Xn}(\mathbf{K})$ the transverse exciton energy dispersion and γ_n the homogeneous broadening. For the latter we use a small letter γ in order to avoid confusion with irreducible representations. By applying the rotating-wave approximation

$$E_X^2 - (\hbar\omega)^2 = 2E_X(E_X - \hbar\omega), \tag{6.116}$$

Eq. (6.115) is simplified to

$$\varepsilon(\mathbf{K}, \omega) = \varepsilon_b + \sum_{n=1}^{N} \frac{2\pi\beta_n E_{Xn}(\mathbf{K})}{E_{Xn}(\mathbf{K}) - \hbar\omega - i\frac{\gamma_n}{2}}. \tag{6.117}$$

The background dielectric constant ε_b measured in Ref. [Ito+98] and shown in Fig. 6.1(a) by black dots, is approximated using the Sellmeier equation

$$\varepsilon_b(E) = 4.202 + \frac{2.564}{1 - \left(\frac{E[\mathrm{eV}]}{3.166}\right)^2}, \tag{6.118}$$

which is shown by the red line in Fig. 6.1(a). It gives a good approximation for energies lower than 2.65 eV. The dispersion relation of blue-series excitons unperturbed by the light field is given by

$$E_{Xn}(\mathbf{K}) = E_{0,n} + \frac{\hbar^2}{2M_n}\mathbf{K}^2, \tag{6.119}$$

with the transverse exciton energy $E_{0,n}$ at $\mathbf{K} = 0$ and the total exciton mass M_n. The oscillator strength density reads

$$\beta_n = \frac{\hbar^2 e^2}{4\pi\varepsilon_0 m_0 E_{Xn}^2}\frac{f_n}{V}, \tag{6.120}$$

with the electron charge e and mass m_0, the vacuum permittivity ε_0, the oscillator strength f_n and the volume of the unit cell V. The best agreement with our experiments is achieved with a value for $\beta_{1SB} = 3.77 \times 10^{-3}$, which is close to the average of the literature values of $\beta_{1SB} = 2.93 \times 10^{-3}$ from Ref. [Dau+66] at $T = 4.2\,\mathrm{K}$ and $\beta_{1SB} = 4.93 \times 10^{-3}$ from Ref. [Ito+98] at room temperature. The values for higher n are obtained by extrapolation using the n scaling

$$\beta_{n,S} = \beta_{1S}/n^3. \tag{6.121}$$

as expected from the hydrogen model. The values for the damping are determined by the empirical law

$$\gamma_n = \frac{13.9}{n}\,\mathrm{meV}, \tag{6.122}$$

which gives a good agreement with the experimentally obtained values for the line width of 13.3 meV for the $1S$ and 7.6 meV for the $2S$ exciton-polariton and extrapolates to higher n.

The splitting between the longitudinal and transverse exciton states is given by

$$\Delta E_{\mathrm{LT},n} = \frac{\hbar^2 e^2}{2\varepsilon_0\varepsilon_b m_0 E_{Xn}}\frac{f_n}{V}, \tag{6.123}$$

and is related to the oscillator strength density. All relevant parameters for the calculation of the exciton-polariton dispersion are summarized in Table 6.1 up to $n = 4$.

As the blue-series excitons are in close energetic proximity, their contribution to the dielectric function has to be considered. Their binding energies are given by

$$E_{\mathrm{bind},n} = \frac{1}{n^2}\frac{\mu_X}{\tilde{\varepsilon}(E_{\mathrm{bind},n})^2}E_{\mathrm{Ryd}}^{\mathrm{H}}, \tag{6.124}$$

with the hydrogenic Rydberg energy $E_{\mathrm{Ryd}}^{\mathrm{H}}$ and the dielectric function $\tilde{\varepsilon}(E)$, which is influenced by optical phonons and can be calculated according to Ref. [Sto+18]

$$\tilde{\varepsilon}(E) = \tilde{\varepsilon}_b \prod_i \frac{(E_{\mathrm{LO,i}}^2 - E^2)}{(E_{\mathrm{TO,i}}^2 - E^2)}, \tag{6.125}$$

Table 6.1 Relevant parameters for the calculation according to Eq. (6.117) of the exciton-polariton dispersion up to $n = 4$ (first column) as shown in Figs. 6.1(b), 6.1(c) and 6.1(d). The exciton binding energies are calculated using Eq. (6.124) and shown in the second column. The dielectric constants in the third column are obtained using Eq. (6.125) The fourth column lists the dampings as calculated according to Eq. (6.122). The fifth column gives the values for the oscillator strength density, which are calculated according to Eq. (6.121). The longitudinal-transverse energy splittings are shown in the last column and are obtained via Eq. (6.123).

n	$E_{\mathrm{bind},n}$ (meV)	$\tilde{\varepsilon}(E_{\mathrm{bind},n})$	γ_n (meV)	β_n	$\Delta E_{\mathrm{LT},n}$ (meV)
1	53.30	7.63	13.9	3.768×10^{-3}	3.93
2	13.35	7.62	7.64	4.582×10^{-4}	0.491
3	6.29	7.41	4.16	1.351×10^{-4}	0.146
4	3.56	7.38	2.70	5.689×10^{-5}	0.061

using $\tilde{\varepsilon}_b = 6.53$ and the following phonon energies:

$$E_{\mathrm{TO},1} = 18.8\,\mathrm{meV}, \qquad E_{\mathrm{LO},1} = 19.1\,\mathrm{meV}, \tag{6.126}$$

$$E_{\mathrm{TO},2} = 78.5\,\mathrm{meV}, \qquad E_{\mathrm{LO},2} = 82.1\,\mathrm{meV}. \tag{6.127}$$

The best agreement with the experimental values for the resonance energies is achieved for a reduced exciton mass of $\mu_X = 0.228\,m_0$, which leads to a binding energy of 53.30 meV.

The results of the quasi-particle solution for the blue series exciton-polariton dispersion are shown in Fig. 6.1(b) and magnified in panel Fig. 6.1(c). The lower polariton branch (LPB) converges to the photon dispersion line, as marked by the dashed nearly vertical line, for lower K and approaches the dispersion of the $1S_T$ exciton for higher K. The upper polariton branch (UPB) converges to the photon dispersion line for higher K and approaches the dispersion of the highest exciton state for lower K. The intermediate polariton branches approach the next lower exciton dispersion for decreasing values of K and the next higher exciton dispersion for increasing K.

A sharp K excitation via the SHG process occurs at the intersection points of the polariton branches and the two-photon dispersion line, which is marked by the gray nearly vertical line at around $K = 3.5 \times 10^7\,\mathrm{m}^{-1}$ and described by

$$E(k) = \frac{c}{n_b(\frac{E}{2})}\hbar k. \tag{6.128}$$

The dots are the experimentally obtained values for the resonance energies, as presented in Sec. 6.4, and have a good agreement with the polariton calculation, as they lie on the dispersion lines (same color as dots) of the corresponding states. It shows that the excitation of the $1S$ exciton-polariton via the SHG process occurs at about 10 meV above the transverse state $1S_T$ of the $n = 1$ exciton. The $2S$ exciton dip in the crystallographic SHG spectrum shown in Fig. 6.6(a) can therefore not correspond to the $2S$ energy, as it is about 3 meV higher than the $2S$ exciton-polariton energy. However, it can be explained as an interference process between the $1S$ and $2S$ SHG signals.

Figure 6.1(c) shows the calculated K dependent radiative damping of the exciton-polariton states, which can be experimentally accessed by measuring the line width of the resonances.

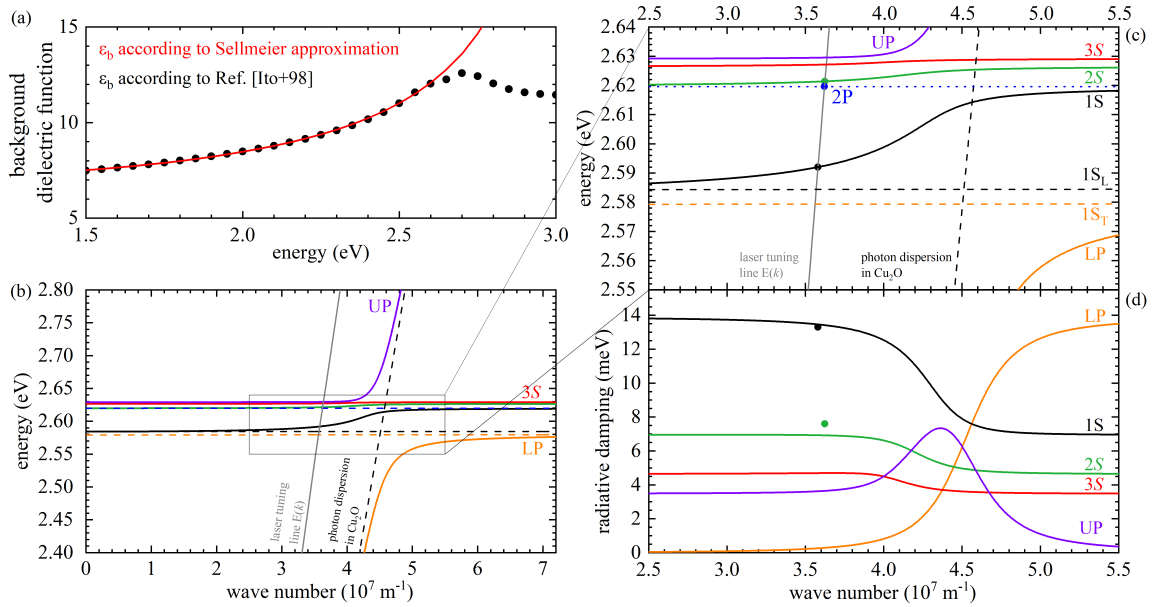

Figure 6.1 (a) Background dielectric constant as measured in Ref. [Ito+98] (black dots) and approximated using the Sellmeier approximation (6.118) (red line). (a) Quasi-particle solution for the blue series exciton-polariton dispersion up to $n = 4$. The lower polariton (LP), shown as the orange line, approaches the photon dispersion in Cu_2O (nearly vertical black dashed line) for decreasing wave numbers and the transverse exciton dispersion for higher K. The upper polariton (UP), shown as the violet line on the high energy side, converges to the photon dispersion for higher K and the $n = 4$ exciton dispersion for decreasing K. The relevant energy and wave number range is magnified in panel (c) and all polariton branches are designated. The colored dots mark the intersection points between the two-photon excitation dispersion and the polariton dispersion, at which a sharp K excitation via the SHG process occurs. Panel (c) shows the K dependent damping of all polariton branches as solid lines. The colored dots are the experimentally obtained line widths from the SHG spectra in Fig. 6.8.

The measured results for the line widths are extracted from the magnetic-field-induced SHG spectra in Fig. 6.8(a) and 6.8(c), shown as colored dots, which have a decent agreement with the calculations, as they only slightly deviate from the expected positions on the colored lines.

As the last point, we want to justify the performed calculations by showing that the necessary criteria for the formation of polaritons with a distinct wave vector are fulfilled. In general, there are two cases. The first case is called the forced harmonics case and applies if the condition

$$\gamma < \sqrt{\frac{8\Delta E_{\mathrm{LT}}\varepsilon_b}{M_X c^2} E_X^2(0)} \tag{6.129}$$

for spatial coherence is fulfilled.

The second case is called the quasi-particle case, which is present if temporal coherence

is fulfilled. For this, the Rabi energy

$$\hbar\Omega_R = \sqrt{\frac{\Delta E_{\mathrm{LT}} E_X(0)}{2}} \tag{6.130}$$

needs to be larger than the damping. In our experiments, the second case is fulfilled, as the Rabi energy of about 70 meV is significantly larger than the homogeneous broadening of about 13 meV.

6.2 Simulation of polarization dependencies

It is not necessary to derive the polarization-dependent SHG intensity for blue excitons from the start. We will show below that the main optically active symmetry component of blue S exciton is the same as for yellow P excitons and vice versa. Then we just access the already derived polarization dependencies for yellow excitons in Sec. 4.1.

According to Eq. (4.50) and the involved Γ_7^+ VB and Γ_8^- CB depicted in Fig. 2.3(c), the symmetry of blue S excitons is given by

$$\begin{aligned} \Gamma_{S,\,\mathrm{blue}} &= \Gamma_7^+(2) \otimes \Gamma_8^-(4) \otimes \Gamma_1^+(1) \\ &= \Gamma_3^-(2) \oplus \Gamma_4^-(3) \oplus \Gamma_5^-(3), \end{aligned} \tag{6.131}$$

with the main optically active component exhibiting Γ_4^- symmetry and therefore having a commonality with yellow P excitons. Analogously, the symmetry of blue P excitons is given by

$$\begin{aligned} \Gamma_{P,\,\mathrm{blue}} &= \Gamma_7^+(2) \otimes \Gamma_8^-(4) \otimes \Gamma_4^-(3) \\ &= \Gamma_1^+(1) \oplus \Gamma_2^+(1) \oplus 2\Gamma_3^+(2) \oplus 3\Gamma_4^+(3) \oplus 3\Gamma_5^+(3), \end{aligned} \tag{6.132}$$

with the main optically active component exhibiting Γ_5^+ symmetry, similar to yellow S excitons.

The dominant crystallographic mechanisms for blue S and P excitons are shown in Figs. 6.2(a) and 6.2(b), respectively. Blue S excitons are excited by an ED-EQ two-photon process [Eq. (4.69)] and emit light by ED emission [Eq. (4.59)] leading to the polarization-dependent SHG intensity according to Eq. (4.70). SHG of blue P excitons involves an ED-ED two-photon excitation [Eq. (4.64)] and an EQ emission [Eq. (4.69)] resulting in the polarization-dependent SHG intensity derived in Eq. (4.65).

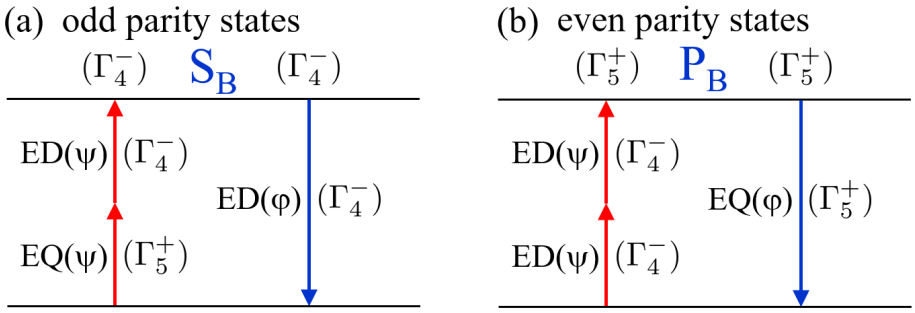

Figure 6.2 Schematics of crystallographic SHG mechanisms for blue-series excitons. (a) Odd-parity Γ_4^- S excitons excited by an ED-EQ two-photon process followed by an ED emission. (b) Even-parity Γ_5^+ P excitons excited by an ED-ED two-photon process followed by an EQ emission.

The magnetic-field-induced SHG mechanisms are sketched in Fig. 6.3. The dominant MSE mechanism [Fig. 6.3(a)] is the same as in the case of the yellow excitons and is thus indicated in Eq. (4.87). It involves an ED-ED excitation of P excitons, which are coupled by an odd-parity effective electric field to S excitons [Eq. (4.86)], which emit light by ED emission. We name the product of the mentioned operators $O_{\mathrm{DD}}^{5+E4-} \cdot O_{\mathrm{D}}^{4-} = O_{\mathrm{MSE}}$.

As blue Γ_4^- S excitons have a higher oscillator strength compared to their P counterparts, the dominant ZE is not the same as for yellow-series excitons. In the case of blue-series excitons the dominant ZE involves ED-EQ excitation of Γ_4^- states, which are coupled by an even-parity magnetic field again to Γ_4^- states [Eq. (4.75)]. Its SHG polarization dependence is given in Eq. (4.76) and sketched in Fig. 6.3(b). The product of the mentioned excitation and emission operators is denoted by $O_{\mathrm{DQ}}^{4-B4-} \cdot O_{\mathrm{D}}^{4-} = O_{\Gamma_4^-\mathrm{ZE}}$.

The dominant ZE of yellow-series excitons, as given in Eq. (4.74) and sketched in Fig. 6.3, contributes only weakly for blue-series excitons. It involves ED-ED excited and magnetic-field coupled Γ_5^+ states [Eq. (4.73)], which emit light by an EQ process. The product of the mentioned excitation and emission operators is denoted by $O_{\mathrm{DD}}^{5+B5+} \cdot O_{\mathrm{Q}}^{5+} = O_{\Gamma_5^+\mathrm{ZE}}$.

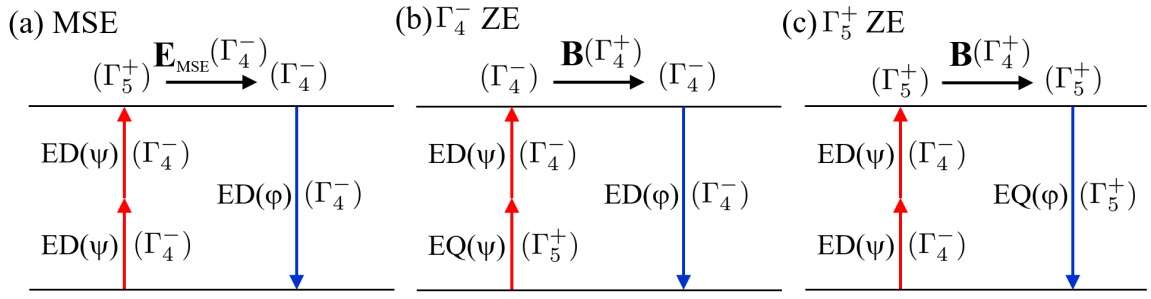

Figure 6.3 Schematics of magnetic-field-induced SHG mechanisms for blue-series excitons. (a) MSE involving excitation of Γ_5^+ P states and emission from Γ_4^- S states. (b) Dominant ZE of Γ_4^- S states. (c) Weak ZE of Γ_5^+ P states.

For our experiments presented in Secs. 6.3 and 6.4 we will use two samples with different orientations. In Sec. 6.3, we perform SHG experiments in the H2a sample (see Tab. 3.1),

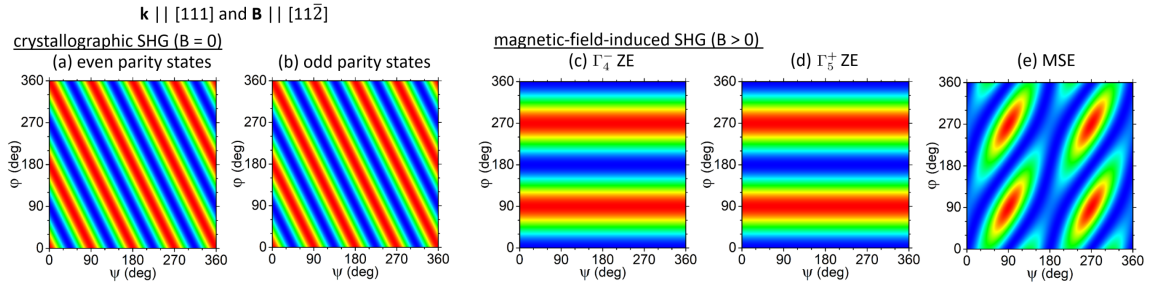

Figure 6.4 Simulation of 2D SHG polarization diagrams of blue-series excitons for excitation along the **k** ∥ [111] and an applied magnetic field along the [11$\bar{2}$] crystal axis. Crystallographic SHG of (a) S and (b) P states as sketched in Fig. 6.2. (c) Γ_4^- ZE, (d) Γ_5^+ ZE and (e) MSE as sketched in Fig. 6.3.

which is symmetry-allowed for crystallographic SHG as **k** is directed along the [111] crystal axis. The 2D polarization diagrams for the relevant SHG mechanisms from Figs. 6.2 and 6.3 are shown in Fig. 6.4. The polarization diagrams for the crystallographic SHG processes of blue S and P excitons are identical, exhibiting diagonal stripes resulting in a sixfold symmetry for the parallel and crossed polarization configurations. The ZE-induced SHG polarization diagrams of blue Γ_4^- and Γ_5^+ states are also identical with a twofold symmetry along φ and constant along ψ. The MSE-induced SHG polarization diagram is irregularly fourfold along ψ and twofold along φ.

In Sec. 6.4, we perform SHG experiments in the H45b sample (see Tab. 3.1), which is symmetry-forbidden for crystallographic SHG as **k** is directed along the [1$\bar{1}$0] crystal axis. The 2D polarization diagrams for the relevant SHG mechanisms from Figs. 6.2 and 6.3 are shown in Fig. 6.5. The polarization diagrams for the crystallographic SHG processes of blue S and P excitons show vanishing SHG for both, blue S and P excitons as expected for a symmetry-forbidden orientation. The ZE-induced SHG polarization diagrams of blue Γ_4^- and Γ_5^+ states show a twofold symmetry along ψ and φ but differ by a 90° shift in ψ and are therefore distinguishable. The MSE-induced SHG polarization diagram is fourfold along ψ and twofold along φ. All three mechanisms can be individually isolated by a specific choice of the polarization setting: For $\psi = 90°$ only the Γ_4^- ZE, for $\psi = 0°$ only the Γ_5^+ ZE and for $\varphi = 0°$ only the MSE induces an SHG contribution. This property will be exploited in Sec. 6.4 in order to measure SHG spectra induced by just one mechanism.

For the magnetic-field-induced SHG signals, the general case of interference will be needed. To have a closer connection to the experiments, the amplitudes are scaled to the SHG signal magnitude and not to the group theoretical magnitude resulting from the coupling coefficient tables so that one can extract the relative SHG contributions for each mechanism from the interfered signal. The SHG intensity consisting of the MSE, the Γ_4^- ZE and the Γ_5^+ ZE contributions is given by

$$I_{\text{interf.}}^{\text{SHG}}(\psi,\varphi) = \left| \alpha_{\mathbf{k}} \frac{O_{\Gamma_4^- \text{ZE}}(\psi,\varphi)}{|\widehat{O}_{\Gamma_4^- \text{ZE}}|} + \beta_{\mathbf{k}} \frac{O_{\text{MSE}}(\psi,\varphi)}{|\widehat{O}_{\text{MSE}}|} + \gamma_{\mathbf{k}} \frac{O_{\Gamma_5^+ \text{ZE}}(\psi,\varphi)}{|\widehat{O}_{\Gamma_5^+ \text{ZE}}|} \right|^2 . \tag{6.133}$$

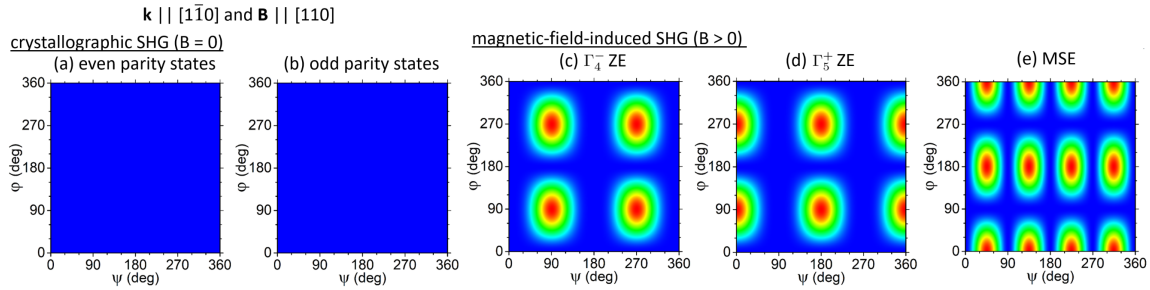

Figure 6.5 Simulation of 2D SHG polarization diagrams of blue-series excitons for excitation along the $\mathbf{k} \parallel [1\bar{1}0]$ and an applied magnetic field along the [110] crystal axis. Crystallographic SHG of (a) S and (b) P states as sketched in Fig. 6.2. (c) Γ_4^- ZE, (d) Γ_5^+ ZE and (e) MSE as sketched in Fig. 6.3.

The division by the absolute values of their maximal amplitudes $\widehat{O}_i$ scales all the contributions to 1, so that the coefficients $\alpha_{\mathbf{k}}$, $\beta_{\mathbf{k}}$ and $\gamma_{\mathbf{k}}$ represent the relative contributions of the real SHG signal induced by the three mechanisms.

6.3 SHG in symmetry-allowed geometry

For the SHG experiments on blue-series excitons, we have used the ps laser and the 0.5 m Acton spectrometer in order to apply the spectral scanning method as described in Sec. 3.2. The fixed wavelength fs laser method, as described in Sec. 3.3, would not work here because the blue excitons are spectrally broader than the fs-laser power spectrum. The lower boundary of the resolution of the scanning method is limited by the spectrometer assuming the scanning steps are in the order of the spectrometer resolution. However, the resolution of about 100 µeV is sufficient, and similarly, small scanning steps are not required, as the typical line width of blue excitons is in the order of several meV. Magnetic fields up to 10 T are applied in Voigt configuration for the experiments.

For the SHG experiments in symmetry-allowed crystal orientations, we have chosen the H2a sample, as characterized in Tab. 3.1. The excitation laser light is directed along the [111] crystal axis, which has been shown in Sec. 4.1 to be symmetry-allowed for crystallographic contributions. Moreover, the sample has quite a large thickness of 3663 µm, which is important for blue series exciton experiments, because the exciton lines are spectrally broad and thin crystals would lead to fringes distorting the exciton line shape.

This section is divided into two parts: First, we will present the experiments at zero magnetic field and discuss the properties and the spectral features of the crystallographic signal. In the second part, we will elaborate on magnetic-field-induced SHG.

6.3.1 Experimental results at zero field

For this experiment, the magnetic field is absent and the linear polarization angles are set to $\psi/\varphi = 0°/0°$. The spectral range of the blue excitons is scanned with the ps laser pulses in steps of 0.55 meV in order to acquire the SHG spectrum, as described in Sec. 3.2, by moving the laser and the spectrometer simultaneously in wavelength. An exemplary spectrum for

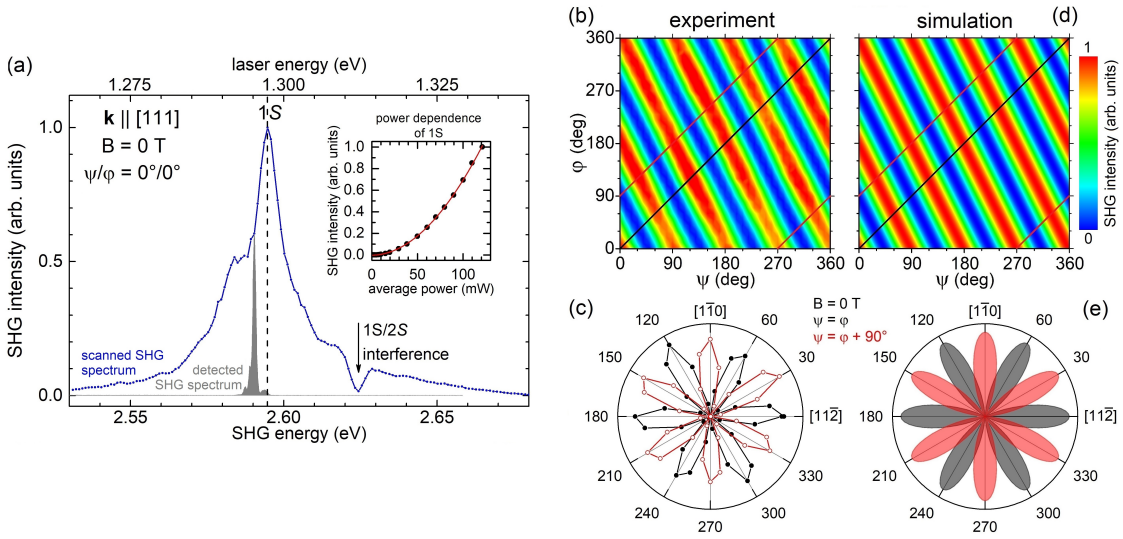

Figure 6.6 (a) Crystallographic SHG spectrum (blue line) scanned with ps pulses in the energy range of blue-series excitons for excitation along the [111] crystal axis in the H2a sample (see Tab. 3.1) and a polarization setting of $\psi/\varphi = 0°/0°$. An exemplary SHG spectrum, as detected by the CCD camera, is shown as the gray area for a laser energy of 1.295 eV and a spectrometer energy setting of 2.590 eV. The inset shows the SHG intensity of the $1S$ resonance, as marked by the vertical dashed line, in dependence on the average excitation power up to 120 mW. The dots are the measured values and the red line is a parabolic fit to the data with a good agreement. Panel (b) shows the 2D SHG polarization diagram as measured at the $1S$ resonance energy. Panel (c) shows a polar plot for the parallel and crossed polarization configurations, as marked by the black and red lines in panel (b). The experimental results show a good agreement with the SHG polarization dependence simulated according to Eq. (4.70), which is shown in the contour plot in panel (d) and the polar plot in panel (e).

the energy setting at 2.59 eV is shown in Fig. 6.6(a) as the gray area. It has the spectral shape of the ps pulse with a line width of about 1.1 meV. Its central pixel is taken for the blue spectrum at the according energy. The scan yields the SHG spectrum represented by the blue line. It has, apart from additional spectral features, a Lorentzian shape with a maximum at an energy of 2.595 eV associated with the blue $1S$ exciton with a shoulder about 10 meV lower in energy. On the high-energy side at about 2.624 eV, there is a dip, which is a consequence of interference of the $1S$ and $2S$ excitons.

The dependence of the SHG signal on the laser excitation power at the maximum of the spectrum, as marked by the vertical dashed line, is shown in the inset for excitation powers up to 100 mW. The dots represent the experimental data and the red line is a quadratic fit to the data implying a good agreement. The polarization dependence of the $1S$ SHG signal at the same energy is shown in Fig. 6.6(b). The parallel and crossed configurations, as indicated by the black and red tuning lines in the contour plot, are shown in a polar plot in Fig.6.6(c) and exhibit sixfold symmetries shifted by 30° to each other. The simulated contour plot for the crystallographic SHG for **k** along [111] is shown in Fig. 6.6(d) and the according polar plots of the parallel and crossed polarization configurations are shown in

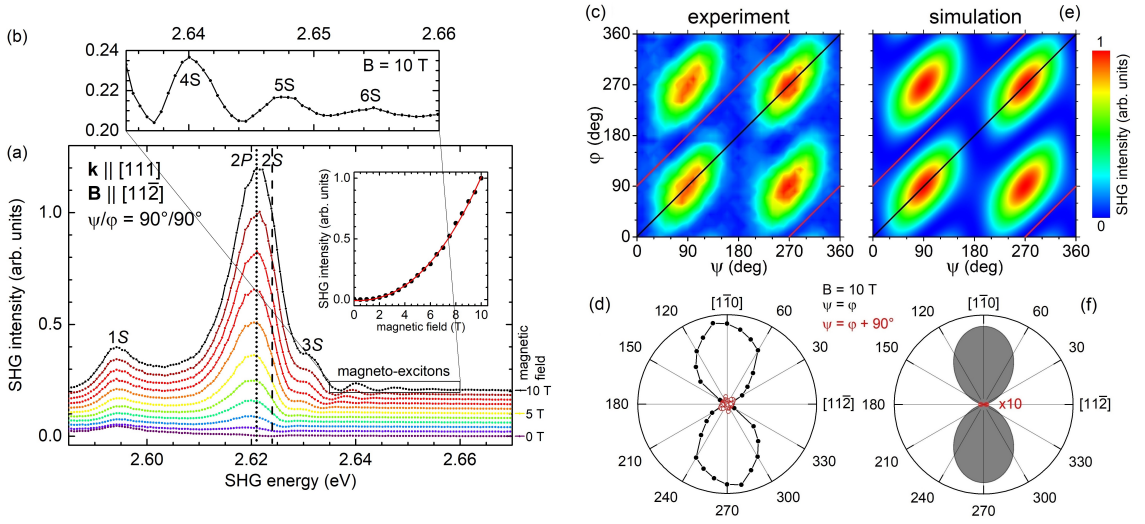

Figure 6.7 (a) Magnetic-field-induced SHG spectra of blue-series excitons for excitation along the [111] crystal axis of the H2a sample (see Tab. 3.1) and a polarization setting of $\psi/\varphi = 90°/90°$ for magnetic fields up to 10 T applied along the [11$\bar{2}$] crystal axis. The inset shows the SHG intensity of the $2S/2P$ resonance maximum, as marked by the vertical dotted line, as a function of the magnetic field up to 10 T. The dots are the measured values and the red line is a parabolic fit to the data with a good agreement. Panel (b) shows a magnification of the magneto-excitons at $B = 10$ T. Panel (c) shows the 2D SHG polarization diagram as measured at the emery of the dip (dashed line), as seen in Fig. 6.6(a). Panel (d) shows a polar plot for the parallel and crossed polarization configurations, as marked by the black and red lines in panel (c). The experimental results show a good agreement with the SHG polarization dependence simulated according to Eq. (6.133) with a coefficient ratio of $\alpha_{[111]}/\beta_{[111]} = 4/3$ and shown in the contour plot in panel (d) and the polar plot in panel (e).

Fig. 6.6(e). The experimental and simulated results are in good agreement.

6.3.2 Experimental results in a magnetic field

In this section, we will analyze the magnetic-field-induced SHG contributions. For this, we suppress the crystallographic SHG signal and maximize the MSE and ZE contributions by setting the linear polarization angles to $\psi/\varphi = 90°/90°$, as can be concluded from Fig. 6.4. This setting needs to be carefully adjusted at zero magnetic field for a minimal SHG signal. Then the magnetic field is ramped up to 10 T and the SHG spectrum is measured by the same ps scanning method. The SHG spectra are measured for magnetic fields between 0 and 10 T in steps of 1 T and the results are shown in Fig. 6.7(a). The spectral features differ from the crystallographic spectrum. At 10 T the $1S$ exciton appears at about 2.592 eV and in addition, the $n = 2$ exciton gives a contribution, which is about five times as strong as the $1S$ exciton. On the high-energy side, there is a shoulder associated with the $3S$ exciton and several oscillatory features magnified in Fig. 6.7(b), which shift to higher energies with increasing magnetic field and are associated with the magneto-excitons up to $n = 6$. We will further investigate them in Sec. 6.5.

The magnetic field dependence up to 10 T of the SHG intensity for the spectral maximum at an energy of 2.621 eV is shown in the inset. The dots are the experimental data and the red line represents a quadratic fit with a good agreement. Although no SHG contribution is expected at zero field, we still detect a weak signal with the shape of the crystallographic SHG shown in Sec. 6.3.1. A reason for it might be a slight misalignment of the sample so that **k** deviates from the [111] direction leading to a slightly different polarization dependence with a crystallographic contribution at $\psi/\varphi = 90°/90°$.

In order to measure the polarization dependence of only the magnetic-field-induced SHG contributions, one has to suppress the crystallographic contribution by choosing an excitation energy for which the crystallographic SHG is minimized and the magnetic-field-induced SHG gives sufficient signals. This is the case for the $1S/2S$ interference minimum, which is indicated by the dashed line in Fig. 6.7(a). The experimentally acquired polarization dependence is plotted in Fig. 6.7(c) and has four intensity maxima at $\psi/\varphi = 90°/90°$ and analogous positions shifted by 180° in either ψ or φ. The parallel configuration (black line) shows a twofold symmetry and is plotted in a polar plot in Fig. 6.7(d). The crossed configuration (red line) is also shown but has vanishingly small signals. The simulation is done according to Eq. (6.133). As both ZEs exhibit the same polarization dependence, they are summarized to one contribution with the coefficient $\alpha_{[111]}$. A ratio of $\alpha_{[111]}/\beta_{[111]} = 4/3$ leads to the polarization diagram shown in Fig. 6.7(e) and yields the best agreement with the experimental data. The according tuning lines are shown in a polar plot in Fig. 6.7(f) and confirm the good agreement.

6.4 SHG in symmetry-forbidden geometry

In this section, we will suppress crystallographic SHG by choice of excitation along a crystal axis, which is symmetry-forbidden for zero-field SHG. For this, we select the H45a sample, for which we can direct **k** along $[1\bar{1}0]$, so no crystallographic SHG is expected. Its thickness of 4880 µm is sufficient to avoid a modulation of the broad spectral lines by fringes. The magnetic field is applied in Voigt configuration along the [110] crystal axis so that the three mentioned magnetic-field-induced SHG mechanisms can be fully separated by choice of the polarization setting, as already demonstrated for this specific crystal orientation for yellow-series excitons in Sec. 4.2.

The simulated diagrams in Fig. 6.5 show the polarization dependence of the crystallographic SHG for blue S excitons in panel (a), blue P excitons in panel (b), the Γ_4^- ZE in panel (c), the Γ_5^+ ZE in panel (d) and the MSE in panel (e). The polarization setting for maximizing the chosen mechanism and suppressing all others is $\psi/\varphi = 90°/90°$ for the Γ_4^- ZE, $\psi/\varphi = 0°/90°$ for the Γ_5^+ ZE and $\psi/\varphi = 45°/0°$ for the MSE. Next, we apply a magnetic field of 10 T and scan the SHG spectrum in the range of blue excitons between 2.565 eV and 2.6725 eV for the three mentioned polarization settings.

The blue line in Fig. 6.8(a) shows the acquired Γ_4^- ZE SHG spectrum. Its spectral features are similar to the magnetic-field-induced spectrum of the symmetry-allowed crystal orientation in Fig. 6.7(a) from Sec. 6.3. The spectrum is again normalized to the intensity of the $2S/2P$ line, which has a line width of about 10.5 meV. The intensity of the $1S$ exciton is about 40 % lower. On the high-energy side, we observe magneto-excitons up to $n = 8$, which are magnified in Fig. 6.8(b). For comparison, the zero-field spectrum with a vanishing

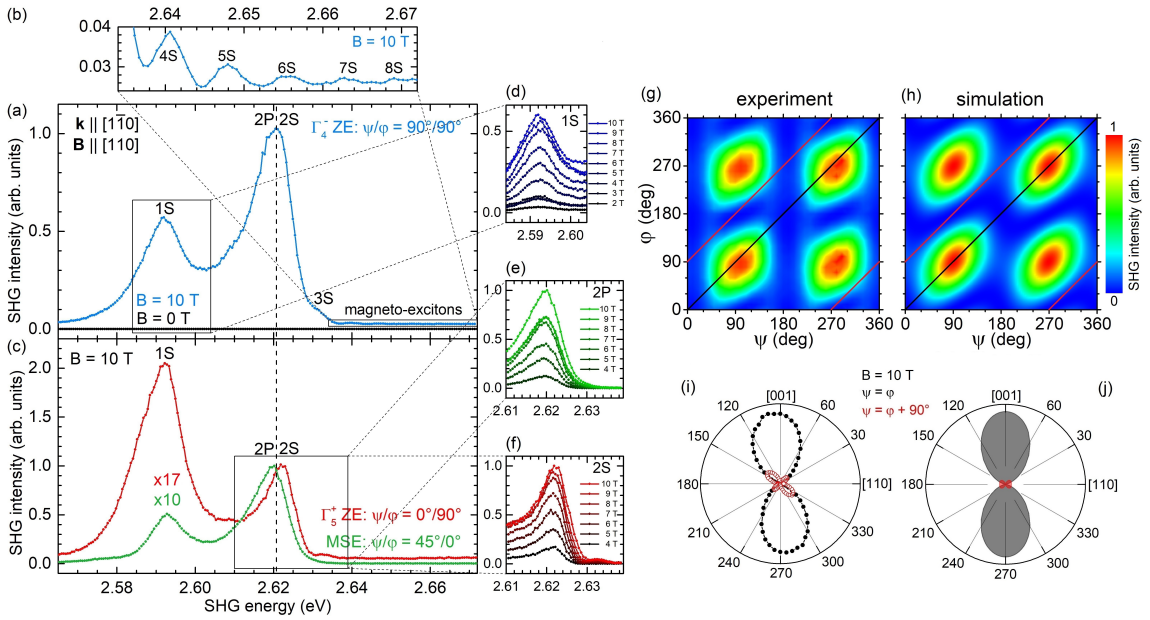

Figure 6.8 Magnetic-field-induced SHG spectra of blue-series excitons for excitation along the [1$\bar{1}$0] crystal axis and a magnetic field of 10 T applied in Voigt configuration along the [110] crystal axis of sample H45b (see Tab. 3.1). (a) Γ_4^- ZE-induced ($\psi/\varphi = 90°/90°$) SHG spectrum at $B = 10$ T (blue line) and 0 T (black line). The spectral region of magneto-excitons in a high-field regime is magnified in panel (b). (c) Γ_5^+ ZE- ($\psi/\varphi = 0°/90°$) and MSE-induced ($\psi/\varphi = 45°/0°$) SHG spectra at $B = 10$ T shown as the red and green lines, respectively. Panels (d), (e) and (f) show the magnetic-field series of the $1S$, $2P$ and $2S$ resonances induced by the Γ_4^- ZE, the MSE and the Γ_5^+ ZE, respectively. Panel (g) shows the 2D SHG polarization diagram as measured at the $2S/2P$ resonance energy (dashed line). Panel (i) shows a polar plot for the parallel and crossed polarization configurations, as marked by the black and red lines in panel (g). The experimental results show a good agreement with the SHG polarization diagrams, which are shown in the contour plot in panel (h) and the polar plot in panel (j) and are simulated according to Eq. (6.133) with the coefficient ratios $\alpha_{[1\bar{1}0]}/\gamma_{[1\bar{1}0]} = 3.5$ and $\alpha_{[1\bar{1}0]}/\gamma_{[1\bar{1}0]} = 4$.

SHG signal is shown as the black line, which is an indication of a good alignment of the experimental geometries.

The red line in Fig. 6.8(c) represents the 10 T SHG spectrum induced by the Γ_5^+ ZE, which is normalized to the $n = 2$ exciton intensity, which is about 17 times weaker, than the $n = 2$ line of the more dominant Γ_4^- ZE-induced spectrum. In contrast to the spectrum in Fig. 6.8(a), the $1S$ exciton is about twice as intense as the $n = 2$ exciton. Moreover, the $n = 2$ exciton with its line width of only 7.6 meV is about 30 % narrower than the $n = 2$ line in panel (a), which is an indication that the Γ_5^+ ZE induces a pure $2S$ exciton-polariton line and the Γ_4^- ZE a mixed $2S/2P$ resonance. Energetically above the $2S$ exciton-polariton, weak indications of magneto-excitons are observed, however, much weaker in comparison.

The green line in Fig. 6.8(c) shows the 10 T SHG spectrum induced by the MSE, which is again normalized to its $n = 2$ excitons intensity, which is about 10 times weaker, than the $2S/2P$ line of the more dominant Γ_4^- ZE. It has a similar intensity ratio as the dominant ZE,

as the $1S$ exciton is about half as intense as the $n = 2$ resonance. The $n = 2$ exciton with its line width of only 9.7 meV is about 8 % narrower than the $n = 2$ resonance in Fig. 6.8(a), which again indicates, that the Γ_4^- ZE induces an SHG signal of a mixed $2S/2P$ resonance. As the $n = 2$ resonance of the MSE is also about 2 meV lower in energy compared to the $2S$ exciton-polariton of the Γ_4^- ZE spectrum, one can draw the conclusion that it is a $2P$ exciton resonance, as it is not subject to the polariton effect (see Fig. 6.1). Energetically above the $2P$ exciton, no indications of magneto-excitons are observable, which indicates that the MSE favors the induction of P type excitons and both ZEs induce more S type exciton signals. This conclusion will be important in Sec. 6.4.1 on the magnetic-field shifts of these three resonances and the mixing behavior between them.

Figs. 6.8(d), 6.8(e) and 6.8(f) show the magnetic-field series of the $1S$ exciton-polariton (2 to 10 T) induced by the Γ_4^- ZE, the $2P$ exciton (4 to 10 T) induced by the MSE and the $2S$ exciton-polariton (4 to 10 T) induced by the Γ_5^+ ZE, respectively. Their spectral shifting behavior will be analyzed in Sec. 6.4.1.

The polarization dependence is measured at an energy of 2.621 eV, marked by the vertical dashed line between the $2S$ exciton-polariton and the $2P$ exciton resonance and shown in the contour plot in Fig. 6.8(g). It is an interference of all three mechanisms, but as the Γ_4^- ZE is the dominant mechanism, the measured polarization plot has the most similarity with it with intensity maxima at $\psi/\varphi = 90°/90°$ and the corresponding points shifted either in ψ or φ by 180° degrees. The slight distortions can be explained by the smaller contributions of the other two mechanisms. The parallel configuration tuning line in Fig. 6.8(i) has twofold symmetry with maxima at $\psi = 90°$ and the crossed one has a fourfold symmetry with maxima starting at 45°. The simulated plot according to Eq. (6.133) is shown in Fig. 6.8(h) and yields the best agreement with the experiment for a coefficient ratio of $\alpha_{[1\bar{1}0]}/\beta_{[1\bar{1}0]} = 3.5$ and $\alpha_{[1\bar{1}0]}/\gamma_{[1\bar{1}0]} = 4$. These ratios are in good agreement with the SHG intensities at this energy, as the squared coefficients $(\alpha_{[1\bar{1}0]}/\gamma_{[1\bar{1}0]})^2 = 3.5^2 = 12.25$ and $(\alpha_{[1\bar{1}0]}/\gamma_{[1\bar{1}0]})^2 = 4^2 = 16$ are similar to the ratios of the SHG intensities between the effects of about 10 and 17. The tuning lines for parallel and crossed polarization configurations are shown in the polar plots in Fig. 6.8(j) and confirm the good agreement with the experimental data in Fig. 6.8(i).

6.4.1 Magnetic-field induced energy shift of $1S$, $2S$ and $2P$ resonances

In this section we analyze the magnetic-field-induced shifting behavior of the $1S$ and $2S$ exciton-polaritons and the $2P$ exciton unaffected by polaritonic effect. In order to obtain the resonance energies of the three lines for each magnetic field, we take the second derivatives of the SHG spectra in Figs. 6.8(d)-6.8(f), and fit each resonance with a Gaussian function. The results are plotted in Fig. 6.9 as full circles with according error bars considering the spectral resolution and the Gaussian fit errors.

We fit the data with an appropriate model, which takes the diamagnetic shifts and the repulsions between the states due to field-induced mixing into account. The diamagnetic

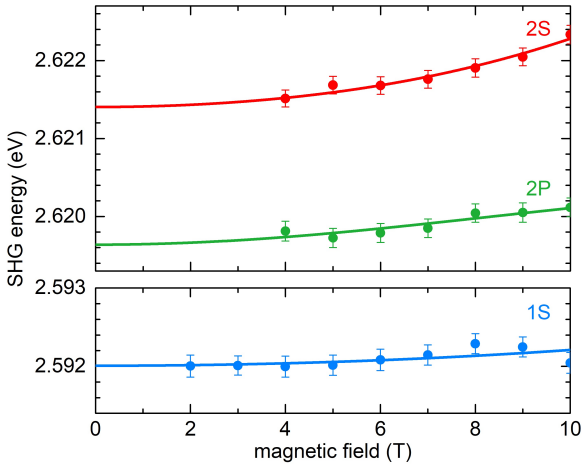

Figure 6.9 Resonance energies of the $1S$ (blue dots), $2P$ (green dots) and $2S$ (red dots) energies in dependence of the magnetic field up to 10 T. The energies are extracted by Gaussian fits to the second derivatives of the SHG spectra in Figs. 6.8(d), 6.8(e) and 6.8(f). The error bars take the spectral resolution and the fit errors of the Gaussians into account. The solid lines are fits according to the eigenvalues of the three-level matrix in Eq. (6.136).

shifts are given by

$$\begin{aligned} H_{\text{dia}}(B) &= \frac{e^2}{8\mu_X}(x^2+y^2)B^2 \\ &= \frac{e^2}{8\mu_X}\frac{2}{3}\langle r_{n,l}^2\rangle B^2 \\ &= d_{n,L}B^2, \end{aligned} \tag{6.134}$$

with the reduced exciton mass μ_X, the electron charge e, the diamagnetic shifts $d_{n,L}$ with the principal and angular momentum quantum numbers n and L, and the average of the squared exciton radius $\langle r_{n,L}^2\rangle$, which is calculated according to

$$\langle r_{n,L}^2\rangle = \frac{a_0^2}{2}n^2[5n^2+1-3L(L+1)]. \tag{6.135}$$

With this equation the diamagnetic shifts $d_{2,1}$ and $d_{2,0}$ of the $2P$ and $2S$ resonances can be expressed in terms of the $1S$ exciton $d_{1,0}$ as $d_{2,1} = 10d_{1,0}$ and $d_{2,0} = 14d_{1,0}$. The effective electric field due to the MSE mixes states of opposite parity ($2P$ with both $1S$ and $2S$). Therefore we get the MSE mixing parameters M_{1S2P} and M_{2S2P}. Consequently, the three-level matrix can be expressed as

$$\mathbf{M}_{\text{3-level}}(B) = \begin{pmatrix} E_{1S}+d_{1,0}B^2 & M_{1S2P}B & 0 \\ M_{1S2P}B & E_{2P}+d_{2,1}B^2 & M_{2S2P}B \\ 0 & M_{2S2P}B & E_{2S}+d_{2,0}B^2 \end{pmatrix}, \tag{6.136}$$

with the zero-field energies E_{1S}, E_{2S} and E_{2P} of the three resonances denoted in the index.

By fitting the eigenvalues of matrix $\mathbf{M}_{\text{3-level}}$ to the experimental data we get

$$E_{1S} = (2.5920 \pm 0.0002)\,\text{eV}, \tag{6.137}$$
$$E_{2S} = (2.6214 \pm 0.0002)\,\text{eV}, \tag{6.138}$$
$$E_{2P} = (2.6196 \pm 0.0002)\,\text{eV}, \tag{6.139}$$
$$M_{1S2P} = (0.106 \pm 0.004)\,\frac{\text{meV}}{\text{T}}, \tag{6.140}$$
$$M_{2S2P} = (0.43 \pm 0.02)\,\frac{\text{meV}}{\text{T}}, \tag{6.141}$$
$$d_{1,0} = (0.62 \pm 0.05)\,\frac{\mu\text{eV}}{\text{T}^2}. \tag{6.142}$$

for the zero-field energies, the MSE mixing parameters and the diamagnetic shift of the $1S$ exciton-polariton. Consequently, the diamagnetic shift parameters of the $2S$ and $2P$ resonances are $d_{2,0} = (8.7 \pm 0.7)\,\mu\text{eV/T}^2$ and $d_{2,1} = (6.2 \pm 0.5)\,\mu\text{eV/T}^2$, respectively.

With the fit results, we can derive two additional parameters for the blue-series excitons: The reduced exciton mass $\mu_{X,b}$ and the exciton Bohr radius $a_{X,b}$. According to Eq. (6.134), the reduced exciton mass is given by

$$\mu_X = \frac{e^2}{8d_{n,l}}\frac{2}{3}\langle r_{n,l}^2\rangle. \tag{6.143}$$

By inserting $\langle r_{0,1}^2\rangle = 3a_0^2$ and the fit value for $d_{1,0} = (0.62 \pm 0.05)\,\mu\text{eV/T}^2$ we get $\mu_{X,b} = 0.226(6)\,m_0$ for the reduced exciton mass of the blue series. This value is in good agreement with the derived value $\mu_X = 0.228\,m_0$ from the polariton theory and about 27% smaller than $\mu_{X,y} = 0.363\,m_0$ [Nak+12] for the yellow exciton series.

For the derivation of the exciton Bohr radius for the blue series, we use the expression

$$a_X = \frac{m_0}{\mu_X}\varepsilon(E_{1S})a_H, \tag{6.144}$$

according to the hydrogen model. With the hydrogen Bohr radius a_H, $\varepsilon(E_{1S}) = 7.63$ and the derived value $0.226(6)\,m_0$ for $\mu_{X,b}$ we get $a_{X,b} = (1.79 \pm 0.05)\,\text{nm}$, which is about two and a half times larger than $a_{X,Y} = 0.7\,\text{nm}$ [Kav+97] for the yellow series.

6.5 Magneto-excitons and anisotropy of conduction band

In this section, we will derive the anisotropic effective electron mass $m_{\mathbf{K}}^{8C}$ of the Γ_8^- CB for $\mathbf{K}$ along three different crystal axis from the experimentally observed magnetic-field dependent shifts of magneto-excitons in the high-field regime, which have already been shown in Figs. 6.7(b) and 6.8(b).

First, we introduce the concept of magneto-excitons in the high-field regime, which are excitons under the influence of strong magnetic fields, so that the cyclotron energy dominates the Coulomb binding energy. At low magnetic fields, the excitons exhibit a diamagnetic energy shift proportional to B^2 according to Eq. (6.134), as demonstrated in Sec. 6.4.1. For increasing magnetic fields, the cyclotron energy $\hbar\omega_\text{c}$ increases linearly and surpasses the Coulomb binding energy at a certain magnetic field, the so-called crossover magnetic field

Table 6.2 Crossover magnetic fields $B_{\mathrm{cross},n}$ for blue series S type magneto-excitons in dependence of the principle quantum number up to $n = 8$ calculated according to Eq. (6.150).

n	1	2	3	4	5	6	7	8
$B_{\mathrm{cross},n}$ (T)	92	17	6.0	2.7	1.4	0.8	0.5	0.4

B_{cross}. As a consequence, the quadratic diamagnetic shift transforms into a linear magnetic shift, as known from Landau levels, and scales with the principle quantum number according to

$$E_{c,n_L}(B) = (n - \frac{1}{2})\hbar(\omega_{\mathrm{c,e}} + \omega_{\mathrm{c,h}}) = (n - \frac{1}{2})\hbar(\frac{eB}{m_{\mathbf{K}}^{8C}} + \frac{eB}{m^{7V}}) \tag{6.145}$$

$$= (n - \frac{1}{2})\frac{\hbar e}{\mu_{\mathbf{K}}^{eh}}B, \tag{6.146}$$

with the cyclotron frequencies $\omega_{\mathrm{c,e}}$ from the electron, $\omega_{\mathrm{c,e}}$ from the hole, the electron charge e, the Γ_8^- CB effective electron mass $m_{\mathbf{K}}^{8C}$ along the crystal axis $\mathbf{K}$, the Γ_7^+ VB effective hole mass and the reduced exciton mass $\mu_{\mathbf{K}}^{\mathrm{eh}}$, which is calculated by

$$\frac{1}{\mu_{\mathbf{K}}^{\mathrm{eh}}} = \frac{1}{m_{\mathbf{K}}^{8C}} + \frac{1}{m^{7V}}. \tag{6.147}$$

The crossover magnetic field, at which the binding energy and the cyclotron energy are equal, is calculated by equating the magnetic length

$$l_n = \sqrt{\frac{2\hbar}{eB_{\mathrm{cross},n}}(n - \frac{1}{2})} \tag{6.148}$$

and the average exciton radius

$$\langle r_{n,l}\rangle = \frac{a_B^X}{2}[3n^2 - l(l+1)]. \tag{6.149}$$

The crossover magnetic field is accordingly expressed by

$$B_{\mathrm{cross},n} = \frac{8\hbar}{9ea_B^{X\,2}}\frac{(n - \frac{1}{2})}{n^4}. \tag{6.150}$$

The crossover magnetic fields are listed in Tab. 6.2 for blue-series excitons as a function of the principle quantum number up to $n = 8$. For $n \geq 3$ the crossover magnetic field lies below 10 T and therefore within the range of our experiments. The slopes of the magnetic-field-dependent energy shifts are expected to have less influence by the parabolic diamagnetic shift for increasing n. Therefore the slopes should converge to the expected Landau level shift according to Eq. (6.146) for higher principal quantum numbers.

The experimental data on the magnetic-field dependent SHG spectra of magneto-excitons are shown in Figs.6.10(a), 6.10(b) and 6.10(c) for the three different crystal orientations, for which $\mathbf{k}$ is directed along the [111], [1$\bar{1}$0] and [001] crystal axis of the H2a, H45b and H45a samples, respectively. The contour plots represent the second derivatives of the SHG spectra

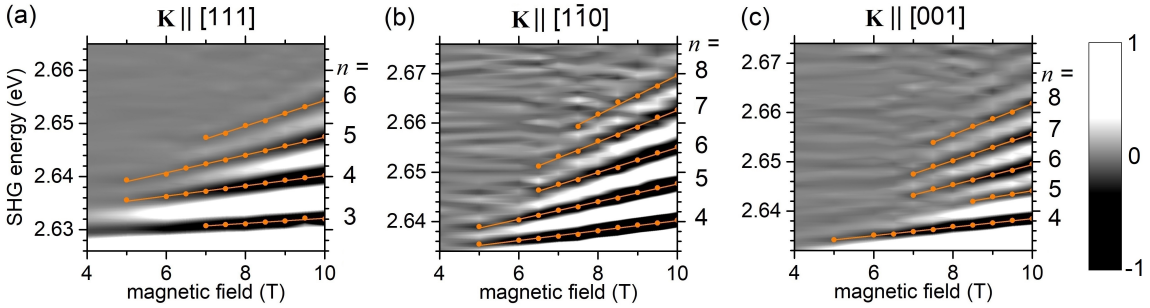

Figure 6.10 Second derivatives of the SHG spectra in the spectral range of blue series magneto-excitons for magnetic fields between 4 to 10 T for the three different crystal orientations: (a) $\mathbf{K} \parallel [111]$ and $\mathbf{B} \parallel [11\bar{2}]$ of the H2a sample, (b) $\mathbf{K} \parallel [1\bar{1}0]$ and $\mathbf{B} \parallel [110]$ of the H45b sample, (c) $\mathbf{K} \parallel [001]$ and $\mathbf{B} \parallel [110]$ of the H45a sample. The orange dots mark the resonance energies and are obtained by Gaussian fits to the second derivatives of the according SHG spectra. The orange lines are linear fits according to Eq. (6.146).

for a better evaluation of the resonance energies. The $n = 4$ magnetoexciton emerges for all crystal orientations at about $B = 5\,\mathrm{T}$. Magneto-excitons with higher n emerge at even higher fields. An exception is the $n = 5$ magnetoexciton in the $\mathbf{k} \parallel [001]$ case, of which clear signals appear at about $B = 8.5\,\mathrm{T}$. For the $\mathbf{k} \parallel [111]$ orientation, magneto-excitons up to $n = 6$ are observed. For the other two orientations, the highest quantum number magnetoexciton, which is clearly observed, is $n = 8$ with even weak indications of $n = 9$ and 10 for $\mathbf{k} \parallel [001]$. The slope of the magnetic-field-dependent energies is increasing for higher n, which leads to a "fan" like appearance. For the $n = 3$ magnetoexciton in Fig. 6.10(a), the influence of the parabolic diamagnetic shift is clearly seen for lower magnetic fields, as the crossover field is at about 6 T.

For the evaluation of the resonance energies, we fit Gaussian functions to the second derivatives of the SHG spectra. The fit values of the central energies of the Gaussians are plotted in Fig. 6.10 as orange dots. The slope for each n is fitted with the linear function

$$s_{\mathbf{K},n} = \frac{\hbar e(n - \frac{1}{2})}{\mu_{\mathbf{K},n}}, \tag{6.151}$$

$$\Leftrightarrow \mu_{\mathbf{K},n} = \frac{\hbar e(n - \frac{1}{2})}{s_{\mathbf{K},n}}, \tag{6.152}$$

according to Eq. (6.146), ignoring the influence of the diamagnetic shift for lower magnetic fields. For higher n the slope is expected to converge to the Landau shift with a linear magnetic field dependence.

In Fig. 6.11, we plot the fit results as color symbols with fit error bars for the slopes converted into the parameter $\mu_{\mathbf{K},n}$, which would correspond to the reduced exciton mass if the influence of the diamagnetic shift would not be present. The inset shows the same results in a logarithmic plot. The converging behavior of the $\mu_{\mathbf{K},n}$ is clearly seen and fitted with the empiric function

$$\mu_{\mathbf{K},n} = \mu_{\mathbf{K}}^{eh} + a_{\mathbf{K}} \exp(-b_{\mathbf{K}} n), \tag{6.153}$$

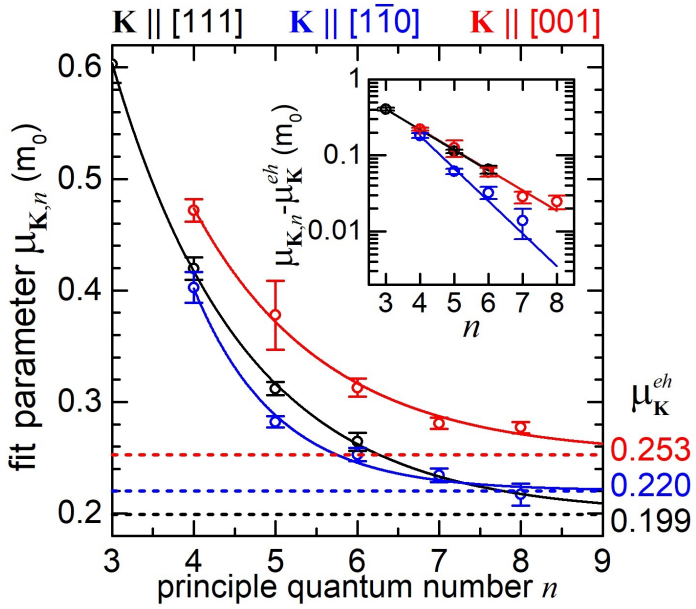

Figure 6.11 n dependent parameter $\mu_{\mathbf{K},n}$ (open circles) calculated according to Eq. (6.152) from the slope parameters of the linear fits of magneto-excitons shifts in Fig. 6.10. The fit error of the slopes is shown as the error bars. The $\mu_{\mathbf{K},n}$ converge to the reduced exciton mass $\mu_{\mathbf{K}}^{\mathrm{eh}}$ for increasing n, which is listed in Table 6.3 and are fitted using the empirical function in Eq. (6.153). The other fit parameters are: $a_{[001]} = 2.609\,m_0$, $a_{[1\bar{1}0]} = 2.595\,m_0$, $a_{[111]} = 9.411\,m_0$, $b_{[001]} = 0.617$, $b_{[1\bar{1}0]} = 0.620$ and $b_{[111]} = 0.987$. The inset shows the same data in a logarithmic diagram.

with the fit parameters

$$a_{[001]} = 2.609\,m_0, \qquad a_{[1\bar{1}0]} = 2.595\,m_0, \qquad a_{[111]} = 9.411\,m_0, \tag{6.154}$$

$$b_{[001]} = 0.617, \qquad b_{[1\bar{1}0]} = 0.620, \qquad b_{[111]} = 0.987 \tag{6.155}$$

of the exponential function and $\mu_{\mathbf{K}}^{eh}$ as the obtained result for the reduced exciton mass, which are shown in the second column of Tab. 6.3 for the crystal orientations listed in the first column.

The Γ_8^- CB effective electron masses for the three crystal orientations are shown in Tab. 6.3 in the third column and calculated according to Eq. (6.147) using the reduced exciton mass for the corresponding crystal axis and the value $m^{7V} = 0.575(50)\,m_0$ for the isotropic Γ_7^+ VB hole mass from Ref. [Nak+12]. The effective electron mass exhibits a significant anisotropy ranging from $0.304\,m_0$ along the [111] crystal axis up to $0.452\,m_0$ along the [001] axis. For comparison, the effective electron masses are extracted from the band structure calculations from Ref. [Fre+08] and listed in the fourth and fifth column in Table 6.3 for the two sub-bands. The experimental data seem to show the best agreement with the $m_{\mathbf{K},\mathrm{theo},1}^{8C}$ values in the fourth column.

Due to the anisotropy of the Γ_8^- CB the reduced exciton mass needs to be calculated

Table 6.3 The crystal axis, along which the excitation laser is directed, are listed in the first column. The second column shows the experimentally obtained electron-hole reduced masses $\mu^{eh}_{\mathbf{K},\mathrm{exp}}$, as shown in Fig. 6.11. The value for the effective electron masses $m^{8C}_{\mathbf{K},\mathrm{exp}}$ is calculated from the reduced mass according to Eq. (6.147) with $m^{7V} = 0.575(50)\,m_0$ from Ref. [Nak+12]. The fourth and fifth columns show the effective electron masses as theoretically calculated from Ref. [Fre+08] for the two Γ_8^- sub-bands distinguished by $i = 1$ and 2.

$\mathbf{K} \parallel$	$\mu^{eh}_{\mathbf{K}}(m_0)$	$m^{8C}_{\mathbf{K},\mathrm{exp}}(m_0)$	$m^{8C}_{\mathbf{K},\mathrm{theo},1}(m_0)$	$m^{8C}_{\mathbf{K},\mathrm{theo},2}(m_0)$
[111]	0.199(17)	0.304	0.261	0.241
$[1\bar{1}0]$	0.220(9)	0.356	0.332	0.201
[001]	0.253(14)	0.452	0.488	0.169

using the relation to the A_8 parameters

$$m^{8C}_{[100]} = 1/(A_8 + A_8^{'}), \tag{6.156}$$

$$m^{8C}_{[111]} = 1/(A_8 - A_8^{''}), \tag{6.157}$$

$$m^{8C}_{[1\bar{1}0]} = 1/\Big(A_8 - \frac{1}{2}\sqrt{A_8^{'2} + 3A_8^{''2}}\Big). \tag{6.158}$$

from Ref. [Krü+19]. Solving the system of equations leads to the values

$$A_8 = 3.39(61)/m_0, \tag{6.159}$$

$$A_8^{'} = -1.17(75)/m_0, \tag{6.160}$$

$$A_8^{''} = 0.11(84)/m_0, \tag{6.161}$$

of the A_8 parameters. Therefore the reduced exciton mass is given by $\mu_X = 0.195(24)m_0$ according to $1/\mu_X = 1/m^{7V} + A_8$. This value deviates by $-14.5\,\%$ from the according value as obtained in Sec. 6.1 and by $-13.7\,\%$ from the reduced exciton mass obtained in Sec. 6.4.1.

6.6 Conclusion

In this chapter, we have presented extensive experimental data on crystallographic and magnetic-field-induced SHG of the blue-series excitons in Cu_2O. The derived SHG polarization dependencies for the yellow series in Sec. 4.1 could also be used here, as blue S (P) excitons have the same optically active symmetry component as yellow P (S) excitons. The Γ_4^- ZE is the dominant magnetic-field-induced SHG mechanism and is interfering for excitation along the [111] crystal axis with the weaker Γ_5^+ ZE and MSE mechanisms. However, these three mechanisms can individually be switched on for $\mathbf{k}$ along the $[1\bar{1}0]$ crystal axis by specific settings of the linear polarization angles, which enabled us to excite the $1S$ and $2S$ exciton-polaritons as well as the $2P$ exciton individually. By measuring their magnetic field series and analyzing their diamagnetic shifts and MSE-mixing-induced repulsions we could extract blue series exciton parameters such as the reduced exciton mass and the Bohr radius. Magneto-excitons up to a principal quantum number of $n = 8$ are observed and the anisotropic effective electron mass of the Γ_8^- CB is extracted from the magnetic field shifts along the three crystal axis [111], $[1\bar{1}0]$ and [001].

Table 6.4 Results for key parameters of blue-series excitons such as the resonance energies and line widths, the Rydberg and bandgap energies, the effective electron masses for different crystal axis, the reduced exciton mass and the exciton Bohr radius, which are obtained by our experiments and polariton calculations. $\mu_{X,1}$ is obtained from the diamagnetic shifts in the three-level model in Sec. 6.4.1 and $\mu_{X,2}$ is obtained from the magnetic field shifts of magneto-excitons and calculated with the A parameters in Sec. 6.5. The third column shows the corresponding literature values from the PL experiments from Ref. [Tak+18] and the fourth column shows the values for the effective electron masses as derived from the band structure calculations from Ref. [Fre+08] for comparison.

parameter	this work [Far+21]	[Tak+18] (PL)	[Fre+08] (theory)
E_{1S}	2.5920 eV		
E_{2S}	2.6214 eV		
E_{2P}	2.6196 eV		
E_{1S_T}	2.579 26 eV	2.5829 eV	
E_{2S_T}	2.619 21 eV	2.6209 eV	
E_g	2.6326 eV	2.6336 eV	
E_{Ryd}	57.1 meV	50.7 meV	
γ_{1S}	13.9 meV	23.9 meV	
γ_{2S}	7.64 meV	20.1 meV	
a_X	1.79 nm		
$\mu_{X,1}$	0.226 m_0		
$m^{8C}_{[111]}$	0.304 m_0		0.261 m_0
$m^{8C}_{[1\bar{1}0]}$	0.356 m_0		0.332 m_0
$m^{8C}_{[001]}$	0.452 m_0		0.488 m_0
$\mu_{X,2}$	0.195 m_0		

Combining the experimental data and the polariton calculations from Sec. 6.1, additional parameters such as the transverse resonance energies, the SHG resonance energy due to the sharp excitation on the upper polariton branch, the bandgap and the Rydberg energy could be determined. The obtained results for the mentioned parameters are summarized in Tab. 6.4 and compared to literature data from previous publications.

SHG measurements can be extended to the violet series in the future. First measurements are performed and presented in Fig. 2.7(b), which shows the Γ_4^- ZE-induced SHG spectra at $B = 10\,\mathrm{T}$ extended to the spectral range of the violet-series excitons. A comparison to one-photon reflection measurements is shown in Fig. 2.7(a). Other nonlinear-optical processes, such as THG with an efficient triple ED excitation and an ED emission, can also be applied to study the properties of the blue-series excitons.

Chapter 7

Difference frequency generation with two-photon excitation of yellow-series excitons

Difference frequency generation with two-photon excitation is a type of four-wave mixing, which turned out to be a suitable optical method for polarization and time-dependent measurements of excitonic states in semiconductors. One pulsed laser performs a two-photon excitation similar to previous SHG experiments. Additionally, the pulsed light of a second laser with a smaller frequency is directed onto the sample with spatial and temporal overlap with the pulses from the first laser and stimulates a signal with the difference frequency of $\omega_{\mathrm{DFG}} = 2\omega_{\mathrm{exc.}} - \omega_{\mathrm{stim.}}$, as shown in Fig. 2.1(d). The configuration of the experimental setup for 2P-DFG experiments is shown in Fig. 3.1(b).

Compared to SHG, 2P-DFG has several benefits: i) Delaying the stimulating relative to the exciting pulses allows measuring time-dependent phenomena such as the coherence of excitons, cross-relaxation processes and beats between excitonic states. ii) The additional photon in the emission channel allows to address a greater variety of states and provides more possibilities for separating different mechanisms. iii) The detected signal originates from the entire crystal thickness, because the crystal is transparent for all involved photons, as opposed to SHG, for which the generated second harmonics photon is strongly absorbed so that only the signal generated in the last section of the sample can escape.

Time-dependent phenomena, such as cross-relaxation, have already been measured in Ref. [Yos+06] at the $1S$ exciton in Cu_2O with a single laser setup. A two-photon excitation along the [110] crystal axis excites the longitudinal orthoexciton component, which is forbidden for single-photon emission. By cross-relaxation into a transverse component, the EQ emission is monitored with a streak camera. A build-up of the signal with the cross-relaxation time with a subsequent decay has been observed. For the same crystal direction, the reverse process has been demonstrated in Ref. [Frö+87] by 1P-DFG. A transverse $1S$ component has been excited by an EQ process and an additional laser pulse has stimulated the two-photon emission of a transverse component, again measuring the cross-relaxation time. This experiment is described in Ref. [Han+98] for excitation along the [111] crystal direction, in which electron and hole spin-flip processes and propagation effects have been measured in the time domain.

Time-resolved transmission experiments have been performed in order to measure polariton propagation beats [Frö+91]. The EQ excitation covers a large range of the upper and lower polariton branches. The beats result from an interference between pairs of pulses on the lower and upper polariton branches having the same group velocity and a phase shift

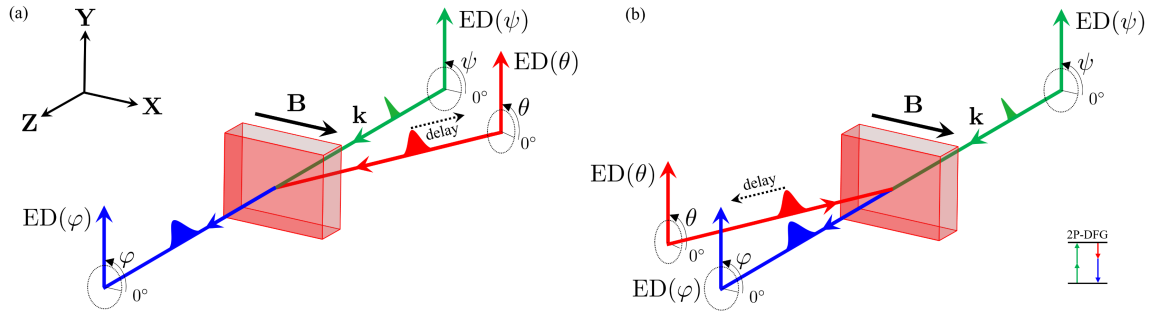

Figure 7.1 Experimental geometry for 2P-DFG experiments with (a) parallel and (b) anti-parallel stimulation relative to the direction of excitation light.

after propagating a certain distance through the crystal. The difference in our experiments is, that the two-photon excitation addresses a sharp point on the upper polariton branch with a specific group velocity resulting in a strong coherence.

In Ref. [Frö+89], a four-photon process was demonstrated in RbI, addressing the lower polariton branch of the $1S$ exciton by a three-photon difference frequency generation $\omega_{\mathrm{LP}} = 2\omega_1 - \omega_2 = \omega_{\mathrm{DFG}}$.

A part of the experimental results in this chapter has been obtained during the Bachelor theses of Sh. Mesgary [Mes21] and G. Uca [Uca22].

This chapter is structured as follows: The polarization-dependent 2P-DFG signal for the Γ_5^+ component of yellow S and D states as well as for the $1S$ exciton in a magnetic field is derived in Sec. 7.1. The Γ_5^+ component is addressed by ED-ED processes both in the excitation and the emission channels. Polarization, time and excitation power dependent 2P-DFG spectroscopy experiments of the $1S$ and higher n excitons are presented in Secs. 7.2 and 7.3, respectively. Section 7.4 elaborates three different cases of magnetic-field-induced quantum beats between the three $1S$ orthoexciton eigenstates in a magnetic field in Voigt configuration, which are set by different choices of the polarization setting of the involved light waves. Moreover, the beat frequencies are measured as function of the magnetic field strength. The average excitation powers of the fs and ps pulsed lasers are set to about 30 mW and about 10 mW, respectively.

7.1 Simulation of polarization dependencies

The polarization selection rules and the derivation of the polarization dependence of SHG processes as described in Secs. 4.1 and 5.3 can easily be extended to the 2P-DFG process. The scheme for the 2P-DFG process of yellow-series S excitons at zero field is shown in Fig. 7.2(a). For the symmetry considerations, the excitation channel of the 2P-DFG process for yellow-series S excitons is identical to that of the SHG process given in Eq. (4.64). As the emission channel also consists of a two-photon process, it is equivalent to the excitation channel and one has to only insert the linear polarization angle θ for the stimulation and φ for the DFG photon. The experimental geometry for parallel and anti-parallel stimulation relative to the excitation light direction is shown in Fig. 7.1. For yellow S excitons the

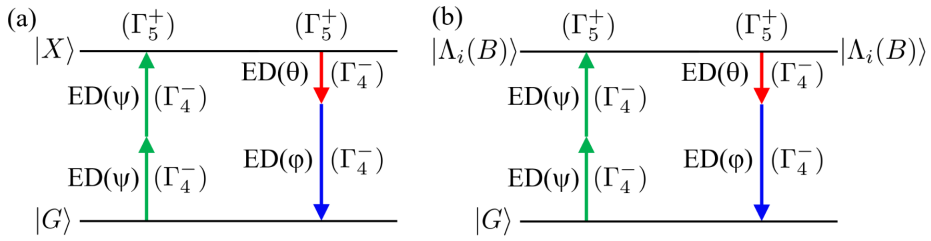

Figure 7.2 Schematics for (a) the crystallographic 2P-DFG process of Γ_5^+ excitons and (b) for magnetic-field-coupled $1S$ orthoexcitons.

ED-ED operator is therefore given by

$$O_{\mathrm{DD}}^{5+}(\psi) = \frac{1}{\sqrt{2}} \begin{pmatrix} d_2(\psi)d_3(\psi) + d_3(\psi)d_2(\psi) \\ d_1(\psi)d_3(\psi) + d_3(\psi)d_1(\psi) \\ d_1(\psi)d_2(\psi) + d_2(\psi)d_1(\psi) \end{pmatrix} \tag{7.162}$$

for the excitation channel and

$$O_{\mathrm{DD}}^{5+}(\theta,\varphi) = \frac{1}{\sqrt{2}} \begin{pmatrix} d_2(\theta)d_3(\varphi) + d_3(\theta)d_2(\varphi) \\ d_1(\theta)d_3(\varphi) + d_3(\theta)d_1(\varphi) \\ d_1(\theta)d_2(\varphi) + d_2(\theta)d_1(\varphi) \end{pmatrix} \tag{7.163}$$

for the emission channel. The 2P-DFG intensity consequently reads:

$$I_{\text{S-exc}}^{\text{2P-DFG}}(\psi,\theta,\varphi) = I_{\mathrm{DD/DD}}^{5+}(\psi,\theta,\varphi) \propto \left| O_{\mathrm{DD}}^{5+}(\psi) O_{\mathrm{DD}}^{5+}(\theta,\varphi) \right|^2 . \tag{7.164}$$

The 2P-DFG polarization dependencies of the $1S$ orthoexciton eigenstates in a magnetic field are analogously derived as in Sec. 5.3. The scheme for the 2P-DFG process of the $1S$ orthoexciton eigenstates in a magnetic field is shown in Fig. 7.2(b). The eigenvectors $\Lambda_i(B)$ of matrix Eq. (5.110) are multiplied with the excitation and emission channel expressions, respectively, before the square of the absolute value of the product of both channels is taken. The polarization-dependent 2P-DFG intensity is thus given by

$$I_{\mathrm{B,1S,i}}^{\text{2P-DFG}}(\psi,\theta,\varphi,B) = I_{\mathrm{DD/DD,i}}^{5+}(\psi,\theta,\varphi,B) \tag{7.165}$$

$$\propto \left| [\Lambda_i(B) \cdot O_{\mathrm{DD}}^{5+}(\psi)][\Lambda_i(B) \cdot O_{\mathrm{DD}}^{5+}(\theta,\varphi)] \right|^2 . \tag{7.166}$$

The polarization-dependent intensity for the individual two-photon processes is given by

$$I_{\mathrm{B,1S,i}}^{\text{2P-excit.}}(\psi,B) = I_{\mathrm{DD,i}}^{5+}(\psi,B) \propto \left| \Lambda_i(B) \cdot O_{\mathrm{DD}}^{5+}(\psi) \right|^2 \tag{7.167}$$

for the excitation and

$$I_{\mathrm{B,1S,i}}^{\text{2P-emit.}}(\theta,\varphi,B) = I_{\mathrm{DD,i}}^{5+}(\theta,\varphi,B) \propto \left| \Lambda_i(B) \cdot O_{\mathrm{DD}}^{5+}(\theta,\varphi) \right|^2 \tag{7.168}$$

for the emission channel. The polarization diagrams for four different crystal orientations are plotted in the first two rows in Fig. 7.3 for the emission channel according to Eq. (7.168) and in the third row for the excitation channel according to Eq. (7.167).

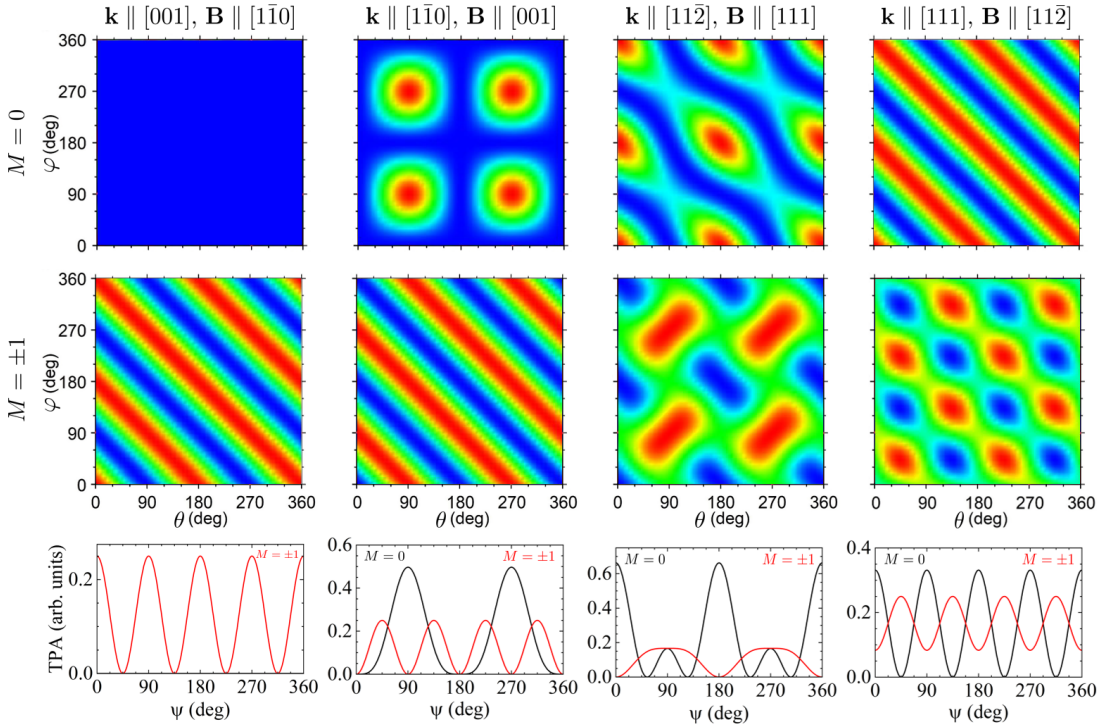

Figure 7.3 2D polarization diagrams for the emission two-photon processes (stimulation and DFG) addressing the $|M| = 0$ (first row) and $|M| = 1$ (second row) 1S exciton eigenstates in a magnetic field in Voigt configuration for excitation along four different crystal axis. The third row shows the 1D polarization diagrams for the two-photon excitation channel for the same states and crystal orientations.

7.2 2P-DFG spectroscopy of yellow $1S$ exciton in time domain

For the 2P-DFG experiments the femtosecond laser is set to 1220 nm (1.016 eV) in order to excite the 1S exciton via a two-photon ED-ED process. The picosecond laser is set to a wavelength of 1707 nm (0.726 eV) and directed onto the same sample spot from the same or the opposite direction (see Fig. 7.1) and its pulses are set into time overlap with the femtosecond pulses as described in Sec. 3.4. The stimulated DFG signal is spectrally resolved by the spectrometer and detected by the CCD camera. An example spectrum is shown in Fig. 7.4(d) as the black line. It consists of a sharp exciton resonance peak at about 1.306 eV, which is the energy difference between the two-photon exciton and the stimulation energy. The FWHM of about 1 meV is determined by the spectral width of the ps laser. The spectrum shows an additional broad spectral feature in the range from 1.29 eV to 1.32 eV. Once the ps pulses are delayed by 2 ps relative to the fs pulses, the excitonic 2P-DFG signal remains, but the spectrally broad signal disappears as shown by the red line in Fig. 7.4. The spectrally broad signal only occurs in the time overlap of both laser pulses and is therefore interpreted as a coherent $\chi^{(3)}$ signal in the sample, which originates from the third order nonlinearity in Eq. (2.13).

The 2P-DFG spectra as a function of delay time will be shown and discussed in Sec. 7.2.1

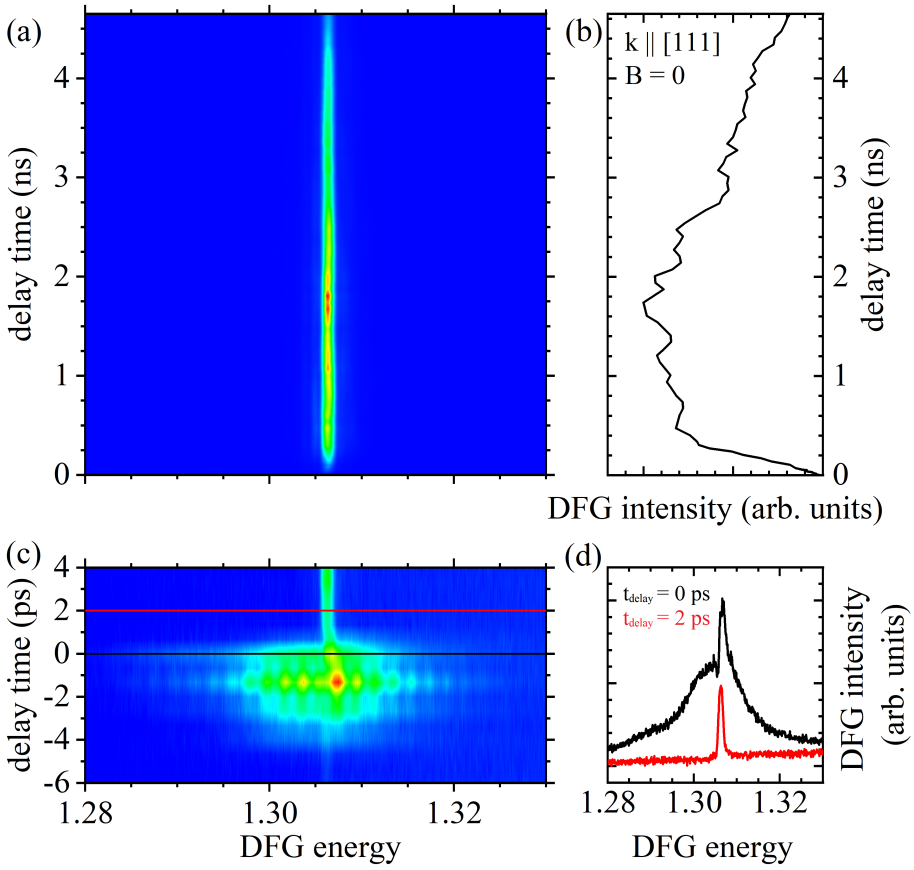

Figure 7.4 (a) 2P-DFG spectra and (b) 2P-DFG intensity of the 1S exciton as a function of the delay time in the range between $t_{\mathrm{delay}} = 0\,\mathrm{ps}$ and 4700 ps. (c) $\chi^{(3)}$ signal in a delay time range between $t_{\mathrm{delay}} = -6\,\mathrm{ps}$ and 4 ps. (d) Spectral cut at $t_{\mathrm{delay}} = 0\,\mathrm{ps}$ (black line) and 2 ps (red line), as marked in panel (c). The measurements are done with the geometry shown in Fig. 7.1(a) in the H2a sample (see Tab. 3.1) at $B = 0$ and $\psi/\theta = 90°/0°$ without polarization optics in the emission channel.

and the coherence time of the 1S exciton as a function of the excitation power will be investigated in Sec. 7.2.2. The polarization dependencies of the excitonic and the $\chi^{(3)}$ signal are presented in Sec. 7.2.3.

7.2.1 Time-dependent measurements of 1S at zero field

As becomes evident from both spectra in Fig. 7.4(d) the 2P-DFG spectral features change significantly as a function of the delay time. In order to investigate the dependence of the excitonic and the $\chi^{(3)}$ signal on the delay time in more detail, the 2P-DFG spectrum is measured for delay times between −6 and 4700 ps and shown in Fig. 7.4(a) in the form of a 2D contour plot. The 2P-DFG intensity is represented by a color scale as a function of the DFG energy on the horizontal and delay time on the vertical axis.

Figure 7.4(b) shows a cut at the energy of maximum intensity of the 1S 2P-DFG signal

along the delay time axis. The excitonic signal drops in intensity immediately after the temporal overlap of both laser pulses and then increases up to about $t_{\mathrm{delay}} = 1.7\,\mathrm{ns}$. After that an exponential decay in the range of several ns is observed. The reason for the raise in signal has not been clarified yet, as one would expect a maximal signal in time overlap with an immediate decay for increasing delay time. However, in Sec. 7.2.2 the stimulating ps laser is directed from the other side of the sample anti-parallel to the excitation laser, as shown in Fig. 7.1(b). After careful adjustment of the involved laser beams the time-dependent 2P-DFG intensity shows the expected behavior of maximum signal in time overlap and a subsequent decay.

Figure 7.4(c) shows a zoom in the delay time range of $-6\,\mathrm{ps}$ to $4\,\mathrm{ps}$, in which the time dependence of the $\chi^{(3)}$ signal becomes evident. It only occurs in the time overlap of both pulses. For larger delay times, the $\chi^{(3)}$ signal vanishes and only the excitonic signal remains.

7.2.2 Excitation-power dependent coherence times

For the experiments in this section the stimulating ps laser pulses are directed from the other side of the sample opposite to the excitation fs laser pulses, as shown in Fig. 7.1(b). The 2P-DFG intensity of the yellow 1S exciton is measured for three different average excitation powers of 20, 28 and 40 mW at a temperature of 1.4 K. Additionally, the measurement with an average excitation power of 40 mW is repeated at a temperature of 1.8 K by slightly closing the valve between the VTI and the helium pump and thus increasing the pressure within the VTI resulting in a raise of the temperature. The experimental data are shown in Fig. 7.5.

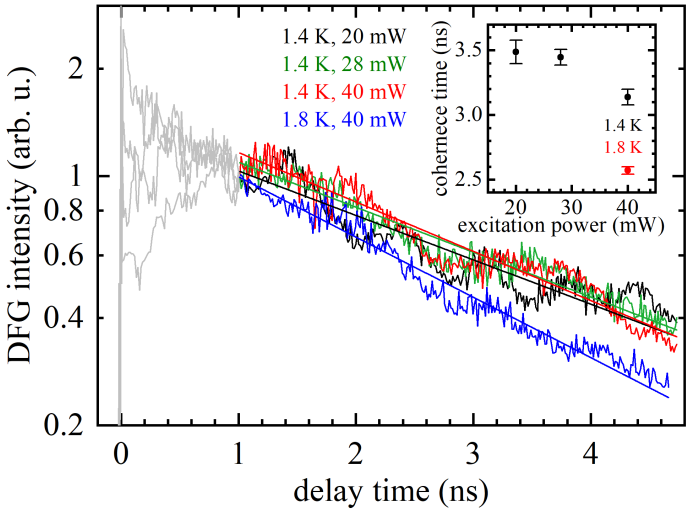

Figure 7.5 (a) 2P-DFG intensity of the 1S exciton at zero field in the H2a sample (see Tab. 3.1) as a function of the delay time for three different average excitation powers and two temperatures in a logarithmic diagram. The inset shows the extracted coherence times as a function of the excitation power for $T = 1.4\,\mathrm{K}$ and 1.8 K.

As the stimulating laser pulses are directed from the opposite side, the 2P-DFG signal does not drop significantly after the time overlap but stays at a high level, although not maximal.

As the signal still raises slightly, the intensity of each measurement is normalized to 1 at a delay time of 1 ns. The exponential function $I_P^{\text{2P-DFG}}(t_{\text{delay}}) = a_i \exp(t_{\text{delay}}/t_{\text{coherence}})$ is fitted to each data set and the coherence times are extracted, and plotted in the inset in Fig. 7.5. It shows qualitatively, that the coherence time decreases for increasing excitation power and increasing temperature. More detailed experiments investigating the coherence times of the $1S$ exciton as a function of the temperature and excitation power will be performed in the future.

7.2.3 Polarization dependent measurements

The 2P-DFG intensity of the $1S$ exciton as a function of the linear polarization angles is measured for a fixed linear polarization angle $\theta = 0°$ of the stimulating ps laser. The linear polarization angle ψ of the excitation laser and φ of the 2P-DFG signal are varied from 0° to 360° degrees each in steps of 10°, as described in Sec. 3.5. As the excitonic signal is interfering with the $\chi^{(3)}$ signal, the polarization dependence of the exciton cannot be directly taken from the measurements, since the background signal needs to be subtracted for each spectrum. In order to achieve this, the intensity of the pixel at $E_{\text{DFG}} = 1.303\,\text{eV}$ [see Fig. 7.4(d)], which is at the same intensity level as the base of the excitonic signal on the $\chi^{(3)}$ signal, is subtracted from the maximal exciton intensity at the pixel at $E_{\text{DFG}} = 1.306\,\text{eV}$ for each spectrum of a distinct polarization setting. With this method, the polarization dependence of the $1S$ exciton is evaluated and shown in Fig. 7.6(b). It shows intensity maxima at $\psi/\varphi = 0°/0°$ and polarization settings shifted by 180° either in ψ or φ, which are distorted and stretched along the diagonal. The simulation plot is calculated according to Eq. (7.164) for a fixed stimulation polarization angle of $\theta = 0°$ and shown in Fig. 7.6(a). It has a good agreement with the experimental plot.

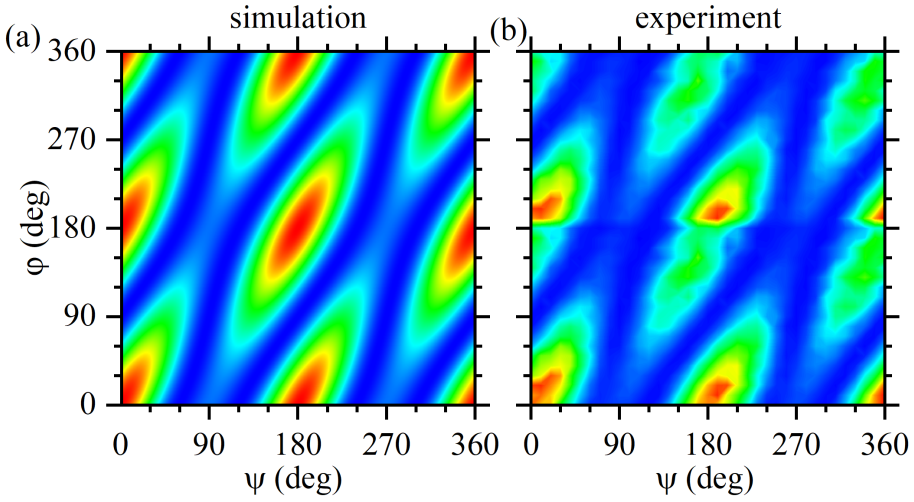

Figure 7.6 (a) Simulated [according to Eq. (7.164)] and (b) experimentally obtained 2P-DFG polarization dependence of the $1S$ exciton in the H2a sample (see Tab. 3.1) at zero field in the temporal overlap of the exciting and stimulating laser pulses, as shown in Fig. 7.4(d).

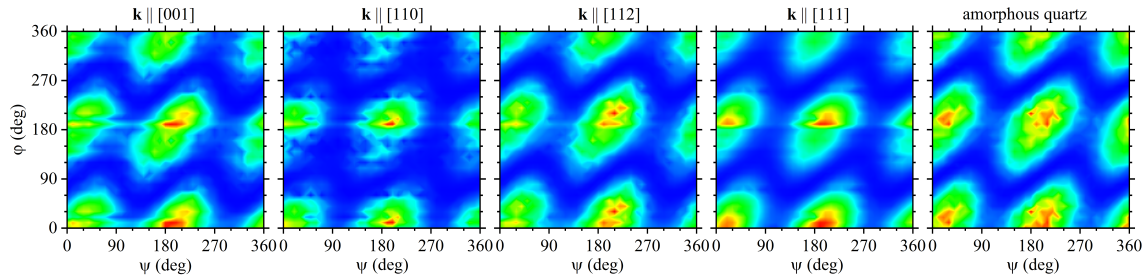

Figure 7.7 (a) Experimentally obtained 2P-DFG intensity of the $\chi^{(3)}$ signal at $B = 0$ and $t_{\mathrm{delay}} = 0$ as a function of ψ and φ for θ fixed to 0°. The polarization dependence is measured for **k** along the [001], [110], [112] and [111] in the H106a, H106b, H2b, and H2a samples (see Tab. 3.1), respectively. The right panel shows the same measurement in amorphous quartz at room temperature. This indicates, that the polarization dependence of the $\chi^{(3)}$ signal is independent of the crystal structure.

The polarization dependence of the $\chi^{(3)}$ signal is directly taken from the measurements at an energy of $E_{\mathrm{DFG}} = 1.303\,\mathrm{eV}$, as already used for subtraction for the evaluation of the $1S$ exciton polarization dependence as described above. It is plotted in the fourth contour plot in Fig. 7.7 for the same sample. It shows maxima at the same angle combinations as the excitonic polarization dependence, however, not as strongly distorted along the diagonal. It has been measured for multiple crystal orientations as well as in amorphous quartz at room temperature for $\theta = 0°$, as shown in the other diagrams in Fig. 7.7. It always shows the same polarization dependence and is therefore not dependent on the crystal structure. Up to now, no method was found to simulate the polarization dependence of the $\chi^{(3)}$ signal.

7.3 2P-DFG of higher n excitons

In this section, the 2P-DFG method is applied to yellow-series S and D excitons with higher principal quantum numbers. Compared to the $1S$ exciton these states exhibit larger line widths, as seen in Fig. 2.5, and are therefore expected to show smaller coherence times. The exciting fs laser is set to half of the $3S$ exciton energy but the second harmonic of its power spectrum covers the whole range from the $2S$ resonance to the bandgap.

Figure 7.8(a) shows the 2P-DFG spectra of higher n excitons in the H106 sample (excitation along $[1\bar{1}0]$, see Tab. 3.1) as a function of the delay time in the range of $-4.5\,\mathrm{ps}$ to $8\,\mathrm{ps}$. For this crystal orientation, SHG is forbidden, which demonstrates, that the 2P-DFG process is not as symmetry restrictive as the SHG process. If all linear polarization angles are equal, 2P-DFG represents an alternative method for two-photon absorption spectroscopy. The $\chi^{(3)}$ signal occurs at delay times between $-3.5\,\mathrm{ps}$ and $0.5\,\mathrm{ps}$ and vanishes after that. Several narrow lines remain and decay within a few ps. Figure 7.8(b) shows the spectral cuts at $0\,\mathrm{ps}$ and $3.3\,\mathrm{ps}$ delay time as marked by the horizontal red and orange lines in Fig. 7.8(a). At $0\,\mathrm{ps}$ the signal of the green $1S$ exciton and the yellow $2S$, $3S$, $3D$ and $4S$ excitons is seen. At $3.3\,\mathrm{ps}$ the 2P-DFG signal of the green $1S$ exciton has almost completely vanished. In contrast, the higher yellow excitons decay more slowly and their signal is still clearly visible. As expected from the decreasing line width for increasing principal quantum

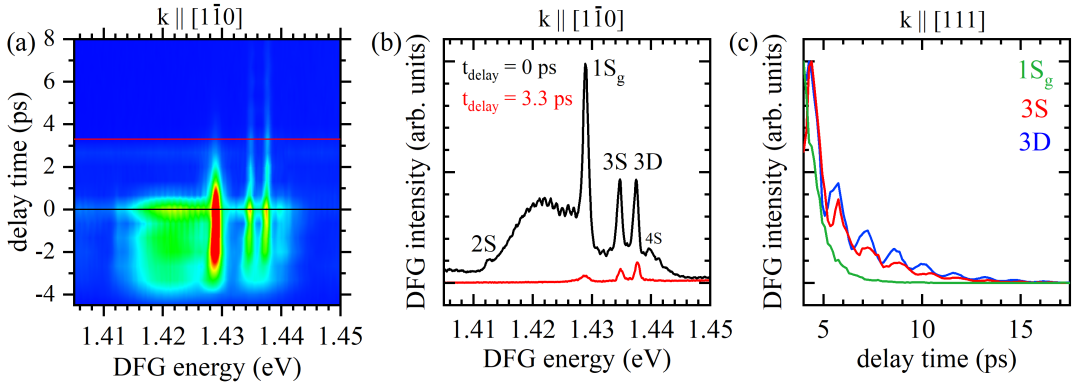

Figure 7.8 (a) Zero field 2P-DFG intensity of higher n excitons in the H106b sample (with $\mathbf{k} \parallel [1\bar{1}0]$, see Tab. 3.1) as a function of the DFG energy and for a delay time range from $t_{\mathrm{delay}} = -4.5\,\mathrm{ps}$ to 8 ps. (b) Spectral cuts at $t_{\mathrm{delay}} = 0\,\mathrm{ps}$ and 3.3 ps. (c) 2P-DFG intensity of the green $1S$ and yellow $3S$ and $3D$ excitons as functions of the delay time. This measurement is performed in the H2a (with $\mathbf{k} \parallel [111]$, see Tab. 3.1) sample for smaller delay time steps and larger integration times.

numbers scaling with n^{-3} [Kaz+14], the coherence time is expected to increase with the inverse of this power.

A cut along the delay time axis from a more detailed measurement is shown in Fig. 7.8(c) for the green $1S$ and yellow $3S$ and $3D$ excitons. The green $1S$ exciton shows a smooth exponential decay with a decay time of about 0.55 ps. The yellow $3S$ and $3D$ excitons have decay times of about 1.07 ps and 1.23 ps, respectively. Additionally, their decay is modulated by oscillations with a beat period of about 1.5 ps equivalent to an energy splitting of about 2.76 meV, which is in good agreement with their spectrally measured energy splitting of 2.744 meV as extracted from the SHG spectrum in Fig. 2.5(d). Measurements of the coherence times of higher n excitons as a function of the average excitation power are planned for the future.

7.4 Magnetic-field-induced quantum beats of 1S exciton

The physics of the $1S$ excitons in a magnetic field is already described in Sec. 5.1. The main points are shortly summarized in the following: The $1S$ exciton is a fourfold state consisting of three optically active Γ_5^+ orthoexciton states and a single pure spin-triplet Γ_2^+ paraexciton state, which is optically inactive and lies about 12.1 meV below the orthoexcitons due to the exchange interaction. Although future efforts will be done to detect a 2P-DFG signal of the paraexciton, it has not yet been achieved. Therefore we will only concentrate on the orthoexciton states in this section. In an externally applied magnetic field, the orthoexciton eigenstates are denoted by the magnetic quantum numbers $M = -1$ and $M = +1$, which exhibit a linear Zeeman splitting proportional to the magnetic field strength and the $M = 0$ state, which shows a weak quadratic shift to higher energies due to a repulsion with the paraexciton, as shown in Fig. 5.2(b).

In a magnetic field, the states are expected to show a beating behavior in the time domain

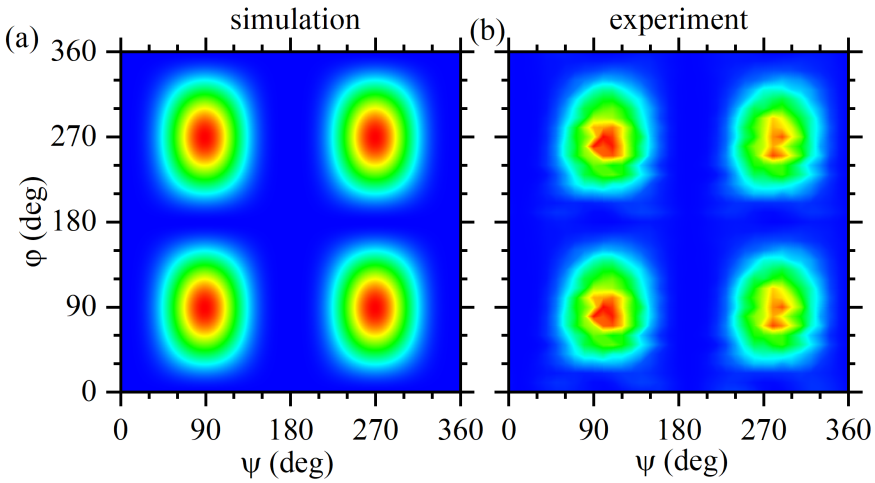

Figure 7.9 (a) Simulated [according to Eq. (7.166)] and (b) experimentally obtained 2P-DFG polarization dependence of the 1S exciton in the H106b sample (see Tab. 3.1) at $B = 10\,\mathrm{T}$ and $t_{\mathrm{delay}} = 0$.

with a frequency determined by the energy splitting of the states, which can be measured by the 2P-DFG method. At 10 T the $M = -1$ and $+1$ states are split by 962 µeV, which would result in a beat frequency of about $f = E/(\hbar 2\pi) \approx 232\,\mathrm{GHz}$ or a beat period of $T = 1/f \approx 4.3\,\mathrm{ps}$. Excitation with the 200 fs pulses is sufficiently short compared to the beat period at $B = 10\,\mathrm{T}$. This would not be the case if the ps laser would be used for excitation.

Just as it has been demonstrated in Sec. 5.3 for the SHG process to separate the signal of the $M = 0$ from the $M = \pm 1$ states by a specific linear polarization setting of incoming laser and outgoing SHG light, it is also possible to select the 2P-DFG signal of different eigenstates for certain polarization settings and therefore detect beats with different frequencies involving different combinations of the three eigenstates. We will distinguish between the following three cases: i) Measure the time-dependent 2P-DFG intensity while detecting only the $M = 0$ state, in which case no beating is expected. ii) The 2P-DFG signal of only the $M = +1$ and -1 states is detected, leading to beats with a single frequency. iii) 2P-DFG signal of all three states is detected resulting in irregular beats containing three different frequencies.

In order to find a suitable experimental geometry we consider the polarization diagrams of the two-photon processes in Fig. 7.3. For our experiments, we choose sample H106b (see Tab. 3.1), for which the laser light is directed along the $[1\bar{1}0]$ and the magnetic field along the [001] crystal axis. At $\psi = 55^\circ$ all three states are excited with a similar intensity. The three cases are then set using the linear polarization setting of θ and φ in the emission channel. Case i) is achieved for $\theta/\varphi = 90^\circ/90^\circ$, case ii) for $\theta/\varphi = 0^\circ/90^\circ$ and case iii) for $\theta/\varphi = 55^\circ/55^\circ$.

The excitonic 2P-DFG signal is measured for the described three cases at $B = 10\,\mathrm{T}$ as a function of the delay time for a range of $-9\,\mathrm{ps}$ to $60\,\mathrm{ps}$ shown in Fig. 7.10. Figure 7.10(a) shows case i) detecting only the $M = 0$ signal. As expected, no beats are observed after

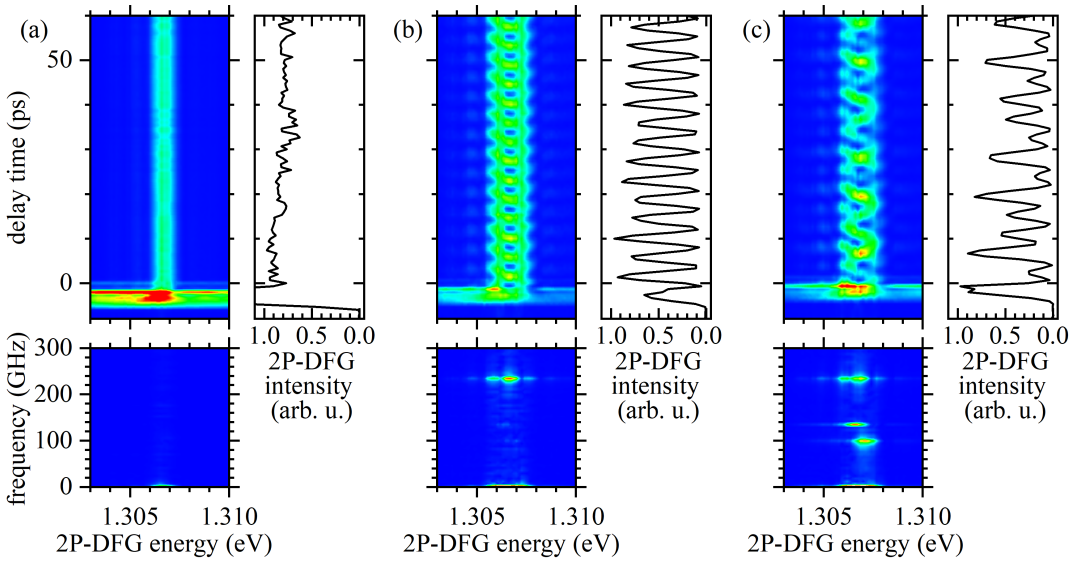

Figure 7.10 2P-DFG intensity of the 1S orthoexciton eigenstates in a magnetic field of 10 T in Voigt configuration in the H106b sample (see Tab. 3.1) as a function of delay time and DFG energy. The fs laser excites all three states with similar intensity with $\psi = 55°$, as shown in the lower panel in the second column in Fig. 7.3. (a) Detection of only $M = 0$ state at $\theta/\varphi = 90°/90°$ with no quantum beats. (b) Detection of $M = +1$ and $M = -1$ states at $\theta/\varphi = 0°/90°$ resulting in single frequency beats. (c) Detection of $M = 0$, $M = +1$ and $M = -1$ states at $\theta/\varphi = 55°/55°$ resulting in triple frequency beats.

the $\chi^{(3)}$ signal. In the time range of 60 ps the decay process is also not noticeable, as it takes several nanoseconds. Therefore the intensity seems to stay constant as also shown in the cartesian plot in the right panel of Fig. 7.10(a) representing the intensity along the cut at the central signal energy. The lower panel shows the Fourier transform (FT), which is calculated along the delay time axis for each pixel corresponding to a 2P-DFG energy. As no beating is observed, there is also no peak visible in the frequency domain.

Figure 7.10(b) represents case i), in which beats between the $M = +1$ and $M = -1$ states are observed, which contain a single frequency with a sin^2 shape corresponding to the energy splitting. The lower FT panel shows a frequency peak at about 233 GHz.

Figure 7.10(c) represents case iii) with irregular-looking beats clearly shown in the right panel along the cut in time containing three frequencies, which are visible in the lower FT panel. The high-frequency peak at 233 GHz corresponds to the beats between the $M = +1$ and -1 states, the second highest frequency peaks results from the beats between the $M = -1$ and $M = 0$ states and the lowest frequency peak corresponds the beat between the $M = +1$ and $M = 0$ states, as their energy splitting is slightly smaller than between the $M = -1$ and $M = 0$ states due to the quadratic shift of the $M = 0$ component moving closer in energy to the $M = +1$ state.

As the beat frequencies correspond to the splitting energy between the states, which are in turn dependent on the magnetic field, they should decrease for decreasing magnetic fields. Therefore the magnetic field series from 10 to 0 T in steps of 1 T is measured for a delay time range from −7 ps to 212 ps and shown in Fig. 7.11 for case iii).

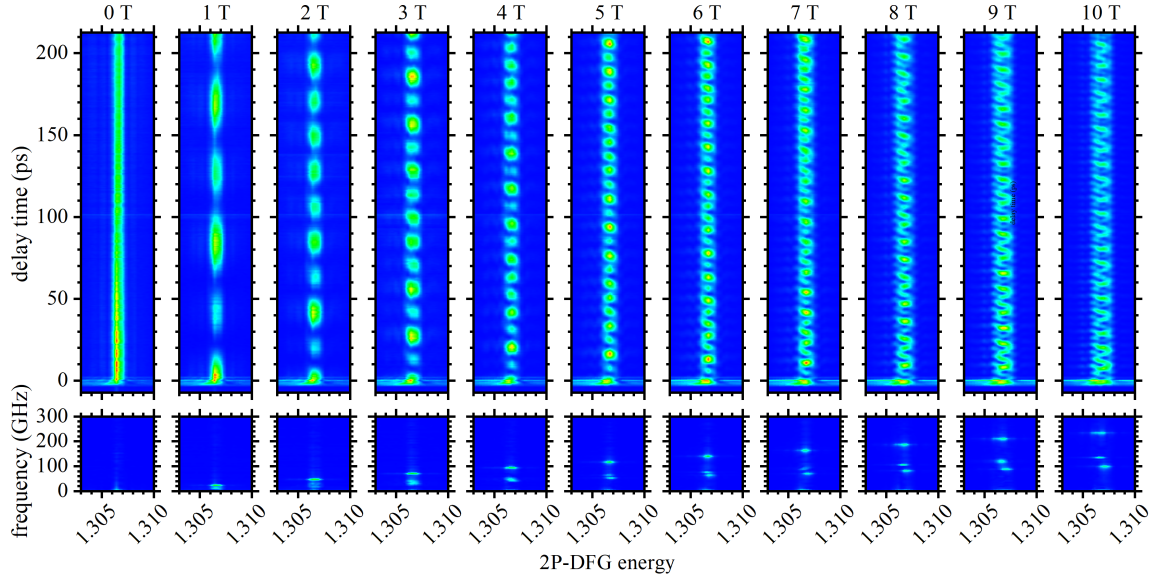

Figure 7.11 Magnetic field series of the triple frequency quantum beats from 0 to 10 T in steps of 1 T in the H106 sample (see Tab. 3.1) introduced in Fig. 7.10(c).

The irregularity of these three-level beats is most evident in the contour diagram for $B = 10\,\mathrm{T}$. The FT panel below shows clearly the three intensity peaks. The peaks in the FT diagrams occur spectrally in the overlap of the 2P-DFG signals of the states involved in the beating. The beats are therefore a result of the interference of the 2P-DFG signal of different states as a function of time. The highest frequency peak at about 233.5 GHz is associated with the beat between the $M = +1$ and -1 states, the middle frequency peak at 135.6 GHz with the beats between the $M = +1$ and $M = 0$ states and the lowest frequency peak at 98.5 GHz with the beat between the $M = -1$ and $M = 0$ states.

The frequencies resulting from the energy differences between the three states as a function of the magnetic field are expressed by

$$\Delta E_{+1,-1} = 2bB, \tag{7.169}$$

$$\Delta E_{+1,0} = bB - \frac{a^2B^2}{\varepsilon}, \tag{7.170}$$

$$\Delta E_{0,-1} = \frac{a^2B^2}{\varepsilon} + bB, \tag{7.171}$$

as derived from Eqs. (5.100) and (5.101) in Sec. 5.1. The two lower frequency peaks decrease for lower magnetic fields and at the same time get closer together in energy. The reason is the magnetic-field-induced quadratic shift of the $M = 0$ state, which converges to the mean energy value of the $M = -1$ and $M = +1$ states for decreasing magnetic fields.

The magnetic field dependence of the beat frequencies becomes evident in the FT panels below the main ones. All frequency peaks are fitted with Gaussians in the time domain and the fit parameter of the central position for each peak is plotted in Fig. 7.12 as a function of the magnetic field. A linear fit of the high-frequency peak according to Eq. (7.169)

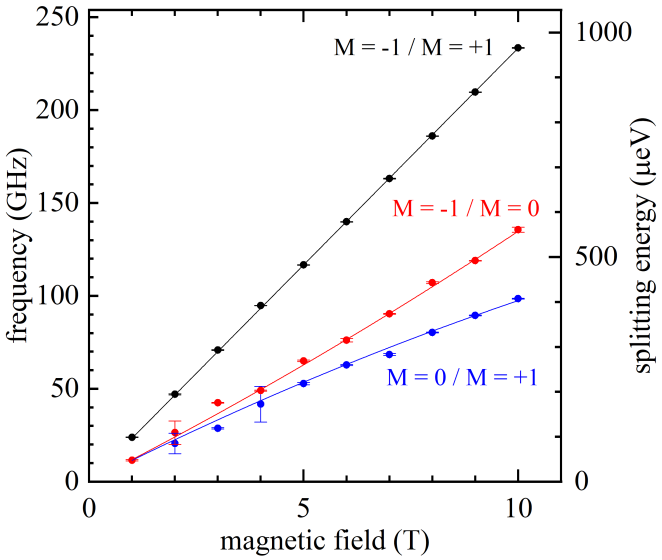

Figure 7.12 Frequency (left axis) and corresponding energy splitting (right axis) obtained from the FT panels of Fig. 7.11 displaying triple-frequency quantum beats as a function of the magnetic field. Dots represent experimentally obtained data with error bars resulting from the fit errors of the Gaussians in the frequency domain. Lines represent the fits according to Eqs. (7.169), (7.170) and (7.171).

yields a Zeeman splitting parameter of $b = 48.25 \pm 0.07$, which deviates by 0.3 % from the one obtained by SHG spectroscopy in Sec. 5.2. Fits of the two lower frequency peaks according to Eqs. (7.170) and (7.171), taking the fit value for b, yield the shift parameters $a_{+1,0} = 98 \pm 2$ and $a_{0,-1} = 95 \pm 4$. Their mean value deviates by 6 % from the one obtained by SHG spectroscopy in Sec. 5.2. It is therefore demonstrated, that the energy splittings can be measured with 2P-DFG experiments in the time domain to a high accuracy.

7.5 Conclusion

In this chapter, we have demonstrated 2P-DFG as a nonlinear optical technique for measuring time-dependent phenomena of excitons. The extensive group theoretical derivation of the polarization selection rules for the SHG process from the three previous chapters is extended to the 2P-DFG process by exchanging the single-photon process in the emission channel by a two-photon process with the linear polarization angles of the stimulating ps laser light θ and of the DFG light φ. The additional photon in the emission channel compared to SHG provides an additional degree of freedom for addressing states of various symmetries. As the 2P-DFG process is not as symmetry restrictive as the SHG process in this regard, it gives access to more exciton states. In the case of $\psi = \theta = \varphi$, 2P-DFG has the same selection rules as two-photon absorption and is therefore an alternative method for two-photon spectroscopy. It is demonstrated in Fig. 7.8 by measuring the 2P-DFG spectrum of higher n exciton for excitation along the $[1\bar{1}0]$ direction in Cu_2O without external perturbations, which is forbidden for SHG. However, the $\chi^{(3)}$ signal represents a difficulty

for 2P-DFG spectroscopy as an alternative for two-photon spectroscopy for excitonic states with lifetimes below a few picoseconds, as it would require measuring the spectrum for short delay times. This would apply to 2P-DFG spectroscopy of green or blue-series excitons. Despite it, a suitable choice of linear polarization settings can improve the intensity ratio of the excitonic versus the $\chi^{(3)}$ signal.

The 2P-DFG intensity as a function of the three linear polarization angles has been explicitly derived for the Γ_5^+ component of yellow-series S and D excitons in absence of any external perturbations and plotted in 2D diagrams for fixed θ. Measurements for the 2D polarization diagrams for the same case have resulted in a good agreement between theory and experiment. Although the polarization selection rules for the $\chi^{(3)}$ signal have not been derived, its polarization diagrams are measured for various crystal orientations and for amorphous quartz and with and without an applied magnetic field. In all cases, the resulting polarization diagrams show the same dependence. Therefore the conclusion is drawn, that the polarization dependence of the $\chi^{(3)}$ signal does not dependent on the crystal structure, which makes it predictable for future experiments.

The time dependence of the yellow $1S$ exciton is measured for stimulation laser light directed from the same and opposite direction as the excitation laser light. For the case of a parallel excitation and stimulation, the 2P-DFG signal drops significantly after the time overlap of both laser pulses and builds up to the maximum signal within 1 to 2 ns, before it starts to decay. Excitation and stimulation from opposite directions enable measuring a decay process for the 2P-DFG signal without an initial drop and build-up of the signal. This confirms the phase matching condition $2\mathbf{k}_{\text{exc.}} - \mathbf{k}_{\text{stim.}} = \mathbf{k}_{\text{DFG}}$. Therefore the opposite excitation-stimulation geometry was adapted during these investigations and is suggested for future experiments. The time dependence for the yellow $1S$ exciton is additionally measured for average excitation powers between 20 and 40 mW. A decrease of the coherence time from 3.488 ns to 3.138 ns is demonstrated qualitatively for increasing excitation power within the measured excitation power range at a temperature of 1.4 K. The coherence time at an excitation power of 40 mW has dropped by 18 % once the temperature has been increased to 1.8 K.

The described method is applied to higher n excitons. The 2P-DFG spectrum of the yellow $2S$, $3S$, $3D$ and $4S$ as well as the green $1S$ exciton is measured. The resolution of even higher n excitons is limited by the spectral width of the stimulating laser pulses. The coherence time for the yellow $3S$ and $3D$ excitons is measured to be larger than that of the green $1S$ exciton.

Magnetic-field-induced beats of the yellow $1S$ exciton, which is split into the $M = +1, 0$ and -1 eigenstates, are detected in time-dependent 2P-DFG measurements. At a polarization setting of $\psi/\theta/\varphi = 90°/90°/90°$ the 2P-DFG signal of only the $M = 0$ state is detected and no beats are observed. At $\psi/\theta/\varphi = 55°/0°/90°$ and $B = 10$ T beats between the $M = +1$ and -1 states with a single frequency of 233 GHz are detected. The beat frequency is measured to be proportional to the magnetic field due to the linear Zeeman splitting of both states. At $\psi/\theta/\varphi = 55°/55°/55°$ beats between all three states with frequencies of 233.5 GHz, 135.6 GHz and 98.5 GHz are detected at 10 T. It is possible to measure beats with a high-intensity contrast, although the involved resonance lines cannot be resolved spectrally.

More extensive coherence time measurements of the yellow $1S$ and higher n excitons as a function of the average excitation power and temperature are planned for the future.

Moreover, the coherence times of yellow P excitons will be measured by 1P-DFG and compared to the coherence times of S and D excitons. For the correct geometry for future 1P-DFG and 2P-DFG experiments, the stimulating laser pulses have to be directed from the opposite direction relative to the excitation pulses. With this geometry new attempts to measure the 2P-DFG signal of the $1S$ paraexciton will be made, in order to look for hints of Bose-Einstein condensation, which has been recently demonstrated in Ref. [Mor+22]. This method will also be applied to excitonic states in other semiconductor materials, such as ZnSe and GaAs.

The experimental setup allows for other two-color experiments such as sum frequency generation. By varying the wavelength ratios of both lasers, one can tune the sharp excitation on the upper polariton branch along k. Recently, a two-color experiment was performed in order to check the power-dependent influence of three-photon excited electron plasma on the line width and spectral position of yellow P excitons. The fs-laser has passed a BBO crystal generating second harmonic light with a Gaussian spectral shape covering the Rydberg P excitons, of which the absorption dips are detected on the Gaussian power spectrum. By setting the SHG of the ps-laser for one case between the $1S$ and $2S$ excitons, which is a spectral region without electronic states, a plasma is induced by three-photon excitation, which blocks the Rydberg excitons and reduces the spectral absorption dips. This effect is compared to the second case, in which the two-photon energy of the ps-pulse is set to the $3S$ energy. In this case, the three-photon process is comparable to the first case, but additionally $3S$ excitons are excited, which additionally interact with the P exciton and influence the absorption spectrum.

A similar experiment can be made for investigating the time-dependent effects of an electron-hole plasma on S and D excitons by using the ps pulses to measure the SHG spectrum of S and D excitons. The two-photon energy of additional fs pulses can be set between the $1S$ and $2S$ energy in order to create a plasma by three-photon excitation. By delaying the ps pulses the exciton-plasma interaction can be measured as a function of time.

Chapter 8

Conclusions and outlook

In this work, we have presented extensive experimental results on second harmonic generation (SHG) spectroscopy of yellow and blue-series excitons in Cu_2O under the influence of magnetic fields. Additionally, the higher-order process of difference frequency generation with two-photon excitation (2P-DFG) was used for measurements of exciton coherence times and magnetic-field-induced quantum beats of yellow-series excitons.

SHG mechanisms are characterized by their polarization diagrams, which are typically shown as polar plots representing the SHG intensity on the radial axis as a function of the linear polarization angle ψ of the incoming laser light. The outgoing SHG light is detected with a linear polarization angle φ, which is parallel or perpendicular to the tuned angle ψ. These two configurations are in most cases sufficient to explain the underlying mechanism. However, the full picture is given if the SHG intensity is measured for all possible combinations of ψ and φ and plotted in 2D diagrams, in which the intensity is represented by a color scale. The experimental acquisition of the full polarization diagrams works well with the fixed wavelength fs pulse method, as the diagrams are obtained for several exciton lines with just one measurement. This gives a large time advantage compared to the narrow bandwidth ps and ns pulses, as they only allow the measurement of the polarization dependence for one exciton resonance at a time.

The polarization diagrams are not only obtained experimentally but also simulated using the point group tables of Koster et al. [Kos+63]. Mund et al. have already derived the polarization selection rules for yellow-series S and P excitons [Mun+18]. Here, we have extended the derivations of polarization selection rules to magnetic-field-induced SHG considering various mechanisms of the Zeeman effect (ZE) and magneto-Stark effect (MSE) involving electric dipole (ED), electric quadrupole (EQ) and magnetic dipole (MD) transitions. Further extensions to magnetic-field-activated dark paraexcitons and to the process of difference frequency generation with two-photon excitation are accomplished. By simulating the polarization diagrams for all possible mechanisms and sample orientations, as shown in Figs. 4.5, 4.7 and 4.10, the most suitable experimental orientation can be quickly found.

This novel approach offers significant benefits for controlling the specific mechanisms contributing to the measured SHG signal. In particular, it allows us to suppress all mechanisms in the SHG spectrum but the one of interest to study its distinct spectral features. An example of this approach is shown in Fig. 4.12, in which SHG spectra of yellow-series excitons are depicted, which are purely induced by a magnetic field due to the Zeeman effect or the magneto-Stark effect. This allowed us to study how the ratio of the intensity contributions of both mechanisms scales with the principal quantum number n. As states of different symmetry also exhibit a characteristic polarization dependence, it allows to suppress SHG

contributions of a certain subset of excitonic states. This allowed choosing certain ψ/φ settings for the detection of the Rydberg series of dark paraexcitons, as a large subset of bright orthoexcitons could be suppressed, which would otherwise overpower the small SHG signals of their dark counterparts. Cu_2O has been the ideal material for the demonstration of this method, as it is characterized by the point group O_h of the highest symmetry and offers a rich spectrum of narrow excitonic states.

In chapter 4 the fixed wavelength femtosecond pulse method described in Sec. 3.3 was used in order to measure the SHG spectra of $n \geq 3$ excitons of the yellow series with spectral resolutions of 80 µeV. The laser light was directed along the high-symmetry crystal axis $[1\bar{1}0]$ in order to suppress crystallographic SHG, which has already been investigated in Ref. [Mun+18]. The magnetic field was directed along the [110] crystal axis, in order to induce the SHG via the dominant ZE and MSE, which are measured at polarization settings of $\psi/\varphi = 0°/90°$ and $\psi/\varphi = 45°/0°$, respectively. The mentioned experimental orientation is the most suitable for the presented experiments. It was chosen based on all simulated polarization diagrams, which have been plotted for all SHG processes and crystal orientations. SHG spectra for varying magnetic fields up to 10 T are measured at both of these settings revealing their spectral features. The ZE involves magnetic-field-coupled Γ_5^+ excitons, which are two-photon excited by an ED-ED transition and emit light via an EQ transition. The MSE involves the same excitation process, but the effective electric field couples the Γ_5^+ states to Γ_4^- states, which then emit light via an ED transition. The ZE and MSE polarization diagrams are measured on the $3S$ and $3D$ excitons, respectively, as they are almost purely induced by the according mechanism. In the general case, an interference of both effects occurs. The polarization dependence at a random exciton line in the $n = 4$ multiplet is measured and modeled successfully including the interfering field amplitudes of the ZE and MSE processes. Several weaker mechanisms have been identified, which involve the magnetic and electric field coupling of Γ_1^+, Γ_3^+ and Γ_4^+ exciton states and other higher-order transitions such as the MD. Their polarization diagram is measured for a fixed $\psi = 90°$. The ratio between the MSE and ZE-induced SHG intensity is found to scale with a power of about 6.4 with the principle quantum number.

Chapter 5 reveals results on SHG spectroscopy of dark paraexcitons, which are pure spin-triplet states with Γ_2^+ symmetry and do not couple to the light field. They gain oscillator strength due to a magnetic field mixing with optically active orthoexcitons. The spectrum of the $1S$ para and orthoexcitons is measured at 10 T at a resolution of 10 µeV using the fixed wavelength method. In this case, not the fs but the ps pulses are used in order to obtain the SHG spectra, as their power spectrum is sufficiently broad to cover the three orthoexciton split at 10 T. But the ps pulses are at the same time narrow enough not to excite the orthoexcitons when set to half of the paraexciton energy, as the 300 times stronger orthoexciton SHG signals would overpower the weak paraexciton signals. Using the group theory method, the polarization selection rules are derived for the dominant SHG mechanism, which involves an ED-ED excitation and an EQ emission. The magnetic-field-induced energy shift of all four states is measured in order to extract the g factors of the VB and the CB, as well as the mixing parameters between the $|M| = 0$ and $|M| = 1$ components. Direct excitation of the Γ_2^+ is shown to be possible via an EQ-MD transition. For the SHG process, the magnetic field admixture of the Γ_5^+ states is still needed for the EQ emission. The polarization diagram is measured in a sample oriented such, that the laser light is directed along the [001] crystal axis, in which the dominant SHG mechanism

with an ED-ED excitation is suppressed, as the EQ-MD mechanism is expected to be much weaker. These mechanisms are clearly identified by measuring their SHG intensity as a function of the magnetic field. The ED-ED SHG mechanism is expected to scale with B^4 and the EQ-MD with B^2. The experimentally obtained values for the power parameter are found to deviate by -7% for the ED-ED and by 25% for the EQ-MD SHG process from the expected one.

The understanding of the polarization selection rules, which are tested and verified on the $1S$ para and ortho excitons, are exploited in order to measure the Rydberg series of paraexcitons up to $n = 6$. The SHG contributions of a large subset of Rydberg exciton states are suppressed by choosing suitable polarization angle settings in order to detect the rather weak paraexciton signals. Plotting the second derivatives of the SHG spectra as a function of the magnetic field instead of the real SHG spectra has helped to identify the weak paraexciton SHG signals. A peculiarity is found for the $2S$ paraexciton, which is energetically located above its orthoexciton against the expectation based on the Hund's rules. This results from the mixing of the yellow $2S$ orthoexciton with the green $1S$ orthoexciton. The experimentally obtained ortho-para splitting energies turned out to be in good agreement with the calculated values by Schweiner et al. [Sch+17b], which were performed four years prior to our experimental study. Further numeric investigations are performed by Rommel et al. [Rom+21], quantifying the influence of different effects on the energy splitting of ortho and para states, such as the spin-orbit coupling.

The excitons of the blue series are studied at an unprecedented level of detail using SHG spectroscopy in magnetic fields and the results are presented in chapter 6. The SHG polarization selection rules derived for yellow excitons in chapter 4 are directly applied to blue excitons, as blue S and yellow P as well as blue P and yellow S excitons have the same optically active symmetry components. The MSE and the ZEs of Γ_4^- and Γ_5^+ excitons are identified as the SHG-inducing mechanism in a magnetic field. The SHG spectrum induced by each one of these mechanisms, while suppressing all others, is measured. It allows to evaluate the magnetic-field-induced energy shifts of the $1S$, $2S$ and $2P$ resonances and extract the reduced exciton mass of $0.226\,m_0$ and the exciton radius of 1.79 nm from the data. Magneto-excitons in the high-field regime are detected up to $n = 8$. Their magnetic-field-induced energy shift approaches a linear trend for higher n and increasing magnetic fields. An analysis yields the anisotropic effective mass of CB electrons ranging from $0.304\,m_0$ along the [111] to $0.452\,m_0$ along the [001] crystal axis. As the oscillator strength of blue transitions is 7 orders of magnitude larger than that of yellow transitions, the polariton effect is considered for the calculations of the dispersion relation of excitons of the blue series by H. Stolz. SHG represents a sharp k excitation on the upper polariton branch. The calculations enabled to quantify the polariton shift of the $1S$ exciton, which is observed about 13 meV higher compared to the transverse $1S$ exciton energy. Furthermore, the Rydberg energy of 57.1 meV and the bandgap of 2.6326 eV is obtained.

In chapter 7 we have presented nonlinear optical measurements of yellow-series excitons in the time domain using difference frequency generation with two-photon excitation (2P-DFG). The fs pulses with a photon energy of 1.016 eV excites a population of yellow $1S$ excitons via a two-photon transition. Additional ps pulse set to 0.726 eV, which are directed onto the sample, stimulate the 2P-DFG signal at 1.306 eV, which is spectrally resolved and detected. With this method a coherence time of about 3.5 ns is measured for the $1S$ exciton at an average excitation power of 20 mW. This is shown in the inset of Fig. 7.5. A reduction

of the coherence time is qualitatively observed with increasing excitation powers and rising temperatures. The $3S$ and $3D$ excitons exhibit coherence times of just over one ps as shown in Fig. 7.8(c). In addition to the decay of their 2P-DFG signals, oscillations are observed with a beat period of about 1.5 ps corresponding to their energy splitting. The polarization diagram for a fixed linear polarization angle of the ps laser at $\theta = 0^\circ$ and varying ψ and φ is measured for the $1S$ exciton for $\mathbf{k}$ along the [111] crystal axis and is in agreement with the simulation indicating the successful extension of the SHG polarization selection rules to the 2P-DFG process by considering an additional photon in the emission channel.

The first experiments have been performed according to the experimental geometry shown in Fig. 7.1(a), in which the ps pulses are directed nearly parallel with the fs pulses onto the sample. Although this geometry resulted in sufficiently large signals, the 2P-DFG intensity of the $1S$ exciton dropped after the temporal overlap of both pulses and has then increased to its maximum for delay times of about 1.7 ns followed by an exponential decay. But according to the phase matching condition in Eq. (2.21), the stimulating pulses have to be directed anti-parallel to the exciting pulses, as shown in Fig. 7.1(b). Using this geometry, the sudden drop of 2P-DFG intensity after the time overlap of both pulses did not occur.

By applying a magnetic field in Voigt geometry, the $1S$ ortho exciton splits into the three eigenstates designated by their magnetic quantum numbers $M = -1$, $M = 0$, and $M = +1$. For excitation along the $[1\bar{1}0]$ and the magnetic field along the [001] crystal axis, all three exciton states are excited at $\psi = 55^\circ$ at about equal intensities. Choosing different polarization settings θ/φ for the emission channel allows to control, which states contribute to the 2P-DFG signal, as they exhibit different polarization dependencies. Measuring the 2P-DFG intensity as a function of time at $\theta/\varphi = 90^\circ/90^\circ$ leads to a simple decay of the signal with the coherence time in the range of several ns. A setting of $\theta/\varphi = 0^\circ/90^\circ$ leads to 2P-DFG signals of the $M = -1$ and $M = +1$ states, which beat with a single frequency of 233.5 GHz corresponding to their energy splitting of 962 meV at 10 T. At $\theta/\varphi = 55^\circ/55^\circ$ all three states contribute to the 2P-DFG signal resulting in quantum beats containing three frequencies, which can be obtained from the FFT analysis. The frequencies are obtained for a series of magnetic fields and the magnetic field mixing parameters a and b are derived, deviating by 0.3 % and 6 % from the values obtained in Sec. 5.2.

2P-DFG turned out to be a useful method for nonlinear optical measurements of excitons in the time domain. Compared to SHG, it has three instead of just two degrees of freedom considering the linear polarization angles and thus offers more possibilities to distinguish between different mechanisms. This property can be used in the attempt of measuring excitons involving transitions from the third highest VB with Γ_3^+ symmetry, as they can clearly be distinguished from Γ_5^+ VB exciton states. This is not possible using SHG, as Γ_3^+ and Γ_5^+ states exhibit the same polarization dependence, as can be seen in Fig. 4.5. Additional efforts will be made to search for 2P-DFG paraexciton signals using the anti-parallel geometry for excitation and stimulation in order to detect hints of Bose-Einstein condensation at temperatures below 1.4 K. We propose to apply this method to the excitons of other semiconductors such as ZnSe. One difficulty is given by the $\chi^{(3)}$ signal, which occurs in the temporal overlap of both laser pulses. If the coherence times of the investigated states are in the range of a few ps and below, their 2P-DFG signal has to be measured at $t_{\mathrm{delay}} = 0$ leading to an interference with the $\chi^{(3)}$ signal. However, the $\chi^{(3)}$ signal exhibits the same polarization dependence independent of the symmetry of the material. Additionally, it

vanishes for certain polarization settings, which would allow measuring pure exciton signals at $t_{\mathrm{delay}} = 0$.

The setup used for 2P-DFG experiments offers possibilities for further two-color experiments in the time domain involving the energetically tunable ps and fs pulses. As an example, the influence of an electron plasma on the Rydberg excitons can be investigated as a function of the delay time. The ps pulses inject an electron plasma via a two or three-photon excitation. The fs pulses probe the Rydberg excitons by measuring their SHG signals in order to look for spectral broadening and shifting of the resonance lines or the reduction in their intensity.

Appendix A

Point group theory tables

$D_0^{\pm}$	Γ_1	$D_{1/2}^{\pm}$	Γ_6
$D_1^{\pm}$	Γ_4	$D_{3/2}^{\pm}$	Γ_8
$D_2^{\pm}$	$\Gamma_3 + \Gamma_5$	$D_{5/2}^{\pm}$	$\Gamma_7 + \Gamma_8$
$D_3^{\pm}$	$\Gamma_2 + \Gamma_4 + \Gamma_5$	$D_{7/2}^{\pm}$	$\Gamma_6 + \Gamma_7 + \Gamma_8$
$D_4^{\pm}$	$\Gamma_1 + \Gamma_3 + \Gamma_4 + \Gamma_5$	$D_{9/2}^{\pm}$	$\Gamma_6 + 2\Gamma_8$
$D_5^{\pm}$	$\Gamma_3 + 2\Gamma_4 + \Gamma_5$	$D_{11/2}^{\pm}$	$\Gamma_6 + \Gamma_7 + 2\Gamma_8$
$D_6^{\pm}$	$\Gamma_1 + \Gamma_2 + \Gamma_3 + \Gamma_4 + 2\Gamma_5$	$D_{13/2}^{\pm}$	$\Gamma_6 + 2\Gamma_7 + 2\Gamma_8$

Figure A.1 Full rotation group compatibility table for O_h point group from Ref. [Kos+63].

O_h	E	$\bar{E}$	$8C_3$	$8\bar{C}_3$	$3C_2$ / $3\bar{C}_2$	$6C_4$	$6\bar{C}_4$	$6C_2'$ / $6\bar{C}_2'$	I	$\bar{I}$	$8S_6$	$8\bar{S}_6$	$3\sigma_h$ / $3\bar{\sigma}_h$	$6S_4$	$6\bar{S}_4$	$6\sigma_d$ / $6\bar{\sigma}_d$	Time Inv.	Bases
Γ_1^+	1	1	1	1	1	1	1	1	1	1	1	1	1	1	1	1	a	R
Γ_2^+	1	1	1	1	1	−1	−1	−1	1	1	1	1	1	−1	−1	−1	a	$(x^2-y^2)(y^2-z^2)(z^2-x^2)$
Γ_3^+	2	2	−1	−1	2	0	0	0	2	2	−1	−1	2	0	0	0	a	$(2z^2-x^2-y^2), \sqrt{3}(x^2-y^2)$
Γ_4^+	3	3	0	0	−1	1	1	−1	3	3	0	0	−1	1	1	−1	a	S_x, S_y, S_z
Γ_5^+	3	3	0	0	−1	−1	−1	1	3	3	0	0	−1	−1	−1	1	a	yz, xz, xy
Γ_1^-	1	1	1	1	1	1	1	1	−1	−1	−1	−1	−1	−1	−1	−1	a	$\Gamma_2^- \times \Gamma_2^+$
Γ_2^-	1	1	1	1	1	−1	−1	−1	−1	−1	−1	−1	−1	1	1	1	a	xyz
Γ_3^-	2	2	−1	−1	2	0	0	0	−2	−2	1	1	−2	0	0	0	a	$\Gamma_3^+ \times \Gamma_2^-$
Γ_4^-	3	3	0	0	−1	1	1	−1	−3	−3	0	0	1	−1	−1	1	a	x, y, z
Γ_5^-	3	3	0	0	−1	−1	−1	1	−3	−3	0	0	1	1	1	−1	a	$\Gamma_5^+ \times \Gamma_1^-$
Γ_6^+	2	−2	1	−1	0	$\sqrt{2}$	$-\sqrt{2}$	0	2	−2	1	−1	0	$\sqrt{2}$	$-\sqrt{2}$	0	c	$\phi(1/2,-1/2), \phi(1/2,1/2)$
Γ_7^+	2	−2	1	−1	0	$-\sqrt{2}$	$\sqrt{2}$	0	2	−2	1	−1	0	$-\sqrt{2}$	$\sqrt{2}$	0	c	$\Gamma_6^+ \times \Gamma_2^+$
Γ_8^+	4	−4	−1	1	0	0	0	0	4	−4	−1	1	0	0	0	0	c	$\phi(3/2,-3/2), \phi(3/2,-1/2)$ $\phi(3/2,1/2), \phi(3/2,3/2)$
Γ_6^-	2	−2	1	−1	0	$\sqrt{2}$	$-\sqrt{2}$	0	−2	2	−1	1	0	$-\sqrt{2}$	$\sqrt{2}$	0	c	$\Gamma_6^+ \times \Gamma_1^-$
Γ_7^-	2	−2	1	−1	0	$-\sqrt{2}$	$\sqrt{2}$	0	−2	2	−1	1	0	$\sqrt{2}$	$-\sqrt{2}$	0	c	$\Gamma_6^+ \times \Gamma_2^-$
Γ_8^-	4	−4	−1	1	0	0	0	0	−4	4	1	−1	0	0	0	0	c	$\Gamma_8^+ \times \Gamma_1^-$

Figure A.2 Character table for O_h point group from Ref. [Kos+63].

Γ_1	Γ_2	Γ_3	Γ_4	Γ_5	Γ_6	Γ_7	Γ_8	
Γ_1	Γ_2	Γ_3	Γ_4	Γ_5	Γ_6	Γ_7	Γ_8	Γ_1
	Γ_1	Γ_3	Γ_5	Γ_4	Γ_7	Γ_6	Γ_8	Γ_2
		$\Gamma_1+\Gamma_2+\Gamma_3$	$\Gamma_4+\Gamma_5$	$\Gamma_4+\Gamma_5$	Γ_8	Γ_8	$\Gamma_6+\Gamma_7+\Gamma_8$	Γ_3
			$\Gamma_1+\Gamma_3+\Gamma_4+\Gamma_5$	$\Gamma_2+\Gamma_3+\Gamma_4+\Gamma_5$	$\Gamma_6+\Gamma_8$	$\Gamma_7+\Gamma_8$	$\Gamma_6+\Gamma_7+2\Gamma_8$	Γ_4
				$\Gamma_1+\Gamma_3+\Gamma_4+\Gamma_5$	$\Gamma_7+\Gamma_8$	$\Gamma_6+\Gamma_8$	$\Gamma_6+\Gamma_7+2\Gamma_8$	Γ_5
					$\Gamma_1+\Gamma_4$	$\Gamma_2+\Gamma_5$	$\Gamma_3+\Gamma_4+\Gamma_5$	Γ_6
						$\Gamma_1+\Gamma_4$	$\Gamma_3+\Gamma_4+\Gamma_5$	Γ_7
							$\Gamma_1+\Gamma_2+\Gamma_3$ $+2\Gamma_4+2\Gamma_5$	Γ_8

Figure A.3 Multiplication table for O and T_d point groups from Ref. [Kos+63].

	$u_2 v_x^4$	$u_2 v_y^4$	$u_2 v_z^4$
ψ_{yx}^5	1	0	0
ψ_{xz}^5	0	1	0
ψ_{yz}^5	0	0	1

Figure A.4 Coupling coefficient table for $\Gamma_1 \otimes \Gamma_4 \to \Gamma_4$ from Ref. [Kos+63].

	$u_1^3 v_x^4$	$u_1^3 v_y^4$	$u_1^3 v_z^4$	$u_2^3 v_x^4$	$u_2^3 v_y^4$	$u_2^3 v_z^4$
ψ_x^4	$-1/2$	0	0	$\sqrt{3}/2$	0	0
ψ_y^4	0	$-1/2$	0	0	$-\sqrt{3}/2$	0
ψ_z^4	0	0	1	0	0	0
ψ_{yz}^5	$-\sqrt{3}/2$	0	0	$-1/2$	0	0
ψ_{xz}^5	0	$\sqrt{3}/2$	0	0	$-1/2$	0
ψ_{xy}^5	0	0	0	0	0	1

Figure A.5 Coupling coefficient table for $\Gamma_3 \otimes \Gamma_4 \to \Gamma_4 \oplus \Gamma_5$ from Ref. [Kos+63].

	$u_{-1/2}^6 v_{-1/2}^7$	$u_{-1/2}^6 v_{1/2}^7$	$u_{1/2}^6 v_{-1/2}^7$	$u_{1/2}^6 v_{1/2}^7$
ψ_2	0	$-1/\sqrt{2}$	$1/\sqrt{2}$	0
ψ_{yz}^5	$-i/\sqrt{2}$	0	0	$i/\sqrt{2}$
ψ_{xz}^5	$1/\sqrt{2}$	0	0	$1/\sqrt{2}$
ψ_{xy}^5	0	$-i/\sqrt{2}$	$-i/\sqrt{2}$	0

Figure A.6 Coupling coefficient table for $\Gamma_6 \otimes \Gamma_7 \to \Gamma_2 \oplus \Gamma_5$ from Ref. [Kos+63].

	$u_x^4 v_x^4$	$u_x^4 v_y^4$	$u_x^4 v_z^4$	$u_y^4 v_x^4$	$u_y^4 v_y^4$	$u_y^4 v_z^4$	$u_z^4 v_x^4$	$u_z^4 v_y^4$	$u_z^4 v_z^4$
ψ_1	$1/\sqrt{3}$	0	0	0	$1/\sqrt{3}$	0	0	0	$1/\sqrt{3}$
ψ_1^3	$-1/\sqrt{6}$	0	0	0	$-1/\sqrt{6}$	0	0	0	$\sqrt{2}/\sqrt{3}$
ψ_2^3	$1/\sqrt{2}$	0	0	0	$-1/\sqrt{2}$	0	0	0	0
ψ_x^4	0	0	0	0	0	$1/\sqrt{2}$	0	$-1/\sqrt{2}$	0
ψ_y^4	0	0	$-1/\sqrt{2}$	0	0	0	$1/\sqrt{2}$	0	0
ψ_z^4	0	$1/\sqrt{2}$	0	$-1/\sqrt{2}$	0	0	0	0	0
ψ_{yz}^5	0	0	0	0	0	$1/\sqrt{2}$	0	$1/\sqrt{2}$	0
ψ_{xz}^5	0	0	$1/\sqrt{2}$	0	0	0	$1/\sqrt{2}$	0	0
ψ_{xy}^5	0	$1/\sqrt{2}$	0	$1/\sqrt{2}$	0	0	0	0	0

Figure A.7 Coupling coefficient table for $\Gamma_4 \otimes \Gamma_4 \to \Gamma_1 \oplus \Gamma_3 \oplus \Gamma_4 \oplus \Gamma_5$ from Ref. [Kos+63].

	$u^4_x v^5_{yz}$	$u^4_x v^5_{xz}$	$u^4_x v^5_{xy}$	$u^4_y v^5_{yz}$	$u^4_y v^5_{xz}$	$u^4_y v^5_{xy}$	$u^4_z v^5_{yz}$	$u^4_z v^5_{xz}$	$u^4_z v^5_{xy}$
ψ_2	$1/\sqrt{3}$	0	0	0	$1/\sqrt{3}$	0	0	0	$1/\sqrt{3}$
ψ^3_1	$1/\sqrt{2}$	0	0	0	$-1/\sqrt{2}$	0	0	0	0
ψ^3_2	$1/\sqrt{6}$	0	0	0	$1/\sqrt{6}$	0	0	0	$-\sqrt{2}/\sqrt{3}$
ψ^4_x	0	0	0	0	0	$1/\sqrt{2}$	0	$1/\sqrt{2}$	0
ψ^4_y	0	0	$1/\sqrt{2}$	0	0	0	$1/\sqrt{2}$	0	0
ψ^4_z	0	$1/\sqrt{2}$	0	$1/\sqrt{2}$	0	0	0	0	0
ψ^5_{yz}	0	0	0	0	0	$1/\sqrt{2}$	0	$-1/\sqrt{2}$	0
ψ^5_{xz}	0	0	$-1/\sqrt{2}$	0	0	0	$1/\sqrt{2}$	0	0
ψ^5_{xy}	0	$1/\sqrt{2}$	0	$-1/\sqrt{2}$	0	0	0	0	0

Figure A.8 Coupling coefficient table for $\Gamma_4 \otimes \Gamma_5 \to \Gamma_2 \oplus \Gamma_3 \oplus \Gamma_4 \oplus \Gamma_5$ from Ref. [Kos+63].

	$u^5_{yz} v^6_{-1/2}$	$u^5_{yz} v^6_{1/2}$	$u^5_{xz} v^6_{-1/2}$	$u^5_{xz} v^6_{1/2}$	$u^5_{xy} v^6_{-1/2}$	$u^5_{xy} v^6_{1/2}$
$\psi^7_{-1/2}$	0	$-i/\sqrt{3}$	0	$-1/\sqrt{3}$	$i/\sqrt{3}$	0
$\psi^7_{1/2}$	$-i/\sqrt{3}$	0	$1/\sqrt{3}$	0	0	$-i/\sqrt{3}$
$\psi^8_{-3/2}$	$-i/\sqrt{6}$	0	$1/\sqrt{6}$	0	0	$i\sqrt{2}/\sqrt{3}$
$\psi^8_{-1/2}$	0	$i/\sqrt{2}$	0	$-1/\sqrt{2}$	0	0
$\psi^8_{1/2}$	$-i/\sqrt{2}$	0	$-1/\sqrt{2}$	0	0	0
$\psi^8_{3/2}$	0	$i/\sqrt{6}$	0	$1/\sqrt{6}$	$i\sqrt{2}/\sqrt{3}$	0

Figure A.9 Coupling coefficient table for $\Gamma_5 \otimes \Gamma_6 \to \Gamma_7 \oplus \Gamma_8$ from Ref. [Kos+63].

Bibliography

[And95] L. C. Andreani. "Optical transisitons, excitons, and polaritons in bulk and low-dimensional semiconductor structures." *in Confined Electrons and Photons: New Physics and Applications*. Plenum, New York, 1995, p. 57.

[Aßm+16] M. Aßmann, J. Thewes, D. Fröhlich, and M. Bayer. "Quantum chaos and breaking of all anti-unitary symmetries in Rydberg excitons." *Nature Materials* **15** (2016), pp. 741–745.

[Aßm+20] M. Aßmann and M. Bayer. "Semiconductor Rydberg Physics." *Advanced Quantum Technologies* **3** (2020), p. 1900134.

[Bal96] N. H. Balshaw. *Practical Cryogenics: An Introduction to Laboratory Cryogenics*. Oxford Instruments (UK), Scientific Research Division, 1996.

[Bar+48] J. Bardeen and W. H. Brattain. "The Transistor, A Semi-Conductor Triode." *Physical Review* **74** (1948), pp. 230–231.

[Bay+00] M. Bayer, O. Stern, A. Kuther, and A. Forchel. "Spectroscopic study of dark excitons in $In_xGa_{1-x}As$ self-assembled quantum dots by a magnetic-field-induced symmetry breaking." *Physical Review B* **61** (2000), pp. 7273–7276.

[Bec+18] M. A. Becker, R. Vaxenburg, G. Nedelcu, P. C. Sercel, A. Shabaev, M. J. Mehl, J. G. Michopoulos, S. G. Lambrakos, N. Bernstein, J. L. Lyons, T. Stöferle, R. F. Mahrt, M. V. Kovalenko, D. J. Norris, G. Rainò, and A. L. Efros. "Bright triplet excitons in caesium lead halide perovskites." *Nature* **553** (2018), pp. 189–193.

[Bee+87] F. Beerwerth and D. Fröhlich. "Investigation of paraexcitons in KI." *Physical Review B* **36** (1987), pp. 6239–6241.

[Bei+17] M. Beian, M. Alloing, R. Anankine, E. Cambril, C. G. Carbonell, A. Lemaître, and F. Dubin. "Spectroscopic signatures for the dark Bose-Einstein condensation of spatially indirect excitons." *Europhysics Letters* **119** (2017), p. 37004.

[Boy08] R. W. Boyd. *Nonlinear Optics*. New York: Academic Press, 2008.

[Bra+07] J. Brandt, D. Fröhlich, C. Sandfort, M. Bayer, H. Stolz, and N. Naka. "Ultranarrow Optical Absorption and Two-Phonon Excitation Spectroscopy of Cu_2O Paraexcitons in a High Magnetic Field." *Physical Review Letters* **99** (2007), p. 217403.

[Bra+09] J. Brandt, D. Fröhlich, C. Sandfort, M. Bayer, and H. Stolz. "Paraexciton polariton propagation beats in cuprous oxide." *physica status solidi (c)* **6** (2009), pp. 556–559.

[Bru+15] D. Brunne, M. Lafrentz, V. V. Pavlov, R. V. Pisarev, A. V. Rodina, D. R. Yakovlev, and M. Bayer. "Electric field effect on optical harmonic generation at the exciton resonances in GaAs." *Physical Review B* **92** (2015), p. 085202.

[Bru14] D. S. Brunne. “Optical harmonic generation at exciton resonances in GaAs, GaN, and Cu_2O semiconductors.” PhD thesis. TU Dortmund, 2014.

[Cer+64] M. Certier, J. B. Grun, and S. Nikitine. “Etude de l’effet Zeeman de la raie n=1 de la série jaune de Cu_2O à 20 °K.” *Journal de Physique* **25** (1964), pp. 361–365.

[Che+14] A. Chernikov, T. C. Berkelbach, H. M. Hill, A. Rigosi, Y. Li, B. Aslan, D. R. Reichman, M. S. Hybertsen, and T. F. Heinz. “Exciton Binding Energy and Nonhydrogenic Rydberg Series in Monolayer WS_2.” *Physical Review Letters* **113** (2014), p. 076802.

[Das+04] G. Dasbach, D. Fröhlich, R. Klieber, D. Suter, M. Bayer, and H. Stolz. “Wavevector-dependent exchange interaction and its relevance for the effective exciton mass in Cu_2O.” *Physical Review B* **70** (2004), p. 045206.

[Das03] G. Dasbach. “Spectroscopy of polaritonic excitations in semiconductors.” PhD thesis. TU Dortmund, 2003.

[Dau+66] A. Daunois, J. L. Deiss, and B. Meyer. “Étude spectrophotométrique de l’absorption bleue et violette de Cu_2O.” *Journal de Physique* **27** (1966), pp. 142–146.

[Dem10] W. Demtröder. *Experimentalphysik 3*. Springer-Lehrbuch. Berlin, Heidelberg: Springer, 2010.

[Dho+20] S. J. Dhoble and G. B. Nair. *The Fundamentals and Applications of Light-Emitting Diodes: The Revolution in the Lighting Industry*. Elsevier Science, 2020.

[Dre+08] M. S. Dresselhaus, G. Dresselhaus, and A. Jorio. *Group Theory: Application to the Physics of Condensed Matter*. Berlin, Heidelberg: Springer, 2008.

[Ell61] R. J. Elliott. “Symmetry of Excitons in Cu_2O.” *Physical Review* **124** (1961), pp. 340–345.

[Far+20a] A. Farenbruch, D. Fröhlich, D. R. Yakovlev, and M. Bayer. “Two-photon absorption and second harmonic generation of 1S para- and orthoexcitons in Cu_2O coupled by a magnetic field.” *Physical Review B* **102** (2020), p. 115203.

[Far+20b] A. Farenbruch, J. Mund, D. Fröhlich, D. R. Yakovlev, M. Bayer, M. A. Semina, and M. M. Glazov. “Magneto-Stark and Zeeman effect as origin of second harmonic generation of excitons in Cu_2O.” *Physical Review B* **101** (2020), p. 115201.

[Far+20c] A. Farenbruch, D. Fröhlich, D. R. Yakovlev, and M. Bayer. “Rydberg Series of Dark Excitons in Cu_2O.” *Physical Review Letters* **125** (2020), p. 207402.

[Far+21] A. Farenbruch, D. Fröhlich, H. Stolz, D. R. Yakovlev, and M. Bayer. “Second-harmonic generation of blue series excitons and magnetoexcitons in Cu_2O.” *Physical Review B* **104** (2021), p. 075203.

[Far18] A. Farenbruch. “Erzeugung der zweiten Harmonischen an Exzitonen in Cu_2O.” M. Sc. thesis. TU Dortmund, 2018.

[Feh+82] G. W. Fehrenbach, W. Schäfer, J. Treusch, and R. G. Ulbrich. "Transient Optical Spectra of a Dense Exciton Gas in a Direct-Gap Semiconductor." *Physical Review Letters* **49** (1982), pp. 1281–1284.

[Fra+61] P. A. Franken, A. E. Hill, C. W. Peters, and G. Weinreich. "Generation of Optical Harmonics." *Physical Review Letters* **7** (1961), pp. 118–119.

[Fre+08] M. French, R. Schwartz, H. Stolz, and R. Redmer. "Electronic band structure of Cu_2O by spin density functional theory." *Journal of Physics: Condensed Matter* **21** (2008), p. 015502.

[Fre+09] M. French, R. Schwartz, H. Stolz, and R. Redmer. "Electronic band structure of Cu_2O by spin density functional theory." *Journal of Physics: Condensed Matter* **21** (2009), p. 015502.

[Fre31] J. Frenkel. "On the Transformation of light into Heat in Solids. I." *Physical Review* **37** (1931), pp. 17–44.

[Frö+06] D. Fröhlich, J. Brandt, C. Sandfort, M. Bayer, and H. Stolz. "High resolution spectroscopy of excitons in Cu_2O." *physica status solidi (b)* **243** (2006), pp. 2367–2374.

[Frö+18] D. Fröhlich and M. Bayer. "Emission of Cu_2O Paraexcitons Confined by a Strain Trap: Hints of a Bose–Einstein Condensate?" *Physics of the Solid State* **60** (2018), pp. 1600–1605.

[Frö+79] D. Fröhlich, R. Kenklies, C. Uihlein, and C. Schwab. "Assignment of the Even-Parity Excitons in Cu_2O." *Physical Review Letters* **43** (1979), pp. 1260–1263.

[Frö+82] D. Fröhlich and R. Kenklies. "Polarization Dependence of Two-Photon Magnetoabsorption of the 1S Exciton in Cu_2O." *physica status solidi (b)* **111** (1982), pp. 247–253.

[Frö+87] D. Fröhlich, K. Reimann, and R. Wille. "Time-Resolved Two-Photon Emission in Cu_2O." *Europhysics Letters* **3** (1987), p. 853.

[Frö+89] D. Fröhlich, S. Kirchhoff, P. Köhler, and W. Nieswand. "Three-photon difference-frequency spectroscopy of polaritons in alkali halides." *Physical Review B* **40** (1989), pp. 1976–1978.

[Frö+91] D. Fröhlich, A. Kulik, B. Uebbing, A. Mysyrowicz, V. Langer, H. Stolz, and W. von der Osten. "Coherent propagation and quantum beats of quadrupole polaritons in Cu_2O." *Physical Review Letters* **67** (1991), pp. 2343–2346.

[Frö+94] D. Fröhlich, M. Itoh, and C. Pahlke-Lerch. "Two-photon spectroscopy of odd-parity states." *Physical Review Letters* **72** (1994), pp. 1001–1003.

[Gal94] T. F. Gallagher. *Rydberg Atoms*. Cambridge: Cambridge University Press, 1994.

[Got+97] T. Goto, M. Y. Shen, S. Koyama, and T. Yokouchi. "Erratum: Bose-Einstein statistics of orthoexcitons generated by two-photon resonant absorption in cuprous oxide [Phys. Rev. B 55, 7609 (1997)]." *Physical Review B* **56** (1997), pp. 4284–4284.

[Gro+52] E. F. Gross and I. A. Karryjew. “The optical spectrum of the exciton.” *Doklady Akademii Nauk SSSR* (1952), pp. 471–474.

[Gro56] E. F. Gross. “Optical spectrum of excitons in the crystal lattice.” *Il Nuovo Cimento (1955-1965)* **3** (1956), pp. 672–701.

[Gro62] E. F. Gross. “Excitons and their motion in crystal lattices.” *Soviet Physics Uspekhi* **5** (1962), p. 195.

[Gru16] M. Grundmann. *The Physics of Semiconductors: An Introduction Including Nanophysics and Applications*. Graduate Texts in Physics. Cham: Springer International Publishing, 2016.

[Han+10] E. Hanamura, Y. Kawabe, and A. Yamanaka. *Quantum Nonlinear Optics*. Springer Berlin Heidelberg, 2010.

[Han+98] L. Hanke, J. Uhlenhut, D. Fröhlich, and H. Stolz. “Time-Resolved Stimulated Two-Photon Emission in Cu_2O.” *physica status solidi (b)* **206** (1998), pp. 65–70.

[Hay+50] M. Hayashi and K. Katsuki. “Absorption Spectrum of Cuprous Oxide.” *Journal of the Physical Society of Japan* **5** (1950), 380B–381.

[Hay+52] M. Hayashi and K. Katsuki. “Hydrogen-Like Absorption Spectrum of Cuprous Oxide.” *Journal of the Physical Society of Japan* **7** (1952), pp. 599–603.

[Hec+17a] J. Heckötter, M. Freitag, D. Fröhlich, M. Aßmann, M. Bayer, M. A. Semina, and M. M. Glazov. “High-resolution study of the yellow excitons in Cu_2O subject to an electric field.” *Physical Review B* **95** (2017), p. 035210.

[Hec+17b] J. Heckötter, M. Freitag, D. Fröhlich, M. Aßmann, M. Bayer, M. A. Semina, and M. M. Glazov. “Scaling laws of Rydberg excitons.” *Physical Review B* **96** (2017), p. 125142.

[Hec+18a] J. Heckötter, M. Freitag, D. Fröhlich, M. Aßmann, M. Bayer, P. Grünwald, F. Schöne, D. Semkat, H. Stolz, and S. Scheel. “Rydberg Excitons in the Presence of an Ultralow-Density Electron-Hole Plasma.” *Physical Review Letters* **121** (2018), p. 097401.

[Hec+18b] J. Heckötter, M. Freitag, D. Fröhlich, M. Aßmann, M. Bayer, M. A. Semina, and M. M. Glazov. “Dissociation of excitons in Cu_2O by an electric field.” *Physical Review B* **98** (2018), p. 035150.

[Hec+18c] J. Heckötter, J. Thewes, D. Fröhlich, M. Aßmann, and M. Bayer. “Landau-Level Quantization of the Yellow Excitons in Cuprous Oxide.” *Physics of the Solid State* **60** (2018), pp. 1625–1628.

[Hec+20] J. Heckötter, D. Janas, R. Schwartz, M. Aßmann, and M. Bayer. “Experimental limitation in extending the exciton series in Cu_2O towards higher principal quantum numbers.” *Physical Review B* **101** (2020), p. 235207.

[Hec+21] J. Heckötter, P. Rommel, J. Main, M. Aßmann, and M. Bayer. “Analysis of the Fine Structure of the D-Exciton Shell in Cuprous Oxide.” *physica status solidi (RRL) – Rapid Research Letters* **15** (2021), p. 2100335.

[Hec20] J. Heckötter. "Strongly interacting Rydberg excitons in Cu_2O." PhD thesis. TU Dortmund, 2020.

[Hög+05] G. B. H. von Högersthal, G. Dasbach, D. Fröhlich, M. Kulka, H. Stolz, and M. Bayer. "Dynamic band gap shifts and magneto-absorption of Cu_2O." *Journal of Luminescence*. 6th International Conference on Excitonic Processes in Condensed Matter (EXCON '04) **112** (2005), pp. 25–29.

[Ito+98] T. Ito, T. Kawashima, H. Yamaguchi, T. Masumi, and S. Adachi. "Optical Properties of Cu_2O Studied by Spectroscopic Ellipsometry." *Journal of the Physical Society of Japan* **67** (1998), pp. 2125–2131.

[Kam10] B. Kaminski. "New mechanisms of optical harmonic generation in semiconductors." PhD thesis. TU Dortmund, 2010.

[Kap+21] P. Kapuściński, A. Delhomme, D. Vaclavkova, A. O. Slobodeniuk, M. Grzeszczyk, M. Bartos, K. Watanabe, T. Taniguchi, C. Faugeras, and M. Potemski. "Rydberg series of dark excitons and the conduction band spin-orbit splitting in monolayer WSe_2." *Communications Physics* **4** (2021), pp. 1–6.

[Kav+97] G. M. Kavoulakis, Y.-C. Chang, and G. Baym. "Fine structure of excitons in Cu_2O." *Physical Review B* **55** (1997), pp. 7593–7599.

[Kaz+14] T. Kazimierczuk, D. Fröhlich, S. Scheel, H. Stolz, and M. Bayer. "Giant Rydberg excitons in the copper oxide Cu_2O." *Nature* **514** (2014), pp. 343–347.

[Kit04] C. Kittel. *Introduction to Solid State Physics*. Wiley, 2004.

[Kli12] C. F. Klingshirn. *Semiconductor Optics*. Berlin, Heidelberg: Springer, 2012.

[Kno63] R. S. Knox. *Theory of Excitons*. Academic Press, 1963.

[Kon+96] S. Kono, N. Naka, M. Hasuo, S. Saito, T. Suemoto, and N. Nagasawa. "Coherent optical processes of 1s ortho-excitons in Cu_2O by two-photon excitations." *Solid State Communications* **97** (1996), pp. 455–458.

[Kos+63] G. F. Koster, J. O. Dimmock, and R. G. Wheeler. *Properties of the Thirty-two Point Groups*. Cambridge, Massachusetts: M.I.T. Press, 1963.

[Krü+19] S. O. Krüger and S. Scheel. "Interseries transitions between Rydberg excitons in Cu_2O." *Physical Review B* **100** (2019), p. 085201.

[Kuw+77] G. Kuwabara, M. Tanaka, and H. Fukutani. "Optical absorption due to paraexciton of Cu_2O." *Solid State Communications* **21** (1977), pp. 599–601.

[Laf+13a] M. Lafrentz, D. Brunne, B. Kaminski, V. V. Pavlov, A. V. Rodina, R. V. Pisarev, D. R. Yakovlev, A. Bakin, and M. Bayer. "Magneto-Stark Effect of Excitons as the Origin of Second Harmonic Generation in ZnO." *Physical Review Letters* **110** (2013), p. 116402.

[Laf+13b] M. Lafrentz, D. Brunne, A. V. Rodina, V. V. Pavlov, R. V. Pisarev, D. R. Yakovlev, A. Bakin, and M. Bayer. "Second-harmonic generation spectroscopy of excitons in ZnO." *Physical Review B* **88** (2013), p. 235207.

[Laf13] M. Lafrentz. "Magnetic field induced optical harmonic generation in the semiconductors ZnO and EuX." PhD thesis. TU Dortmund, 2013.

[Liu+05] Y. Liu and D. Snoke. "Resonant two-photon excitation of 1s paraexcitons in cuprous oxide." *Solid State Communications*. Spontaneous Coherence in Excitonic Systems **134** (2005), pp. 159–164.

[Mai60] T. H. Maiman. "Stimulated Optical Radiation in Ruby." *Nature* **187** (1960), pp. 493–494.

[Mes21] S. Mesgary. "Differenzfrequenzerzeugung mit Zwei-Photonen-Anregung an Exzitonen der gelben Serie in Cu_2O." B. Sc. thesis. TU Dortmund, 2021.

[Mic+96] J. S. Michaelis, K. Unterrainer, E. Gornik, and E. Bauser. "Electric and magnetic dipole two-photon absorption in semiconductors." *Physical Review B* **54** (1996), pp. 7917–7920.

[Mor+22] Y. Morita, K. Yoshioka, and M. Kuwata-Gonokami. "Observation of Bose-Einstein condensates of excitons in a bulk semiconductor." *Nature Communications* **13** (2022), p. 5388.

[Mun+18] J. Mund, D. Fröhlich, D. R. Yakovlev, and M. Bayer. "High-resolution second harmonic generation spectroscopy with femtosecond laser pulses on excitons in Cu_2O." *Physical Review B* **98** (2018), p. 085203.

[Mun+19] J. Mund, C. Uihlein, D. Fröhlich, D. R. Yakovlev, and M. Bayer. "Second harmonic generation on the yellow 1S exciton in Cu_2O in symmetry-forbidden geometries." *Physical Review B* **99** (2019), p. 195204.

[Mun+20] J. Mund, D. R. Yakovlev, M. A. Semina, and M. Bayer. "Optical harmonic generation on the exciton-polariton in ZnSe." *Physical Review B* **102** (2020), p. 045203.

[Mun19] J. Mund. "Nonlinear optical spectroscopy of exciton-polaritons in Cu_2O, ZnSe and semiconductor quantum wells." PhD thesis. TU Dortmund, 2019.

[Mys+79] A. Mysyrowicz, D. Hulin, and A. Antonetti. "Long Exciton Lifetime in Cu_2O." *Physical Review Letters* **43** (1979), pp. 1123–1126.

[Mys+83] A. Mysyrowicz, D. P. Trauernicht, J. P. Wolfe, and H.-R. Trebin. "Stress dependence of the paraexciton in Cu_2O." *Physical Review B* **27** (1983), pp. 2562–2564.

[Nak+00] N. Naka and N. Nagasawa. "Experimental study on two-photon oscillator strength of hydrogenic yellow excitons in Cu_2O." *Solid State Communications* **116** (2000), pp. 417–419.

[Nak+02] N. Naka and N. Nagasawa. "Nonlinear paraexciton kinetics in a potential trap in Cu_2O under two-photon resonance excitation." *Physical Review B* **65** (2002), p. 245203.

[Nak+12] N. Naka, I. Akimoto, M. Shirai, and K.-i. Kan'no. "Time-resolved cyclotron resonance in cuprous oxide." *Physical Review B* **85** (2012), p. 035209.

[Nak+99] N. Naka and N. Nagasawa. "High precision two-photon spectroscopy on emission of 1s ortho-excitons in Cu_2O." *Solid State Communications* **110** (1999), pp. 153–157.

[NIS23] NIST. “National Institute of Standards and Technology: Atomic Spectra Database Lines Form” (2023). URL: https://physics.nist.gov/PhysRefData/ASD/lines_form.html.

[Nol11] W. Nolting. *Grundkurs Theoretische Physik 3.* Springer Berlin Heidelberg, 2011.

[Nol17] W. Nolting. *Theoretical Physics 6.* Cham: Springer International Publishing, 2017.

[Pas+91] A. Pasquarello and A. Quattropani. “Polarization dependence of multiphoton transitions.” *Physical Review B* **43** (1991), pp. 3837–3846.

[Pas61] I. Pastrnyak. “Absorption, reflection, and nature of the electron optical transitions in Cu_2O crystals.” *Soviet Physics Solid State* **3** (1961), p. 633.

[Pei+09] F. Pei, S. Wu, G. Wang, M. Xu, S.-Y. Wang, L.-Y. Chen, and Y. Jia. “Electronic and Optical Properties of Noble Metal Oxides M_2O (M = Cu, Ag and Au): First-principles Study.” *Journal of the Korean Physical Society* **55** (2009), pp. 1243–1249.

[Poe+10] E. Poem, Y. Kodriano, C. Tradonsky, N. H. Lindner, B. D. Gerardot, P. M. Petroff, and D. Gershoni. “Accessing the dark exciton with light.” *Nature Physics* **6** (2010), pp. 993–997.

[Rom+18] P. Rommel, F. Schweiner, J. Main, J. Heckötter, M. Freitag, D. Fröhlich, K. Lehninger, M. Aßmann, and M. Bayer. “Magneto-Stark effect of yellow excitons in cuprous oxide.” *Physical Review B* **98** (2018), p. 085206.

[Rom+20a] P. Rommel, J. Main, A. Farenbruch, J. Mund, D. Fröhlich, D. R. Yakovlev, M. Bayer, and C. Uihlein. “Second harmonic generation of cuprous oxide in magnetic fields.” *Physical Review B* **101** (2020), p. 115202.

[Rom+20b] P. Rommel, P. Zielinski, and J. Main. “Green exciton series in cuprous oxide.” *Physical Review B* **101** (2020), p. 075208.

[Rom+21] P. Rommel, J. Main, A. Farenbruch, D. R. Yakovlev, and M. Bayer. “Exchange interaction in the yellow exciton series of cuprous oxide.” *Physical Review B* **103** (2021), p. 075202.

[Sän+06a] I. Sänger, B. Kaminski, D. R. Yakovlev, R. V. Pisarev, M. Bayer, G. Karczewski, T. Wojtowicz, and J. Kossut. “Magnetic-field-induced second-harmonic generation in the diluted magnetic semiconductors $Cd_{1-x}Mn_xTe$.” *Physical Review B* **74** (2006), p. 235217.

[Sän+06b] I. Sänger, D. R. Yakovlev, B. Kaminski, R. V. Pisarev, V. V. Pavlov, and M. Bayer. “Orbital quantization of electronic states in a magnetic field as the origin of second-harmonic generation in diamagnetic semiconductors.” *Physical Review B* **74** (2006), p. 165208.

[San+11] C. Sandfort, J. Brandt, C. Finke, D. Fröhlich, M. Bayer, H. Stolz, and N. Naka. “Paraexcitons of Cu_2O confined by a strain trap and high magnetic fields.” *Physical Review B* **84** (2011), p. 165215.

[Sän06] I. Sänger. “Magnetic-field-induced second harmonic generation in semiconductors and insulators.” PhD thesis. TU Dortmund, 2006.

[Sch+13] J. Schmutzler, D. Fröhlich, and M. Bayer. "Signatures of coherent propagation of blue polaritons in Cu_2O." *Physical Review B* **87** (2013), p. 245202.

[Sch+16a] F. Schöne, S.-O. Krüger, P. Grünwald, H. Stolz, S. Scheel, M. Aßmann, J. Heckötter, J. Thewes, D. Fröhlich, and M. Bayer. "Deviations of the exciton level spectrum in Cu_2O from the hydrogen series." *Physical Review B* **93** (2016), p. 075203.

[Sch+16b] F. Schweiner, J. Main, M. Feldmaier, G. Wunner, and C. Uihlein. "Impact of the valence band structure of Cu_2O on excitonic spectra." *Physical Review B* **93** (2016), p. 195203.

[Sch+17a] F. Schweiner, J. Main, G. Wunner, M. Freitag, J. Heckötter, C. Uihlein, M. Aßmann, D. Fröhlich, and M. Bayer. "Magnetoexcitons in cuprous oxide." *Physical Review B* **95** (2017), p. 035202.

[Sch+17b] F. Schweiner, J. Main, G. Wunner, and C. Uihlein. "Even exciton series in Cu_2O." *Physical Review B* **95** (2017), p. 195201.

[Sem+19] D. Semkat, H. Fehske, and H. Stolz. "Influence of electron-hole plasma on Rydberg excitons in cuprous oxide." *Physical Review B* **100** (2019), p. 155204.

[Sha+15] S. Sharma, K. Jain, and A. Sharma. "Solar Cells: In Research and Applications—A Review." *Materials Sciences and Applications* **06** (2015), pp. 1145–1155.

[She+96] M. Y. Shen, S. Koyama, M. Saito, T. Goto, and N. Kuroda. "Second-harmonic generation resonant to the 1S orthoexciton level of cuprous oxide." *Physical Review B* **53** (1996), pp. 13477–13481.

[She84] Y. R. Shen. *The Principles of Nonlinear Optics*. New York: Wiley, 1984.

[Sno+14] D. Snoke and G. M. Kavoulakis. "Bose–Einstein condensation of excitons in Cu_2O: progress over 30 years." *Reports on Progress in Physics* **77** (2014), p. 116501.

[Sto+18] H. Stolz, F. Schöne, and D. Semkat. "Interaction of Rydberg excitons in cuprous oxide with phonons and photons: optical linewidth and polariton effect." *New Journal of Physics* **20** (2018), p. 023019.

[Tai72] W. C. Tait. "Quantum Theory of a Basic Light-Matter Interaction." *Physical Review B* **5** (1972), pp. 648–661.

[Tak+18] M. Takahata and N. Naka. "Photoluminescence properties of the entire excitonic series in Cu_2O." *Physical Review B* **98** (2018), p. 195205.

[The+15] J. Thewes, J. Heckötter, T. Kazimierczuk, M. Aßmann, D. Fröhlich, M. Bayer, M. A. Semina, and M. M. Glazov. "Observation of High Angular Momentum Excitons in Cuprous Oxide." *Physical Review Letters* **115** (2015), p. 027402.

[Tho+60] D. G. Thomas and J. J. Hopfield. "Direct Observation of Exciton Motion in CdS." *Physical Review Letters* **5** (1960), pp. 505–507.

[Tho+61] D. G. Thomas and J. J. Hopfield. "A Magneto-Stark Effect and Exciton Motion in CdS." *Physical Review* **124** (1961), pp. 657–665.

[Uca22] G. Uca. "Differenzfrequenzerzeugung mit Zwei-Photonen-Anregung an magnetfeldgekoppelten 1S-Exziton-Komponenten der gelben Serie in Cu_2O." B. Sc. thesis. TU Dortmund, 2022.

[Uih+81] C. Uihlein, D. Fröhlich, and R. Kenklies. "Investigation of exciton fine structure in Cu_2O." *Physical Review B* **23** (1981), pp. 2731–2740.

[Ver+21] M. A. M. Versteegh, S. Steinhauer, J. Bajo, T. Lettner, A. Soro, A. Romanova, S. Gyger, L. Schweickert, A. Mysyrowicz, and V. Zwiller. "Giant Rydberg excitons in Cu_2O probed by photoluminescence excitation spectroscopy." *Physical Review B* **104** (2021), p. 245206.

[Wal+18] V. Walther, S. O. Krüger, S. Scheel, and T. Pohl. "Interactions between Rydberg excitons in Cu_2O." *Physical Review B* **98** (2018), p. 165201.

[Wan37] G. H. Wannier. "The Structure of Electronic Excitation Levels in Insulating Crystals." *Physical Review* **52** (1937), pp. 191–197.

[War+18] W. Warkentin, J. Mund, D. R. Yakovlev, V. V. Pavlov, R. V. Pisarev, A. V. Rodina, M. A. Semina, M. M. Glazov, E. L. Ivchenko, and M. Bayer. "Third harmonic generation on exciton-polaritons in bulk semiconductors subject to a magnetic field." *Physical Review B* **98** (2018), p. 075204.

[Yak+18] D. R. Yakovlev, V. V. Pavlov, A. V. Rodina, R. V. Pisarev, J. Mund, W. Warkentin, and M. Bayer. "Exciton Spectroscopy of Semiconductors by the Method of Optical Harmonics Generation (Review)." *Physics of the Solid State* **60** (2018), pp. 1471–1486.

[Yos+06] K. Yoshioka and M. Kuwata-Gonokami. "Dark excitons in Cu_2O crystals for two-photon coherence storage in semiconductors." *Physical Review B* **73** (2006), p. 081202.

[Zhi+69] A. G. Zhilich, J. Halpern, and B. P. Zakharchenya. "Magnetoabsorption Oscillations and the Zeeman Effect of Excitons for Forbidden Interband Transitions in Cu_2O Crystals." *Physical Review* **188** (1969), pp. 1294–1302.

[Zie+19] S. Zielińska-Raczyńska, D. A. Fishman, C. Faugeras, M. M. P. Potemski, P. H. M. v. Loosdrecht, K. Karpiński, G. Czajkowski, and D. Ziemkiewicz. "Magneto-excitons in Cu_2O: theoretical model from weak to high magnetic fields." *New Journal of Physics* **21** (2019), p. 103012.

[Zie+21] D. Ziemkiewicz, G. Czajkowski, K. Karpiński, and S. Zielińska-Raczyńska. "Rydberg magnetoexcitons in Cu_2O quantum wells." *Physical Review B* **103** (2021), p. 035305.

List of Publications

[Far+20a] **A. Farenbruch**, D. Fröhlich, D. R. Yakovlev, and M. Bayer. "Two-photon absorption and second harmonic generation of $1S$ para- and orthoexcitons in Cu_2O coupled by a magnetic field." *Physical Review B* **102** (2020), p. 115203.

[Far+20b] **A. Farenbruch**, J. Mund, D. Fröhlich, D. R. Yakovlev, M. Bayer, M. A. Semina, and M. M. Glazov. "Magneto-Stark and Zeeman effect as origin of second harmonic generation of excitons in Cu_2O." *Physical Review B* **101** (2020), p. 115201.

[Far+20c] **A. Farenbruch**, D. Fröhlich, D. R. Yakovlev, and M. Bayer. "Rydberg Series of Dark Excitons in Cu_2O." *Physical Review Letters* **125** (2020), p. 207402.

[Far+21] **A. Farenbruch**, D. Fröhlich, H. Stolz, D. R. Yakovlev, and M. Bayer. "Second harmonic generation of blue series excitons and magnetoexcitons in Cu_2O." *Physical Review B* **104** (2021), p. 075203.

[Rom+21] P. Rommel, J. Main, **A. Farenbruch**, D. R. Yakovlev, and M. Bayer. "Exchange interaction in the yellow exciton series of cuprous oxide." *Physical Review B* **103** (2021), p. 075202.

[Rom+20a] P. Rommel, J. Main, **A. Farenbruch**, J. Mund, D. Fröhlich, D. R. Yakovlev, and M. Bayer. "Second harmonic generation of cuprous oxide in magnetic fields" *Physical Review B* **101** (2021), p. 115202.

[Mun+20] J. Mund, **A. Farenbruch**, D. R. Yakovlev, A. A. Maksimov, A. Waag, and M. Bayer. "Optical second- and third-harmonic generation on excitons in ZnSe/BeTe quantum wells" *Physical Review B* **102** (2020), p. 125433.

D. Semkat, H. Stolz, P. Grünwald, **A. Farenbruch**, N. Siverin, D. Fröhlich, D. R. Yakovlev, and M. Bayer. "Interaction between Rydberg excitons in cuprous oxide revealed through second harmonic generation" Submitted to *Physical Review B*

J. Heckötter, **A. Farenbruch**, D. Fröhlich, M. Aßmann, D. R. Yakovlev, M. Bayer, M. A. Semina and M. M. Glazov, P. Rommel, J. Ertl, and J. Main, H. Stolz. "The energy level spectrum of the yellow exciton series in cuprous oxide" close to submission in *Physics Reports*

List of Symbols

symbol	meaning
$\mathbf{A}$	vector potential
A_0	amplitude of the plane wave for the vector potential
a_B^X	hydrogen Bohr radius
a_B^H	hydrogen Bohr radius
a_{lat}	lattice constant
a	magnetic field mixing parameter between $M = 0$ orthoexciton and paraexciton
$\mathbf{B}$	magnetic flux density
B_i	spatial components of magnetic field
B_{cross}	crossover magnetic field, at which magnetic length is equal to exciton radius
c	speed of light in vacuum
$\mathbf{D}$	electric displacement
d	laser beam diameter
d_i	components of the electric dipole vector
$d_{n,L}$	diamagnetic shift parameter
$\mathbf{E}$	electric field strength
E_0	amplitude of electric field wave
E_i	spatial components of electric field
E_g	band gap
$E_{g,\mathrm{y}}$	bandgap of yellow transitions
$E_{g,\mathrm{g}}$	bandgap of green transitions
$E_{g,\mathrm{b}}$	bandgap of blue transitions
$E_{g,\mathrm{v}}$	bandgap of violet transitions
e	elementary charge
$\mathbf{e}$	unit vector of polarization
$E_{\mathrm{CB}}(k)$	dispersion relation of the conduction band
$E_n^X(\mathbf{K})$	exciton dispersion
E_{kin}	kinetic energy
E_{bind}	exciton binding energy
$E_{\mathrm{Ryd}}^{\mathrm{X}}$	Rydberg energy of an exciton
$E_{\mathrm{Ryd}}^{\mathrm{H}}$	Rydberg energy of a hydrogen atom
ΔE_{LT}	longitudinal transverse splitting
E_R	Rabi energy

$\Delta E_{\mathrm{ZE,spin}}$	energy splitting of spin Zeeman effect
$\Delta E_{\mathrm{ZE,orbit}}$	energy splitting of orbital Zeeman effect
E_{MSE}	effective electric field of the magneto-Stark effect
$E_{\mathrm{c},n_{\mathrm{L}}}$	cyclotron energy
$\|\uparrow_e\rangle$	spin up electron state in conduction band
$\|\downarrow_e\rangle$	spin down electron state in conduction band
E_{1S_p}	zero field energy of paraexciton
$E_p(B)$	magnetic field dependent energy of paraexciton
$E_{o,0}(B)$	magnetic field dependent energy of $M = 0$ orthoexciton
$E_{o,\pm1}(B)$	magnetic field dependent energy of $M = \pm1$ orthoexciton
$E_{\mathrm{LO,i}}$	Energy of longitudinal optical phonons
$E_{\mathrm{TO,i}}$	Energy of transverse optical phonons
E_{DFG}	energy of difference frequency generation photon
$\Delta E_{+1,-1}$	splitting energy between the $M = +1$ and $M = -1$ orthoexciton states
$\Delta E_{+1,0}$	splitting energy between the $M = +1$ and $M = 0$ orthoexciton states
$\Delta E_{0,-1}$	splitting energy between the $M = 0$ and $M = -1$ orthoexciton states
$\mathbf{F}_{\mathrm{L}}$	Lorentz force
f_i	focal length of a lens
A_i	aperture of a spectrometer
f_p	oscillator strength of paraexciton
f	beat frequency
g_e	Landé factor of electron
g_h	Landé factor of hole
G	grating width
g_c	Landé factor of conduction band
g_v	Landé factor of valence band
$\hbar$	reduced planck constant
$\mathbf{H}$	magnetic field strength
$\mathbf{H}_{\mathrm{el}}$	Hamiltonian of an electron in a crystal potential
$\mathbf{H}_{\mathrm{int}}$	Hamiltonian of an electron interacting with a light wave
$\mathbf{H}_{\mathrm{dia}}$	Hamiltonian of an electron affected by the diamagnetic shift
$\mathbf{H}_{\mathrm{exch}}$	Hamiltonian for exchange interaction between spin-singlet and spin-triplet states
$\mathbf{H}_{\mathrm{B}}(a,b,B)$	Hamiltonian for magnetic-field coupled $1S$ exciton states
$H_{g\to e}^{\mathrm{int}}$	transition probability
$\langle r_{n,l}^2 \rangle$	average of squared exciton radius
$\|\uparrow_H\rangle$	spin-orbit coupled hole state in valence band with spin up
$\|\downarrow_H\rangle$	spin-orbit coupled hole state in valence band with spin up
$\|\uparrow_h\rangle$	spin up hole state in valence band
$\|\downarrow_h\rangle$	spin down hole state in valence band
$I_{\mathrm{st/u}}^{i\pm}$	SHG intensity for a jk excitation and u emission [j,k,u can be D

	(electric dipole), Q (electric quadrupole with Γ_5^+ symmetry), Q3 (electric quadrupole with Γ_3^+ symmetry) or MD (magnetic dipole)] process on a $\Gamma_i^\pm$ symmetry state
$I_{\mathrm{st/uv}}^{i\pm}$	2P-DFG intensity for a jk excitation and uv emission [j,k,u can be D (electric dipole), Q (electric quadrupole with Γ_5^+ symmetry), Q3 (electric quadrupole with Γ_3^+ symmetry) or MD (magnetic dipole)] process on a $\Gamma_i^\pm$ symmetry state
$I_{\mathrm{st/u}}^{i\pm Fj\pm}$	SHG intensity for a jk excitation and u emission [j,k,u can be D (electric dipole), Q (electric quadrupole with Γ_5^+ symmetry), Q3 (electric quadrupole with Γ_3^+ symmetry) or MD (magnetic dipole)] process on a $\Gamma_i^\pm$ symmetry state, which is coupled to a $\Gamma_j^\pm$ symmetry state by a field F [can be magnetic field B or electric field E]
$\mathbf{j}$	electrical current density
$\bar{J}_0$	exchange interaction strength
$\mathbf{k}$	wave vector of light
$\mathbf{K}$	wave vector of exciton
k	wave number of light
$\mathbf{k}_{\omega_i}$	wave vector of light with a frequency ω_i
$\mathbf{k}_e$	wave vector of electron
$\mathbf{k}_h$	wave vector of hole
k_i	components of the wave vector of light
L	angular momentum quantum number
l_n	magnetic length
$\mathbf{M}$	magnetization density in a medium
m_0	electron mass
m_e	effective electron mass in the conduction band
M	total mass of exciton or magnetic quantum number
M_{y}	total mass of yellow-series excitons
μ	reduced mass of exciton
$\mathbf{M}_{\mathrm{rot}}$	rotation matrix
m_i	components of the magnetic dipole vector
$\mathbf{M}_B(a,b,\mathbf{B})$	magnetic field mixing matrix for the $1S$ ortho and paraexciton states
M_{1S2P}	magneto-Stark effect mixing parameter between the $1S$ and $2P$ excitons
$m_{\mathbf{K}}^{8C}$	effective mass of an electron in the Γ_8^- conduction band along the crystal direction $\mathbf{K}$
m^{7V}	effective mass of a hole in the Γ_7^+ valence band
$\mu_{\mathbf{K}}^{\mathrm{eh}}$	reduced exciton mass along the crystal direction $\mathbf{K}$
n	principal quantum number
n_L	Landau level quantum number

n_{air}	refractive index of air
n_b	refractive index at half of the exciton energy related to the background dielectric constant
$O_{\text{st}}^{i\pm}$	operator for a st [s,t can be D (electric dipole), Q (electric quadrupole with Γ_5^+ symmetry), Q3 (electric quadrupole with Γ_3^+ symmetry) or MD (magnetic dipole)] transition to a $\Gamma_i^\pm$ symmetry state
$O_{\text{st}}^{i\pm\text{F}l\pm}$	operator for a st [s,t can be D (electric dipole), Q (electric quadrupole with Γ_5^+ symmetry), Q3 (electric quadrupole with Γ_3^+ symmetry) or MD (magnetic dipole)] transition to a $\Gamma_i^\pm$ symmetry state coupled by the field F [can be magnetic field B or electric field E] to a $\Gamma_l^\pm$ symmetry state
$\lvert O_{xy}\rangle$	ortho exciton state
$\mathbf{P}$	polarization density vector in a medium
$\mathbf{P}^{(2)}$	polarization density vector of second order in a medium
$\mathbf{P}_{\text{2P-DFG}}^{(3)}$	2P-DFG terms of third order polarization density vector in a medium
P_i	spatial components of polarization density vector
$\mathbf{p}$	electron momentum
$\lvert P\rangle$	para exciton state
q	electric charge
q_i	components of the Γ_5^+ electric quadrupole vector
$q_{3,i}$	components of the Γ_3^+ electric quadrupole vector
$\mathbf{r}$	position in space
$\mathbf{r}_e$	electron position in space
$\mathbf{r}_h$	hole position in space
r_n^X	exciton radius
$\lvert S\rangle$	spin-singlet state
S	total Spin of combined electron and hole spins
$s_{\mathbf{K},n}$	slope parameter of magneto-exciton magnetic shift for motion along crystal direction $\mathbf{K}$
t	time
t_{delay}	delay time between ps and fs pulses
$\lvert T_i\rangle$	spin-triplet state
$t_{\text{coherence}}$	coherence time of a two-photon excited exciton
T	beat period
$\mathbf{v}$	velocity
$\mathbf{v}_{\text{g}}$	group velocity
$\mathbf{v}_{\text{ph}}$	phase velocity

V	periodic crystal potential
V_{uc}	volume of unit cell
$w_{g\to e}$	optical transition rate between the ground state and an excited state
$w^{\mathrm{SHG}}_{g\to v\to e\to g}$	optical transition rate for SHG process
x	retro-reflector position
$\mathbf{X}$	horizontal crystal direction perpendicular to the excitation light direction
$\mathbf{Y}$	vertical crystal direction
$\mathbf{Z}$	horizontal crystal direction along the excitation light direction
β	oscillator strength density per unit cell
β_{y}	oscillator strength density per unit cell of yellow transitions
β_{b}	oscillator strength density per unit cell of blue transitions
$\Gamma_i^{\pm}$	irreducible representation with index i and even or odd parity + or −
γ	radiative damping
δ	quantum defect
$\delta(r)$	probability density of electron and hole at postition r
ε_0	permittivity of vacuum
ε_r	permittivity of a medium
ε_s	static dielectric constant
ε_b	background dielectric constant
ε	exchange energy
$\tilde{\varepsilon}$	dielectric constant, influenced by optical phonons
θ	linear polarization angle of the stimulation laser light
λ	wavelength of light
$\Lambda_i(B)$	eigenvector of $1S$ state i in a magnetic field B
μ_0	permeability of vacuum
μ_r	permeability of a medium
μ_B	Bohr magneton
μ_{y}	reduced mass of yellow excitons
π	ratio of circumference to diameter of a circle
ρ	charge density
$\rho(E_e)$	density of states at energy of excited states

φ	linear polarization angle of the signal (SHG or 2P-DFG) light
ϕ_{xy}	Wannier function from Cu $3d$ orbital
χ	electric susceptibility
χ_m	magnetic susceptibility
$\chi_{ij}^{(1)}$	spatial components of electirc susceptibility tensor of first order
$\chi_{ijk}^{(2)}$	spatial components of electirc susceptibility tensor of second order
$\lvert\psi_g\rangle$	ground state
$\lvert\psi_e\rangle$	excited state
$\lvert\psi_v\rangle$	virtual state
ψ_e	wave function of electron
ψ_h	wave function of hole
ψ_X	wave function of exciton
$\psi_{n,l,m}^{\mathrm{env}}$	envelope function
ψ	linear polarization angle of the excitation laser light
ω	photon frequency
ω_X	exciton frequency
Ω_R	Rabi frequency
$\omega_{\mathrm{c,e}}$	cyclotron frequency of an electron
$\omega_{\mathrm{c,h}}$	cyclotron frequency of a hole

List of Abbreviations

Abbreviation	meaning
SHG	second harmonic generation
DFG	difference frequency generation
1P-DFG	difference frequency generation with one-photon excitation
2P-DFG	difference frequency generation with two-photon excitation
ED	electric dipole
EQ	electric quadrupole
MD	magnetic dipole
EQ3	electric quadrupole with Γ_3^+ symmetry
MSE	magneto-Stark effect
ZE	Zeeman effect
CB	conduction band
VB	valence band
UPB	upper polariton branch
LPB	lower polariton branch
OPA	optical parametric amplifier
SHBC	second harmonic bandwidth compressor
GT	Glan-Thompson prism
VTI	variable temperature insert
CCD	charge-coupled device
BBO	barium beta borate
2D	two-dimensional
FT	Fourier transform
FFT	fast Fourier transform
FWHM	full width at half maximum

Acknowledgments

At this point, I would like to express my sincere gratitude to everyone, who supported me during this exciting time as a PhD student.

First of all, I would like to extend my deepest gratitude to Prof. Dr. em. Dietmar Fröhlich for the generosity with his time and expertise. His knowledge and enthusiasm for Cu_2O, group theory and experimental physics have been remarkably motivating. I am grateful for the many hours of interesting discussions and experiments we had in the lab. My special thanks go to my doctoral supervisor Prof. Dr. Dmitri R. Yakovlev, who has given me the opportunity to work in his research group and provided his guidance and support at all times. I also thank Prof. Dr. Manfred Bayer for his knowledgeable input and the joint effort in the search for the Rydberg series of dark excitons. I would also like to acknowledge my cooperation colleagues Prof. Dr. Heinrich Stolz, Dr. Marina Semina, Prof. Dr. Mikhail Glazov, Dr. Patric Rommel and Prof. Dr. Jörg Main, for the fruitful discussions and their valuable contributions to our joint scientific projects.

I thank all of my E2 colleagues for the pleasant atmosphere, the interesting discussions and the support I have received in many forms. The free time activities have made this time more enjoyable and fulfilling. I am grateful to Johannes Mund for his excellent supervision during my Bachelor and Master theses, which provided me with the foundational lab skills required for my research. I thank Julian Heckötter for the exchange of ideas about excitons in Cu_2O. The time and experiences with Erik Kirstein and Stefan Grisard in Singapore and Australia during the ICPS are unforgettable. I thank Nikita Siverin for working with me in the lab and improving the setup with his matlab programs. The company of Aleksandr Kamenskii during late-night measurements is greatly appreciated. I am thankful for my Bachelor students Shabnam Mesgary and Gülistan Uca, who have given me the opportunity to develop my supervision skills. My PhD would not have been possible without the administrative work and support by Michaela Wäscher and Katharina Goldack and the reliable supply of liquid helium and nitrogen by Lars Wieschollek and Daniel Tüttmann.

Finally, I would like to express my appreciation for my parents for their endless support and patience and to all of my friends, who provided me with enjoyable and stress-relieving experiences to maintain a healthy balance in my life. A special thanks to Egor Evsenin for supporting and pushing me through more stressful times, especially in the final stages of my thesis writing process.